Label free imaging of biological samples using mass spectrometry imaging and Stimulated Raman scattering microscopy

Jan Majer

PhD Thesis

School of Biosciences

Cardiff University

August 2023

This thesis is the result of my own independent work, except where otherwise stated, and the views expressed are my own. Other sources are acknowledged by explicit references. The thesis has not been edited by a third party beyond what is permitted by Cardiff University's Use of Third Party Editors by Research Degree Students Procedure.

This thesis is being submitted in partial fulfilment of the requirements for the degree of Doctor of Philosophy (PhD).

This work has not been submitted in substance for any other degree or award at this or any other university or place of learning, nor is it being submitted concurrently for any other degree or award (outside of any formal collaboration agreement between the University and a partner organisation).

I hereby give consent for my thesis, if accepted, to be available in the University’s Open Access repository (or, where approved, to be available in the University's library and for inter-library loan), and for the title and summary to be made available to outside organisations, subject to the expiry of a University-approved bar on access if applicable.

Acknowledgements

I would like to express my deepest gratitude to my supervisor and manager, Dr Steve Hood (GSK), for giving me this research opportunity and for his steady support and exceptional guidance throughout the past four years.

I would also like to thank my supervisors, Dr Peter Marshall (GSK) and Dr Nisha Mistry (GSK), who granted me the use of their instruments and also provided me with invaluable insight, training, and words of encouragement without which I would not reach this stage of my career.

I am grateful to my academic supervisor at Cardiff University, Prof Peter Watson, for his guidance and support he provided me with throughout my studies.

I want to thank all my supervisors for creating and maintaining a friendly and supportive work environment, especially during difficult times during lockdown. On that note, I want to thank everyone in the 2S133 office in Stevenage, who I have been working alongside, and drank litres of coffee during my time in the Bioimaging group at GSK. Special thanks go to the great team of people in the Dr Watson group at Cardiff University, who introduced me to Guardian crosswords.

I am grateful for the privilege to meet and build a network of colleagues and friends among the MUSIQ consortium students, supervisors, and partners who made this PhD a great experience both in and out of working hours.

I want to thank my family in Pilsen for their long-term unwavering support and for always encouraging me to study and pursue my interests.

Finally, I would like to extend my heartfelt appreciation to my partner, Tez, for choosing to move from Prague to Stevenage with me, and for the understanding, patience, and belief in me during the past few stressful months of the write-up.

This project received funding from the European Union's Horizon 2020 Research and Innovation Programme under the Marie Sklodowska-Curie grant agreement no. 812992.

Table of content

Abstract ii

List of abbreviations iii

List of figures vi

List of tables ix

1. Introduction 1

1.1. Label-free imaging 1

1.2. Optical methodologies 4

1.2.1. Fluorescence microscopy and fluorescent labels 4

1.2.2. Raman spectroscopy 5

1.2.3. Other nonlinear microscopy methods 15

1.3. Mass spectrometry 17

1.3.1. Ionisation techniques 18

1.3.2. Ion separation techniques 24

1.4. Complex *in vitro* models (CIVMs) 26

1.5. Physicochemical properties of small analytes 28

2. Aims and experimental 31

3. Materials and methods 33

3.1. Cell culture 33

3.1.1. Preparation of imaging slides of cell samples 34

3.1.2. API treatment of cells 34

3.1.3. Cell sample processing 35

3.2. Mimetic model preparation 35

3.3. Cryosectioning 36

3.4. DIUTHAME application 37

3.5. Matrix and solvent deposition 38

3.6. Mass spectrometry 39
3.6.1. Mass spectra acquisition 39
3.6.2. Mass spectrometry imaging 41
3.6.3. Peak picking in MS spectra 41
3.7. Spontaneous Raman spectroscopy 41
3.8. Lightsheet microscopy 42
3.8.1. Sample preparation 42
3.8.2. Microscope imaging settings 43
3.9. Stimulated Raman scattering microscopy 43
3.10. SRS data processing 45
3.10.1. FFT line scan artifact removal 46
3.10.2. XYZ drift correction of hyperspectral SRS images 47
3.10.3. SVD denoising of hyperspectral SRS data 48
3.10.4. LAS X tile stitching 49
3.11. Data analysis of hSRS 50
3.11.1. NMF-based component separation with sklearn 50
3.11.2. Cell type classification with SRS spectra using machine learning 51
4. Identification of samples suitable for SRS-MALDI translation method development 54
4.1. Introduction 54
4.2. MALDI MS of pure test compounds 58
4.3. MALDI MS of tool compounds in tissues 63
4.4. MALDI MS of tool compounds in cell culture 72
4.5. Raman analysis of pure tool compounds 76
4.6. SRS analysis of tool compounds in tissues 80
4.7. Raman analysis of tool compounds in cell culture 84
4.8. Discussion 86

4.8.1. Physicochemical properties with MALDI 87
4.8.2. Physicochemical properties with SRS 89
4.8.3. GSK4 and GSK90 in cell cultures 90
5. Translation of biological samples from Stimulated Raman scattering microscopy to laser desoprtion/ionisation mass spectrometry imaging 92
5.1. Introduction 92
5.2. Optimisation of the SRS system for tissue imaging 94
5.2.1. Conductive materials in SRS microscopy 94
5.2.2. Comparison animal tissues in aqueous and dry environments in SRS microscopy 96
5.2.3. Stimulated Raman histology 98
5.2.4. Stimulated Raman histology of full tissue sections 103
5.2.5. Effect of different solutions on tissue morphology 106
5.3. Application of conductive materials on glass slide surfaces 114
5.3.1. Copper-tape glass slide modification in MALDI 114
5.3.2. DIUTHAME as a candidate for SRS-to-MSI 119
5.3.3. Evaluation of DIUTHAME in murine brain 123
5.3.4. Development of DIUTHAME application with improved analyte extraction 127
5.3.5. Comparison of MALDI and SALDI MSI in murine kidney 134
5.3.6. Evaluation of DIUTHAME in SALDI MSI of cells 137
5.4. Translation of the same sample between SRS and SALDI MSI 142
6. Imaging of liver-on-chip complex *in vitro* models 151
6.1. Characterisation of liver CIVM scaffolds with fluorescence and SRS microscopy 152
6.2. Cell classification in CIVM scaffolds with hyperspectral SRS 158
6.3. CIVM imaging with light sheet microscopy 164
6.4. Mass spectrometry imaging of liver CIVM scaffolds 168
7. SRS-based cell segmentation with the Leica SP8 176

7.1. Introduction 176
7.2. SRS and SHG of cell monocultures and tricultures 177
7.3. Cell classification with SRS spectra 182
7.4. Chapter summary 189
8. Discussion and future perspectives 191
8.1. Identification of samples suitable for SRS-LDI translation method development 191
8.1.1. Physicochemical properties in MALDI 192
8.1.2. Physicochemical properties in SRS 194
8.1.3. GSK4(x) and GSK90 in cell cultures 196
8.2. Translation of biological samples from SRS microscopy to MALDI/SALDI MS 198
8.2.1. Conductive materials in SRS microscopy 198
8.2.2. SRS microscopy of tissues in an aqueous sample chamber 201
8.2.3. SRS-to-MSI with DIUTHAME 204
8.3. Imaging of liver organ-on-chip complex *in vitro* models 205
8.4. SRS-based cell segmentation with the Leica SP8 207
8.5. Future perspectives 209
9. References 213
Appendix 237

Abstract

Unlike fluorescence microscopy techniques, label-free imaging techniques avoid perturbation of the biological environment, which enable the analysis of samples in their native state. Label-free imaging methods for tissues and cells rely on the intrinsic properties of a sample to generate an image contrast. Laser desorption ionisation mass spectrometry imaging (LDI MSI) is a label-free technique that allows visualisation of sample composition based on analyte mass. Stimulated Raman scattering (SRS) microscopy, also label free, uses the vibrational properties of molecular bonds in a sample to generate images. This work describes the combination of LDI MSI and SRS imaging to improve the precision of the characterisation of the chemical components in a single sample based on their mass and vibrational properties. However, the conductive LDI slides required necessary for the ionisation process in LDI MSI, caused interference during SRS microscopy. The LDI-slide intrinsic interference required a replacement of LDI slides with standard non-conductive glass slides and an adhesive and conductive DIUTHAME membranes. Use of DIUTHAME bypassed the incompatibility issues and allowed the first described SRS and LDI MSI analyses of the same tissue sample. LDI MSI and SRS microscopy were successfully applied in the imaging of 2D cell cultures and complex *in vitro* models (CIVMs). SRS microscopy of heterocultures classified the individual cell types and cell phenotypes based on hyperspectral data from a small region of the Raman spectrum. The variability in the cell phenotype in hepatocyte CIVMs was also associated with differences in the intracellular antisense oligo (ASO) distribution. Thus, a successful approach for SRS-to-LDI MSI analysis of a single sample was achieved. This was applied in tissues and has great potential for applications in cell cultures and CIVMs. It is also demonstrated that SRS microscopy shows potential for the classification of cells based on their chemical composition.

List of abbreviations

(N)IR	(Near) infra-red
2PEF	2-photon excitation fluorescence
3PEF	3-photon excitation fluorescence
API	Active pharmaceutical ingredient
ASO	antisense oligonucleotide
BSL2	Biosafety level 2
C≡C	Alkyne bond
C≡N	Nitrile bond
CaCO-2	Human colon carcinoma cell line
CARS	Coherent anti-Stokes Raman scattering
CCD	Charge-coupled device
C-D	Carbon-deuterium bond
CH_3 - CH_2	CH_3 minus CH_2
CIVM	Complex *in vitro* model
ConA	Concanavalin A
CRS	Coherent Raman scattering
DCS	Developability classification system
DESI	Desorption electrospray ionisation
DIC	Differential interference contrast
DIUTHAME	Desorption ionisation using through hole alumina membrane
DMEM	Dulbecco's minimal essential medium
EdU	5-ethynyl-2'-deoxyuridine
ESI	Electrospray ionisation
FBS	Foetal bovine serum
FFPE	Formalin-fixed, paraffin embedded
FFT	Fast Fourier transformation
FLIM	Fluorescence lifetime imaging microscopy
FSC^3	Factorisation into spectra and concentrations of chemical components
FTICR	Fourier transform ion cyclotron resonance
GalCer	Galactosyl ceramide
GUI	Graphic user interface

H&E	Haematoxylin and eosin
HIA	Hyperspectral Image Analysis
HCMV	Human cytomegalovirus
HPMA	Hydroxypropyl methacrylate
HSA	human serum albumin
hSRS	hyperspectral stimulated Raman scattering
IAM	Immobilisation artificial membrane
IgG	Immunoglobulin G
ISE	Ion suppression effect
ITO	Indium-tin oxide
LASX	Leica Application Suite
LDI	Laser desorption/ionisation
LID	Laser induced dissociation
LOD	Limit of detection
LOQ	Limit of quantification
LUT	Look-up table
m/z	Mass-to-charge ratio
MALDI	Matrix-assisted laser desorption/ionisation
MPS	Microphysiological system
MRI	Magnetic resonance imaging
MS	Mass spectrometry
MSI	Mass spectrometry imaging
MW	Molecular weight
NA	Numerical aperture
NMF	Non-negative matrix factorisation
OPO	Optical parametric oscillator
PBS	Phosphate buffer saline
PC	Chapter 5: Phosphatidyl choline
PC	Chapter 7: Principal component
PCA	Principal component analysis
PCh	Phosphocholine/ phosphatidyl lipid head group
PCIS	Precursor ion selector/selection
PD	Photodiode
PDL	Poly-D-lysine

PE	Phosphatidylethanolamine
PET	Positron emission tomography
PFA	Paraformaldehyde
PLSM	post-LIFT metastable suppressor
PMT	Photomultiplier tube
ppm	Parts per million
QD	Quantum dot
ROI	Region of interest
SALDI	Surface-assisted laser desorption/ionisation
SEM	Scanning electron microscopy
SHG	Second harmonic generation
SIMS	Secondary ion mass spectrometry
SNR	Signal-to-noise ratio
SPEF	Single photon excitation fluorescence
SRG	Stimulated Raman gain
SRH	Stimulated Raman histology
SRL	Stimulated Raman loss
SRS	Stimulated Raman scattering
STORM	Stochastic optical reconstruction microscopy
SVD	Singular value decomposition
TFA	Trifluoracetic acid
THG	Third harmonic generation
TIC	Total ion current
TOF	Time-of-flight
UV	Ultra-violet
αCHCA	α-Cyano-4-hydroxycinnamic acid

List of figures

Figure 1.1 Scattering light-matter interactions 6
Figure 1.2 Raman spectrum illustration 8
Figure 1.3 Jablonski diagrams in coherent Raman scattering 12
Figure 1.4 Output pump and Stokes laser trains 15
Figure 1.5 Principles of 2PEF and SHG 16
Figure 1.6 The MALDI ionisation process 22
Figure 1.7 MALDI TOF schematic 24
Figure 3.1 CIVM tape transfer onto an Intellislide 38
Figure 3.2 FFT line scan removal 47
Figure 4.1 Molecular structures of test compounds 56
Figure 4.2 DCS and binding of tool compounds 58
Figure 4.3 MALDI mass spectra of featured tool compounds 60
Figure 4.4 MS/MS spectra of featured tool compounds 62
Figure 4.5 MALDI MS/MS of tool compounds spotted on tissues 65
Figure 4.6 Tissue homogenate in MS/MS analysis of GSK90 67
Figure 4.7 Mimetic model MS/MS experiment overview 69
Figure 4.8 Calibration curves of tool compound mimetic models analysed by MALDI MS/MS 71
Figure 4.9 MS analysis of GSK4 in cell culture 73
Figure 4.10 MALDI MSI of methanol-fixed SW480 cells 74
Figure 4.11 MS/MS spectra of tool compounds in Calu-3 cells 75
Figure 4.12 Full Raman spectra of pure tool compounds 77
Figure 4.13 SRS of tool compounds in DMSO 79
Figure 4.14 Tissue homogenate spot analysis with SRS 81
Figure 4.15 SRS analysis of mimetic models 83
Figure 4.16 Cell uptake of tool compounds with SRS microscopy 86
Figure 5.1 Effect of ITO-doped slides on SRS data quality of a pure GSK90 sample 95
Figure 5.2 Sample configuration in the microscope light path 97
Figure 5.3 Evaluation of wet and dry brain tissues in SRS microscopy 98
Figure 5.4 SRH in fresh murine brain tissues 100
Figure 5.5 SRH specificity assessed by fluorescence microscopy 103

Figure 5.6 SRS imaging of a whole mouse brain cryosection 105
Figure 5.7 Effect of optical media on a kidney morphology 110
Figure 5.8 3D analysis of tissue in various optical media 112
Figure 5.9 Single point MALDI MS of in brain tissues using a Cu-taped glass slide and an Intellislide 117
Figure 5.10 MALDI MSI comparison between a Cu-taped glass slide and an Intellislide in brain..... 118
Figure 5.11 Sample schematic of a cover glass with an Intellislide and a DIUTHAME 120
Figure 5.12 Analysis of background SALDI mass spectra of a DIUTHAME sample 121
Figure 5.13 SALDI/MALDI comparison in brain tissues 125
Figure 5.14 Solvent application in DIUTHAME..... 128
Figure 5.15 Evaluation of the solvent spraying effect on extraction of tissue components and the impact on SALDI MSI 131
Figure 5.16 Evaluation of the solvent spraying effect on average mass spectra.... 132
Figure 5.17 Evaluation of the solvent spraying effect on extraction of endogenous components and GSK90 in a brain section 133
Figure 5.18 A comparison of MALDI and SALDI for mouse kidney cryosections ... 135
Figure 5.19 SALDI MSI in a 2D cell culture using DIUTHAME..... 139
Figure 5.20 MALDI MSI in a 2D cell culture 140
Figure 5.21 Stimulated Raman histology of a mouse brain tissue prior to mass spectrometry imaging..... 143
Figure 5.22 S/MALDI mass spectra of brain tissues 146
Figure 5.23 Effect of solvent exposure in MSI..... 148
Figure 6.1 CN Bio perfused system..... 153
Figure 6.2 Characterisation of a liver-on-chip CIVM with fluorescence microscopy155
Figure 6.3 Simultaneous SRS and fluorescence microscopy of a CIVM scaffold... 157
Figure 6.4 PCA of hyperspectral SRS of CIVM cells 159
Figure 6.5 Heterogeneity of hepatocyte physiology using hyperspectral SRS 163
Figure 6.6 Schematic of embedding the CN Bio scaffold strip into a glass capillary. 165
Figure 6.7 Lightsheet microscopy of CIVM scaffolds..... 167
Figure 6.8 DIUTHAME-mediated SALDI MSI of intact CIVM scaffolds 171

Figure 6.9 DIUTHAME-mediated SALDI MSI of CIVM scaffold sections..... 172
Figure 6.10 Thin CIVM scaffold cryosections in MALDI and SALDI 174
Figure 7.1 CH3 and CH2 SRS and SHG microscopy in a cell culture 180
Figure 7.2 Intensity line profiles of cell nuclei and cytoplasm 180
Figure 7.3 CH3 and CH2 SRS and SHG microscopy of a heart triculture 182
Figure 7.4 PCA with SRS spectra of fibroblasts and endothelial cells..... 185
Figure 7.5 PCA with H2O-normalised SRS spectra of fibroblasts and endothelial cells..... 187
Figure 7.6 K-means and random forest analyses of principal component in monocultures data..... 189

List of tables

Table 3.1 TM Sprayer matrix/solvent deposition settings 39
Table 3.2 Calibration standard exact mass peaks for positive mode MALDI MS 40
Table 3.3 Fluorescent dyes, emission maximum wavelengths and excitation laser wavelengths used in the microscope 43
Table 3.4 Hyperspectral SRS microscope acquisition settings 45
Table 3.5 Polystyrene standard sample SRS acquisition settings 45
Table 5.1 Radical metal ions in DIUTHAME membrane 122
Table 7.1 Heart triculture features observed with SRS and SHG 181

1. Introduction

1.1. Label-free imaging

A microscope is one of the most common analytical instruments in a life sciences laboratory. Brightfield microscopy is the fastest way to visually assess any sample at a magnified scale, whether it is the viability of a cell culture, providing a cell count or examining the structure of a tissue sample. However, the range of accessible information available to an observer is limited to readouts such as cell sizes, shape and numbers due to the low optical contrast in cells.[1] Low-cost improvements to a microscope, such as phase contrast and differential interference contrast (DIC) techniques, can increase the resolution of low-contrast specimens (e.g., cells) by employing high numerical aperture (NA) objectives[2] which can lead to precise observations of cell membranes[3] and cell nuclei[4].

The subcellular information becomes convoluted in structurally higher-ordered tissues. To make visualisation easier, chemical staining can be introduced using either chromophores or fluorophores, chemical compounds that emit light following a light excitation; each of which can vary in specificity from large structures (e.g., nucleic acids in nuclei, cytoplasm, extracellular matrix) to specific targets (e.g., protein receptors, specific DNA/RNA sequences). Although useful, this approach is material and labour intensive in comparison with label-free techniques, such as the aforementioned brightfield microscopy. There is also a limit on the number of fluorescent labels which can be applied in a single imaging experiment due to the overlap between their emission spectra. Spectral unmixing methods can be used to separate some spectrally overlapping fluorophores in fixed samples in standard imaging setups and can partially alleviate the issue of crowded labelling. This approach can be further translated into live cell imaging with the application of multi-array detectors, which can collect signal across the spectral range.[5,6]

Turning a sample chromo- or fluorogenic, by labelling, renders that sample inapplicable for further down-stream analyses and therefore this has to be the final step in many analytical pipelines since it is changed from its original state. It is highly desirable to maximise the amount of information that can be obtained from a single sample by doing multiple experiments on the same sample to elucidate its chemical

composition. However, to do this it would be critical to not have modified the sample with any external labels. Advantages of this would include a reduction of material and labour costs and potential reduction of animals used in a scientific study.

One label free analytical method is Matrix-Assisted Laser Desorption/Ionisation (MALDI) mass spectrometry imaging (MSI), which is a well-established label-free technique that can be used in both tissue imaging[7-9] and spatial omics[10,11]. MSI generates hyperspectral data cubes (i.e., spatial, and spectral data) describing the chemical composition of a sample based on the molecular weight of its ionisable constituents. MALDI MSI analysis is sensitive to contaminants and chemical sample modifications and therefore, MSI analysis should be carried out prior to any histological staining.[11-13] Alternatively, a microscopy image-driven MSI analysis could be done on an adjacent/consecutive sample section in tissues,[14] but this potentially decreases the precision in spatial overlap between the microscopy and MSI data. Such decrease in spatial error was acceptable in the early years of MALDI MSI, when the spatial resolution of MALDI MSI was limited (50 – 200 µm). However, recent advances in MALDI MSI technology and the introduction of transmission mode MALDI-2-MSI has pushed the spatial resolution limit and the sensitivity to an intra-cellular level.[15] High precision image co-registration is now required to ensure the extracted information is spatially accurate and reflects the ground truth. For this reason, alternative imaging approaches are necessary in a microscopy image-driven MALDI analysis of the same tissue section and cell cultures.

Another novel approach applies brightfield imaging combined with virtual staining achieved through deep learning, where machine learning networks are trained on corresponding brightfield and histology-stained images to produce virtual histology images. These approaches are fast with a low relative error.[16] Additionally, deep learning can be successfully applied via label-free autofluorescence to haematoxylin and eosin-(H&E) stained image translation.[17,18] These approaches require large training datasets but offer swift virtual staining transformation once trained. The data sets can however be limited to the range of tissue types available in the training datasets.

Therefore, there is still a need for other alternatives to fluorescence and brightfield imaging to obtain chemically and structurally-relevant spatial information,

which could be further applied in an image-driven MSI analysis. Raman spectromicroscopy was identified as a potential alternative and successfully applied in this endeavour. Spontaneous Raman spectroscopy retrieves information about the composition of molecular vibrational modes and their spatial distribution in a sample.[19-21] Similarly to brightfield techniques, Raman imaging is label-free and does not modify or damage the sample during the image acquisition process, unlike MALDI MSI which requires matrix deposition on a sample surface and ablates the sample surface during ionisation.

Spontaneous Raman spectroscopy is a low probability phenomenon, where an incident photon is scattered by a molecule non-elastically, i.e., leaving the scattering site with a different energy. The Raman scattering cross-section is in the order of 10^{-29} cm^2/sr,[22] which is less than the excitation cross-section of single photon excitation fluorescence (SPEF; ~10^{-14} cm^2/sr)[23]. Consequently, spontaneous Raman spectroscopy requires long acquisition times to enable the accumulation of enough scattered photons and can often be accompanied by an unwanted fluorescence background. In contrast, stimulated Raman scattering (SRS) is a non-linear Raman microscopy which uses a combination of coherent pulsed lasers improving the probability and signal-to-noise ratio (SNR) of Raman scattering whilst focusing on a narrow spectrum of vibrational frequencies without background noise.[24,25] Therefore, SRS offers a useful first instance imaging tool which could precede an MSI and/or fluorescent analysis. Non-invasiveness and deep sample penetration (>1 mm in cleared tissues)[26] enable the application of SRS in chemical imaging in a wide range of fixed and live biological samples from cell cultures grown in a monolayer through spheroids and organoids to *in vivo* tissues.[27] SRS is a chemically sensitive spectroscopic method which can provide spatial and spectral information about chemical components, such as lipids, proteins and nucleic acids in a biological sample,[27] or a distribution of active pharmaceutical ingredient (API) polymorphs and excipients in a drug tablet.[28]

As there is no universal imaging approach to analyse a biological matrix, often multiple analyses are required and need to be carried out on multiple samples. Where compatible, multimodal imaging, which combines multiple imaging techniques, and developed to reduce the cost of separate analyses, can be used.

The majority of multimodal analyses are conducted in the same instrument housing which facilitates compatible technologies, such as positron emission tomography – magnetic resonance imaging (PET-MRI) scanners,[29] scanning electron microscopy with energy dispersive X-ray,[30] secondary ion mass spectrometry (SIMS)-MALDI,[31,32] and a plethora of microscopy techniques including a combinatory fluorescence lifetime imaging microscopy (FLIM), Raman and optical coherence tomography microscope system,[33] and second and third harmonic generation (SHG, THG), combined with single-, two- and three-photon excitation fluorescence microscopy (SPEF, 2PEF, 3PEF).[34] However, sample-related incompatibilities can arise between the different multimodal approaches, for instance in the label-free Raman and MALDI analysis due to matrix application which results in a layer of crystals on a sample surface, which introduce strong exogeneous signal and a morphological alteration during crystallisation, which would be likely to skewer the spatial and the chemical information of the sample.

1.2. Optical methodologies

1.2.1. Fluorescence microscopy and fluorescent labels

Owing to high chemical specificity and the high probability of fluorescent labels to emit light,[23] fluorescence microscopy is a versatile imaging tool which can result in imaging data with a spatial resolution below the diffraction limit of light (~200 nm) and even reach single molecule detection.[35-37] Fluorescent labelling is however accompanied by unwanted effects in the physiological environment, such as photon/thermally-induced cytotoxicity.[38,39] Furthermore, fluorescent labels are prone to photobleaching[40], where the excitation energy permanently alters the molecular structure of a fluorophore into a non-fluorescent configuration.

Fluorescent labels can be of endogenous or exogenous origin. Endogenous fluorescent labels are proteins which can be produced in a genetically modified biological system. However, fluorescent protein expression has been accompanied by cell phenotype alterations [41,42] and a negative effect on the function of a native protein,[38,39] such as the protein motors, to which the fluorescent proteins are fused to.[43] Furthermore, the fluorescence intensity strongly depends on the pH of the surrounding environment.[44,45]

Exogeneous fluorescent probes are synthesized and delivered into a fixed or a live sample. These can be small molecule fluorescent dyes, such as nucleic acid stain DAPI (277.3 Da) or antibody-conjugated fluorescent dyes. Antibody immunolabelling employs large complexes of primary and secondary antibodies, for example, the fluorescent label Alexa Fluor 488 (546.4 Da) covalently binds to a secondary antibody such as immunoglobulin G (IgG, 150 kDa, ~10 nm)[46], which is bound to a primary antibody of a similar size. In this instance, the antibody link between the target molecule and the fluorophore is approximately 20 nm.

Hypothetically, two target molecules which are covalently coupled and labelled with two different singular fluorescent immunocomplexes, the largest possible distance between the two fluorophores would be ~40 nm excluding the size of the target molecules, which could result in false negative signal overlap in super-resolution techniques. The issue of large immunocomplexes was addressed by the development of nanobodies,[47,48] which consist of only one subunit of an antibody (~15 kDa) and thus significantly reduce the “linker” size.[49]

Although the advantage of fluorescence microscopy is the target specificity achieved by an introduction of highly specific labels, there is also an established label-free approach to measure the metabolic state of cells in living specimens through autofluorescence. Cells and tissues produce endogenous fluorophores such as nicotinamide adenine (phosphate) dinucleotide (NAD(P)H) and flavin adenine dinucleotide (FAD), which can be used as markers of the redox ratio in a cell culture.[50-53]

1.2.2. Raman spectroscopy

1.2.2.1. Raman scattering and Raman labels

A photon can either be temporarily absorbed or directly scattered by a molecule during a light-matter interaction. In fluorophores, the absorption of a photon can lead to the excitation of an electron from a ground electronic state to an excited electronic virtual state, which is below the energy level needed for an excitation in the fluorescence process. As the electron returns to the ground state the energy is then emitted as a red-shifted fluorescence (Fig. 1.1b).[54]

Light scattering is dominated by elastic scattering, named Rayleigh scattering, during which the energy of a scattered photon exiting the site of light-molecule interaction matches the energy of the same photon prior to scattering. However, a miniscule fraction of scattered radiation gets scattered inelastically, where both molecule and the photon in the scattering interaction change their respective energies, as first described by Raman and Krishnan in India and Landsberg and Mandelstam in USSR in 1928.[55,56] Raman scattering can occur in molecules, which exhibit a change in their polarizability during the vibrational movement (e.g., symmetric rocking, scissoring).

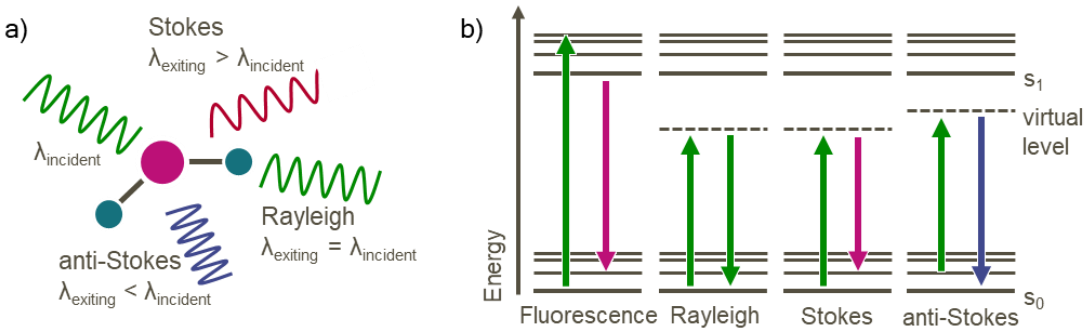

Figure 1.1 Scattering light-matter interactions. a) Scattering of a photon by a molecule can result into a scattered photon with the energy equal to the energy of an incident photon (Rayleigh scattering),a higher energy photon (Raman anti-Stokes), or a lower energy photon (Raman Stokes). b) A simplified Jablonski diagram shows the standard process of fluorescence, which begins with an excitation of an electronic state s_0 to s_1. The energy is partially released as heat radiation and the remaining energy as a photon emission, which returns the electronic state back to s_0. Scattering processes involve virtual energy levels of the electron singlets. Rayleigh scattering energy transfer results in the same energies of a photon and a molecule. Stokes Raman scattering involves interaction between a ground state molecule which exits the scattering interaction with higher energy and the photon is red-shifted. To achieve an anti-Stokes Raman scattering, the scattering molecule has to be in a higher vibrational state prior to an interaction with a photon, whereafter the exiting photon gains energy (blue shift).

Depending on the direction of energy transfer, the Raman scattered photon is either red-shifted with lower energy known as Stokes or blue-shifted with higher energy (anti-Stokes) (Fig. 1.1). In non-coherent Raman techniques, the overall intensity of an anti-Stokes Raman scattering will always be lower than the Stokes Raman scattering owing to the Boltzmann probability distribution. This, explains why the higher energy state is less populated than the excited state.[57] Therefore, most spontaneous Raman scattering instruments collect the Stokes-shifted signal.[58-60]

The advantage of anti-Stokes Raman scattering is the diminishment of the red-shifted fluorescence background caused by the laser excitation by using appropriate shortpass filters, which block the laser and red-shifted signal.[61] The blue shift is exploited in Coherent anti-Stokes Raman scattering (CARS), where the ground vibrational state is excited through an application of pulsed lasers driving specific vibrational modes in a sample.[62] CARS will be further discussed in chapter 1.3.4.

Raman spectroscopy is a powerful tool which reveals the molecular vibrational properties of a sample. Since each type of molecular bond vibrates in a different mode and frequency, a biological sample scatters an array of well annotated Raman peaks characteristic to functional groups in the molecule when probed with a laser.[63,64] A Raman shift is recorded in wavenumbers *v,* which are defined as the number of wavelengths per distance (cm^{-1}), which inversely corresponds to a wavelength λ. The biology-relevant Raman spectrum spans over 400 cm^{-1} – 3100 cm^{-1}. The spectrum is separated into a fingerprint region (400 cm^{-1} – 1700 cm^{-1}), a cell-silent region (1800 cm^{-1} – 2400 cm^{-1}), and a CH region (2800 cm^{-1} – 3100 cm^{-1}) (Fig. 1.2).

The fingerprint region is information rich and contains the key vibrational bands that characterise the molecule. It has been extensively studied to gain information about the structure and distribution of biomolecules such as nucleic acids[65-67], proteins[63,68,69], lipids[63,70,71], glycogen[63]. Additionally, the fingerprint region spectrum is also used in Raman-based classification analyses of cell cultures[72-74] and cancer/healthy tissue segmentation owing to its heterogeneity in contrast with the CH region.[75,76]

In contrast, the CH region is a smaller, spectrally congested section of the Raman spectrum which overlaps with the O-H vibrational mode of H_2O. The CH region contains the high energy vibrational bands of CH_2 and CH_3 and is of particular interest in lipid and protein analyses.[77-79]

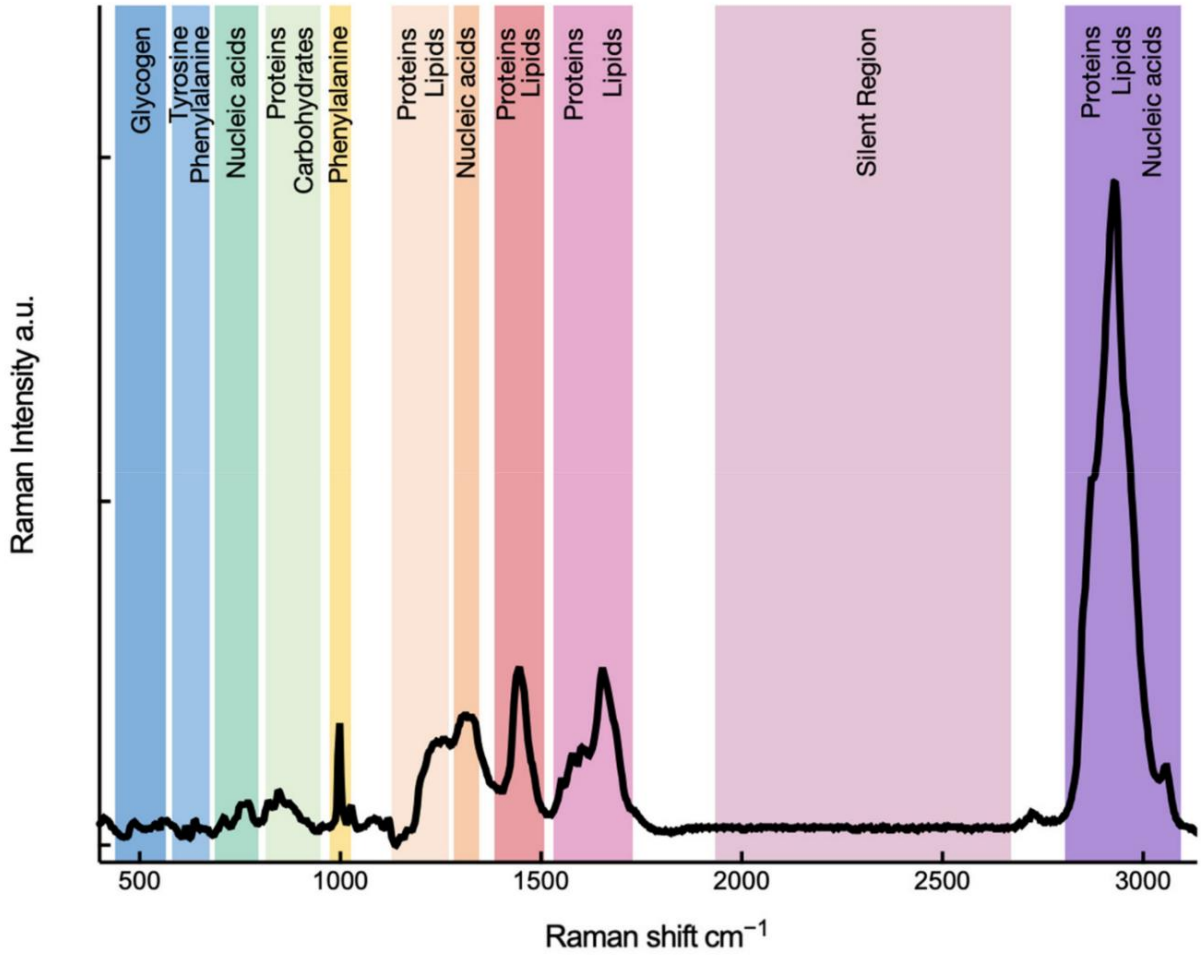

Figure 1.2 Raman spectrum illustration. The Raman shift is measured in wavenumbers (cm^{-1}). From Xu et. al., 2021 Copyright Creative Commons CC-BY v4.0.[64]

As the denomination suggests, the cell silent region is devoid of Raman signal in unperturbed mammalian biological matrices. However, certain bio-orthogonal molecular bonds are active in this region. Carbon-deuterium (C-D), alkyne (C≡N), and nitrile(C≡C) molecular bonds generate spectral peaks in this region and are readily applied in a plethora of bioconjugation and microscopy localisation studies.[78,80-85] Since these molecular bonds scatter in the cell silent region, they can be chemically conjugated to other biomolecules as tags. The number of these Raman tags which can simultaneously be detected with a Raman microscope is limited by the vibrational constraints of the above-mentioned bonds to approximately 2100 cm^{-1} – 2300 cm^{-1} range of the cell silent region. Alkynes can be further separated in this region into a terminal alkyne region (~2100 cm^{-1}), a silyl and halo-alkyne region (2150 cm^{-1} – 2200 cm^{-1}), and an internal alkyne region (2200 cm^{-1} – 2300 cm^{-1}).[84] The literature also indicates that the intensity of the Raman tags is

strictly in the following order: C-D < –C≡N < –C≡C– < –C≡C–C≡C– < –C≡C–C≡C–C≡C–, where diynes and triynes exhibit the strongest signal to noise ratio (SNR). It has also been demonstrated that the intensity of the tag can be modulated by the length of the internal polyynes.[84,86] Other studies show the alkyne signal is susceptible movement/shift of the vibrational band position in the Raman spectrum through the introduction of carbon isotopes.[87] For example, the replacement of a single ^{12}C carbon with a ^{13}C isotope in the 5-ethynyl-2'-deoxyuridine (EdU) results in a 29 cm^{-1} positive Raman shift and replacing both alkyne carbons with ^{13}C positively shifted the EdU alkyne signal by 77 cm^{-1}.[88] All three alkyne peaks were easily separated in the Raman spectra across these distances due to their relatively narrow spectral peak width in contrast with fluorescence emission spectra, which are typically very broad.[89] This has led to the development of a Raman label system constituting of 15 bis-arylated polyynes dubbed "CARBOW" with a variable number of conjugated alkyne bonds and carbon isotope substitutions populating the cell silent region between 2018 cm^{-1} – 2262 cm^{-1}. Similarly, this approach has been developed using xanthene scaffolds of various ring numbers conjugated with nitriles and nitrile ^{15}N isotopes in the nitrile bond structure.[90] It has also been observed that the Raman spectrum peak position is affected by substitutions outside the triple bond, which in combination with isotope substitution can lead to a production of 22 different nitrile tags which were simultaneously acquired and discerned using SRS microscopy.[91]

The C≡N and C≡C bonds measure 1.14 Å and 1.18 Å in length, respectively,[92] which in contrast with fluorescent small organic molecules with their size in the range of nanometres and antibodies (~10 nm) suggests a lower probability on an impact of the labelled molecular dynamics. This is even more pronounced in the case of hydrogen-deuterium substitution, which increases the size of a molecule by only a single neutron while giving a clear signal in the cell silent region. The C-D bond is known for producing a poor signal intensity in the Raman spectra.[93] Thus, the concentration of C-D bonds in a Raman focal point needs to be high for a sufficient SNR. C-D labelling is, therefore, widely applied in lipid metabolism imaging owing to the large number of hydrogen-deuterium substitutions available along the long fatty acid long chains, which are spatially condensed owing to their hydrophobic properties.[94,95]

The molecular weight of polyynes and xanthene-based Raman tags are close to the molecular weight of small molecule fluorophores and thus they are not advantageous over fluorophores in their size. However, these Raman labels are not photo-bleachable which makes them superior to fluorophores in long repetitive imaging experiments where signal quantification is required. Furthermore, the quantification of Raman signal in SRS is directly proportional to the concentration of an analyte in the focus point.[96]

Alkyne and nitrile bonds have been also used in a label-free Raman microscopy in drug delivery studies of therapeutic tyrosine kinase inhibitors.[96-98] Tyrosine kinase inhibitors are a group of active pharmaceutical ingredients (APIs) which disrupt the tyrosine signalling pathway and are used in various therapies. Erlotinib with a terminal alkyne conjugated to a benzene ring was successfully detected in a cell culture experiment at 100 µM concentration using a spontaneous Raman scattering microscope.[98] Using the same system, neratinib which contains a nitrile bond was detected in cells incubated at 5 µM concentration.[97] Replacing the spontaneous Raman techniques with SRS further pushed the limit of detection in a ponatinib study where the alkyne was localised in a conjugated system between an imidazopyridazine and a benzene in the centre of the molecular structure. Based on density functional theory calculation, the cell silent region peak of ponatinib was predicted to exhibit an ~18-fold increase in signal intensity of the alkyne vibrational mode in comparison to erlotinib. However, with the combination of the increased signal intensity due to the alkyne and the use of SRS, ponatinib was successfully detected in cells which were treated at 500 nM concentration.[96]

1.2.2.2. Spontaneous Raman spectromicroscopy

The Raman scattering effect is very low – approximately 1 in 10^7 photons is scattered inelastically.[24] Therefore, spontaneous Raman confocal microscopes are normally equipped with continuous wave lasers to concentrate a large quantum of photons on a sample through high numerical aperture (NA) objective lens to increase the phenomenon occurrence. The Raman-scattered photons are dispersed with a reflective surface relief grating or a transmissive holographic grating and afterwards collected by a photomultiplier tube (PMT) detector arrays or charge coupled device

(CCD) cameras. The occurrence of Rayleigh scattered light is higher than the occurrence of Raman scattering by several orders of magnitude and therefore it must be filtered by long pass filters or notch filters prior to detection.

As briefly mentioned above, spontaneous Raman spectro(micro)scopy is hindered by its acquisition speed. The acquisition speed of a single spectrum can take 10s, which can result in very long acquisition times for large images.[99] However, improvements and modifications through the development of line laser excitation in a single-photon avalanche system diode has the potential to reduce acquisition times ten-fold.[100] Additionally, the spontaneous Raman systems provide 3 cm^{-1} spectral resolution[101] which surpasses the resolution of commercially available tuning coherent Raman systems.

1.2.2.3. Stimulated Raman Scattering (SRS)

SRS is a coherent Raman scattering technique (CRS), which is a class of Raman scattering where two spatially and temporally synchronised lasers - named pump and Stokes - induce selective molecular vibrations at a resonance corresponding to the resonance difference between the pump and Stokes laser beams. CRS techniques increase the signal intensity by a factor of 10^7 in comparison with the spontaneous Raman scattering effect. The CRS class entails stimulated Raman gain (SRG), stimulated Raman loss (SRL), CARS, and coherent Stokes Raman scattering. Coherent Stokes Raman scattering will not be discussed due to its poor applicability at the current state of the research.[57]

SRG and SRL are interlinked as they occur at the same time in the SRS process. SRS was first discovered in 1962 after the emergence of lasers.[102] In SRS, two incident light beams at a pump frequency (ω_p) and a Stokes frequency (ω_S) are used to drive a difference frequency (ω_Δ). When the delta frequency in $\omega_\Delta = |\omega_S - \omega_p|$ corresponds to a vibrational frequency of a molecular bond, the electronic state of a molecule increases from a ground vibrational state to a virtual state and subsequently drops into a higher vibrational state (Fig. 1.3a). Unlike spontaneous Raman scattering, SRS does not result in a scattered emission. SRS is a dissipative process which uses energy transfer between the propagating laser light fields and the molecules. This results in an intensity reduction (SRL) of a pump and an intensity

increase in Stokes (SRG) during the coherent process if $\omega_\Delta = |\omega_s - \omega_p|$ is true.[57] The pump gain and Stokes loss (ΔI) in intensity (I) are small enough ($\Delta I/I = 10^{-3} - 10^{-7}$) that the signal can be lost in the noise and therefore, the detection process in an SRS instrument must differ from other CRS techniques.[57,103]

1.2.2.4. Coherent anti-Stokes Raman scattering (CARS)

All CRS phenomena happen simultaneously and therefore, it is possible to detect SRS and CARS simultaneously.[24] As in SRS, two oncoming synchronised pump and Stokes beams are used to induce a higher vibrational state with the intermediate virtual state in a target molecular bond which results in a steady molecular beating at a ω_Δ frequency. Unlike in SRS, a third beam (probe beam) is then inelastically scattered by the ω_Δ with an anti-Stokes shift owing to the higher vibrational state of a target molecular bond at a frequency ω_{aS}. Typically, the probe beam vibrational frequency matches the pump laser frequency. Therefore, the frequency of an inelastically scattered signal can be expressed as $\omega_{aS} = |2\omega_p - \omega_S|$ (Fig. 1.3b).

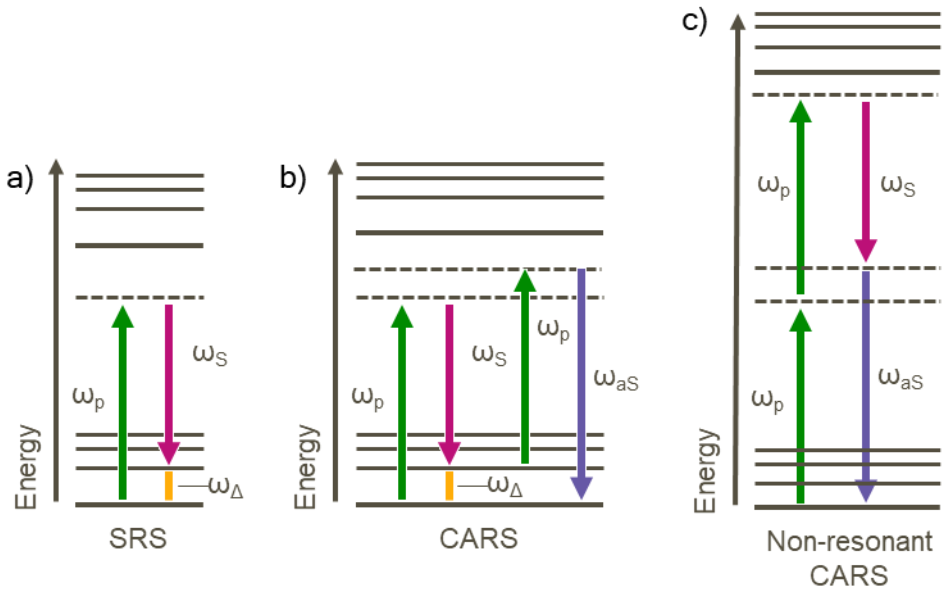

Figure 1.3 Jablonski diagrams in coherent Raman scattering. a) In SRS, pump and Stokes beams interact with a target molecule vibrational frequency to generate SRG or SRL. b) In CARS, a four-wave mixing occurs, where a combination of 2 pump lasers, a Stokes laser and a molecular bond vibration generates anti-Stokes inelastic light scattering. c) Four-wave mixing interaction between the pump, Stokes, and anti-Stokes emission in the nonlinear medium results in generation of non-resonant CARS background.

The resonant CARS is however accompanied by a non-resonant CARS background during which the two pump and a Stokes lasers interact with the nonlinear optical medium instead of the vibrational bond (Fig. 1.3c). In fact, the CARS intensity is a combination of three components. The first contributor is a resonant component containing the total vibrational information of the sample. The second component is the non-resonant CARS signal which is constant. Finally, a mixing between a resonant and non-resonant CARS term, named as the heterodyne term, causes a CARS-specific spectrum distortion in comparison with a ground-truth Raman spectrum.[104] Therefore, complex data processing pipelines need to be in place in order to obtain the Raman-like spectra.[105-107]

1.2.2.5. Hyperspectral and dual-Stokes SRS

Unlike spontaneous Raman scattering, SRS does not use grating and a single wavelength continuous wave laser to obtain a Raman spectrum information. Instead, SRS utilises 2 pulsed picosecond narrowband lasers,[108] which are very efficient in obtaining single vibrational information (e.g., CH_3 stretch). To scan a part of the Raman spectrum, wavelength tuning in picosecond lasers is used iteratively across a spectrum. This is typically achieved by an optical parametric oscillator (OPO) which can precisely tune the wavelength of one laser line by changing the precisely temperature of the OPO crystal, whereas the second laser remains static. Using picosecond lasers provides <10 cm^{-1} bandwidth, but OPO tuning is relatively slow.[109]

Alternatively, femtosecond pulsed lasers can be applied in SRS. Femtosecond lasers have inherently broad bandwidth accompanied by poor spectral resolution in comparison with the picosecond systems. The spectral resolution can be however improved by chirping and spectral focusing. The femtosecond pulses are short in time and spectrally broad. During chirping, a dispersive glass material is placed in the laser beam pathway, which causes broadening of the laser pulse spectral profile in a temporal domain. Chirping allows the use of precise spectral tuning by overlapping only a part of the vibrational frequencies of pump and Stokes beam, whereas the remainder of the spectral profile is hastened or delayed. Spectral tuning is then carried out by delaying the temporal overlap between the pump and Stokes laser pulses by an extension of the length of the light path for one of the two beams.[110] By avoiding laser tuning, the spectral information precision is improved.

However, large laser powers are necessary since the chirping elongates a total pulse energy along a temporal axis.

Additionally, SRS is accompanied by excess laser noise, which is difficult to remove.[111] To address this issue, two spectrally separated Stokes beams were implemented in some wavelength tuning[112] and the spectral focusing setups[113], for on-resonance and off-resonance imaging. The off-resonance is then used as a baseline subtraction. This setup enables live tracking with an improved SNR.[112] Moreover, dual-Stokes systems can be applied to the simultaneous imaging of lipids and proteins in living samples.[113] Dual-Stokes SRS microscopy has been used in stimulated Raman histology (SRH), a technique which transforms Raman data into H&E-like images.[114] By the simultaneous acquisition of CH_3 and CH_2 stretch vibrations a combination of protein and lipid images, can be acquired. By performing an image subtraction ($|CH_3 - CH_2|$), proteins in a sample are highlighted. When overlayed, these images can be used to highlight cytoplasm and nuclei separately without any additional markers or sample processing. By applying customised look-up table (LUT) colour coded gradients, histologically relevant images, similar to H&E stained images can be recreated.[114-117]

1.2.2.6. SRS detection

SRS is highly forward-directional along a propagation vector of incident pump and Stokes beams. Therefore, the SRL in a pump laser line is typically detected using a photodiode (PD) in a transillumination setting, but epi-detection (i.e. the same lens was used for illumination and signal collection) was applied in opaque or large biological samples as well.[28]

Owing to the very low signal intensity of the SRL, a modulation/demodulation scheme[111] is applied, where the Stokes beam is modulated by an acousto-optic modulator or an electro-optic modulator. The modulated signal is filtered after it passed through a sample and then, only temporally separated trains of Stokes pulses remain. As the SRS energy transfer occurs only when the Stokes pulses are present, the SRL in the pump beam can be detected in a photodiode (Fig. 1.4). The signal from a photodiode is transported to a lock-in amplifier filtering device, which also collects a reference pump beam signal that does not pass through the

microscope. In the lock in amplifier, the ratio between the reference pump intensity and the pump with intensity loss are measured and denoised.

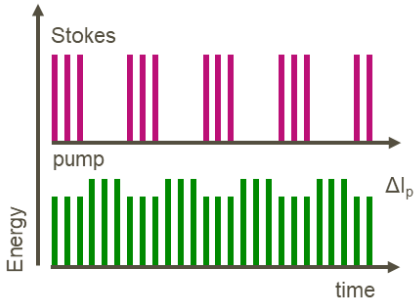

Figure 1.4 Output pump and Stokes laser trains. The modulated and filtered Stokes pulse train interacts with temporally overlapping pump, which in the presence of ω_Δ results in SRL (ΔI_p) in the Stokes-overlapping pump pulses.

1.2.3. Other nonlinear microscopy methods

SRS and CARS are optical methods, where a light is non-linearly inelastically scattered. A non-linear optical response can be observed in light-matter interactions, where photons at a high concentration in a very short temporal range coincide with a probed molecule. Because the volume where the sample-light interaction occurs is significantly reduced, a pinhole is unnecessary for signal bleeding from adjacent planes since the majority of the material, where the laser beams propagate through, is not interacting with light.

1.2.3.1. Two photon excitation fluorescence (2PEF)

Single photon fluorescence (SPEF) microscopy, where single photon excitation results in a single photon blue-shifted emission, is a widely used method in bioimaging. However, this method faces limitations in maximal imaging depth, which is influenced by elastic scattering and absorption, and phototoxicity from the continuous wave lasers, which illuminate and excite molecules across an entire illumination volume (Fig. 1.5a).

In 2PEF, a fluorescent molecule is excited by two photons with a sum energy, which elevates the molecules electronic state into an excited electronic state, from where the energy follows the same pathway as in SPEF. Moreover, the effective

excitation volume in a 2PEF process is less than 1fl,[118] which significantly reduces the phototoxic effect that can be otherwise observed in SPEF.[119] Additionally, 2PEF microscopy improves the depth penetration limitation of SPEF microscopy to up to 1.6mm.[120] Therefore, 2PEF imaging became popular and the method of choice for tissue imaging including live brain cortex imaging in murine brains.[121-123] 2PEF and three photon excitation fluorescence (3PEF) microscopy has also been applied to the analysis of endogenous fluorescent species NAD(P)H and FAD in cell redox experiments.[51,124,125] Because NAD(P)H and FAD are excited by high energy wavelengths (330 nm – 465 nm), 2PEF is preferential over SPEF owing to the lower phototoxicity of the small excitation volume and the use of low energy wavelengths.[126]

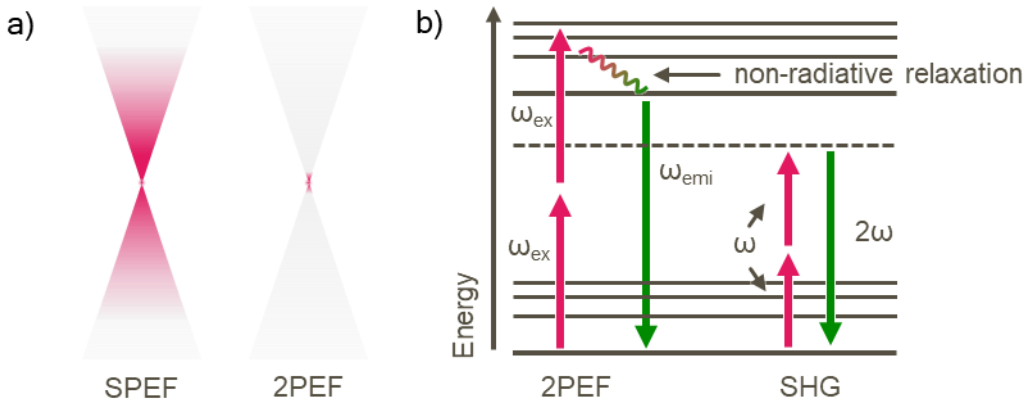

Figure 1.5 Principles of 2PEF and SHG. a) The SPEF is likely to excite a large volume of the illuminated sample, whereas an efficient 2PEF effect happens in less than a femtoliter volume. b) In 2PEF, excitation of a fluorescent molecules has to be caused by two photons (ω_{ex}) with a sum energy, which transfers the electron from a ground to an excited state. After non-radiative relaxation, anti-Stokes shifted fluorescence (ω_{emi}) is emitted. In SHG, two photons with a frequency ω_i which reach a virtual state, where the photon energies are combined into a photon with a frequency 2ω.

1.2.3.2. Second and third harmonic generation (SHG, THG)

SHG and THG are nonlinear processes that involve a generation of new frequencies of light through interaction light-matter interactions, which do not lead to a molecule excitation and fluorescence. In SHG and THG, two or three photons of the same energy are instantaneously annihilated in a nonlinear environment, which in turn generates a new photon which retains exactly the sum energy of the incident photons in SHG or THG, respectively (Fig. 1.5b).[127,128] This process is free of energy

transfer between a scattering molecule and the photons and thus significantly reduces the phototoxic effect and the signal cannot be photobleached.

SHG is a process, which occurs exclusively in non-centrosymmetric structures, such as collagen fibres[34,129], microtubules[130] and myosin fibres[131,132] in biological matrices. THG occurs in the interfaces of the optical media with mismatching refractive indices, whereas destructive interference occurs in a medium with a homogeneous refractive index, which results in a signal absence.[128,133] This technique is mostly used for the detection of water-lipid and water-protein interfaces in biological samples, such as lipid droplets[134], cells[135] and extracellular structures[34].

All of the above-mentioned nonlinear optical methods can be assembled into multimodal systems in one instrument housing owing to their overlapping requirements for signal generation, which allows the simultaneous collection of harmonic, multi-photon fluorescence, and coherent Raman signals simultaneously.[34,114,136,137]

1.3. Mass spectrometry

Mass spectrometry (MS) is an analytical technique which is used to separate individual molecular constituents from a sample based on their mass and charge, specifically, their mass-to-charge ratio (*m/z*), which is then recorded as a mass spectrum. Since the introduction of mass spectrometry at the turn of the 20th century, multiple MS methods have been developed.[138] The principle of mass spectrometry can be divided into three conserved processes: I) The mass spectrometer first ionises the analyte sample by introducing a charge to the molecules in the analyte. The gas phase ions, consisting of molecular ions, analyte adduct ions e.g. $[M+Na]^+$, $[M+K]^+$ in positive mode and $[M-Cl]^-$ in negative mode are then directed into a mass analyser by a magnetic or electric field, II) where the molecular ions are then separated based upon their molecular weight and charge-state. III) The separated ions are then recorded as a signal using a detector, which are typically microchannel plate detectors or electron multipliers.[139,140] Within this introduction, only “soft” ionisation techniques applicable to mass spectrometry imaging will be described.

1.3.1. Ionisation techniques

The ionisation process occurs in an ion source in non-imaging MS instruments, where a neutrally-charged analyte becomes a positively or negatively charged. The ionisation of the analyte can be induced by high energy electron or proton particles. In imaging MS instruments, this process occurs on or near the sample surface, which is typically bombarded by charged particles or photons. Ionisation techniques are categorised as either hard or soft ionising techniques depending on the energy which is used to ionise an analyte. High energy ionisation techniques cause fragmentation of the analysed molecules and are regarded as hard ionisation techniques. Soft ionising techniques do not typically induce fragmentation, they include techniques such as Matrix Assisted Laser Desorption/ionisation (MALDI), Surface-Assisted Laser Desorption/Ionisation (SALDI), electrospray ionisation (ESI) and Desorption electrospray ionisation (DESI).[141] These latter techniques enable the analyses of large, intact biomolecules.

1.3.1.1. Electrospray Ionisation (ESI)

ESI is an ionisation technique which generates ions by the application of a high voltage to a liquid containing the analyte streaming from a capillary, which is vaporised into aerosol droplets. The analyte charge is likely generated through the acid-base reaction with the solvent or the redox reaction with the metal capillary tip. The liquid solvent is typically a volatile compound which increases the evaporation rate.[142] The gradual evaporation eventually reaches a “critical point” known as the Rayleigh limit. Past this limit, the repulsive Coulomb forces between same charged-ions in a droplet result in Coulomb fission, which causes ions to separate from the droplet. This process was dubbed multiple ion droplet separation. The direction of aerosol and ion movement is determined by the capillary and mass analyser inlet polarities and the electrochemical properties of the dissolved analyte.[143,144]

The need for an analytical capability in MS with the ability to measure extremely low sample volumes (e.g. a single cell) was one of the driving forces to a develop and apply nanoESI.[145,146] These techniques require ultra-fine capillaries and thus, the emission capillaries in nanoESI have pulled tips with an outlet diameter of <5 µm, and are used with a miniscule analyte flow in pl to nl/min.[147,148]

1.3.1.2. Desorption electrospray ionisation (DESI)

DESI has been successfully used in MSI experiments in biological samples.[149] Due to the raster movement of the sample stage which is in close vicinity of the solvent-spraying outlet and the MS inlet, DESI is an ideal technique for MS imaging experiments. One of the main advantages of DESI is that it does not require complicated sample preparation and it is conducted under atmospheric pressure[150-154]

A DESI ion source consists of a movable sample stage, a sprayer outlet, and a mass spectrometer inlet. Similarly, to ESI, the outlet, is under high voltage and ejects a flux of charged solvent droplets. On impact with the sample, a thin solvent layer is created on the surface, where analyte extraction, desorption and ionisation of analytes occurs. The driven flux and impact of primary droplets ejects secondary droplets of charged solvent with the analyte droplets, which then undergo the evaporation as briefly discussed earlier in the ESI section.[150]

The typical limit of spatial resolution of DESI is approximately 100-150 µm,[149] although 35 µm resolution has been reported.[155] The limitation arises from the sampled region of the analyte, which is partially dissolved by the primary plume. To address the issue of the limited spatial resolution, nanoDESI has been developed.[155,156]

The design of the ion source for nanoDESI differs slightly from that used in DESI. The transfer solvent is sprayed closer towards the sample through a thin capillary and the secondary droplets are collected with a second capillary. The capillaries are positioned at a 30° angle to each other and very close to the sample surface. A liquid bridge is formed between the two capillaries over the sample surface.[157,158] A spatial resolution of 7µm has recently been achieved from a mouse brain MSI study.[159]

1.3.1.3. Matrix Assisted Laser Desorption Ionisation (MALDI)

Since its introduction in the early 1980s, MALDI has become the most commonly used ionisation techniques for MSI of biological samples due to its ability

to ionise molecules across a wide range of molecular weight without their fragmentation. [160,161] The MALDI ion source introduces charge to the analytes contained within a sample by using a matrix and laser energy under a vacuum. The ions are then directed into the mass analyser inlet through an electric field.

A matrix is the corner stone of this method and is essential for the system sensitivity by the co-crystallisation of the analyte with the matrix on the sample surface and the subsequent ionisation energy mediation. The matrix is applied as a saturated solution to the surface of the sample. The analytes are extracted from the sample whilst the matrix is dissolved. As the solvent evaporates and dries, the matrix and analytes co-crystalise. Analytes outside of the co-crystallised matrix-analyte mixture are unlikely to be properly ionised in the MALDI process.[161]

The matrix is typically a small acidic molecule which contains a conjugated π-system in aromatic rings, which enables photon absorption from the UV laser, and a functional group for ionisation (e.g., COOH). The most commonly used matrices are α-cyano-4-hydroxycinnamic acid (αCHCA) for positive mode MALDI MSI[162], and dihydroxybenzoic acid for negative mode MALDI MSI.[163] The selection of matrix and the system polarity is determined by the properties of the analyte. MALDI mass spectra using αCHCA and other small molecule matrices contain matrix-related background ions which can in some cases hinder analyte detection due to an overlap in the *m/z*. In addition to the monoisotopic matrix mass ion, various ion adducts (Na^+, K^+, Cl^-, …), isotopes, matrix oligomers and fragment ions may also be present. For successful MSI experiments, the matrix must be homogeneously deposited onto the sample and generate the smallest crystal possible whilst at the same time, extracting sufficient amount of analyte from the sample. The two most commonly used methods of matrix application are automated spraying devices and sublimation.[164]

The most frequently used matrix application device used by the MSI community is the HTX TM-Sprayer. This automated spraying device nebulises the matrix in a solution at a high temperature and then deposits it onto the sample directly beneath the sprayer nozzle. The sprayer nozzle traverses above the sample at a constant speed and a constant flow of matrix solution. The spraying process can be fine-tuned by adjustments such as pressure, raster speed, nozzle temperature, and matrix flow rate and concentration. Inappropriate settings can result in “matrix flooding” which

causes analyte redistribution, otherwise known as delocalisation.[165] On the other hand, an overly dry matrix application will limit the degree of analyte extraction from the sample and result in low levels of analytes and poor sensitivity in the MSI experiment. Furthermore, matrix selection and the matrix sprayer settings affect the size of the matrix crystals after drying. Matrix crystal size is one of the main limitations in achieving maximum spatial resolution (the others being laser pitch and laser spot diameter).[164,166,167]

Alternatively, matrix sublimation, which is a solvent-free method can also be used for matrix application.[168] The sublimation approach is a two-step process, the matrix in solvent is first heated (>100 °C) under vacuum, which results in matrix sublimation. This is followed by desublimation, during which the system cools down and the matrix is deposited as crystals onto the surface of a separately placed sample. This technique has been demonstrated to produce matrix crystal sizes of ~1 µm and below,[169,170] which pushes MALDI technology into subcellular resolution.

The MALDI ionisation process occurs in an ion source, whereby a sample with the analyte-matrix crystals on its surface is fired upon using a UV laser. This causes a small-scale desorption of material from the sample surface. The desorbed plume consists of ions and neutral species (Fig. 1.6). The thermal proton transfer theory discusses the ion generation process.[171] In this model, the incident UV photons are absorbed by the matrix molecules. The photon energy is translated into thermal energy in the matrix molecules. A build-up of thermal energy occurs which results in temporary crystal melting, where heat-induced chemical reactions occur. This is immediately followed by sample desorption initiated by the excess of thermal energy. Following desorption from the surface, the analyte-matrix molecules generate a high-density plume of gas which expands and cools down rapidly in the evacuated MALDI ion source.[172] It should be noted that the MALDI ionisation process is still a subject of debate.

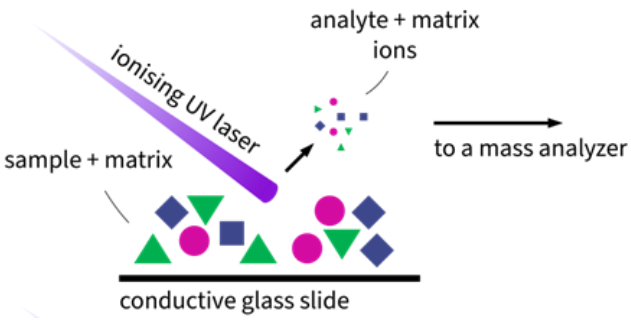

Figure 1.6 The MALDI ionisation process. MALDI matrix, which is either mixed with a sample or deposited on a sample surface is desorbed from a surface and partially ionised by a fast repetition high power laser. The ions are directed towards the mass analyser in an electric field.

Whilst matrix deposition can achieve sub-micron crystal sizes, the maximum spatial resolution of a typical MALDI imaging experiment is between 5 µm and 15 µm,[173-175] and is governed by the diameter of the laser spot on the sample surface. The sensitivity (or limits of detection) of the analyte is directly proportional to the amount of desorbed material and therefore the sensitivity of the instrument decreases with the decrease in laser spot diameter. MALDI-2-MSI is a recently developed post-ionisation technique, which addresses this issue of sensitivity by using a second UV laser pulse, which is focused across the desorbed plume of ions and neutrals that are generated by the first UV laser impact. The second ionisation, or post-ionisation, significantly increases the sensitivity of the experiment.

Another major advance in MALDI technology to address the spatial resolution issue is known as transmission mode MALDI-2 The primary ionisation beam is positioned in a transmissive configuration.[176] This approach, pioneered by the Dreisewerd group, was capable of transmission mode MALDI-2 analysis of tissues and cells with a spatial resolution of 600 nm.[177]

Boskamp and Soltwisch have demonstrated that different classes of lipids in lipid mixtures were more likely to be detected by MALDI at the cost of the rest of lipid species in a sample.[178] This effect was appropriated to an ion suppression effect, where molecular constituents in an ionised sample “compete” for the ionising energy. This effect can lead to false-negative detection of analytes. Furthermore, intensities of analytes cannot be directly correlated with analyte concentrations.[179] Thus, MALDI MSI cannot be a reliable quantification technique especially in tissues, such as brain, where the ion suppression is known to generate significant differences between

white and grey matter.[180] However, the introduction of mimetic models[99,181] of analytes and the deposition of internal standards,[7,182] have considerably improved quantitative measurements of analytes.

1.3.1.4. Surface-assisted laser desorption ionisation (SALDI)

It is essential that the material used for mounting the sample of interest is conductive in order to generate a suitably polarised electric field, which directs the flow of analysed ions into the mass analyser inlet.[183] Therefore, the ionisation process of samples which are not on placed conductive substrates will not occur efficiently and the ions will not be directed towards the mass analyser. Typically, the electric circuit is closed by a steel plate onto which a sample is deposited in non-imaging MS analyses. To achieve the same with glass slides, their surface has been coated with indium-tin oxide (ITO). Alternatively for configurations which are not compatible with ITO coated slides, conductive copper[183] and graphene[184] adhesive tapes can be employed.

Recently, Hamamatsu Photonics, Ltd. released a novel conductive desorption ionisation approach known as Desorption Ionization Using Through Hole Alumina Membranes (DIUTHAME), which can be applied as a conductivity substitute. DIUTHAME is a surface-assisted laser desorption/ionisation (SALDI) technique substrate, which unlike MALDI does not require complex matrix application and requires minimal sample preparation as the membrane is simply pressed onto the sample mounted on a glass slide. Additionally, SALDI techniques are not plagued by background ions originating from matrix molecules. DIUTHAME is an ultrathin aluminium-platinum membrane consisting of small diameter pores ($d \approx 200$ nm), which extract analytes in liquid phase from the sample by capillary forces on the membrane surface. The analytes are then ablated by the MALDI UV laser from the surface of the membrane.[185,186] The DIUTHAME technique has been used in the study of lipids in murine tissues.[187] In this study, MALDI outperformed DIUTHAME by approximately 1 order of magnitude in sensitivity. This difference was likely due to the lower extraction efficacy of the DIUTHAME compared to with the matrix extraction process. Nevertheless, DIUTHAME MSI produced an improved image contrast and signal homogeneity compared to MALDI.

1.3.2. Ion separation techniques

Time of flight (TOF) mass analysers are commonly used in MALDI MS Imaging systems (Fig. 1.7). TOF mass analysers can separate ions at high speed at the expense of spectral resolution, which is typically not precise enough to separate isobaric species. However, their speed makes them favourable analysers in high-throughput spectrometers[188] and in clinical diagnostics applications.[189]

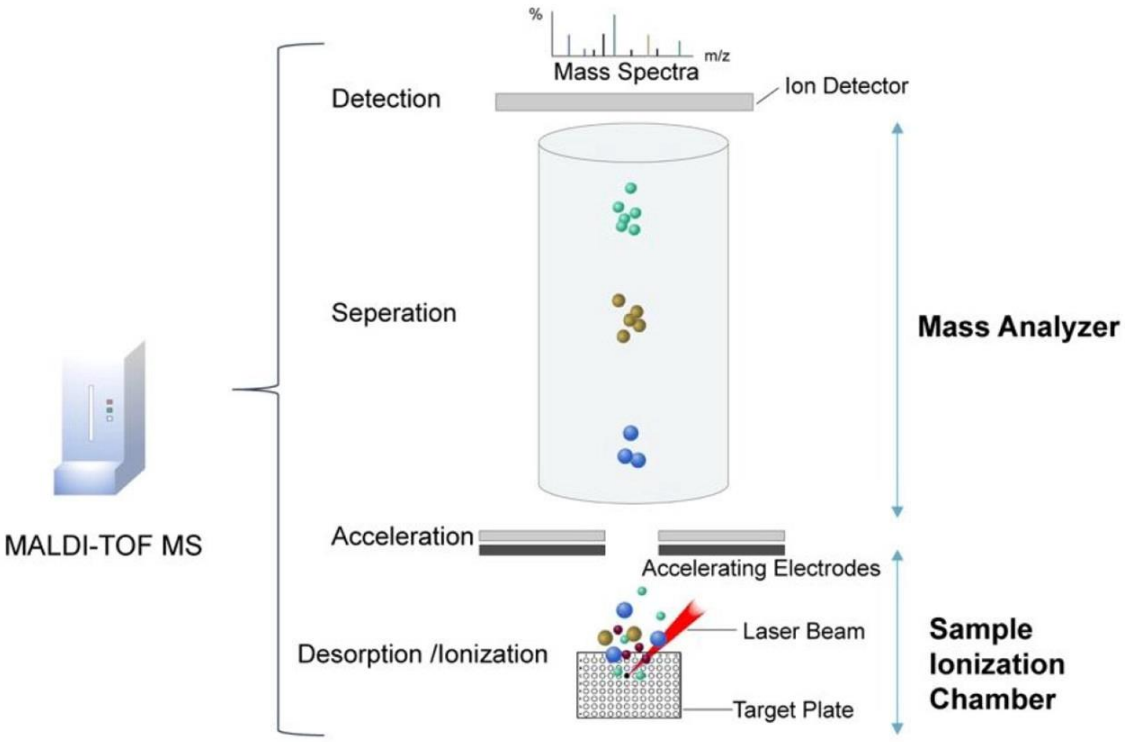

Figure 1.7 MALDI TOF schematic. Ions are generated by high energy laser impact on a sample plate in the ion source inside an evacuated sample ionisation chamber. From there, ions are accelerated by an electric field into a TOF tube, where they are separated based on their mass and charge, until they reach a detector which leads to mass spectra generation. From Li et. al., 2022, Copyright Creative Commons CC BY NC ND 4.0.

Upon ionisation, the ions are directed into a high-voltage electric field, where they are accelerated and passed into a TOF tube, which is free of a magnetic or electric field. The travel time (t) and the velocity (v) of each ion in the TOF tube path (d) is of quadratic inverse proportionality to the ion's mass (m) and its potential energy given by the ions charge (q) and the voltage (U) as shown in the equations 1.1 and 1.2, respectively.[190] MALDI is characteristic for its production of low-charged ions mostly constituting of singly charged ions (q = 1; q = -1).[191] Because all ions are

exposed to the same voltage, the only velocity differentiating factor between single-charged ions is effectively their mass.

$$t = d\sqrt{\frac{m}{2qU}} \qquad \text{Eq. 1.1}$$

$$v = \sqrt{\frac{2qU}{m}} \qquad \text{Eq. 1.2}$$

The mass resolving power of TOF analysers can be improved by increasing the length of the flight path and by using an ion reflectron at the end of the TOF tube. A reflectron comprises of a series of electrodes generating a constant electric field gradient which reduces the kinetic energy spread and reflects the ions towards the detector, which leads to an improved mass resolving power and mass accuracy.[192] Alternatively, TOF analysers can benefit from fragmentation studies desirable in isobaric species separation, where the ions of interest are fragmented in either a collision-, laser-induced dissociation, which uses either a gas or laser to fragment the parent ions, which are then further separated in a second TOF tube.[193] Alternatively, a post-source decay coupled with a LIFT cell can be used (Section 3.6.1). The LIFT method detects ions which were generated after the initial high-power ionisation in MALDI. The LIFT unit separates fragmented ions in a user-selected mass window from the remainder of the non-fragmented ions, which are then released into the second TOF tube with an elevated potential energy.[194]

Apart from TOF and other sector-based analysers, ions can also be analysed by ion trapping in either magnetic or electric fields.

Fourier transform ion cyclotron resonance (FTICR) mass analysers use a magnetic field to trap ions inside a cyclotron which consists of exciting plates and detection plates forming a ring structure. The exciting plates transmit a radial electric field which drives the ion oscillation, whereas the detection plates detect the ion frequencies which are then transformed into a mass spectrum using the Fourier transformation.[195]

Alternatively, Orbitrap analysers capture ions in an electrostatic field which is generated by an oppositely-polarised spindle electrode (dubbed Kingdon trap), around which the trapped ions orbit and move along the longitudinal axis. A second electrode (Knight trap) is used to collect the frequency information, which is

transformed with the Fourier function into a mass spectrum in the same manner as the FTICR signal processing.[196]

The sample analysis time is significantly prolonged for FTICR in comparison with TOF analysis, however, the mass resolution and accuracy of FTICR and Orbitrap allows direct separation of isobaric species. At *m/z* 200, mass resolution of Orbitrap was found to surpass the mass resolution of TOF instruments four-fold. The FTICR analyser was found to exceed the maximum resolution of TOF analysers by fifteen-fold at *m/z* 400.[197]

1.4. Complex *in vitro* models (CIVMs)

The success rate for drug approval is notoriously poor and the price of developing a single drug can reach beyond 2 billions of US dollars[198] over the span of 10 to 15 years. The steep financial and time costs associated with a drug research and development mean that a reduction in a drug attrition rate (removal of a therapeutic compound from a drug development pipeline) is increasingly sought-after to improve the success rate and the number of new therapeutics reaching patients sooner.[199]

It has been projected that the implementation of CIVM, such as the organ-on-chip technology, may reduce the cost of bringing a new drug to the market by 10 % – 26 %.[200] The CIVM technology was designed with a purpose to substitute the use of animal models that have been an inseparable cornerstone of the drug development pipeline to fulfil ethical and legal obligations of pharmaceutical companies to evaluate the safety and efficacy of a new drug prior to dosing in humans during clinical trials.[201] However, there are instances where the results obtained are not representative of the human body.[202] 2D cell cultures, where the cells are grown on a glass slide in a monolayer and minimal structural complexity provide easy access including access for imaging, but at the same time, the low structural complexity falls short of representing the *in situ* phenotype in highly structured and complex tissues. Thus, the development of alternative approaches using human-relevant samples, such as CIVMs, are an encouraging area of exploration. Albeit animals studies may still be necessary e.g., toxicology studies, the implementation of CIVMs into the drug development process will likely lead to a big reduction in the number of animals needed, which is very advantageous from an ethical viewpoint. This has been also

reflected by the FDA Modernization Act 2.0, which refutes the original requirement from the 20th century, which required mandatory animal testing for every new drug on the market and opened the possibility.[203]

The simplest transformation of a 2D cell culture into a 3D is growing cell in spheroids – self-assembled circular aggregates of cells.[204] The advantage of growing cells in a spheroid over a 2D culture is the closer representation of physiological cell shape and a prevalence of cell-to-cell contact instead of the cell-glass surface contact.[205] Monocultures and cocultures can further create a tissue-relevant physiological microenvironment inside the spheroid. The core of large spheroids are often consisted of dead cells due to a an insufficient exchange of nutrients and metabolites in the hypoxic spheroid centre.[206] Spheroids have been applied to cancer research[207] since the necrotic core is a characteristic shared with many solid tumours, caused by a poor vascularisation.[208] However, spheroids are prone to grow in heterogeneous shapes and sizes and therefore a pre-selection of samples is necessary to obtain reproducible data.[209]

Organoids are a type of self-assembling cell aggregates, which are often derived from stem cells.[210] Unlike spheroids, organoids are more complex in structure and cell heterogeneity, which enables the organoid to mimic the physiological function of a full organ. At the same time, the complexity of organogenesis in organoids gives rise to strong heterogeneities in the final morphology and function between samples caused by the stochastic self-organisation of cells and pose a difficulty to reach reproducibility between organoid replicates.[211]

The organ-on-chip models are highly ordered anatomically and physiologically human-relevant systems, which are used to mimic the environment in the human body. Organs-on-chip typically consist of scaffolds which are used to grow human-like cell heterocultures in a physiologically relevant environment. The scaffolds provide mechanical “cues” which support cells and determine their shape, orientation and localisation in the sample, which in turn improves the reproducibility,[212] unlike in the self-assembled spheroids and organoids. Organ-on-chips are often connected to flow systems, which mimic the flow of nutrients and metabolites to maintain microphysiological conditions. The organ-on-chip systems can be further

interconnected in modular CIVM configurations, where multiple model organs can be cross-connected for up to several weeks.[213,214]

The most scrutinised organ in drug development is the liver since it plays a crucial role in drug metabolism. [215] Additionally, these tissue models were a subject to liver diseases, such as type B hepatitis[216] and the non-alcoholic steatohepatitis[217]. Majority of cell in liver are hepatocytes from ~60 %, followed by Kupffer cells (~15 %).[218], which are also the cell types commonly used in liver-on-chip systems. Kupffer cell is a liver tissue-specific macrophage, which is necessary for pathogen response and for injury and liver repair.[219] The scaffolds in liver-on-chip CIVMs typically consist of flat, hard polymer with perforations, wherein the cells are seeded and grown.

Although this configuration allows single photon excitation fluorescence confocal microscopy of the sample surface and the upper layers of cells grown in the scaffold pores, the majority of the cells in a sample are not accessible with a standard confocal microscope due to the light scattering caused by the adjacent layers of cells and the polymer scaffold. Label-free imaging using SHG, THG or Raman spectromicroscopy is likely to be limited, albeit the use of multiphoton system could improve the depth penetration.

The high complexity of organ-on-chip samples requires an attention to scaffold design, which allows for a desired analytical technique and circumvents the inaccessibility of cells in a sample, e.g. liquid chromatography-MS,[217] and viability assays[220] and spontaneous Raman scattering micro-spectroscopy.[221] To date, a MALDI MSI method which would allow a direct analysis of cells grown in an organ-on-chip system is not a common practice and instead, 3D cell and tissue samples are removed from chips and then imaged.[222,223] This is mostly due to a lack of conductivity necessary for MALDI ionisation. However, Jo *et. al.* reported a successful application of MALDI MSI in visualisation of peptide release in neuronal cells grown on chip with the use of a conductive substrate.[224]

1.5. Physicochemical properties of small analytes

Pharmacokinetics, drug localisation and drug dynamics in living systems are significantly influenced by the physicochemical properties of the drug molecule.

Understanding and optimising physicochemical properties required for the drug uptake is cornerstone to success in drug development, and plays an important role in reducing the attrition rate of drug candidates.[225]

One of the first set of parameters for consideration are known as the “Lipinski Rule of 5”.[226] This states, that the likelihood of sufficient drug solubility and permeability for successful absorption is increased if the drug has ≤ 5 H-bond donors, mass of ≤ 500 Da, ≤10 H-bond acceptors, and a partition coefficient LogP ≤ 5. Butler et. al. proposed a developability classification system (DCS) an optimised categorisation framework of drug candidates based on factors limiting oral absorption. This system categorised drug candidates into 4 quadrants based on their “poor” and “good” solubility and permeability properties. Successful drug candidates were expected to populate the good solubility and permeability quadrant, and partially the poor solubility/good permeability quadrant.[227] The DCS serves as a tool for the identification of formulation strategies to improve poor absorption of drug candidates.

More physicochemical properties, such as lipid binding and protein binding were discovered to play an important role in in drug localisation, and dosing.[228] Analyte solubility and permeability were found to be a significant factors in analyte extraction in MALDI MSI experiments, during which the likelihood of extraction is closely linked with the relative matrix and analyte solubility.[229] Although some of these physical properties (e.g., oil-H_2O partition coefficient) can be predicted *in silico*,[230] the physicochemical information about a drug candidate is obtained through routine experiments, which are conducted on 25 000 samples per year at GSK.[228]

The effect of physicochemical properties in MALDI imaging has not been extensively studied although some where partially explored. For instance, the relative solubilities of an analyte and a MALDI matrix were proposed to affect the ionisation efficiency of an analyte, which was potentially a result of analyte-matrix segregation.[229] The permeability of analytes was explored in the relationship to the permeation of cell membranes in MALDI MS.[231] However, these physicochemical properties were not yet explored in terms of the interaction between an analyte and tissues during the MALDI matrix tissue extraction process. Similarly, the correlation between the protein and lipid affinity of an analyte during the analyte extraction has not been explored either. Furthermore, the protein affinity to tissues and lipids can result in increased propensity of an analyte drug to bind specifically and non-

specifically to tissues,[232] which is likely to alter the efficiency of analyte extraction from tissues.

2. Aims

The aim of this project was to develop a translation method which would allow imaging analyses of a single biological sample using MALDI MSI and SRS microscopy. DESI was considered as a more suitable approach, which would simplify the sample preparation development. This route was abandoned due to travel and off-site work restrictions caused by Covid-19 pandemic and the Covid-19-linked working governance at GSK. Therefore, MALDI was used to assess the only in-house available MSI instruments with the aim to introduce novel protocols for SRS-to-MALDI translation studies. MALDI was benchmarked in biological material of increasing complexity ranging from cell cultures to tissues. In addition, the detection sensitivity of small molecule drugs was assessed based on a technique-comparative MALDI and SRS study in correlation with physicochemical properties, which were likely to influence the drug localisation and any imaging system-specific drug detection capability.

In Chapter 4, test compounds with specific chemical structures, which were favourable for detection with MALDI and SRS, and known physicochemical properties – solubility, permeability, lipophilicity, and protein affinity – were detected in series of increasingly complex biological matrices. The acquired data was discussed in context with the physicochemical properties.

In Chapter 5, the incompatibilities present in a sequential analysis of a single sample between MALDI MSI and SRS microscopy were identified and removed by the application of a modified, published and commercially available, matrix-free method, which enabled SRS-to-MSI analyses. This method was evaluated in tissues and cell cultures in comparison with the standard MALDI analysis.

In Chapter 6, the capability of hyperspectral SRS Leica system was applied in Raman-based cell classification in formalin-fixed cell heterocultures in liver-on-chip CIVM scaffolds. SRS, confocal and light sheet fluorescence microscopy were also applied in a CIVM sample characterisation and an investigation of best procedures for an optical analysis of the CIVM sample. The CIVMs were imaged using MALDI MSI and the modified MSI protocol applied in the SRS-to-MSI experiments in Chapter 5.

In Chapter 7, heart tri-culture grown on glass slides was applied to examine and classify individual cells by hyperspectral SRS and SHG using multiple machine learning techniques.

3. Materials and methods

The human biological samples were sourced ethically, and their research use was in accord with the terms of the informed consents under an IRB/IEC approved protocol.

All animal studies were ethically reviewed and carried out in accordance with the Animals (Scientific Procedures) Act 1986 and the GSK Policy on the Care, Welfare and Treatment of Animals.

3.1. Cell culture

4 % paraformaldehyde (PFA)-fixed primary hepatocyte and Kupffer cells co-culture in complex *in vitro* model scaffolds were obtained from CN Bio in a phosphate buffered saline(PBS) solution.

Human primary iCell Cardiomyocytes and Endothelial Cells were sourced from Cellular Dynamics International, USA. Cardiac fibroblasts were purchased from PromoCell, UK. Cells were cultured in appropriate growth media by an internal collaborator. Cell samples were supplied formalin-fixed on cover glass for microscopy analyses.

Cryopreserved SW480, Calu-3 and Caco-2 cell lines used in the experiments in Chapters 4, 5 and 7 were obtained from American Type Culture Collection (ATCC). Cells were grown in T-25 cell culture flasks, in an incubator at 37 °C in a 5 % CO_2 atmosphere. Adherent cells were cultured in a high glucose Dulbecco's Modified Eagle Medium (DMEM) supplemented with GlutaMAX™ (Gibco, UK) and with 10 % (v/v) foetal bovine serum (FBS) (Gibco, UK). All work was conducted in a biosafety level 2 (BSL2) cabinet.

Cells were passaged every 3 – 5 days after reaching approximately 70 % – 80 % confluency as determined with a brightfield microscope. During the cell passage, cells were washed with phosphate buffer saline (PBS) solution and then incubated with 2ml of TrypLE (Gibco, UK) to detach the cells from the flask bottom surface (5 – 10 min) in 37 °C. In a BSL2 cabinet, the cell suspension was mixed with 3 ml of fresh incubation medium in a sterile 15 ml Falcon tube and centrifuged at

200×G for 5 min at a room temperature. In a safety cabinet, the supernatant was discarded, and the cell pellet was resuspended in 2 ml of fresh culture media. 80 % of the cell suspension was discarded. The suspension was refilled with fresh culture media to a total volume of 6 ml and transferred into a T-25 flask.

Where necessary, cells were counted in suspension using a Countess II cell counter (Thermo Scientific, UK). 10 µl of cells in suspension were mixed with 10 µl of trypan Blue (0.4 %). The mixture was pipetted on a Countess™ cell counting chamber slide and inserted into the imaging slot of the cell counter which provided the concentrations of live and dead cells within the chamber.

3.1.1. Preparation of imaging slides of cell samples

For sufficient cell adhesion and proliferation for the MALDI MSI experiments, conductive Intellislides (Bruker Daltonics, UK) required a poly-D-lysine (PDL; Fisher Scientific, UK) surface treatment. Cell cultures also required wells to avoid sample drying. Therefore, silicone isolators (Fisher Scientific, UK) with 9 mm-wide hollow centres were adhered to Intellislides to form wells. These were then sterilised by ethanol submersion for 15 min before drying in a BSL2 cabinet. Slides were handled in sterile petri dishes to avoid contamination. After drying, the wells were filled and incubated with ~20 µl of poly-D-lysine at room temperature. After 1 h, the slide wells were washed with sterile H_2O and left to dry.

For microscopy experiments, 0.17 mm-thick square glass cover slips were adhered to Invitrogen™ Secure-Seal™ spacers or silicone isolators, depending on whether the samples were planned for SRS only or SRS-to-SALDI experiments, respectively. Slides with spacers were sterilised by washing in ethanol for 15 min. Cover glass was handled in sterile 6-well culture plates.

For non-imaging MALDI MS experiments, cells were grown in 12-well Falcon cell culture plates (Fisher Scientific, UK).

3.1.2. API treatment of cells

Cells were seeded into wells at a ~10 % density for microscopy and SALDI analyses and at ~30 % density for MALDI analyses in fresh DMEM solution

(GlutaMAX, 10 % FBS). After 2 days, methanol dissolved GSK4, GSK4x and GSK90 were mixed with fresh incubation medium to final concentrations of 0, 25, 50, 100 and 200 µM whilst maintaining the API concentration ≤2 % v/v. The old DMEM was replaced by the API-spiked DMEM and incubated for up to 2 h (37 °C, 5 % CO_2). Samples were 1× washed with PBS and then processed depending upon the subsequent analysis.

3.1.3. Cell sample processing

Microscopy samples were fixed with 10 % neutral-buffered formalin (Sigma, UK) for 12 min and washed 3× with PBS. Cells on cover glass with gaskets were then sealed with a second 0.17 mm-thick cover glass in a PBS solution.

Samples for MALDI MSI were fixed by a sample submersion in a chilled 70 % ethanol (-20 °C) for 12 min. Samples were washed with ammonium phosphate (10 mM) and dried.

MALDI MS cell samples were detached from the well bottom with TrypLE and centrifuged (400 G, 4 min). The supernatant was removed and the live cells in pellets were frozen and stored in a -80 °C freezer until use.

3.2. Mimetic model preparation

Mimetic models are serial dilutions of spiked APIs into tissue homogenates which are used to determine the limit of detection (LOD) with MALDI MS and with SRS. The homogenates were prepared from either mouse brain or liver tissue from control animals (undisclosed mouse strain) taken from unrelated studies. The mimetic model sample preparation was modified from the protocol devised by Barry *et. al.*[233]

Frozen tissues (-80 °C) were thawed and cut into small pieces and placed into Precellys lysing tubes (VWR, UK) containing magnetic beads and homogenised in an MP Fast Prep 24 (MP Biomedicals, USA) at 1600 RPM for 3×30 s. The brain and liver tissue homogenates were separated from the beads by adhering the beads to a vial lid using magnets on top of a vial cap followed by low-speed centrifugation

(400×G, 8 min). The resulting homogenates were divided into 1 g aliquots and added to new lysing vials and frozen (-80 °C).

The APIs used for homogenate spiking were dissolved in HPLC-grade methanol. Brain and liver homogenate aliquots were mixed with the APIs into 0 – 500 µg/g (API/tissue) and a v/v concentration below 2 %. API-spiked homogenates were mixed using magnetic beads and MP Fast Prep 24 at 1600 RPM for 30 s. Samples were kept on ice to minimise any potential API metabolism. Homogenates were separated from the beads by centrifugation at (400×G, 8 min) and stored at -80 °C.

The mould for the mimetic model cylinders was prepared by cutting off the end of a plastic 6 ml syringe barrel. The plunger stem was cut off and pushed inside the bottom of the tube to create a sealed mould. The mould was submerged into a dry ice-chilled ethanol bath. Using a positive displacement pipette tip, ~300 µl of blank tissue homogenate was pipetted into the bottom of the mould. Once the layer was solid, a similar volume of the remaining spiked homogenates were stacked on top of each other at an increasing API concentration. ~1-2 min pause in between stacks was necessary for the homogenate to solidify. Mimetic models were stored at -80 °C overnight and then pushed out of the moulds for cryosectioning.

3.3. Cryosectioning

Mouse brain and liver tissues were received snap-frozen and were stored at -80°C. Working on dry ice, whole organs and organ mimetic models were mounted onto cryostat sectioning chucks using 1 % w/v solution carboxymethylcellulose (Merck, UK).

In clean plastic moulds, CIVM liver-on-chip scaffolds were placed on the bottom with the cell rich side facing the plastic. A 10 % hydroxypropyl methacrylate (HPMA) aqueous solution was poured over the scaffold. The mould was frozen in a dry ice-chilled ethanol bath. Afterwards, the mould was removed, and the sample was fixed on a cryostat chuck with 1 % carboxymethylcellulose. Samples were then placed in the Leica CM3050S cryostat (Leica Biosystems, UK) with the sample temperature

set to -18 °C and the chamber temperature set to -19 °C. Cryosections were cut at thicknesses varying between 6 – 100 µm depending upon the application.

In most samples, an anti-roll glass was used to ensure samples landed flat onto the sampling stage. Glass slides, cover glass squares or Intellislides depending upon the application were carefully placed on top of the sections to adhere, a process known as thaw-mounting. To maximise adherence via the thaw-mounting procedure finger or the palm of the hand was pressed on the underside of the glass slide. Samples were then dried in ambient conditions on a benchtop prior to further processing for an MSI or an SRS analysis.

Alternatively, CryoJane adhesive tapes (FisherScientific, UK) were used to support and transfer the 6µm complex *in vitro* model (CIVM) cryosection during the MALDI MSI sample preparation procedure. The adhesive tape prevented scaffolds from curling which otherwise occurred during cryosectioning. A tape was adhered to the sectioned face of the sample of interest. After a layer of a sample was cryosectioned, the tape and the cryosection were attached to an Intellislide and thawed. After thawing, the Intellislide was quickly frozen again with a Frostbite freeze spray (Leica Biosystems, UK) to strongly bond the slide to the sample, whilst the CryoJane tape was pulled off, leaving the sample to dry on an Intellislide.

3.4. DIUTHAME application

In thin (≤30 µm) tissue sample SALDI experiments, standard imaging DIUTHAME (Hamamatsu Photonics, UK) substrates were used. The protective sheet of plastic was removed from the adhesive at the bottom of the membrane frame using tweezers. For tissue experiments, the DIUTHAME was attached to a cold imaging slide with sample already thaw-mounted. In cell experiments, DIUTHAME was attached at room temperature to the wet, live sample.

In thick (≥30 µm) CIVM scaffold analysis, a blotting DIUTHAME membrane was applied. The DIUTHAME was placed on a dust-free, clean surface upside down (adhesive side up). The still wet scaffold was carefully laid on the DIUTHAME membrane with cell-rich side facing towards the membrane, followed by an Intellislide. Without sealing the DIUTHAME frame to the Intellislide, the scaffold was turned upside-down. The scaffold was then gently pressed against the Intellislide. After drying, the scaffold was sprayed with the TFA solvent (Table 3.1).

CryoJane cryosectioning adhesive tapes were used again to ensure the scaffolds remained flat during the sectioning and sample transfer onto a slide. The advantage of using DIUTHAME over MALDI matrix was that the conductive surface was moved above the sample and therefore, the tape did not have to be separated from the sample as it would not interfere with the current transfer. A scaffold in a HPMA block was mounted on a cryosectioning chuck. The tape was attached to the sample surface and a cryosection was made below the tape. After sectioning the sample on the tape, it was transferred onto an Intellislide and sandwiched and thaw-mounted with the DIUTHAME membrane (Fig. 3.1).

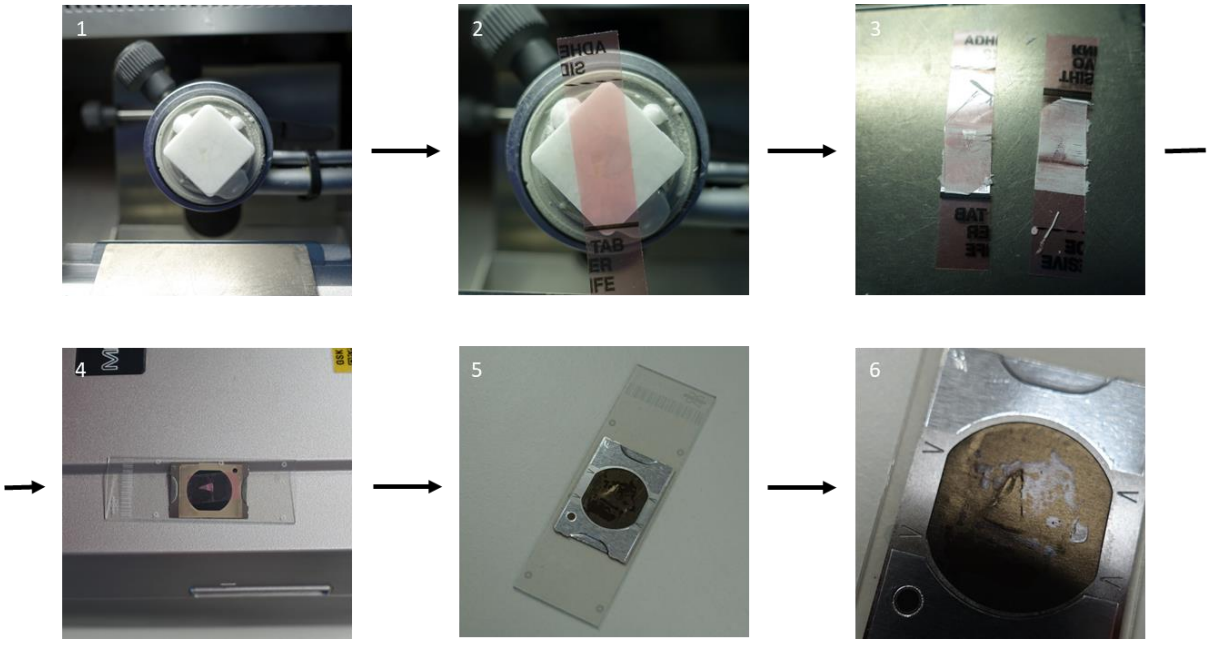

Figure 3.1 CIVM tape transfer onto an Intellislide. A scaffold in a HPMA block was mounted on a cryosectioning chuck (1). The tape was attached to the sample surface (2) and a cryosection was made below the tape. Afterwards, the samples on tapes were transferred onto an Intellislide and sandwiched with a DIUTHAME membrane, and thaw-mounted (4-6).

3.5. Matrix and solvent deposition

The matrix used for all MALDI experiments was α-Cyano-4-hydrocycinnamic acid (αCHCA; Bruker Daltonics, Germany) dissolved in 0.2 % (v/v) trifluoracetic acid (TFA) in 70 % methanol (aq) at a 7 mg/ml concentration. 0.2 % TFA in 70 % methanol (aq) was also used in SALDI experiments.

For the analysis of API standards and cell suspensions on a target plate by MALDI MS and MS/MS, a “sandwich method” was used. For this method, 1 µl of

matrix was first spotted onto the MALDI target plate and dried. Then 1 µl of the selected sample was added to the dried matrix spot and also allowed to dry, before adding another 1µl of matrix and allowing to dry.

For tissue samples mounted on glass slides (Intellislides) matrix was sprayed using the TM-Sprayer (HTX Technologies, USA). The spray nozzle of the sprayer was set at a distance of 40 mm from the sample plate. Other conditions used for sample spraying are shown in Table 3.1.

MALDI samples were sprayed with αCHCA matrix directly, while SALDI samples were first mounted to a DIUTHAME and then sprayed with a TFA solution.

Application	Solution	Temp.	Solvent flow	XY speed	Gas pressure	# of passes
Tissues	αCHCA	75 °C	0.12 ml/min	1200 mm/min	10 psi	8
CIVM and tissues	TFA	65 °C	0.12 ml/min	1350 mm/min	10 psi	4 (20 s drying)
Cells	αCHCA or TFA	65 °C	0.09 ml/min	1200 mm/min	10 psi	4

Table 3.1 TM Sprayer matrix/solvent deposition settings.

3.6. Mass spectrometry

All MALDI and SALDI data were acquired using the Bruker ultrafleXtreme TOF/TOF mass spectrometer (Bruker Daltonics, UK) equipped with a Smartbeam-II Nd:YAG laser at 355 nm wavelength. The instrument was controlled with the flexControl software v 3.4 (Bruker Daltonics, UK), which was also used for single point spectral acquisition. Mass spectrometry imaging experiments were defined and acquired using the flexImaging software v 5.0 (Bruker Daltonics, UK).

3.6.1. Mass spectra acquisition

Single point TOF spectra were acquired with a mass range of 100 – 1500 *m/z* (100 – 1700 *m/z* in an instrument calibration). The laser attenuator was set to 25 – 50% in MALDI and 50 – 90% in SALDI experiments. The laser fired 2000 shots with a fire rate of 2 kHz in MALDI and 1 kHz in SALDI with a random walk spot analysis.

The Smartbeam laser diameter was set to “large.” The digitiser was set to a high resolution 5 GS/s setting. The ion sources 1 and 2 were set to 25 kV and 22.57 kV, respectively. The lens was set to 7 kV and the reflectors 1 and 2 were set to 26.45 kV and 13.42 kV.

Each experiment was preceded by a system calibration using a peptide/αCHCA mixture with mass peaks shown in Table 3.2. Maximum error tolerance was set to 500ppm.

αCHCA $[M+H]^+$	190.050 *m/z*	Angiotensin I $[M+H]^+$	1296.685 *m/z*
αCHCA $[2M+H]^+$	379.092 *m/z*	Substance P $[M+H]^+$	1347.735 *m/z*
Angiotensin II $[M+H]^+$	1046.542 *m/z*	Bombesin $[M]^+$	1619.822 *m/z*

Table 3.2 Calibration standard exact mass peaks for positive mode MALDI MS.

A pseudo-MS/MS approach, known as LIFT mode, was used to generate fragment spectra of analytes using the MALDI method. Single spot LIFT analysis was conducted in positive mode, where the analytes were ionised and fragmented through an application of high intensity laser during a laser induced dissociation (LID) process. In the first TOF, parent and fragment molecules reached a precursor ion selector (PCIS) unit at the same time. The PCIS unit filtered out all other ions travelling at different speeds. The precursor and fragment ions were further accelerated in the LIFT unit. Parent masses were manually input based on previously measured MS spectra of the analytes and with a 0.45 % PCIS window range. The laser attenuator was set to 50 % in parent mode. The laser was set to 92 % in fragment mode. The ion sources 1 and 2 were set to 7.5 and 6.65 kV, respectively. A lens voltage was set to 3.9 kV. Reflectors 1 and 2 were set to 29.5 kV and 14 kV, respectively. The LIFT 1 and 2 units were set to 19 kV and 3.8 kV, respectively. The minimum detected mass was set to 40Da, and the maximum was variable based on the analyte molecular weight. The detector gain was set to 2991 V, and the digitizer was set to 0.63 GS/s.

Single point spectral data were saved in proprietary Bruker filetypes folder/filetypes “.d.” Spectra were visualised and compared in flexAnalysis v 3.4 (Bruker Daltonics, UK) and exported in mzXML format.

3.6.2. Mass spectrometry imaging

In the flexImaging GUI, sample positions were registered using brightfield images of samples on MALDI slides generated on the Reflecta scanner with the TissueScout image acquisition software (Bruker Daltonics, UK). The number of spectral datapoints per raster spot was reduced to a preset 8000 and automated spectral baseline subtraction was applied. Scan areas were manually selected, and the raster step size was set to 25 – 250 µm. The spot sampling was set to random walk with a diameter limit set to less than or equal to the raster step size.

Mimetic models were imaged using the MALDI LIFT method, with 200 shots per spot were fired at a 200 µm step size. The SALDI and MALDI imaging of tissue sections was done with 25 – 500 µm raster size and 500 shots per spot.

Data was not normalised for mimetic models and tissues in Chapter 4. The MSI data shown in Chapters 5 and 6 was normalised to the total ion current (TIC), which scaled individual spectra to a relative abundance of all detected ions in a given spectrum/acquisition. Single ion images were generated through setting up mass filter along the spectral axis (e.g., *m/z* 184) with an *m/z* ± 0.2 mass range which highlighted the spatial distribution of this mass with a false-coloured heat map intensity scaling. Overall spectra or ROI spectra were extracted into.*csv* files. Further baseline subtraction (if necessary) and peak picking was done using the scikit.signal Python toolkit.[234]

3.6.3. Peak picking in MS spectra

A baseline of mass spectra was determined using the Savitzky-Golay filter[235]. After spectrum baseline subtraction, peaks were selected by introducing a sample-unique peak prominence lower limit to remove the noise.

3.7. Spontaneous Raman spectroscopy

A JY Horiba LabRAM ARAMIS Confocal Raman Microscope (HORIBA UK) was used for Raman spectral acquisition from a single point in the sample. The microscope was equipped with 633 nm HeNe and 785 nm diode continuous lasers

and a charge-coupled device (CCD) detector. A diffraction grating with 600 grooves/mm density was used. The spectrum range was set to 500 – 3500 cm^{-1}. Pure APIs as solids were analysed on a glass slide using a short working distance dry 50× objective lens. GSK4x spectra were acquired using 300 mW (100 %) laser power for the 785 nm laser with a delay of 15 s and 5 accumulations. GSK90 Raman spectrum was acquired with a 633 nm laser at a 17 mW (100 %) power and a 3 s delay for 15 accumulations. GSK4 spectra were acquired in the laboratory of Prof Andreas Zumbusch at the University of Konstanz using the MonoVista CRS Raman System equipped with 488 nm, 633 nm, and 785 nm continuous wave lasers in a back reflection configuration with variable grating and an Andor CCD camera DU420A-OE.

3.8. Lightsheet microscopy

Lightsheet Microscopy was performed on a Zeiss Light Sheet Z.1 at the Cardiff University Bioimaging Hub Core Facility (RRID:SCR_022556) with the support of Professor Peter Watson.

3.8.1. Sample preparation

PFA-fixed CIVM of liver tissue treated with MALAT1 ASO were examined with a light sheet microscope. MALAT1 is a long noncoding RNA localised in cell nuclei.[236] ASO and GalNAc ASO were delivered to cells carrier-free. Control samples were treated only with the ASO solvent – H_2O.

CIVM scaffolds (GalNAc-ASO-A488-treated, 1h timepoint) were not treated with membrane penetrating reagents since no internal labelling was necessary. Samples were washed in PBS and incubated with Cell Mask 647 (dilution 1:500), Concanavalin A 571 nm (dilution 1:500) and Hoechst 33342 (dilution 1:5000) for 1 h. Afterwards, scaffolds were thoroughly washed with PBS and prepared for loading into the microscope sample holder.

CN Bio liver-on-chip scaffolds were cut into thin strips to fit into the appropriate glass capillaries used in the Lightsheet sample holder. 1.5 % v/v low melting point agarose was preheated in a microwave and kept in a heated H_2O bath to avoid

agarose solidification. A glass capillary with a plunger and pipette tips were kept on a hot plate (>50 °C). With a preheated pipette tip, agarose was transferred on a hot plate, where it was aspirated with a glass capillary. A pore-free scaffold strip end was submerged in agarose in a capillary, whilst keeping the pore side of the scaffold outside the agarose. After agarose solidification, PBS was aspirated into the capillary to prevent sample drying.

The Imaging chamber of the Lightsheet Z.1 instrument was filled with PBS. Glass capillaries were placed into a sample holder secured with appropriate gaskets. The sample, attached to a column of solid agar was pushed out of the glass capillary to reduce light scatter from the glass interface.

3.8.2. Microscope imaging settings

Images were acquired with the Zeiss Light Sheet Z.1 using a W Plan-Apochromat 20×/1.0 Corr objective lens, immersed in PBS for detection. Fluorescence labels used in fluorescence microscopy are captured in Table 3.3. 405/488/561/640 nm laser blocking filters were applied. The lightsheet thickness was set to 4 – 6.6 µm. Imaging data were processed and flattened into maximum intensity projection in Arivis.

Fluorescent dye	Dilution	Excitation laser	Emission maximum wavelength
Hoechst 33342 (Invitrogen, UK)	1:5000	405 nm	461 nm
ASO Alexa Fluor 488	-	488 nm	520 nm
Cell Mask Deep Red (Life Technologies, UK)	1:500	638 nm	572 nm
Concanavalin A tetramethyl rhodamine (Invitrogen, UK)	1:500	561 nm	580 nm

Table 3.3 Fluorescent dyes, emission maximum wavelengths and excitation laser wavelengths used in the microscope.

3.9. Stimulated Raman scattering microscopy

A SP8 TCS CARS/SRS confocal microscope system (Leica Microsystems, UK) was coupled with the picoEmerald picosecond laser source (APE, Germany) and

controlled by the LAS X software. The laser source output consisted of two beams – a fixed Stokes beam (λ_{Stokes}) at 1031.2 nm and a tuneable pump beam (λ_{pump}) at 740 nm – 940 nm (3816 cm^{-1} – 940 cm^{-1}), which coherently drove molecular vibrations at a wavenumber (ω_{vib}) corresponding the vibrational frequencies of the pump and Stokes lasers. The relationship between wavelength and wavenumber is explained by equation 3.1.

$$\omega_{vib} = 10^7 \times (\frac{1}{\lambda_{pump}} - \frac{1}{\lambda_{Stokes}}) \quad \text{Eq. 3.1.}$$

25× Fluotar VISIR (0.9 NA) and 40× HC PL IRAPO (1.1 NA) H_2O immersion objective lenses were preferred because of their flat transmittance in the near infrared and infrared region of the light spectrum. Because the Raman signal was sharing the direction of pump and Stokes laser propagation, the SRS signal was collected in trans-illumination settings with a condenser lens. To collect maximal possible signal, a condenser with a numerical aperture (NA) higher than the NA of an objective lens was necessary. Therefore, the 1.4 NA oil immersion condenser S1 (Leica Microsystems, UK) with a ~1.1mm working distance was used. Additionally, a second harmonic generation (SHG) signal was collected in the epi-direction.

The output SRS signal is weak relative to the vibration-driving beams and therefore the UHFLI lock-in amplifier (Zurich Instruments, Switzerland) was coupled with the forward photodiode detector (PD) and the reference detector in the picoEmerald to extract the measured pump loss signal from the collected bulk signal. The time constant in the lock-in control GUI was set to 50 % of the pixel dwell time shown in the LAS X GUI. This ensured the signal sampling period of the lock-in did not overlap with acquisition with adjacent pixels, as the failure to do this would otherwise cause signal line artifacts in the images. Frame averaging was used in fast scans (>200 Hz) to further improve the SNR in the SRS channel. The hyperspectral images were also denoised in the downstream image processing (Chapter 3.10.2.3).

The system was used to generate single SRS vibrational images (XY) at 838 nm (2235 cm^{-1}), 791 nm (2945 cm^{-1}) and 796 nm (2866 cm^{-1}) which correspond to the C≡C, CH_3 and CH_2 vibrational bands.

The overarching settings for the collection of hyperspectral data cubes (XYλ) were summarised in Table 3.4.

Region	Wavelength (nm)	Wavenumber (cm^{-1})	Step size (cm^{-1})	Pixel dwell time (µs)	Time constant (µs)
CSR	832 - 845	2123 - 2322	7.8	5.2	2.6
CHR	780 - 801	2781 - 3058		2.88	1.44

Detector gain (V)	Pump power (mW)	Stokes power (mW)	Power attenuator (%)		
			Pure compound	Tissues	Cells
50 - 200	150	300	5 - 70	50 - 100	70 - 100
120 ± 25			5 - 50	25 - 50	35 - 60

Table 3.4 Hyperspectral SRS microscope acquisition settings.

Saturation of pixels would cause inaccurate results in downstream analyses and therefore was avoided in the hyperspectral data acquisition. However, a strong signal to noise ratio (SNR) was necessary to reach a sufficient dynamic range in the 8-bit pixel depth which would highlight nuanced differences in different cellular compartments for example. Finally, the pulsed laser power in SRS caused sample burning at high intensities. Therefore, a compromise between these three factors was necessary.

Polystyrene in H_2O was used as an imaging standard during the SRS system state assessment through a CH region SRS acquisition with settings shown in Table 3.4.

Objective lens	XYZ size	Spectral range	Scan speed	Frame averages
25×	256×256×41	780-800 nm	400 Hz	3

Pixel dwell time	Time constant	Laser attenuator	SRS PD gain
2.88 µs	1.45 µs	25 %	50 V

Table 3.5 Polystyrene standard sample SRS acquisition settings.

3.10.SRS data processing

SRS data were accompanied by sample non-related artifacts, which consisted of line scan artifacts, XYZ focus and sample drift and noise contribution in the images. the source of the artefact line pattern was identified in the picoEmerald laser source and resolved by an instrument engineer in the last 9 months of the project.

Before this was fixed, due to time constraints, the analysis was conducted regardless of the image artefact. These artefacts were limiting the efficiency of data analysis so to minimise the impact of these artefacts the following additional processing methods were employed.

3.10.1. FFT line scan artifact removal

The Leica TCS SP8 SRS system often produced images with a repetitive diagonal line scan pattern in the SRS channel. These were clearly visible in the homogeneous polystyrene droplet samples (Fig. 3.1a). The scan line patterns were reduced by frame averaging (3 – 12 frames) in single wavelength images. Alternatively, Fourier fast transform (FFT) could be used to remove the line patterning. In Fiji ImageJ, images were transformed into a 2D spatial frequency domain (Fig 3.1b) where the repetitive artifacts were found in high intensity line shapes. Through manual removal of these horizontal and vertical lines and by using the reversed FFT function, a pattern-free image was recovered (Fig. 3.1c) with a corrected FFT domain image, where the deleted lines appeared dark (Fig. 3.1d). The line pattern was removed from the majority of the image, however a small area at sides of the image and in the corners remained patterned. The incomplete removal was likely a result of a dynamic change in pattern frequency in scan region corners which was attributed to a gradual change in the speed of the scanning galvo mirrors as it reached the edge of the scanned area. A more thorough removal in the FFT domain would increase the efficiency of FFT-based image correction.

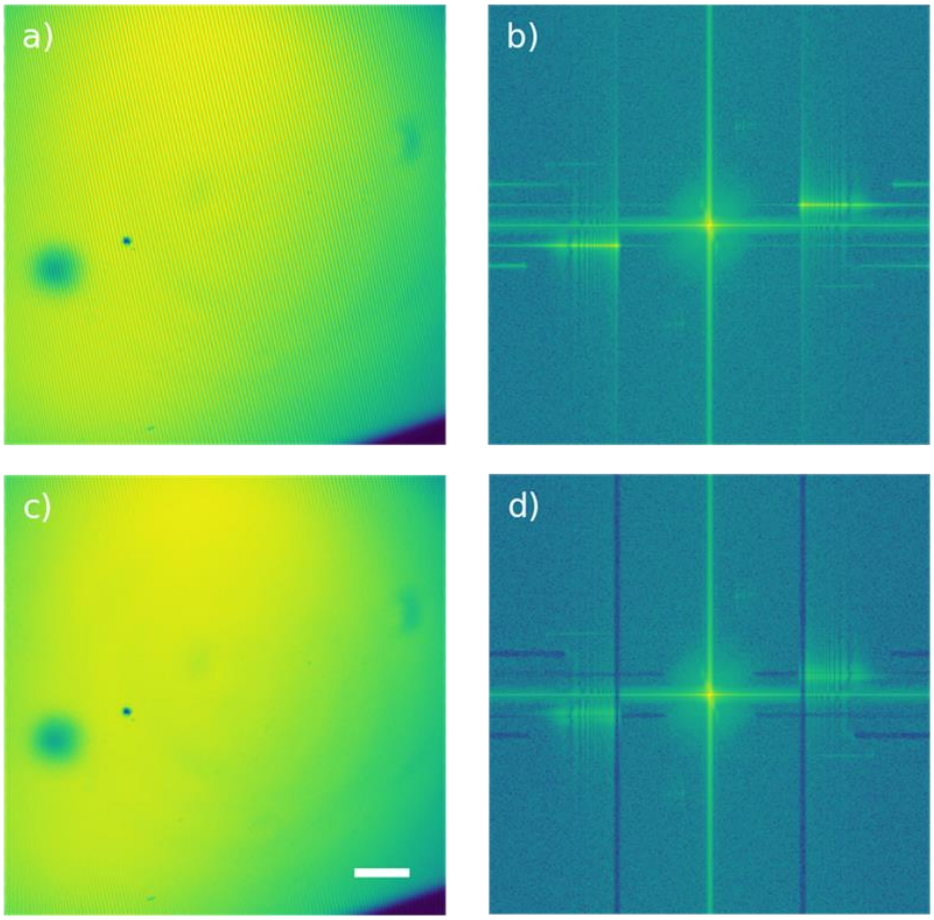

Figure 3.2 FFT line scan removal. a) Polystyrene droplet imaged with a single scan at a λ_{pump} = 791 nm (2945 cm^{-1}) resulted in periodically repeating lines. b) FFT 2D translation was used to highlight repetitive motives in an image. A majority of the image was smoothed (c) by removing 10 bright vertical and horizontal lines (d), now dark. Scale bar = 50 µm.

3.10.2. XYZ drift correction of hyperspectral SRS images

Drift in XYZ directions was prevalently observed in CIVM scaffold samples, but also in tissues and cells. The drift was likely a result of sample heating from the laser. Therefore, samples were first pre-heated by exposure of sample to the laser for 2 min which decreased the rate of sample movement. Then, the Correct 3D drift plugin in Fiji ImageJ was applied.[237] SHG channel, which captured autofluorescence, fluorescence and non-centrosymmetric interfaces, was used instead of the SRS channel, because unlike in the hSRS, the SHG signal distribution was stable throughout a scan. This tool was especially effective in hyperspectral Z-stacks which were generated in the highly drift-prone CIVM scaffolds.

3.10.3. SVD denoising of hyperspectral SRS data

Singular value decomposition (SVD) is a matrix factorisation tool which was used to remove noise components whilst preserving chemically relevant components in the hyperspectral images. The acquired hSRS matrix *X* was decomposed into *U, Σ,* and V^T matrices, where *U* and a transposed V^T were orthogonal matrices and *Σ* was a diagonal matrix as shown in equation 3.2.

$$X = U\Sigma V^T \qquad \text{Eq. 3.2.}$$

Standardly, the processed matrix is arranged into $m^2 \times n$, where *m* represents the number of spatial pixels in the X and Y directions, and *n* represents the number of spectral points. The *U* matrix is arranged into sequence of hierarchical m^2 XY components of the matrix *X*. The hierarchy orders the singular vectors with decreasing magnitude based on their ability to describe the variance in the columns of *X*. Eigenvectors of V^T are arranged hierarchically to describe the individual spectral *n* components of the *X* matrix. *Σ* consists of hierarchically ordered, diagonally arranged, non-negative singular, and decreasing values σ stretching over an $m^2 \times n$-shaped matrix (Eq. 3.3.).

$$(m^2 \times n) = (m^2 \times m^2) \times (m^2 \times n) \times (n \times n) \qquad \text{Eq. 3.3.}$$

The standard SVD approach is highly demanding on computer memory. The HIA and the uses an “economic” version of the SVD to decrease the computing memory load. The HIA reshapes the matrix *X* as $n \times m^2$ to describe a new basis for the spectra. U is $n \times n$ and describes the new basis for the spectra. *Σ is a* $n \times n$ is a thresholded diagonal matrix and contains the eigen values. and VT is $n \times m^2$ and describes the spatial distribution of the components (Eq. 3.4)

$$(m^2 \times n) = U\Sigma V^T = (n \times n) \times (n \times n) \times (n \times m^2) \qquad \text{Eq. 3.4.}$$

The first eigenvectors of *U* and V^T and the first *σ* singular values of *Σ* described the most significant components of *X* matrix. The increasing index of the elements on the diagonal of *Σ* represented components (σ^i) with a decreasing significance. Noise was a dominant component of high σ^i and therefore, a replacement of these singular values with 0 was used to clip the orthogonal matrices and remove the noise

components. In the Hyperspectral Image Analysis software (HIA), the clipped σ was manually selected based on the single σ component reconstructed images (i.e., the columns of V^T). Alternatively, an optimal hard threshold method[238] which automatically determined the cut-off σ^i was used in a Python-based fast non-negative matrix factorisation (NMF) data processing pipeline which was developed for this project and also used the economic SVD version. The new Σ was used to calculate the matrix X using the Equation 3.4.

3.10.4. LAS X tile stitching.

Tiles were acquired with 10% – 20% overlap. Mosaic merging in LAS X was set to “Smooth,” where the intensity of overlapping pixels is weighted based on the distance between a pixel and the tile image centre leading to smooth transition between tiles.

3.11. Data analysis of hSRS

3.11.1. NMF-based component separation with sklearn

Non-negative matrix factorisation (NMF) is a dimension reduction method which finds two non-negative matrices *(H,W > 0*) whose product approximates the matrix *X* by locally optimising the distance between *X* and the product of *W* and *H* summarised in equation 3.5. [239] *W* matrix contains new spectral basis vectors which are used to approximate the original matrix *X.* Whereas, *H* matrix contained weights which in combination with *W* components were used to approximate columns of *X*.[240] In NMF, components are superimposed in additive manner without subtracting. Therefore, well-constrained models can produce reality representable model interpretations.

$$X \approx WH \qquad \text{Eq. 3.5.}$$

The sklearn.decomposition.NMF[234] function was used with a random initiation parameter. The NMF can be improved by regularisation which also prevents potential overfitting. The L1_ratio regularisation method, which promotes solution where small subsets of factors have significant non-zero values which aids the interpretability of the data. The L1_ratio was set to 0. The best observed matrix convergence was found when the regularisation terms were multiplied by the *αW* set to 0.0001 and the *αH* set to 1 and the total number of components was equal to 6. The *α* regularisation terms controlled the sparsity (components density) of the factorisation by influencing a penalising constraint of a magnitude of close-to-zero components in W and H matrices.

3.11.1.1. Factorisation into susceptibilities and concentrations of chemical components (FSC^3)

FSC^3 is an unsupervised NMF algorithm, which was written by Francsesco Masia at Cardiff University, factorises hyperspectral data into non-negative absolute concentrations and spectra with the possibility to introduce a normalization of the H and W matrices (i.e., to minimise the deviation of 1 of the sum concentration) or introduce a weight to the data using the weighted algorithm.[106] The combination of all

chemical components per pixel was set to one and therefore chemical component absolute concentration can be determined.[106]

FSC^3 analyses were performed on SVD-denoised SRS hyperspectral data in the HIA software. A total of 6 components was selected using a spatial correlation constraint, which applied a Gaussian filter of 1 pixel to the data and the matrix H, which avoided very large deviation and produced images where adjacent pixels had correlation to mimic the effect of limited spatial resolution of the microscope objective. An adjustment of weighing was used to reduce the noise dominated local signal deviations to uncover small localised chemical components. The weighing was controlled by α, α' and γ parameters and a constraint [107] were set to 0.5, 0.5 and 1, respectively.

3.11.2. Cell type classification with SRS spectra using machine learning

3.11.2.1. Internal standard normalisation of hSRS data

The normalisation was introduced to reduce the effect of the laser power fluctuation which occurred during the SRS data acquisition. Hyperspectral SRS data was first drift-corrected and denoised with SVD. H_2O SRS spectra were used as an internal standard for cross-sample spectral normalisation. Voxels in cell cytoplasm and reference extracellular H_2O were transferred into separate matrices by manually selecting the ROIs. Each ROI matrix was subsequently averaged into a single spectrum. H_2O ROI matrices were averaged per image into single image spectra, which were further averaged with the remaining H_2O image spectra into a total H_2O mean spectrum. H_2O image spectra were individually divided by the total H_2O average mean, which produced correction matrices. Corrected cell sample spectra were a result of a cytoplasm ROI matrices multiplication by the correction matrices which corresponded to the appropriate hSRS images.

3.11.2.2. PCA analysis of SRS spectra

Sample spectra were scaled using the MinMax scaler (Eq. 3.6.) in the scikit Python package.[234] Scaling to minimum and maximum values was used since no outliers were expected in averaged data, H_2O-normalised data.

$$x_{scaled} = \frac{x - x_{min}}{x_{max} - x_{min}} \qquad \text{Eq. 3.6.}$$

Scaled sample spectra in an array were analysed using the principal component analysis (PCA). PCA searches for a maximum variance of all features in an original matrix by generating a covariance matrix, where eigenvectors and eigenvalues correspond to principal components (PCs) and weights, respectively. Both weights and principal components are ordered hierarchically, where the first PCs and values explain the largest covariance in the original matrix.[241]

PCA dimensionality reduction was executed with the sklearn.decomposition.PCA Python function from scikit-learn.[234] Resulting PCs were examined in pairs in 2D plots. Moreover, scoring and loadings matrices were visualised in colour-coded heatmaps. Scoring matrix was used to examine the weight of individual PCs in the samples and features matrix was used to examine the relationship between features (wavenumber data points) and PCs.

3.11.2.3. K-means

K-means is a clustering algorithm which is applied in dataset separation into clusters of similar data points. This algorithm was used as means to automatically separate the PCA-processed data. The K-means algorithm generates given number of centroids, K at random positions. The datapoints are assigned to their closest centroid based on their Euclidean distance. The centroid is iteratively moved closer to a cluster centre based on the mean of all the data assigned to each centroid, until the distance between a centroid and the sum of assigned datapoints reaches a stable minimum.[242]

The algorithm of scikit learn sklearn.cluster.Kmeans[234] was adopted in this analysis. The number of K clusters was set to a number of sample types (e.g., 2 in

cell heterocultures). The *init* parameter was set to *k-means*-++ which ensured random and distant initial localisation of K clusters. The number or initialisation was set to 4, where the analysis reached convergence, i.e., the last two iterations resulted in the same cluster centroid positions and further iterations had no impact.

3.11.2.4. Random forest classifier

Random forest was used as a classification instead of clustering. Random forest is a combinatory extension of decision trees, where outputs from all trees are averaged* with the aim to generate a model which predicts values of future variables through the learning of decisions based on preset splitting criterions. [243] Decision tree consists of decision nodes with a condition resulting in further decision nodes or leaf (end) nodes. The splitting criterion at each node was set to Gini impurity, which measured the probability of a feature mislabelling, if it were labelled randomly.[244] The number of decision nodes was not limited. The number of maximum features was constrained to a square root of total feature number. Furthermore, model bootstrapping, which ensured the individual trees were trained on different data combinations, which reduced sensitivity to the original dataset and the correlation between individual tree structures. The number of decision trees in the random forest machine learning model equalled the number of features in the dataset. The random forest classification precision was evaluated in a confusion matrix. The data analysis was conducted with the sklearn.ensemble.RandomForestClassifier.[234] The train/test separation was set to 30%/60% of the dataset. To improve the robustness of the analysis, the random forest was initialised 100× with random selection of train and test datasets.

* The original Breiman publication implemented random forest with a voting system instead of averaging.

4. Identification of samples suitable for SRS-MALDI translation method development

4.1. Introduction

SRS microscopy and MALDI MSI are both complementary powerful tools in the field of label-free imaging. SRS is used to probe the vibrational properties of a sample, whereas MALDI is applied in measuring the exact masses of individual molecules in a sample. Both methods generate hyperspectral images which provide complex information about the molecular state of unperturbed samples. However, both analytical methods have specific sample requirements which are incompatible with a sample preparation process of the other method and also dictate properties of suitable analytes. The combination of SRS and MALDI can be used to create precise SRH-generated H&E images from a tissue section used directly for MALDI. Moreover, the combination of SRS and MALDI can be exploited to generate high resolution images of lipid distribution in a sample accompanied by precise chemical identification of individual lipids.

Therefore, a toolbox of analytes which were likely to be detected in both SRS and MALDI had to be first assembled and explored with both techniques in terms of limit of detection (LOD) using both modalities. At the same time, physicochemical properties of the compounds were cross-examined with the aim to find properties that could be used to predict the probability of detection in either system or a drug localisation in a sample.

SRS detects Raman-active molecular bond vibrations in biological samples. However, detection of chemical bonds specific to an endogenous analyte in mammalian biological samples is not possible due to an abundance of other endogenous molecules with the same molecular bonds. Typically, vibrational properties of molecules in biological systems manifest in the Raman spectrum in the fingerprint region and CH region which are separated by the cell silent region. The cell silent spectral region is devoid of Raman signal in common biological samples and thus can be exploited by an introduction of molecular bonds active in this region. In order to shift the vibrational frequencies into cell silent region, hydrogen atoms in

C-H bonds can be substituted by deuterium atoms creating C-D bonds. Alternatively, target molecules can be chemically modified with alkynes and nitriles.[93]

There are many drug molecules in the internal GSK database, however most were not suitable for this study owing to the absence of cell silent region-active molecular bonds necessary for Raman analyses or due to their physicochemical properties, which were considered inapplicable in MALDI analyses. Therefore, the sample database was refined to small molecules with deuterium atoms, alkyne, and nitrile bonds. Remaining compounds were then filtered manually according to their projected susceptibility to ionise in positively charged MALDI MS based on the distribution of functional groups containing nitrogen and oxygen atoms with focus on variable chemical structure. The molecular weight of tool compounds ranged between 100 Da – 800 Da.

In the test compounds given in Fig. 4.1 hydrogens were substituted with deuterium in various functional groups. The deuterium was introduced to the phenol group of GSK1/D4-paracetamol a common analgesic and antipyretic with an inhibitory effect of cyclooxygenases 1 and 2, which produce prostaglandins (Fig. 4.1a).[245] The H atoms in the aliphatic chain of GSK2/D7-human cytomegalovirus (HCMV) DNA synthesis inhibitor maribavir were replaced by deuterium (Fig.4.1b).[78] HCMV is a herpesvirus which causes lifelong infection in humans and is present in ~60 – 90 % of the worldwide population. The disease is kept in check in healthy individual, however the virus can replicate to high levels in patients with compromised immune systems after stem cell and organ transplant and lead to serious organ diseases.[246,247] Maribavir competitively inhibits adenosine triphosphate binding site of a UL97 Ser/Thr kinase, which prevents viral DNA replication and encapsidation.[248] GSK4/D8-H2 histamine receptor inhibitor (Fig. 4.1c) and GSK10/dopamine D3 receptor antagonist (Fig. 4.1e) were deuterated in the pyrrolic saturated heterocycle and in the sulphide aliphatic chain, respectively. Highly selective H2 receptor inhibitors are used in the treatment of acid-peptic diseases, such as peptic ulcers. The inhibitors act on gastric parietal cells, which are the producers of gastric acids.[249] GSK10 was a drug candidate developed with the outlook of treatment of substance abuse and addiction by targeting the D3 receptor in the central nervous system.[250] Furthermore, alkynes or nitriles conjugated through

delocalised electrons of connected p-orbitals to aromatic ring, dienes and diyene will generate enhanced Raman signal in the cell silent region.[81,84] GSK4 (Fig. 4.1c) and deuterium-free GSK4x (Fig. 4.1d) are H2 histamine receptor inhibitors that contain C≡C bonds conjugated to the aromatic ring. The alkyne bond in GSK90/ponatinib is linking the conjugated system of imidazopyridazine and benzamide (Fig. 4.1f). Ponatinib was developed to inhibit the activity of overexpressed receptor tyrosine kinases by steric inhibition of ATP substrate binding mediated by the ethenyl triple bond in the inhibitor structure, which overcomes the T315I mutation in ~25 % of patients suffering with chronic myeloid leukaemia.[251]

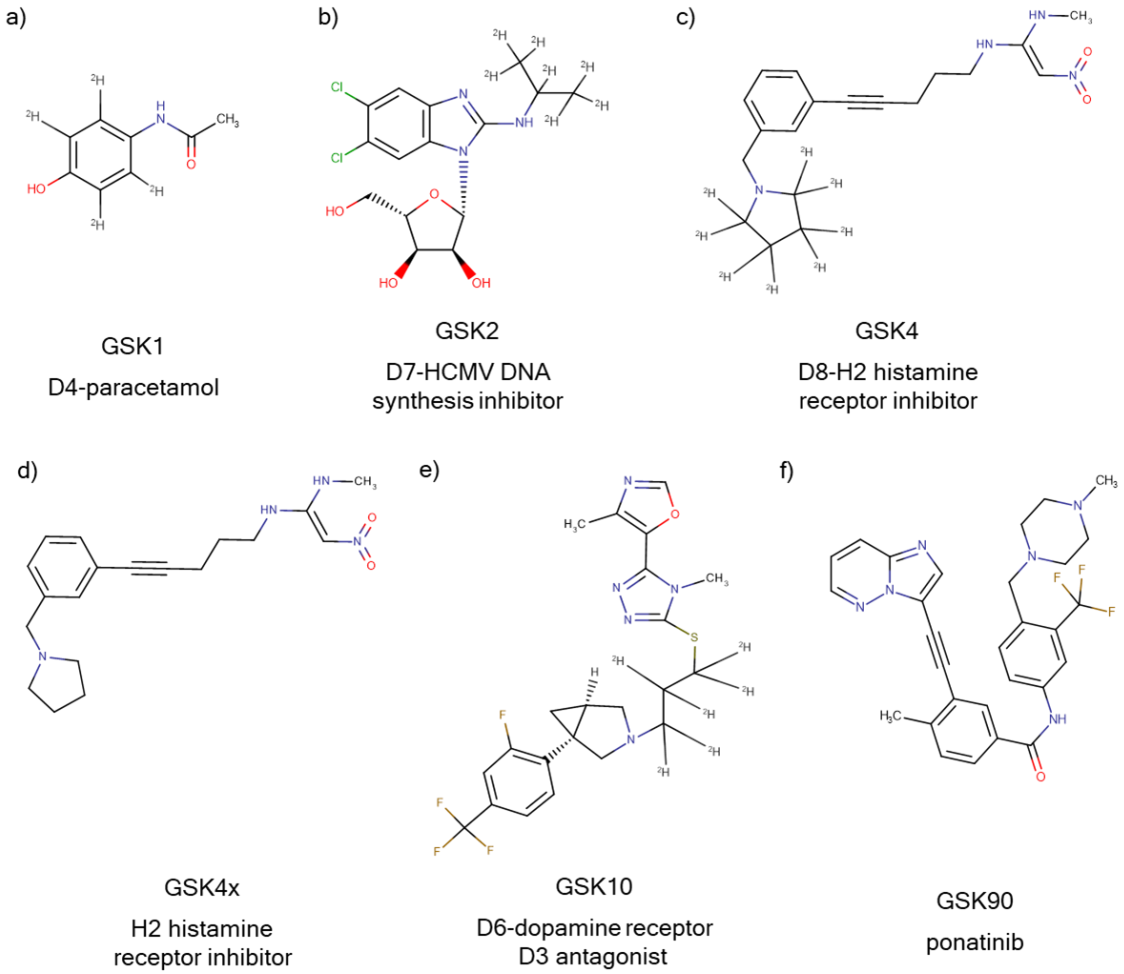

Figure 4.1 Molecular structures of test compounds. a) GSK1 is deuterated in the phenol substructure. b) GSK2 is a weak base with a deuteration in the aliphatic chain and with two Cl atoms which generate a specific ion pattern in a mass spectrum. GSK4 (c) is a D8-H2 histamine receptor inhibitor with alkyne bond and a benzene ring in a conjugated system and 8 deuterium atoms on the pyrrole ring. (d) GSK4x is non- deuterated. (e) GSK10 is a D6-dopamine D3 antagonist with deuterium atoms in the sulphide aliphatic chain and (f) GSK90/ponatinib contains alkyne in a conjugated system with two heterocycles.

As discussed in the introductory chapter, physicochemical properties dictate the interactions and dynamics between drugs and a biological system.[226] The mechanisms behind the effect of physicochemical properties on the ability to detect the drugs by MALDI MS and by SRS in biological matrices ranging from tissues to individual cells was investigated. The drugs in the GSK repository were often already analysed in terms of their physicochemical properties. A DCS table[227] was populated with selected tool compounds based on their permeability and solubility data generated in house. The DCS table separates the drugs into four categorical quadrants – good solvent + good permeability; good solvent + poor permeability; poor solvent + good permeability; poor solvent + poor permeability (Fig. 4.2 a). The featured drugs – GSK1, GSK2, GSK4, GSK10 and GSK90 were distributed across two of the quadrants. The exact experimental measurements were shown in Appendix 1. Samples which exhibited very low solubility and permeability were excluded from this study because they were not successfully dissolved in MALDI-applicable solvents.

Lipid and plasma protein affinity of each compound was obtained from immobilised artificial membrane (IAM) and human serum albumin binding (HSA), respectively.[228] Similarly, to DCS, the tool compounds were plotted based on their lipid and protein affinity measured by IAM assay and HSA binding assay, respectively. Among the featured drugs, GSK2, GSK10 and GSK90 exhibited strong affinity to HSA and furthermore, GSK90 exhibited strong lipophilicity. Whereas GSK1 and GSK2 exhibited low affinity to both lipids and HSA.

The stocks of GSK4 became unavailable during the course of the experiments. GSK4x was used as an alternative instead of removing the GSK4 data all together. This decision was based on the expectation of minimal impact of deuteration on molecule chemistry and interactions with the biological environment.

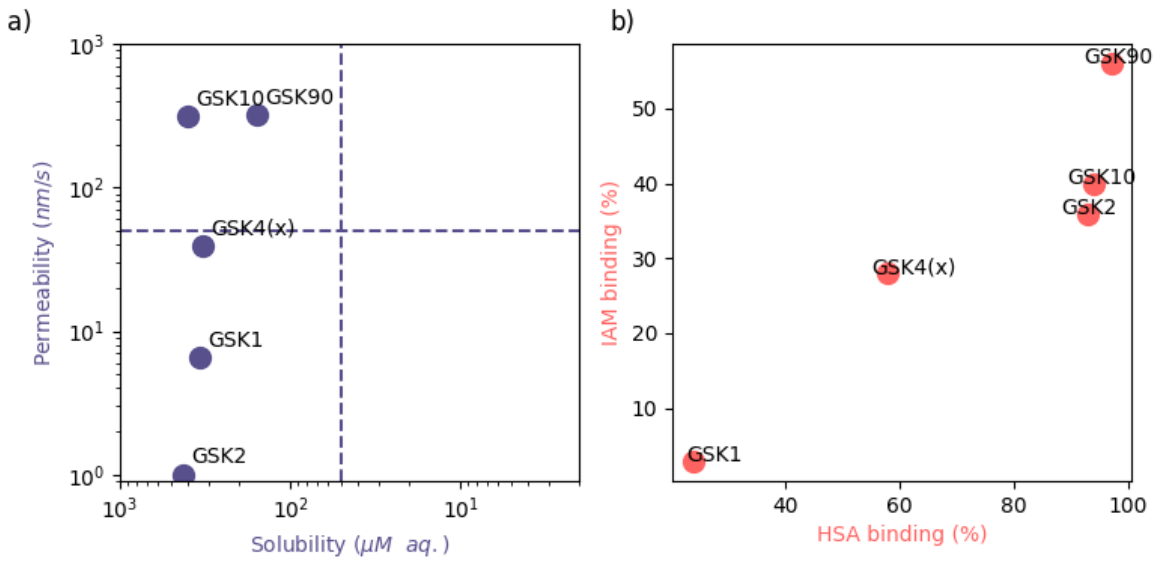

Figure 4.2 DCS and binding of tool compounds. a) DCS table segments small molecules into 4 quadrats (dashed lines) based on an evaluation of their solubility and permeability physicochemical properties. Solubility data show the concentration of analyte dissolved from DMSO into an aqueous phase. Permeability reflects the ability of an analyte to pass through membranes. Historically, the permeability scale has been reversed to show best permeable drugs on a left side of a plot. Dashed area highlights most desirable physicochemical properties in drug development pipeline. b) Test compounds were visualised based on the percentage of analyte immobilised in HSA protein and on an IAM, which represented lipid binding.

The objectives of this chapter was to identify small analyte molecules suitable for cross-analysis between MALDI and SRS in biological matrices and attempt to find physicochemical properties which could be used to predict the applicability of individual small molecules in cells and tissues. These objectives were explored by:

- SRS and MALDI instruments were examined for their capacity to detect analyte molecules.
- For this purpose, a following set of increasingly complex biological matrices was developed: chemical solvent, a tissue (homogenate) section analyte deposition, mimetic models, and a cell culture.

4.2. MALDI MS of pure test compounds

Detection feasibility of test compounds in MALDI MS, was evaluated using a set of increasingly complex biological matrices. Firstly, to assess the detection feasibility/ionisation efficacy, pure compounds mixed with αCHCA matrix in methanol were analysed in positive reflection mode using the UltrafleXtreme II TOF.

Acquired mass spectra contain information on the molecular mass of analyte ions which reached the MS detector (Fig. 4.3). Only the molecular ions $[M+H]^+$ were in scope of this study. Samples with matrix alone were used as a control. Serial dilutions at 100 µg/ml, 10 µg/ml, and 1 µg/ml for each of the selected test compounds were all successfully ionised. Matrix ions did not overlap with any of the ions derived from the tool compounds. A noise baseline (σ) was calculated for each mass spectrum by averaging all intensity values in the mass spectrum and the LOD was set to be 5× above the noise baseline (SNR = 5) in these single spot analyses. At *m/z* 156.1, GSK1 was detected with ~ 3500 counts at the highest concentration. A large drop-off in ion intensity and SNRs <15 (Appendix 2) were observed for the 10 µg/ml and 1 µg/ml concentration samples. A comparable ion count was detected in the GSK2 samples at the expected *m/z* 384.2. However, an *m/z* 383.2 ion was detected with stronger intensity. The $^{35,\ 37}$Cl isotope pattern at *m/z* 383.2 and *m/z* 385.2 suggested the high intensity ions contained the Cl atoms as well. Thus, the 1 Da lower *m/z* value could have been attributed to a deuterium loss or inefficient deuteriation – a D3-GSK2 variant. GSK4 and GSK10 ions were detected at *m/z* 451.3 and *m/z* 488.3, respectively. GSK4 and GSK10 showed additional losses from expected *m/z* of −1, −2, −3, −4 and −5, which was possibly caused by an incomplete deuteration or an absence of deuteration. Moreover, the overall ion intensity of GSK4 and GSK10 surpassed GSK1 and GSK2 by 1 order of magnitude. The intensity difference was attributed to the ratio between amino-groups and oxygenated functional groups. The non-deuterated GSK90 has a high nitrogen-to-oxygen ratio and exhibited higher ion count in comparison with the remaining analytes) apart from the lowest drug concentration, which exhibited very low signal (SNR = 3). Owing to this loss of signal and an observation of additional peaks with losses of *m/z* -1 and -4, an instability of the structure during the ionisation process or alternative synthesis products were considered.

Matrix ions did not overlap with most of the compounds in the tool set and therefore MS experiments were sufficient for pure sample analysis. However, an overlap between an analyte ion and a biological matrix ion was highly probable due to an increased likelihood of isobaric molecular species, which share the same nominal mass, but their composition differs. Molecular fragments deriving from various isobaric species in a biological environment are likely to differ in their

molecular weight and therefore ion fragmentation or MS/MS was applied. In the UltrafleXtreme II instrument, a LIFT unit was employed.

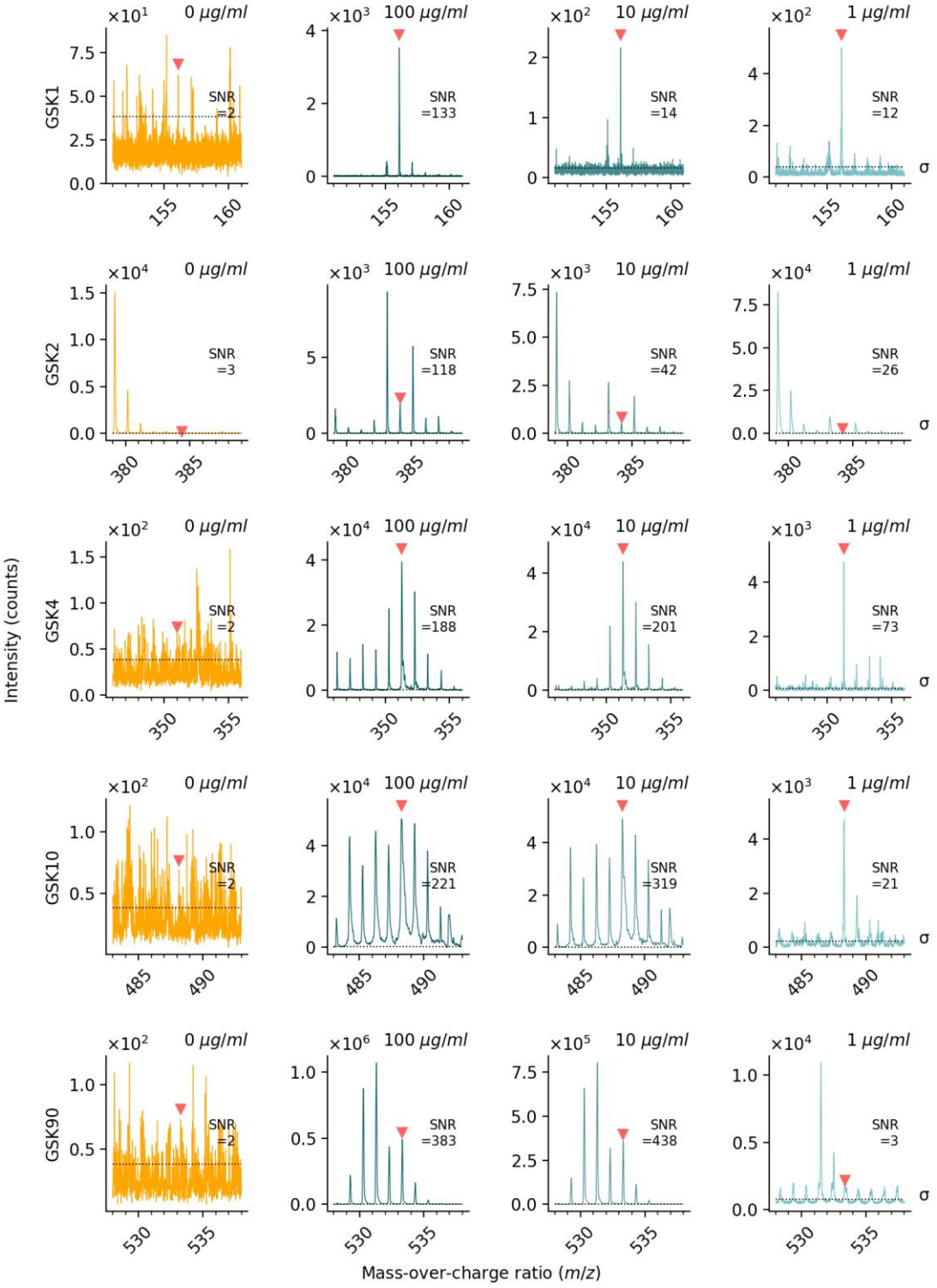

Figure 4.3 MALDI mass spectra of featured tool compounds. Spectral windows focusing on GSK1, GSK2, GSK4, GSK10 and GSK90 in tool compound analytes samples at 100 µg/ml, 10 µg/ml, and 1 µg/ml concentrations and pure matrix samples (0 µg/ml) show no overlap between analyte and matrix ion. Red triangles point to $[M+H]^+$ ions. The noise (σ) for the SNR was calculated based on the average intensity value of all points in a mass spectrum.

In LIFT mode, the ions were first resolved in TOF-1 and subsequently deflected by a timed selector. Only the pre-selected ions (precursor ions) passed through the selector into a LIFT cell with >20 kV potential energy added to the fragment ions. From there, ions were focussed through TOF-2 and eventually into the detector.[194]

As per instrument default settings, the mass window was set to *m/z* ±4 to cover the entire ion isotope pattern. Generated MS/MS (fragment) spectra showed the "fingerprint" pattern of the analyte as well as the manually computed chemical structure of the fragments (Fig. 4.4). GSK1 MS/MS experiment generated only one fragment ion which was successfully annotated with a corresponding structure at *m/z* 113.2. Other possible fragments were not detected. Fragmentation of GSK2 sample resulted in four distinctive peaks. Only one of the peaks was successfully assigned to a molecule fragment. The two *m/z* 180 and *m/z* 200 distinctive ions were attributed to αCHCA matrix. The matrix peaks (*m/z* 173.6, *m/z* 191.8) were detected as a result of the mass window including both the parent GSK2 ion at *m/z* 384.2 and the matrix isotopes at *m/z* 380.1 and *m/z* 381.1 (Fig. 4.3). A single molecular fragment of GSK4 was successfully attributed to an ion peak at *m/z* 243.9. GSK10 generated two large bands of ion peaks at *m/z* 239.1 and *m/z* 293.0, respectively. The surrounding peaks at *m/z* −1- −4 position were plausibly fragment ions of non-deuterated synthesis products. Three distinct fragmentation structures were attributed to the MS/MS fragment ion peaks of GSK90 at *m/z* 101.0, *m/z* 259.0 and *m/z* 433.2. The extracted MS/MS spectra for each tool compound were used as reference for all future MS/MS studies to distinguish between the exogenous drug and the endogenous components.

The majority of the tool compounds that were either not detected or detected with poor SNR (<5) in positive MS in their pure form were acids or were difficult to dissolve.

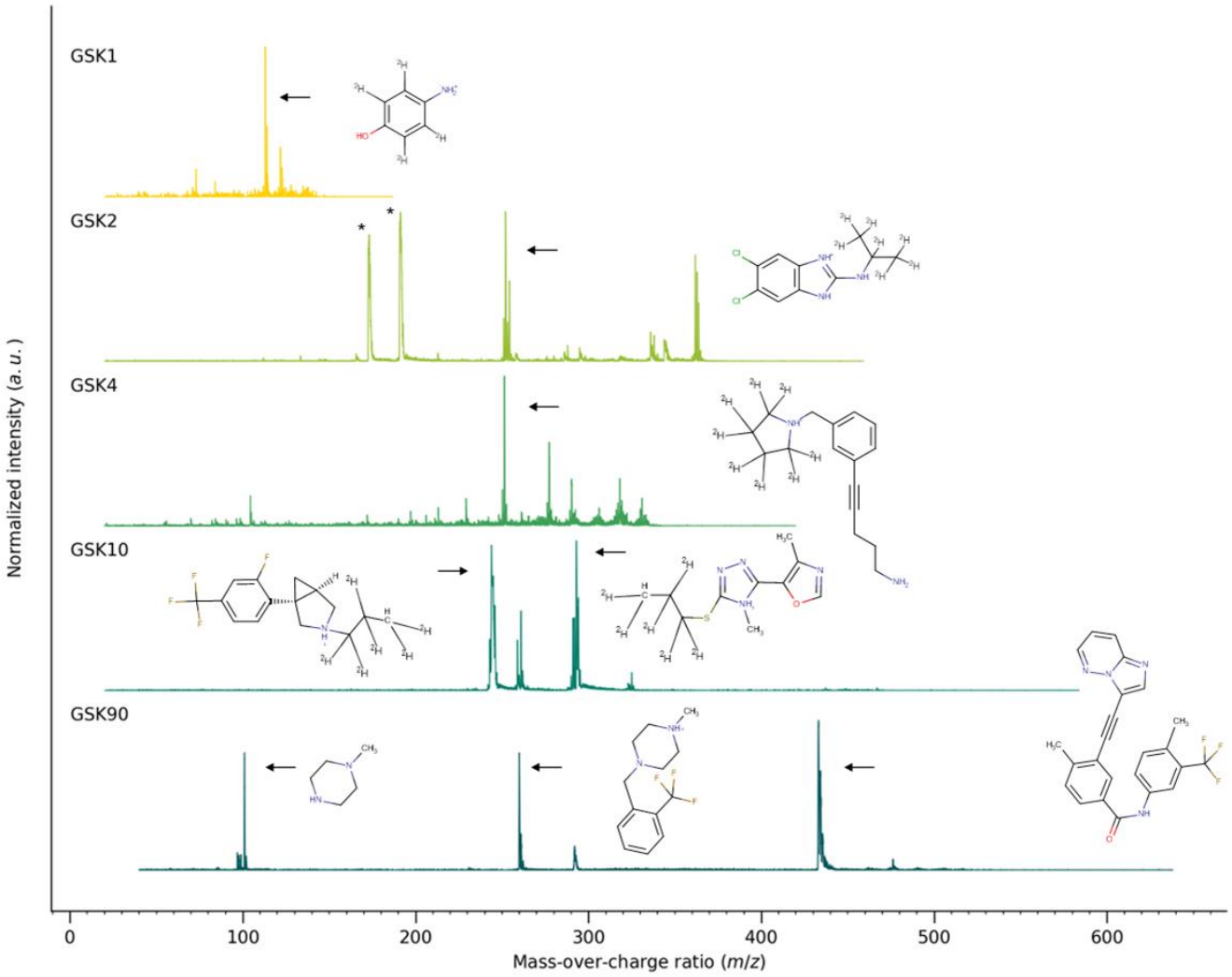

Figure 4.4 MS/MS spectra of featured tool compounds. Fragmentation spectra and their respective chemical structures of GSK1, GSK2, GSK4, GSK10 and GSK90, respectively. Black arrows connect the highest ion peaks with the corresponding chemical structure. Asterisks denote matrix spectra.

4.3. MALDI MS of tool compounds in tissues

In comparison to the analysis of pure drug mixed with matrix, the ionisation efficiency of test compounds was expected to decrease when the drug was spotted onto tissue or spiked into homogenised tissue. Moreover, some molecules are prone to sequester the ionising energy from the UV laser to a greater extent than the analyte during the ion suppression effect, which is particularly prevalent in the presence of lipids.[252] The affinity of tool compounds towards proteins and lipids in tissues and their solubility and permeability can also affect the ionisation efficiency most likely through the matrix co-crystallisation process.[253,254] Furthermore, when sprayed on tissue samples, the matrix is less abundant in volume than with 1:1 (v/v) mixing with the analyte during the pure sample analysis; and therefore, the matrix extraction efficiency of an analyte becomes crucial. To understand how tissue affected the ultimate ion yield of an analyte and whether analytes with different physicochemical properties had different ionisation efficiency, MALDI LIFT analysis was repeated in tissues in an MSI experiment, where the test compounds were deposited in the form of spots or homogenised in the tissues. Brain and liver samples were used to investigate how a lipid-rich brain environment and a liver environment with relatively low concentration of lipids differ in terms of ion yield using multiple tool compounds.

Firstly, a spot analysis on a tissue cryosection surface was conducted to determine whether the tool compounds ionised comparably. Samples were generated by a manual deposition of single 1 µl droplets of H_2O and 1 µl droplets of tool compound diluted in methanol in serial dilutions (1 mg – 1 µg) on 12 µm-thick rat liver and mouse brain cryosections on a MALDI slide. Deposition of H_2O prior to analyte deposition prevented analyte dispersion. An off-tissue control spot of pure drug (100 µg/ml) was used to generate a tissue-free reference spectrum repeating the same procedure. The matrix was applied by a HTX TM-Sprayer to reach a homogeneous matrix distribution.

GSK1 ionised comparably in both tissues at high concentrations, but it was not detected in the lowest concentration of either tissue (Fig. 4.5a). This finding alone would suggest that the low permeability and low lipid binding properties of GSK1 resulted in poor ionisation of a low concentration GSK1 in liver and brain. However,

based on the pure analysis which showed a poor ionisation for GSK1, it was concluded that the GSK1 analyte ionised poorly overall in the mass spectrometer (Fig. 4.3) and the signal in tissues was masked by a tissue-derived noise.

Like GSK1, GSK2 had low permeability properties, but the pure MS analysis showed stronger ionisation at low analyte concentrations (Fig. 4.3), which is likely the reason GSK2 was detected at a 1 µg/ml concentration in either tissue sample, although near the LOD (Fig. 4.5). The LOD in MSI LIFT experiments was set to 2× the intensity of a solvent-only spot. GSK2 surpassed GSK1 in this LOD experiment, likely owing to the enhanced ionisation properties of GSK2. Interestingly, the MS/MS image of GSK2 100 µg/ml spot in brain section displays lower ion intensity in contrast with the corresponding liver section spot. Such difference may be attributed to increased lipid binding of GSK2. The lipid and protein affinity of GSK1 and GSK2 was the only notable difference in the four discussed physicochemical properties assessed for these compounds (Fig. 4.2). Potentially, GSK1 dispersed further into the tissue section and thus diluted the analyte concentration immediately available for the matrix extraction.

Both GSK4 and GSK10 were detected across all investigated concentrations in rat liver tissue sections. GSK4 was detected at similar intensities in liver and brain (Fig. 4.5c). In contrast with GSK2, measured permeability and protein binding properties of GSK 4 were lower, suggesting a potential correlation between these chemical properties and their ionisation efficacy across tissues. The signal intensity of GSK10 fragment ions surpassed GSK4 by one order of magnitude (Fig. 4.5d). Counter intuitively, while both compounds exhibited similar affinity to lipids, GSK10 ionised poorly in brain when compared to GSK4. However, the increased permeability of GSK10 over GSK4 was potentially the reason for the poor detection of GSK10 in brain tissues. Additionally, the SNR of GSK10 suggested that the GSK10 fragment ion (*m/z* 243.9) was enhanced in tissues, which was contradictory to the ion intensity map in brain tissues. Moreover, the control spot showed GSK10 SNR was ~10× stronger than SNR of other analytes. This was possibly caused by a signal contribution from tissue-intrinsic ions. These findings suggests that ion yield in small molecules cannot be predicted solely on lipid binding properties, but rather by a combination of factors. Moreover, due to the mass spectrum interference in tissues, GSK10 was not further examined.

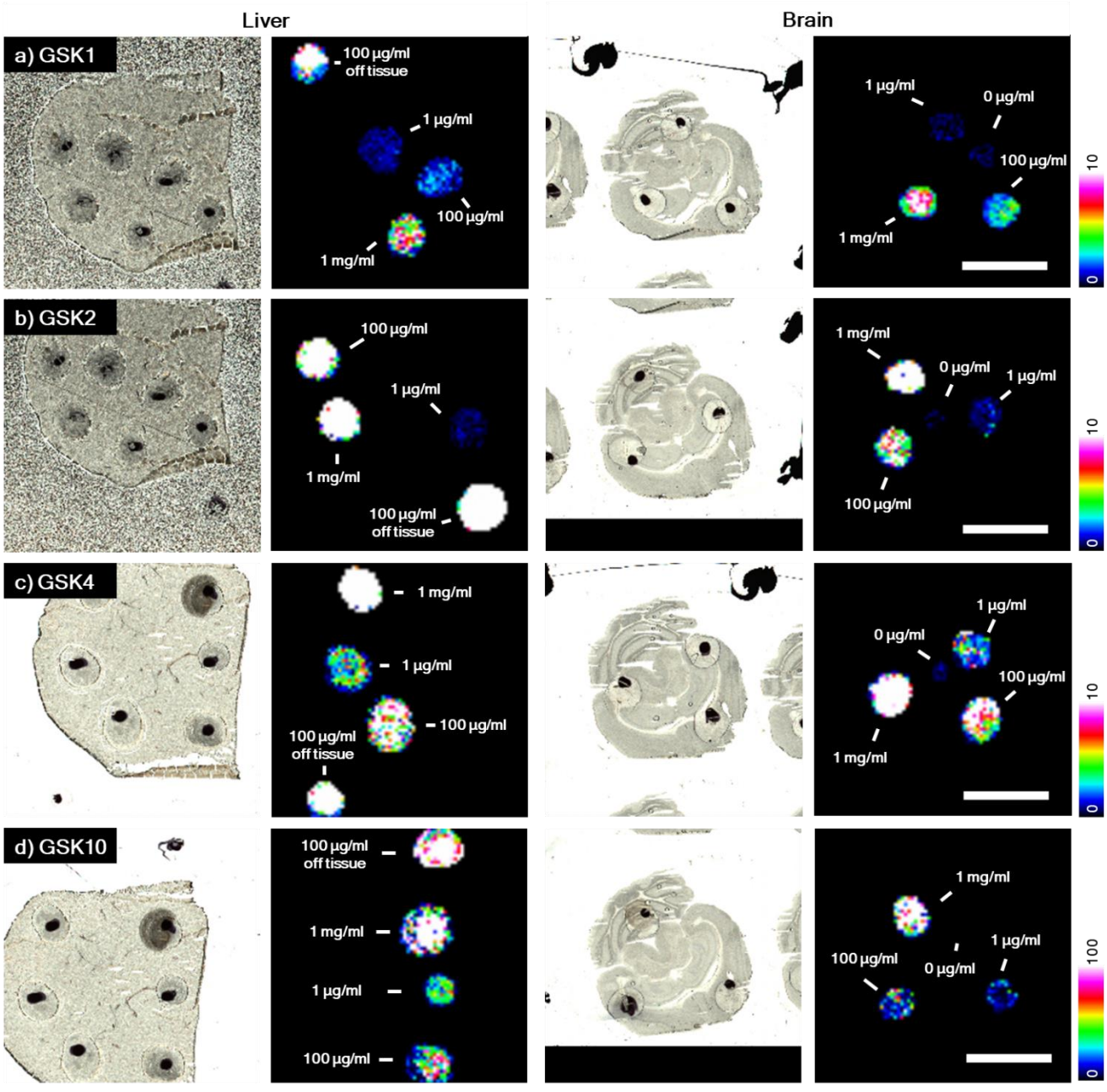

e)

	Liver				Brain				Slide
	1000 µg/ml	100 µg/ml	1 µg/ml	0 µg/ml	1000 µg/ml	100 µg/ml	1 µg/ml	0 µg/ml	100 µg/ml
GSK1	15.7	4.5	0.5	nan	32.8	9.6	0.0	0.1	88.5
GSK2	573.5	203.0	0.1	nan	439.0	118.8	3.4	0.2	122.8
GSK4	218.7	101.8	28.4	nan	131.3	121.0	35.7	0.3	31.9
GSK10	1006.0	1893.2	2306.0	nan	567.4	578.0	230.0	4.7	75.5

Figure 4.5 MALDI MS/MS of tool compounds spotted on tissues. Widefield images depict tissue sections after analyte spotting. MS/MS images visualise the spatial distribution and signal intensity of analyte fragments on and off tissue at multiple drug concentrations. Left two columns and right two columns represent rat liver and mouse brain data, respectively. Rows a, b, c, d correspond to GSK1 (*m/z* 113.21 ± 0.2), GSK2 (*m/z* 251.0 ± 0.2), GSK4 (*m/z* 251.3 ± 0.2) and GSK10 (*m/z* 243.9 ± 0.2) fragments, respectively. Scale bar = 5 mm. e) Average SNR per each drug spot was tabularised.

Understanding the interaction of small molecules with tissues based on the physicochemical properties is beneficial to MALDI MSI since an ion yield of an analyte is susceptible to fluctuations. These fluctuations in ion yield–arise from the heterogeneous distribution of lipids and other endogenous species across the tissue, potentially resulting in the ion suppression effect[255] and spatial availability of analytes, which possibly impacted the previous MALDI results. Indeed, based on the analyte spot position on the tissue, the data in the mouse brain (Fig. 4.5b,c) showed no discrepancies between the white and grey matter in terms of an analyte intensity. Intensity discrepancies in MALDI MSI were already reported to be caused by the ion suppression effect.[180]

The heterogeneous information extracted from analytes spotted on a tissue surface yields an insight into the relationship between tissue structures and ionisation efficiency. However, the use heterogeneous tissue may lead to false observations or absence of analytes in tissues and their imprecise quantification. Therefore, the tissues were homogenised using a bead homogeniser in order to reduce the effect of tissue variability. Moreover, section thickness was included as another variable in the analysis, with the aim of exploring the ability of the analyte distribution through the tissue during a thaw-mounting process and the subsequent extraction during a matrix application with the outlook of potentially using this metric to correlate the effect of permeability of analytes in tissues (i.e., it's maximum reached tissue depth) and their solubility in a matrix solvent.

Spot analysis of an analyte on tissue homogenate was conducted with GSK90, which was spotted on 12 µm and 20 µm thick rat liver homogenate cryosections at concentrations of 1 µg/ml, 10 µg/ml, and 100 µg/ml. 100 µg/ml spots were also applied on a MALDI slide and dried prior to tissue homogenate thaw-mounting on top of the dried droplet. GSK90 fragment ion (*m/z* 97.1 ± 0.2) was detected across all spots in the 12 µm sample including the blank control spot on the tissue where only solvent was deposited(Fig 4.6b). Owing to the circular shape of the analyte signal, contamination in a solvent was likely the cause of the blank spot detection. Additionally, the ion signal distribution across the spot was generally more homogenous in contrast with the tissue section data (Fig. 4.5). Average spectra of the individual spots suggest the signal in the blank spot was arising from background

noise or a similar fragment ion generated from an endogenous tissue component. Thus, the presence of an analyte in the lowest concentration spot was not confirmed. As would be expected, GSK90 ion yield in a 20 µm section decreased (Fig. 4.6d). The loss of signal is likely associated with the inverse proportionality between the increasing matrix-extractable molecules and the surface-spotted analyte. Additionally, 100 µg/ml GSK90 spots underneath the homogenate sections were successfully detected in both tissue samples at approximately the same intensity level as 10 µg/ml surface spots, which suggested a strong matrix extraction took place. Although the tissue thickness resulted in decrease of ion yield and lower SNR in bottom spots (Fig. 4.6e), it was not clear whether it could be associated with any physicochemical properties. Moreover, the high efficiency of matrix extraction through the tissue thickness convoluted the analyte penetration through the tissue.

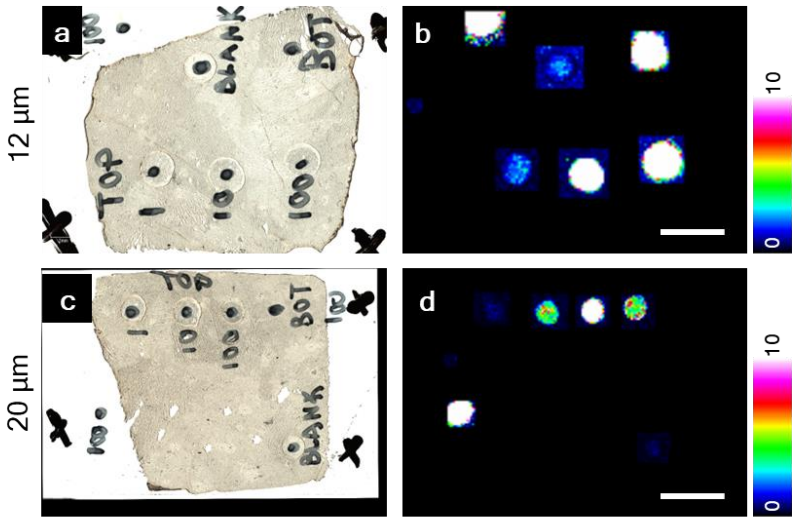

e)

	100 µg/ml	10 µg/ml	1 µg/ml	0 µg/ml	100 µg/ml below tissue	100 µg/ml of tissue	0 µg/ml off tissue
12 µm	981.8	234.1	18.5	5.7	809.1	775.1	3.7
20 µm	869.1	63.7	8.7	4.9	163.1	963.7	2.9

Figure 4.6 Tissue homogenate in MS/MS analysis of GSK90. Widefield images depict tissue sections after analyte spotting. MS/MS images visualise the spatial distribution and signal intensity of analyte fragments on and off tissue at multiple drug concentrations. Figure shows the difference between data from a 12 µm (a, b) and a 20 µm (c, d) cryosection. Markings TOP describe spots applied on tissues; BOT describe spots below tissues (a, c). GSK90 fragment mask = *m/z* 97.1 ± 0.2. Scale bar = 5 mm. e) SNR values were tabularised.

It is possible that physicochemical properties of various molecules would result in various ion yields depending on the thickness of the tissues where analytes are spotted on top or below the cryosection. To the current knowledge, the amount of analyte ionised during a MALDI analysis is dependent on two processes taking place

during the sample preparation – the penetration of the drug in wet tissues during thaw-mounting; and the combination of extraction in the matrix solvent and subsequent co-crystallisation of an analyte and matrix on a sample surface.

Correlating selected physicochemical properties to multiple processes which were potentially not connected was considered cumbersome. Therefore, the variability of drug permeability in wet tissues was separated from the matrix application-induced extraction by homogenous mixing of the drug in solution with the tissue homogenate.

By adopting an already established mimetic model protocol for MALDI MSI, drug-doped tissue homogenates with multiple drug concentrations were examined with MALDI.[233] To create mimetic models, homogenates of both murine liver and brain were doped with GSK4 and GSK90 to final concentrations 500, 400, 300, 200, 100 and 0 µg/g (analyte/tissue) and stacked into a column. Samples were sectioned at 12, 16 and 20 µm thickness (Fig. 4.7a). GSK4 MALDI MS/MS analysis confirmed a gradually decreasing ion intensity in both liver and brain homogenate sections Furthermore, the ion suppression effect in brain tissue was apparent as solvent-delocalised analyte was detected outside the brain tissue (Fig. 4.7b). The 300 µg/g concentrated liver homogenate segment ionised unexpectedly poorly presumably due to an error in a centrifugation step in sample preparation. In Fig. 4.7a, the discolouration suggests the tissue has increased density which may affect the matrix extraction efficiency.

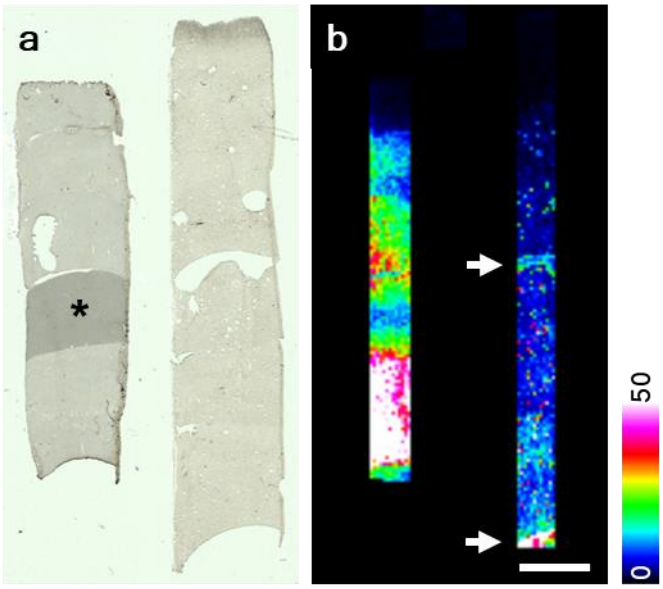

Figure 4.7 Mimetic model MS/MS experiment overview. A) Widefield scan image shows 16 µm liver (left) and brain (right) cryosections of GSK4 samples prior to matrix application. An above-average dense homogenate was found in the liver homogenate and marked with "*" b) Ion intensity map of GSK4 fragment (*m/z* 250.8) of ROI scan through the sample columns. Strong GSK4 fragment signal was observed in brain sample on tissue edges (white arrows). Scale bar = 5 mm.

Analyte fragment intensities were averaged and plotted per individual ROIs of mimetic models and calibration curves were fitted (Fig. 4.8). The analyte ion yield reached the highest intensities in 12 µm liver sections in GSK4 and GSK90 samples. The ion intensities of GSK4 grew at a seemingly inversely proportional exponential rate with the decreasing tissue thickness. Furthermore, the error in the sample preparation of the 300 µg/g GSK4 liver homogenate, which appeared as a dark segment in the mimetic model (Fig. 4.7a), was confirmed since the datapoint deviated from the calibration curve. The drop in intensity was associated with an increased tissue density, based on the segment colour and signal intensity.

In a brain homogenate, GSK4 intensities reached approximately half of the intensities measured in a liver sample per each section thickness. The decrease was most likely caused by either the ion suppression effect or the lipid affinity of GSK4. Despite the decreased signal intensity in brain, the drug was detected in the 100 µg/ml samples in both tissues. The ion intensities of each compound increased was directly proportional to the increase in concentration.

500 µg/g GSK90 liver samples reached linearly spaced intensities of ~8, ~10 and ~13. The ion intensity of the GSK90 in a 12 µm sample was therefore 4.17× lower than the intensity of GSK4 in the equally thick section, whereas the 16 µm and

20 µm samples exhibited similar ion intensities, which were also at similar intensity range of the GSK4 liver mimetic model.

The ion intensities of a 500 µg/g GSK90-spiked brain homogenates reached ion intensities of 1.5 – 10.5 and thus, were considered to match the intensities of GSK4 brain mimetic models. Indeed, the independent variables of the fitted trendlines were 0.002, 0.006 and 0.0019 in GSK4 and 0.003, 0.005 and 0.018 in GSK90 brain mimetic models.

Both GSK4 and GSK90 were detected above the noise level in majority of the liver mimetic model segments. On the other hand, the SNR of majority brain mimetic model segments with drug concentrations below 400 µg/g was equal to the noise level (SNR = 1). Interestingly, GSK90 was detected well above the noise level in 16 µm 500 µg/g – 200 µg/g brain segments but showed the same SNR in the remaining sections as GSK4 brain samples.

The results likely indicate that the matrix solution wetted the thinnest sample completely allowing longer time for analyte extraction and co-crystallisation, whereas the 16 µm and 20 µm sections were not saturated with matrix. This possibility was however likely to be in contradiction with the spot analysis of an analyte below a tissue homogenate, which was successfully extracted (Fig. 4.7b).Alternatively, permeability could still an important aspect of the MALDI process despite the homogeneous distribution of an analyte in tissues. The SNR comparison also showed that the most ideal thickness of a sample for MALDI MSI may be dependant on analyte properties and tissue type.

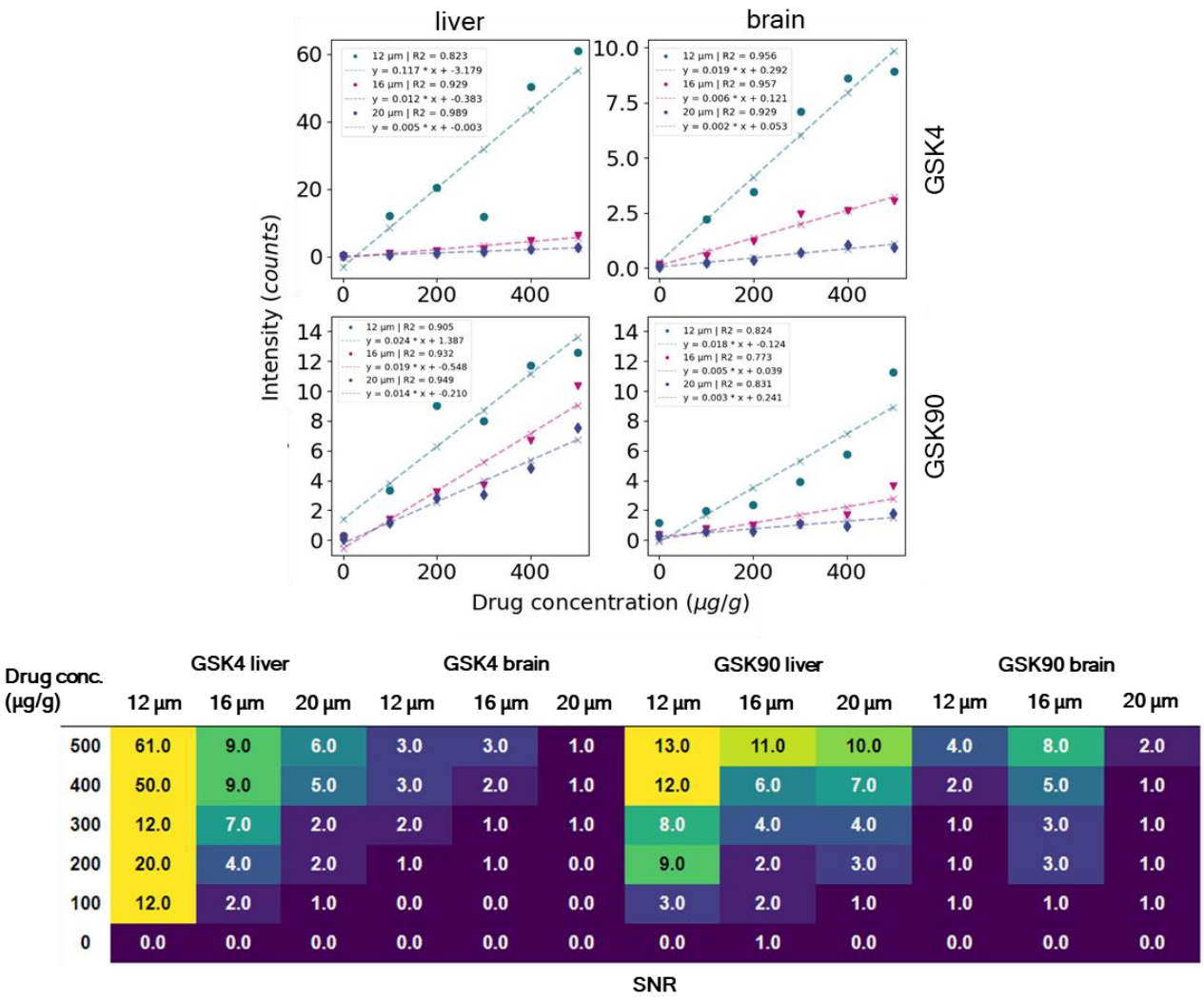

Drug conc. (µg/g)	GSK4 liver			GSK4 brain			GSK90 liver			GSK90 brain		
	12 µm	16 µm	20 µm	12 µm	16 µm	20 µm	12 µm	16 µm	20 µm	12 µm	16 µm	20 µm
500	61.0	9.0	6.0	3.0	3.0	1.0	13.0	11.0	10.0	4.0	8.0	2.0
400	50.0	9.0	5.0	3.0	2.0	1.0	12.0	6.0	7.0	2.0	5.0	1.0
300	12.0	7.0	2.0	2.0	1.0	1.0	8.0	4.0	4.0	1.0	3.0	1.0
200	20.0	4.0	2.0	1.0	1.0	0.0	9.0	2.0	3.0	1.0	3.0	1.0
100	12.0	2.0	1.0	0.0	0.0	0.0	3.0	2.0	1.0	1.0	1.0	1.0
0	0.0	0.0	0.0	0.0	0.0	0.0	0.0	1.0	0.0	0.0	0.0	0.0

SNR

Figure 4.8 Calibration curves of tool compound mimetic models analysed by MALDI MS/MS. Average ion intensities of selected GSK4 and GSK90 fragments in liver and brain mimetic models were plotted and fitted with a calibration curve. Samples were sectioned at 12 (green), 16 (purple) and 20 µm (blue). Dashed line represents the linear calibration curves. SNR of mimetic models was also tabulated.

4.4. MALDI MS of tool compounds in cell culture

The results of studying the detection limit of the selected tool compounds in tissues using MALDI MSI put forward GSK4 and GSK90 as the strongest ionising agents within the set. However, these studies only mimicked the dynamics of the tool compounds in tissues by artificial mixing of tissue homogenates with the drug. Therefore, cell cultures were used to assess the MALDI process in *in vitro* models. The scope of this MALDI study was to examine whether a) the drug is attached to or enters the cell; b) whether MALDI MS is an instrumentation which can detect the drug in cell cultures.

SH-SY5Y isolated from a neuroblastoma and Caco-2 colon carcinoma cell lines were selected for MSI and SRS cell assays owing for their reported expression of relevant Histamine H2 receptor to which GSK4 was designed to act as an inhibitor.[256,257] Colon-derived epithelial cell line SW-480 and lung adenocarcinoma-isolated Calu-3 were mistakenly used for their histamine H_2 receptor expression, which upon review was revealed to be a H_1 receptor.[257] No samples were infected with the HCMV and thus no target was expected. Hence, the GSK2 was expected to localise in the cytoplasm.

Firstly, cells were assessed for their ability to bind and internalise GSK4 and GSK90 in MS spot analysis. At the same time, detection feasibility of drugs in tissues using the mass spectrometer was conducted as well using cells at high concentration prior to employing MSI. Calu-3, SH-SY5Y and SW-480 cell lines were used in this study. Firstly, GSK4 was mixed with H_2O, PBS and DMEM (Fig. 4.9a-c). Compared to a H_2O sample, PBS increased the ion yield, possibly through promotion of crystallisation, whilst DMEM decreased the GSK4 signal intensity, due to the ion suppression effect from one or more of the components in the DMEM buffer. Cells were incubated with GSK4 (100 µM) for 2 hours. Afterwards, cells were collected, washed twice in PBS and twice in ammonium acetate in suspension and frozen as pellets. During the workflow, the GSK4-DMEM supernatant, 2nd PBS wash, 1st ammonium acetate wash were sampled and analysed by MALDI MS (Fig. 4.9d-f). The data displays the gradual loss of the GSK4 ion peak (*m/z* 351). Importantly, the data shows that at least 3 washes were necessary to wash out the analyte. The

presence of cells in the pellet after 4 washing steps was confirmed in MS by focusing on a phosphatidyl choline ion of the phospholipid head group $[PCh+H]^+$ (*m/z* 184, Fig. 4.9g-j), a common cell marker in MALDI MS. Finally, the presence of GSK4 was confirmed in Calu-3 and SH-SY5Y pellets (Fig. 4.9g, i) as opposed to undosed Calu-3 and SH-SY5Y (Fig. 4.9h, j). Therefore, the presence of GSK4 in cells by co-incubation of the analyte with cells was confirmed by MALDI MS. However, the concentration of ionisable material in a spotted sample exceeded the amount of ionisable material available in a single raster spot in an MSI experiment of a cell monolayer.

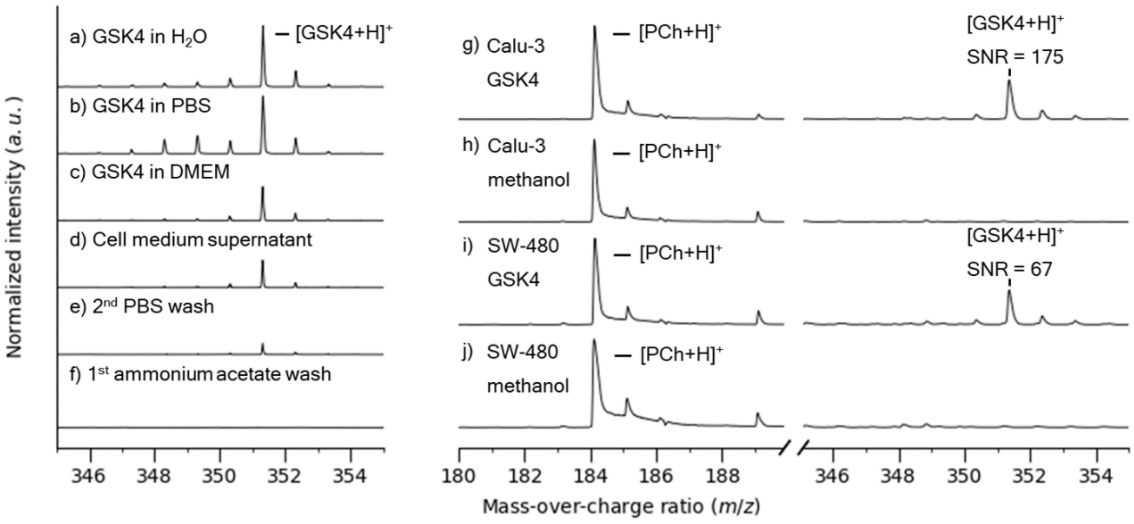

Figure 4.9 MS analysis of GSK4 in cell culture. GSK4 was mixed with H_2O, PBS and DMEM (a-c). DMEM-GSK4 mixture was sampled after a 2h incubation with cells (d). 2nd PBS wash and 1st ammonium acetate wash supernatant of cells in suspension were analysed with MALDI MS (e, f). After 4 washing steps the presence of cells (*m/z* 184) was confirmed in all samples (g-j). An analyte (*m/z* 351) was confirmed in Calu-3 (g) and in SW-480 (i). GSK4 ion was not detected in negative control pellets of Calu-3 (h) and SW-480 (j).

Adjustments to the experimental setup of an MSI experiment below were necessary to enable imaging of cell culture instead of tissue sections. The MALDI glass slides used routinely for tissue analysis were lacking surface treatment for cell culture. Therefore, slides were treated with poly-D-lysine to enhance cell adhesion. Cells were incubated on slides for 4 days and fixed in chilled methanol and dried at an ambient temperature and pressure. Moreover, the amount of matrix which was sprayed on cell samples was reduced due to the sparse amount of sample compared to tissues and to minimise delocalisation. Due to low abundance of substrate, 25 µm sampling area was the minimum spot size used despite the

standard spatial resolution given by the instrument is lower, A small area of the cell monolayer was scratched with a pipette tip before a matrix application (Fig. 4.10a) and thus creating a morphological landmark in the biological samples whilst not affecting the matrix distribution. As in the previous series of experiments, the $[PCh+H]^+$ ion (*m/z* 184.1) was used again as a cell marker (Fig. 4.10b), however it was not detected in this experiment. This is likely due to the methanol-fixing sample preparation step during which most of the lipids present in cells were washed off. The distribution of αCHCA $[M+Na]^+$ ion (*m/z* 212.1) matrix molecules was homogeneous with a spot missing in the top right corner, likely due to a presence of an unknown impurity (Fig. 4.10c). The *m/z* 306.1 ion was in line with the spatial distribution of cells captured in the brightfield image (Fig. 4.10d). However, this ion was not successfully characterised. This result could mean that the lipids were indeed washed off during the exposure to methanol during cell fixing and matrix application.

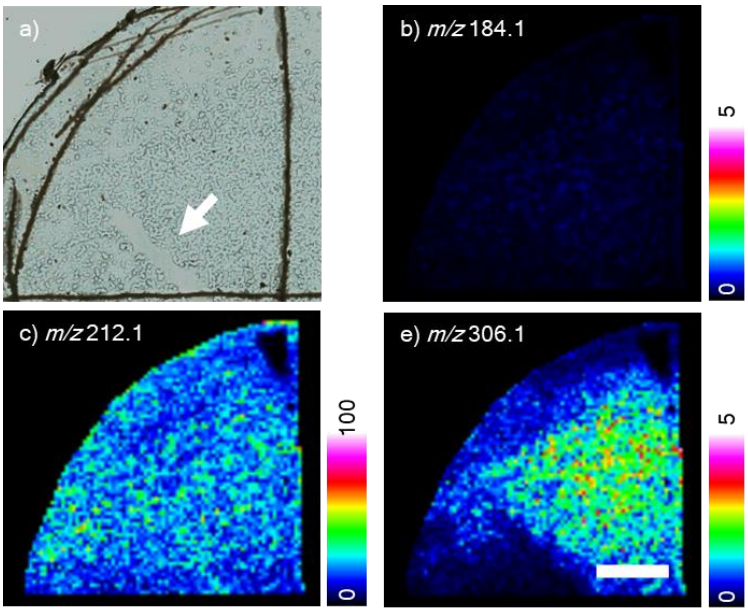

Figure 4.10 MALDI MSI of methanol-fixed SW480 cells. Untreated cells were incubated on a MALDI slide. a) Brightfield image of analysed cells before matrix application. An arrow indicates a scratch mark. Ion maps show the distribution of b) *m/z* 184.1 phosphatidyl choline $[M+H]^+$, c) *m/z* 212.1 αCHCA $[M+Na]^+$, and d) *m/z* 306.1 uncharacterised ion. Scale bar = 1 mm.

The presence of GSK4x and GSK90 was examined despite the possible lipid loss observed in the untreated SW480 cell culture. GSK4 was replaced by its non-deuterated form because of a sudden material unavailability. SW480 and Calu-3 cells were incubated with GSK4x (200 µM) and GSK90 (25 µM) for 2 h. SW480 cells

disassociated from the Intellislide surface during this step and only Calu-3 were further processed and imaged. Samples were fixed in chilled methanol and dried at an ambient temperature and pressure. Finally, cell samples were dried and spray-coated with αCHCA matrix. The MALDI MS/MS imaging was set to detect fragments of GSK4x and GSK90 parent ions. Multiple ions were observed across the sample, which laterally overlapped with cells in the registered brightfield image. However, these fragments were not matching the fragment patterns of GSK4x (Fig. 4.11a) and GSK90 (Fig. 4.11b), which were measured in a pure form and hence the presence of GSK4x and GSK90 were not confirmed in the MALDI MS/MS imaging experiment.

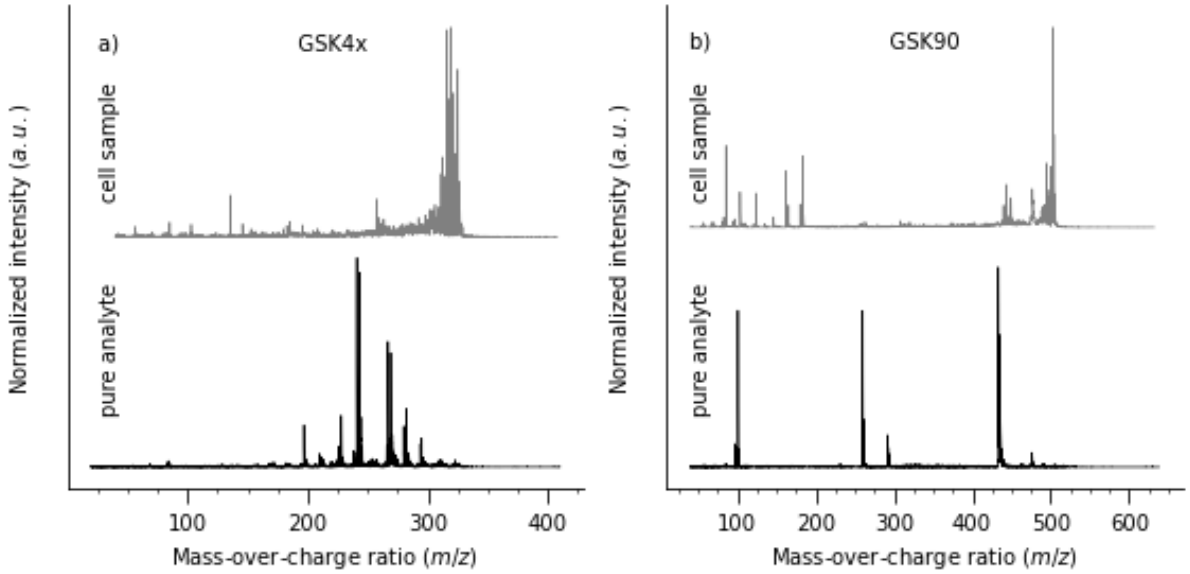

Figure 4.11 MS/MS spectra of tool compounds in Calu-3 cells. Fragmentation mass spectra were extracted from MS/MS imaging analysis (grey) of a) GSK4x and b) GSK90 and were compared with the pure analyte fragmentation spectra (black).

Methanol fixing was likely the reason of lipid and analyte delocalisation, which resulted in the signal absence in the MSI data. Therefore, alternative cell fixing approaches should be explored, such as formalin fixing. However, formalin fixing is used to preserve a cellular structure by cross-linking amino acids in proteins[258] and amine-containing lipid[259] classes via methylene bridges, which causes formation of new artificial analytes that may contribute to a mass spectrum.

4.5. Raman analysis of pure tool compounds

Raman tags introduced through hydrogen-deuterium substitution or addition of moieties with C≡C or C≡N bonds usually generate a signal at a vibrational frequency in the cell silent region of Raman spectrum which is generally otherwise absent of any signal in Raman spectroscopy. These tags allow tracking a larger number of analytes in a chemically complex sample in comparison with fluorescent tags owing to their narrow spectral bandwidth.[91] Hence, analytes with Raman tags were specifically selected in the test compound set to increase the odds of identifying the most suitable candidates for further Raman-to-MS experiment. Tool compounds were tested in the same set of biological matrices as in the MALDI studies which were already described in this chapter.

Confocal spontaneous Raman scattering can be used to collect a full spectrum of a sample 500–3500 cm^{-1} range in a few minutes. This can then be used to confirm deuterated peaks or alkyne peaks are present and their wavenumber positions. Pure tool compounds were first analysed as a pure solid on a glass slide. Vibrational peaks of interest in the cell silent region were found using the custom-built confocal spontaneous Raman systems at University of Konstanz(Fig. 4.12a) and the commercially available system (Fig. 4.12b, c). The spontaneous Raman microscopy suffered from different levels of fluorescence background. Therefore, baseline correction of Raman spectra were required. For GSK4, the strongest cell silent region vibrational mode was detected at 2235 cm^{-1}, which corresponded to the alkyne (C≡C) vibrational mode.[88] At least two more bands were detected between 2030 cm^{-1}-2160 cm^{-1}, corresponding to the range of C-D vibrational modes (Fig. 4.12a).[93] The analysis of GSK4x resulted in a single alkyne peak at 2233 cm^{-1} (Fig. 4.12b). GSK90 displayed sharp peak at 2227 cm^{-1} with a strong intensity. Both GSK4x and GSK90 spectra were absent of any signal in the CH region. This was likely due to an analysis or instrumentation setup of the LabRAM system at the Stevenage site. GSK4 was measured with a custom-built system in Zumbusch lab at Konstanz University, where the spectrum was acquired in 3-4 regions and required manual stitching and smoothing of the spectra. The commercially available LabRAM confocal microscope (JY Horiba, Japan) was an automated system which did not require a spectrum stitching or smoothing. Most likely, the use of two different

systems with possibly different settings, caused the 2 cm^{-1} shift difference between C≡C peaks of GSK4 and GSK4x, rather than the deuterium substitution.

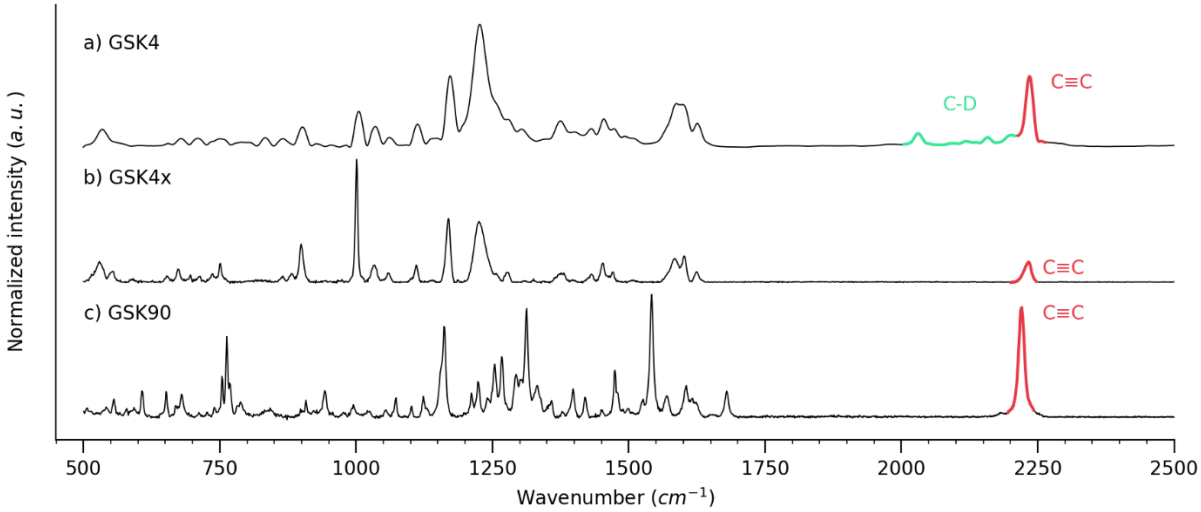

Figure 4.12 Full Raman spectra of pure tool compounds. Tool compounds in powder form were analysed with a spontaneous Raman scattering microscope. The spectra were in 500 cm^{-1} – 3500 cm^{-1} range. All samples display variability in the fingerprint region and prominent C≡C-associated peaks at ~2230 cm^{-1}. a) GSK4 exhibits further C-D peaks between 2100 cm^{-1} – 2300 cm^{-1}. GSK4x (b) and GSK90 (c) show C≡C peak only in the cell silent region.

Spontaneous Raman scattering confocal microscopy is an efficient Raman technique for spectral information acquisition of a sample owing to the instrumentation capability to generate single point Raman spectrum in seconds. However, the long acquisition time of high definition images in biological samples using spontaneous Raman confocal microscopy[260] is not applicable in live imaging. Therefore, experiments in biological matrices were conducted using SRS, which coherently drives molecular vibrations in cells, which leads to fast acquisition. Moreover, unlike spontaneous Raman scattering techniques, SRS data is not associated with background fluorescence.[260] The presence of cell silent region bands of the test compounds in powder form and their detection limit was assessed with the Leica SP8 SRS microscope using a dilution series of analytes in DMSO focusing only on the cell silent region. Analyte in solvents were used in order to reduce the scattering in the close working distance transillumination optical configuration. The different tags and their position in the structures of the test compounds were expected to resonate at different intensities.[261] The intensities of alkynes and nitriles in π-conjugated systems were found to surpass the intensities

outside of these systems and C-D bonds were typically detected at poorer intensities in comparison with C≡C and C≡N.[99] GSK2, GSK4 and GSK90 were dissolved in DMSO at 0 mM – 100 mM.

GSK4 and GSK90 were detected down to 5 µM and confirmed the linear relationship between SRS signal intensity and sample concentration (Fig. 4.13a). Moreover, The GSK90 C≡C peak (2227 cm^{-1}) was narrower and with higher SNR in comparison with GSK4 (2236 cm^{-1}). Additionally, the signal intensity of GSK90 surpassed GSK4 intensity. Spectra were normalised to the maximum intensity of the highest analyte concentration.The C-D vibrational bands of GSK4 at ~2050 cm^{-1} and 2170 cm^{-1} had low intensities compared to the alkyne peak at 100 mM and 50 mM concentration and were below the limit of detection in a 10mM sample.

Deuterium containing GSK2 was analysed in the cell silent region to observe the deuterium-label in in the absence of any alkyne. Four peaks at 2073.8 cm^{-1}, 2141.1 cm^{-1}, 2230 cm^{-1} and 2332.8 cm^{-1} were observed (Fig. 4.13b) in contrast with GSK4, where maximum of three peaks were detected using SRS. The 2230 cm^{-1} peak was not detected due to the spectral resolution of the SRS system. In the spontaneous Raman spectrum of GSK4, this C-D peak was still distinguishable from the C≡C peak (Fig. 4.12a).

The first three peaks were not discriminated from noise below the 50 mM sample concentration in conjuncture with the GSK4 data (Fig. 4.13a). Interestingly, the intensity of the peak at 2332.8 cm^{-1} in GSK2 remained unchanged across all samples suggesting a potential contamination of DMSO since the peak intensity was independent of analyte concentration. Furthermore, this background peak was observed in all measurements including GSK4 and GSK90. The origin of the 2332.8 cm^{-1} peak was investigated in a fresh sample of DMSO, PBS, cover glass and air. The peak was detected across all samples, with the highest intensity accompanied with background noise in DMSO and comparable SNR in PBS, glass, and air (Fig. 4.13c). The background peak was observed using the Leica SP8 SRS systems at two different institutes and thus was not considered as a microscope-related artefact. Therefore, the spectral band were likely originating from an N_2 molecule, which is present in air and can become trapped in glass[262].

GSK2 compound was eliminated from the tool compound set due to the measured low detection feasibility of C-D bonds in SRS at concentrations below 50 µM (SNR > 3) (Appendix 3). Moreover, the data provided information on the cell

silent region peak position of analytes and the intrinsic noise and a N_2 vibrational component which could otherwise be considered as a false-positive result. This peak was also found in GSK4 and GSK4x cell silent region SRS spectra, likely owing to the low scattering intensity in contrast with GSK90.

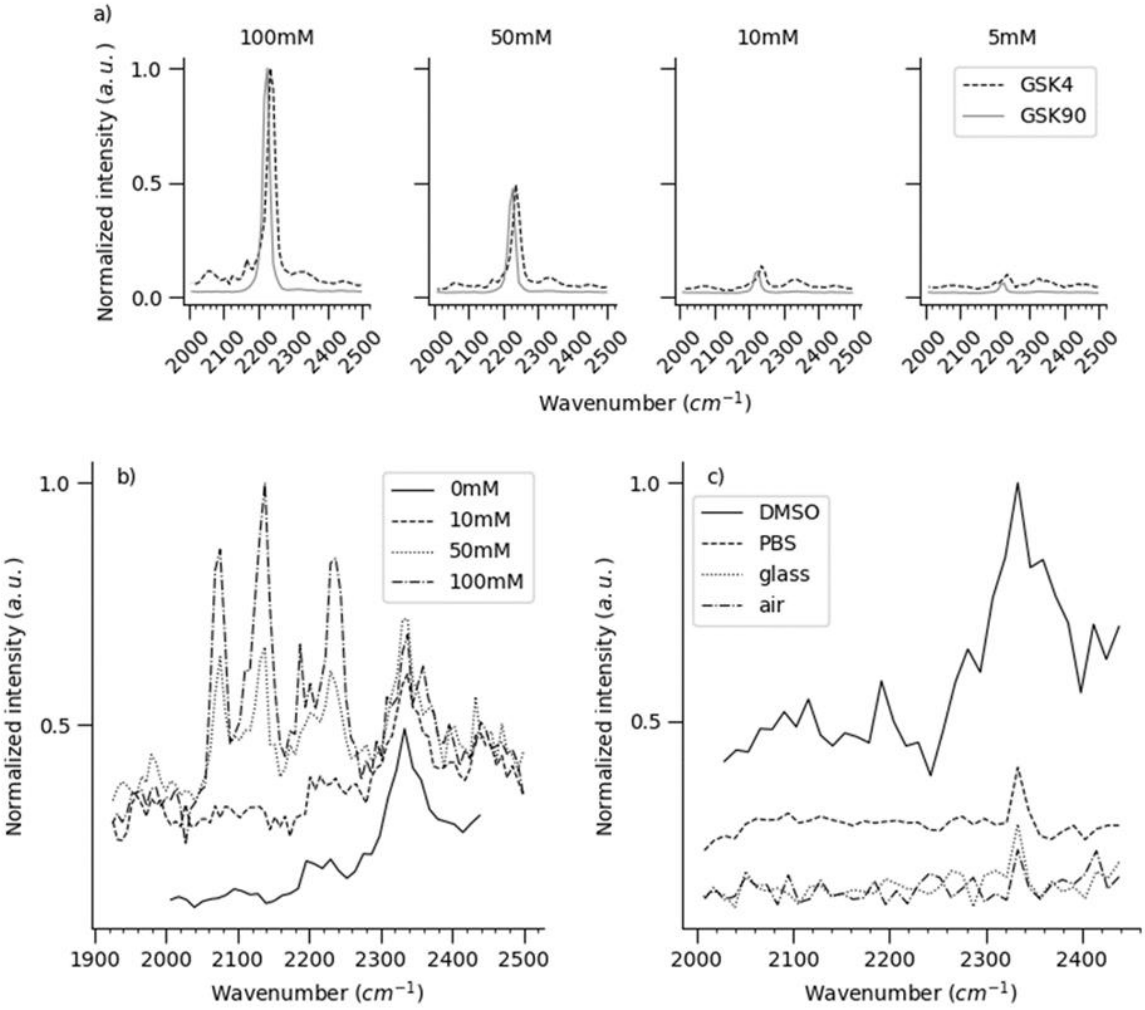

Figure 4.13 SRS of tool compounds in DMSO. Tool compounds were dissolved in dilution series and measured in the cell silent region (2000 cm^{-1} – 2500 cm^{-1}) All compound data were normalised to the maximum intensity at the highest concentration. a) GSK4 and GSK90 with a C≡C peak (2236 cm^{-1} and 2227 cm^{-1}) exhibited high SNR and were detected in the lowest concentrations. b) GSK2 tagged with only C-D Raman tag was detected at 100 mM and 50 mM concentrations only, where three peaks between 2073 cm^{-1} and 2230 cm^{-1} C-D-corresponding peaks were observed. Peak at 2332.8 cm^{-1} was likely an artifact of unknown origin. c) The 2232.8 cm^{-1} peak artifact was detected in DMSO, PBS, glass, and air. Y intensity was scaled to the highest concentration signal intensity for each analyte.

4.6. SRS analysis of tool compounds in tissues

The LOD examination of the test compounds in solvents using SRS revealed that compounds containing alkyne bonds are most likely to be successfully detected in the cell silent region in biological matrices, whereas deuterated molecules were not expected to be detected based on the signal absence is SRS spectra of pure compounds. Although the cell silent region is inherently free of typical endogenous signals arising from the biological sample, the analyte detection can still be hindered in an SRS analysis by sample dispersion and mixing with a biological matrix, which was potentially dictated by the physicochemical properties of the tool compounds. Unlike in MALDI, protein binding, lipid affinity and matrix extraction were unlikely to affect the SRS intensity of an analyte. Therefore, SRS was expected to be applied as a ground truth comparative analysis to the MALDI MSI data.

As in data shown in Figure 4.13, SRS analysis was focused on the cell silent region, which typically lacks Raman vibrational peaks in biological matrices. Rat liver homogenates were used. 12 µm cryosections were mounted on standard glass slides and dried. After drying, 0.1 – 5 mM methanol solutions of GSK4x and GSK90 were spotted on liver homogenate sections. Due to local safety rules, requiring biological samples to be sealed in the SRS/CARS room, dry samples were enclosed by a cover glass and sealed with adhesive for SRS analyses. An absence of an optical media with an appropriate refractive index was expected to create a scattering effect. This was expected to impact the spatial resolution and the LOD. In SRS measurements, LOD was defined as 2× noise intensity, which was calculated by the median intensity value of averaged SRS spectra. The spectral range and step size were set to 2152 – 2294 cm^{-1} and 7 cm^{-1}, respectively.

A representative SRS image of GSK4x spot on a liver homogenate showed the sample morphology under a 25× lens (Fig. 4.14a). The dashed line highlighted the dried droplet edge separating the GSK4x positive sample and the undosed sample section. The dosed segment of the image shows high intensity signal following the homogenate morphology. Small cracks in an undosed part of a tissue were cracks which formed by tissue drying, while the large gaps in spotted tissue a result of a tissue wash-off during the spotting. However, the GSK4x alkyne signal was not detected in the gaps and was therefore considered to be present only in the

remaining tissues GSK4x was successfully detected at 0.4 mM, 0.2 mM, and 0.1 mM spot concentrations. The off-spot sample area (Fig 4.14a) showed flat intensity across the cell silent region spectrum (Fig. 4.14b), and thus confirmed no analyte delocalisation outside the spot border. Furthermore, the spectral analysis showed that the SRS detection limit of GSK90 was approximately at 0.6 mM, which was poorer than GSK4x (Fig. 4.14c). This finding shows opposing correlation between SNR of GSK4x and GSK90 in solutions and in dried tissue homogenates. The unexpectedly poor signal of GSK90 (SNR ≤ 3) compared to GSK4x (SNR > 12) (Appendix 4) in spots on tissues was possibly related to the permeability, and protein and lipid affinity which was potentially connected to an increased miscibility and penetration of the drug into the tissue. GSK4x which showed less lipid and protein affinity was more concentrated at the top of the tissue section.

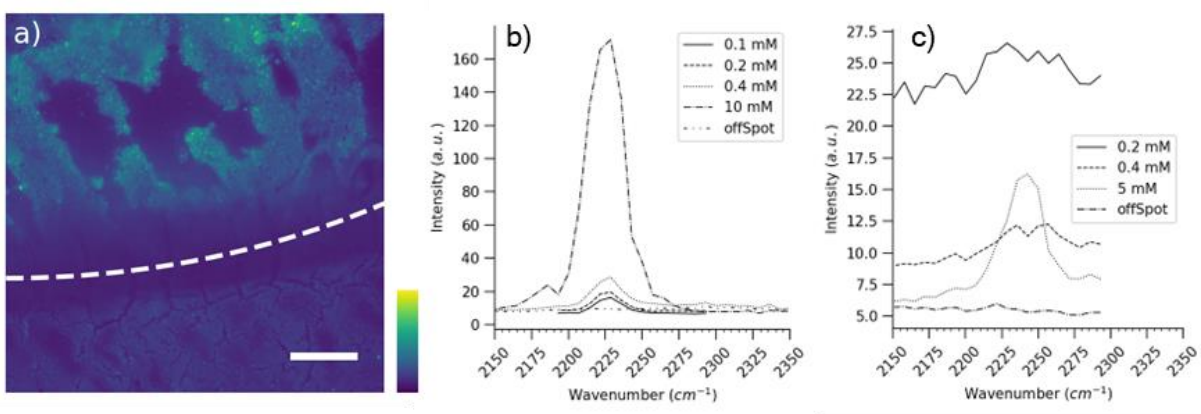

Figure 4.14 Tissue homogenate spot analysis with SRS. Liver homogenate cryosections were spotted with tool compounds in solution. a) SRS image (2228.6 cm^{-1}) of a spot edge. The dashed line separates unperturbed tissue (bottom) and tissue after GSK4x solution application (top). b) Alkyne peaks of GSK4x were detected at low concentrations (up to 0.1 mM) whereas c) GSK90 alkyne peak was obscured at 0.2 mM and 0.4 mM concentrations. Scale bar = 50 µm.

The use of mimetic models can potentially remove the variability originating from drug crystal autofluorescence and tissue penetration and miscibility since all analytes were mixed in the tissues with homogeneous distribution (Chapter 4.3). Rat liver and mouse brain GSK4x and GSK90 mimetic models (0 µg/g – 500 µg/g) applied in MALDI research were used for SRS analysis of the cell silent region. Samples were cryosectioned (12 µm) and presented into the microscope sample holder dry and enclosed between glass slide and a cover glass. ROIs of approximately 300 µm × 300 µm per homogenate segment were scanned averaged

along the cell silent region into single point SRS spectra using the same instrument settings as in the Figure 4.14-related experiment. The 500 µg/g GSK4 segment of the brain mimetic model is shown, where a peak is present, however it is either noise or the N_2 spectral component. Furthermore, 0 µg/g dosed samples exhibited flat spectrum as expected (Fig. 4.15a). On the other hand, GSK90 was detected in the brain mimetic model in 500 µg/g – 200 µg/g. The alkyne peak in the 100 µg/g concentration sample was too weak to be distinguished from the surrounding noise (Fig. 4.15b). GSK90 was also detected in liver mimetic model, in 500 µg/g and 400 µg/g. The rest of the concentration series in the sample was below the LOD (SNR < 2), potentially caused by the intrinsic background noise arising from the liver homogenate (Fig. 4.15c). There was more background noise in the cell silent region originating from liver tissue in contrast to the brain tissue, which was deduced based on the spectrum baselines of each sample and from the calculated SNR of putative analyte alkyne peaks (Fig. 4.15d). The liver baseline intensities varied between 4 – 16, however the SRS intensity baseline from brain tissues showed a stable intensity of ~ 2.

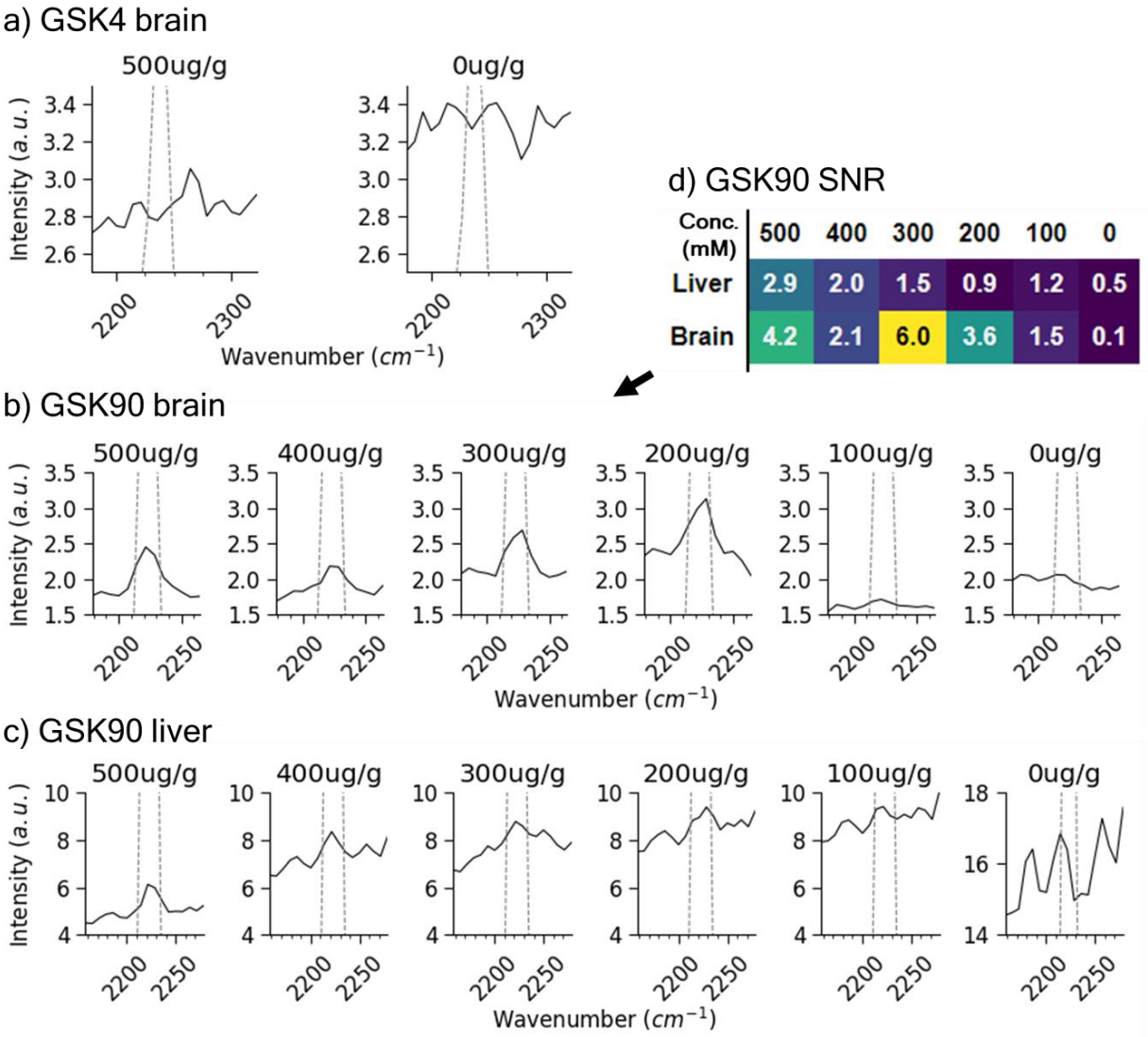

Figure 4.15 SRS analysis of mimetic models. GSK4 and GSK90 brain and liver mimetic models were imaged in cell silent region. Mimetic model data (solid line) and respective position of C≡C Raman band (dashed line)in the pure compound were plotted. a) GSK4 was not detected in mimetic models as no spectral peak fitted the GSK4 alkyne band. b) GSK90 fitted the expected alkyne spectral band in 500 µg/g – 200 µg/g concentrated samples in a brain homogenate. No signal above the noise was observed in 100 µg/g and 0µg/g samples. c) GSK90 in liver mimetic model was successfully detected in 500 µg/g and 400 µg/g homogenate samples. The alkyne peak was not detected with certainty due to noisy spectra. 0 µg/g concentration exhibited exceptionally high background. d) SNR of GSK90 SRS signal in liver and brain was tabulated.

4.7. Raman analysis of tool compounds in cell culture

Tool compounds were successfully detected in tissue homogenates and mimetic models which are useful for the investigation of LOD and a relationship between a signal yield and physicochemical properties. However, these artificial samples do not reflect a biologically relevant environment. Cell culture was therefore examined as a simplest living biological matrix for its applicability in the examination of cell silent region-active, where the analyte distribution can be observed at a high resolution.

Calu-3 cells were grown on cover glass squares treated with poly-D-lysine in a 6-well plate in DMEM. Cells were treated with 100 µM GSK4, 25 µM GSK90 and with methanol in a fresh DMEM in an incubator (37 °C, 5 % CO_2) for 2 hours. Afterwards, cells were fixed in 10 % neutral-buffered formalin (NBF) for 12 min. Cell samples on cover glass were imaged whilst submerged in PBS and sealed with a sticky gasket and a second cover glass. The cell silent region between ~2100 – 2300 cm^{-1} and CH region between 2800 – 3000 cm^{-1} to co-register the C≡C and the C-H Raman signal with SRS. Hyperspectral scans were then processed using the Correct 3D Drift plugin for Fiji ImageJ [263] to offset the lateral drift of the sample generated during the scanning period. Samples were denoised by applying a single value decomposition (SVD).[264,265] Calu-3 cells dosed with GSK4 contained alkyne signal at ~2236 cm^{-1} (Fig. 4.16a). The C≡C signal was distributed into well-defined punctae in cytoplasm near cell membranes. The C-H_3 vibrational mode at 2946 cm^{-1} highlighted entire cell and small circular structures (potentially endosomes), some of which overlapped with the GSK4 alkyne signal (Fig. 4.16b). GSK90 was also detected in Calu-3 cell line at 2227 cm^{-1} (Fig. 4.16c). The relative alkyne signal of GSK90 exceeded the maximum GSK4 alkyne signal in cell silent region. GSK90 was distributed across the whole cells, with the highest concentration in large vesicles. GSK90 was likely toxic to cells. Small number of cells was observed in the field of view owing to the cytotoxic effect of GSK90. Despite this adverse physiological effect, GSK90 was found internalised in cells. GSK90 appeared to be located on the plasma membrane, which highlighted faint bubbles and hair-like structures on the cell surface suggesting some pathological cell state. The 2946 cm^{-1} of GSK90-treated sample highlighted mostly membranes and large vesicular structures in the cytoplasm, thus further suggested

altered metabolic state of cells (Fig 4.16d). The imaging of cells treated with methanol displayed random noise. However, SVD processing removed most of the noise and reconstructed a very faint image of cells (Fig. 4.16e). Furthermore, Calu-3 cells in control samples showed a flat spectral phenotype in CSR and visible nucleoli (Fig. 4.16f). Cell area pixels from the cell silent region hyperspectral images were averaged and plotted along the spectral axis to verify the spectral peak and shape of alkynes and to comparatively quantify the alkyne intensity between samples (Fig. 4.16g). The overall SRS intensity of the alkyne bond in GSK90 was ~6.5-fold higher than intensity of nitrile bonds in GSK4 and GSK4x. The relatively low GSK4 intensity is also likely to cause the peak broadening. Finally, the GSK4 sample and the control sample spectra also feature the N^2 Raman peak, which is another indicator of low Raman probe intensity, since it was found only in SRS measurements of low-concentrated analytes or in weak scatterers, such as C-D deuterium bonds.

GSK4 and GSK90 were successfully detected in cells at subcellular resolution above limit of quantification (LOQ) despite low incubation concentrations in contrast with mimetic models concentrations. The spatial concentration of analytes focused on intracellular vesicles was a key reason of the high intensity detection of GSK4 and GSK90. Moreover, the relative background noise was miniscule because there is no tissue material surrounding the cells.

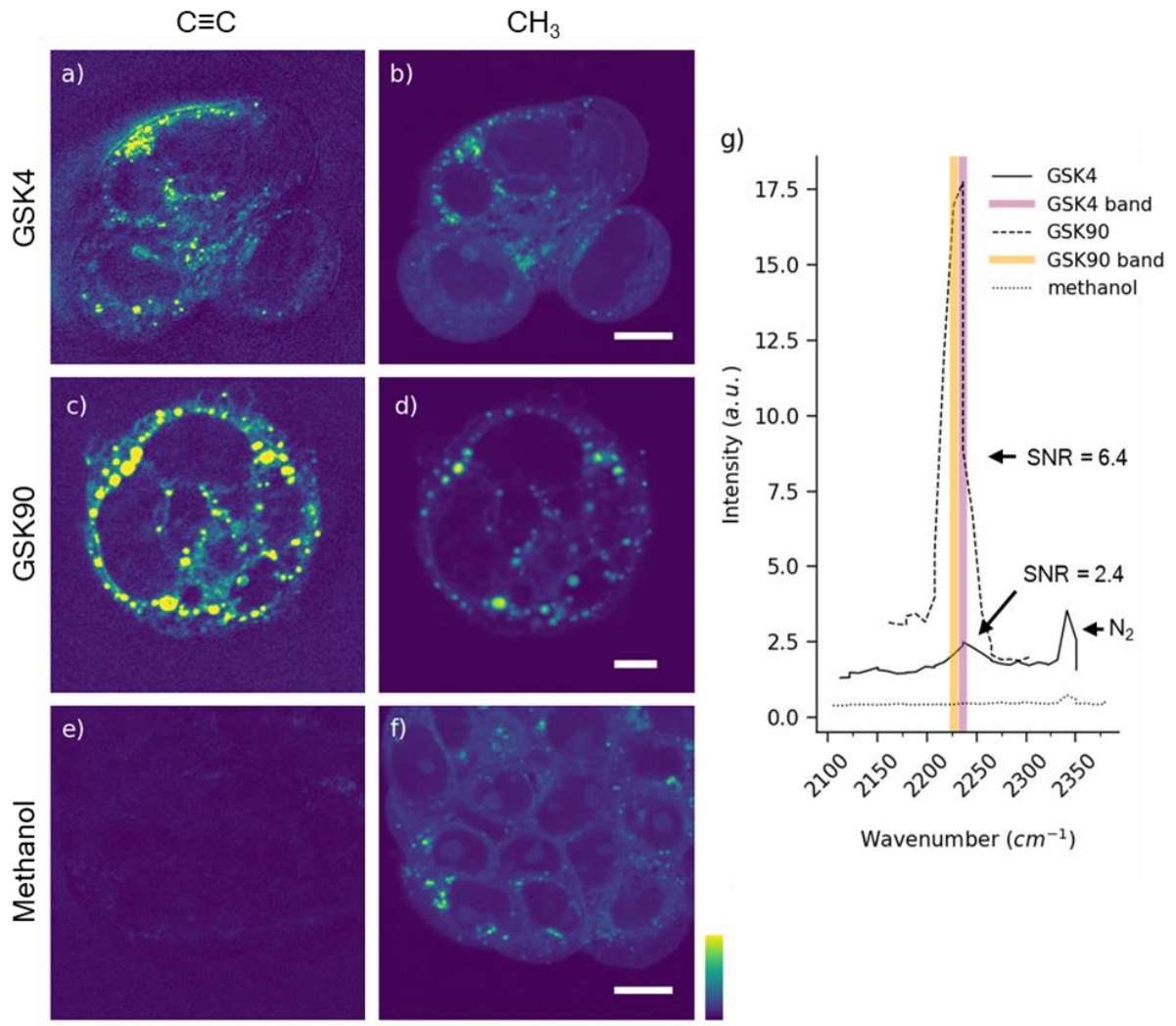

Figure 4.16 Cell uptake of tool compounds with SRS microscopy. SRS intensity colour-coded images of fixed Calu-3 cells with lasers tuned to the C≡C Raman vibrational mode (a, c, e) and the CH_2 mode (b, d, f). Cells were treated with 100 µM GSK4 (a, b), 25 µM GSK90 (c, d) and with methanol (e, f). Scale bar = 10 µm (b, f), 5 µm (d). The average spectra of manually selected cells were plotted and compared with expected peaks based on pure compound data (columns).

4.8. Discussion

Tool compounds were small molecules with the potential to generate strong signal in cell-silent region of the Raman spectrum. Detection feasibility was experimentally assessed with MALDI silent region in the MS and with SRS microscopy in parallel, in series of increasingly complex environments with the aim to select test compounds applicable in SRS-to-MSI experiments. Moreover, the analyses were correlated with solubility, permeability, lipophilicity, and protein affinity

properties of each test compound in order to determine which physicochemical properties are affecting the ionisation efficiency of an analyte compound.

A majority of test compounds was removed from the sample set owing to a poor ion yield in tissues in MALDI and due to a lack of sufficient signal in the cell silent region of SRS spectra, which were all deuterium-modified compounds. The remaining compounds contained alkyne bonds, which were typically associated with strong signal in cell silent region SRS signal. Furthermore, it was confirmed that compounds, which contained alkynes in a π-conjugated system with aromatic cycles exhibited enhanced SRS signal intensity of the alkyne peak.[96] In the MALDI MS study, two compounds – GSK4 and GSK90 – showed the strongest alkyne SRS intensity and high ion yield in MALDI MS. GSK90 was likely stronger ionising analyte in comparison with GSK4 based on a higher nitrogen-to-oxygen ratio in a molecular structure of GSK90, which in turn increases the probability of a molecule to ionise in a positive polarity MS instrument. Solubility of GSK4 was higher than GSK90 and was therefore likely a secondary factor in the analyte ion yield in a pure sample powder form.

SRS analysis of deuterated samples in solution (100 mM – 5 mM) revealed poor signal intensity of C-D vibrational bands (SNR ≤ 3) and a Raman peak at ~2300 cm^{-1} at a constant intensity, which was independent of a test compound and an intensity. The peak was thought to be related to N_2, based on available literature. Since this peak became prominent in low-concentrated analyte samples, it posed an issue in determination of LOD by masking an alkyne or C-D bond SRS signal in the cell silent region.

4.8.1. Physicochemical properties with MALDI

Analyte concentrations used in these experiments were higher in comparison with the physiologically relevant drug concentrations which are typically used for *in vivo* dosing. For instance, an effective plasma concentration of GSK90 (ponatinib) in phase one clinical study was 40 nM (<20 ng/ml).[266] However, the drug is generally expected to accumulate heterogeneously in the organism according to their loci of action, which in turn leads to a local increase in concentration. Such conditions can be simulated through an animal dosing or an organ perfusion, but these experiments

were not ethical in a method development study. Instead, by using high concentrations of analytes, it was possible to meet the sensitivity levels of the MALDI and SRS instruments.

A study in rats revealed that the highest lipid concentration in dry tissue was found in brain (~77 mg/g), followed by liver (~43 mg/g).[267] Therefore, ionisation differences between low lipid-binding analytes and high lipid-binding analytes were expected to play a major role between tissues and also in different regions. In humans, the concentration of lipids was reported to be ~49-66 % and ~36-40 % in white and grey matter, respectively.[268] This finding suggested that white matter would likely suppress an analyte. The spot analysis of test compounds on tissue sections showed heterogeneity between the analytes, but it also showed a dependency on the spot positioning in mouse brain tissues, where the grey and white matter affected the ion intensity of an analyte compound. Unexpectedly, the ion images of GSK2, GSK4 and GSK10 in Fig. 4.5. showed a higher ion intensity of an analyte in the white matter as opposed to grey matter. Boskamp *et. al.* recently discovered that the ionisation efficiency is also dependant on lipid structure,[178] and thus suggesting that apart from an overall lipid concentration and distribution, lipid species composition can have an impact on the ion suppression effect of other analytes in a sample.

Although the MS signal heterogeneity in brain tissues revealed important interactions between different brain regions, quantification of analyte spotting data was imprecise owing to the heterogeneity between biological samples and the manual positioning of the analyte spots. Therefore, tissue homogenates were used instead, which were devoid of high structures in tissues. Mimetic models, which consisted of serial dilutions of drug-spiked homogenates revealed GSK4 enhancement in liver tissues which was opposed the MALDI results in pure compounds. Both compounds performed equally in brain mimetic models. It was likely that any interaction between the analytes and lipids was masked by the ion suppression effect in the brain tissues, during which lipid components with high-ionisation probability sequestered the ionising energy. The impact of lipid binding on an analyte ionisation efficiency is therefore very unlikely to be examined with MALDI alone in brain tissues owing to the lipid-intrinsic ion suppression effect. Nonetheless,

it was found that GSK4 ionised stronger than GSK90 in thin liver mimetic models. Based on these results a preliminary correlation relationship was proposed, where solubility and permeability were expected to positively affect an analyte ionisation efficiency by improving the rate of matrix-mediated analyte dissolution and transportation through the tissue. On the other hand, protein binding was expected to negatively affect an ionisation efficiency by slowing down the transport through the tissue during matrix-mediated extraction.

Furthermore, 12µm mimetic model sections were likely saturated with matrix which prolonged the matrix exposure of samples and an analyte extraction, which caused a 3-5× increase in intensity of 12µm in comparison with 16µm sections in all samples apart from a GSK90 mimetic model.

To summarise, the mimetic model were still complex models in the correlative study between a test compound ionisation efficiency and physicochemical properties and therefore further sample preparation methods and analyte environments, which can lead to a separation of the physicochemical properties need to be considered. A replacement of matrix with DIUTHAME membrane (applied in chapters 5 and 6) is an excellent option, which can change the weight of the solubility by using the tissue moisture only. Furthermore, proteins standards are potentially useful in an analysis of protein affinity by removing the permeability and lipid binding properties. Finally, more test compounds need to be analysed in order to provide a robust dataset to prove the discussed statements.

4.8.2. Physicochemical properties with SRS

In SRS analyses of analytes in pure forms, GSK90 was also observed to generate a stronger alkyne signal in the cell silent region in comparison with GSK4. The enhanced alkyne signal in GSK90 was most likely caused by the alkyne positioning between the two π-conjugated heterocycles, which were shown to play a major role in alkyne signal modifications.[91,96]

Unlike in MALDI MS analyses, GSK4 was not detected in mimetic models, whereas GSK90 was detected. The SRS signal was accompanied by background noise in liver homogenates which were associated intrinsic fluorescent components of liver since brain homogenates spectrum baselines were smoother. A study of liver

mimetic models with spontaneous Raman microscopy suggested an improvement in LOD through sample photobleaching which reduces the intensity of the autofluorescent background.[99] As expected, the sensitivity of SRS (SNR ranged between 6 – 1) was found to be inferior to MALDI MS, which detected analytes in the lowest mimetic model concentrations (100 µg/g, SNR = 12). SRS was considered to be not affected by the outlined physicochemical properties since the analytes were imaged *in situ* without extraction, which was supported by the GSK90 and GSK4 results in mimetic models. However, spotting analyses showed a lower GSK90 ion intensity in comparison with GSK4, which was likely caused by tissue-specific ion peak enhancement or by GSK90 dissipation into the tissue, whereas GSK4 remained closer to the tissue surface. Therefore, protein and lipid binding were considered as the potential physicochemical properties relevant to GSK90 dissipation into liver tissues. Hence an analysis of analytes spotted on tissues adds an artificial variability to the complex problem of ionisation efficiency in MALDI MS, where an analyte ionisation is affected by the analytes ability to passively penetrate into the tissue during spotting.

In consensus with the MALDI analyses, new test compounds need to be found and analysed to confirm whether protein and lipid affinity are the driving force behind a drug permeation through tissues.

4.8.3. GSK4 and GSK90 in cell cultures

Finally, both techniques were examined for their feasibility of test compound detection in a cell culture.

GSK4 and GSK90 were successfully detected in Calu-3 cells, although the latter induced a cytotoxic effect, which strongly affected the number of living cells in time of formalin fixation. Nonetheless, GSK4 was detected in small punctae in cell cytosol, some of which overlapped with lipid-rich vesicles. Furthermore, a punctate distribution suggested that GSK4 was actively endocytosed by cells, rather than penetrating the cell membrane which would be expected to form a diffuse signal. GSK90 was however detected in entire cells, including membrane structures and large punctae. Additionally, GSK90-treated Calu-3 cells exhibited cytotoxic phenotype, such as membrane blebbing and very large vesicular bodies, which also

exhibited GSK90 signal. The different uptake mechanism of GSK4 and GSK90 was likely connected to the lipophilicity and permeability physicochemical properties, where GSK4 was labelled as poorly permeable according to the DCS chart and weakly binding to lipids, where GSK90 was a highly lipophilic and permeable molecule, which suggested that the latter was more likely to pass through cell membranes.

GSK4 was successfully detected in MALDI MS study of cell pellets, which required multi-step washing, which decreased the GSK4 concentration in supernatant below the LOD of the mass spectrometer. The presence of cells was confirmed by focusing on a phospholipid head group fragment. A detection of GSK4 and the same phospholipid head group ions was unsuccessful in a MALDI MSI experiment detection of a test compound and the phospholipid headgroup in MSI experiments due to sample fixing, which was potentially correlated with a delocalisation of lipids and GSK4. Moreover, the sensitivity of imaging, where single raster ionisation spot is spatially and thus material-wise constrained, whereas a spotted pellet analysis can sample large area and thus more material.

5. Translation of biological samples from Stimulated Raman scattering microscopy to laser desorption/ionisation mass spectrometry imaging

5.1. Introduction

SRS microscopy and laser desorption/ionisation (LDI) MSI have been widely employed to identify the chemical composition of tissues in their native state, without the need to modify the samples using fluorescent or chromogenic dyes.[82,91,93,261] MALDI MSI provides molecular weight and composition information for the measured sample, while Raman spectroscopy provides vibrational information of the molecular structure and chemical composition of a sample. The combination of these methods can provide complementary information about the molecular composition and structural properties of a sample, thus leading to a more comprehensive understanding of biological systems. However, the processes for generating SRS and MALDI data are fundamentally different, and the samples require different preparation procedures. Therefore, new methodologies need to be devised to allow comparative SRS and LDI MSI of the same sample.

MALDI is one of a number of preferred ionization techniques for MSI of tissues because it is a soft ionisation technique, which increases the probability of ionising analyte molecules into single-charged ions.[141] In MALDI, analytes are adsorbed into a matrix which significantly increases the ionisation probability of an analyte, which is then ionised using a high intensity laser before analysis in a mass spectrometer.

A crucial component of the MALDI ionization process is the matrix. The matrix is a small organic acid with UV-absorbing properties that is deposited on the surface of the sample. The role of a matrix in the ionization process is to mediate and distribute laser energy through the sample. Matrix can be deposited on the surface through two main techniques – automated spraying[166] and sublimation[168]. In all cases, the matrix is first dissolved in a solvent and then transferred to the sample surface, where it forms crystals while drying. During drying, the matrix extracts and co-crystallizes the components from the sample. These co-crystallized components

are thought to represent the major constituents of the sample ions detected with a mass spectrometer.

MALDI mass spectrometers use high-power UV lasers for sample surface desorption and ionization.[269] A UV laser is the most suitable light source because of its low penetration depth, which is associated with the high UV light absorption by the matrix. Hence, most of the energy accumulates in the top layer of the surface.[270] During ionisation, the chemical components on a sample surface are desorbed into the space above the sample upon the impact of high-energy photons. The plume of particles consists of (among other components) charged chemical species called ions, which then continue onward into the mass analyser. The complete MALDI ionization process is described in more detail in Chapter 3.6.

The tissue samples, typically fresh-frozen tissue section, must be in a dry state prior to matrix deposition. Sample wetness can exacerbate issues including crystal size increase (one of the main denominators of MALDI MSI spatial resolution), sample delocalization and matrix crystallization pattern heterogeneity.[164] However, for high-resolution SRS microscopy using commercially available instruments, samples should be immersed in optical media which are compatible with a microscope setup.[271] Standardly, these media are water-based (e.g., PBS buffer), which are Raman background-free or glycerol-based media (e. g. MOWIOL), which however introduce Raman background.

Sample conductivity is an essential requirement for optimal ionisation in MALDI instruments. In the mass spectrometer, the sample holder is connected to a source of high voltage which accelerates ions with one of two polarities. Sufficient conductivity is provided by using steel plates and conductive-coated glass slides as sample carriers. ITO (Indium tin oxide)-doped glass slides are translucent and potentially useful for standard brightfield and fluorescence microscopy. Attempts to introduce conductive elements to non-conductive slides and samples through spray-coating[272] or by attaching conductive surfaces[185] have been reported. DIUTHAME, a novel matrix-free surface-assisted laser desorption/ionisation (SALDI) method reportedly enables LDI MSI with high reproducibility and decrease in sample preparation time compared to matrix application. By introducing a thin, porous membrane consisting of aluminium and platinum metals on the sample surface,

sufficient conductivity is accomplished to accommodate the current of high voltage in the mass spectrometer.[186]

The objective of this chapter was to identify and overcome any incompatibilities between SRS microscopy and MALDI MSI methodologies with the aim to achieve an SRS-MSI cross-analysis of the same biological samples. The work was separated into following smaller objectives:

- Description of an ideal tissue sample configuration for SRH.
- Evaluation of SRS using conductive substrates.
- DIUTHAME-enabled SALDI and MALDI cross-comparison.
- Apply the sample configuration and DIUTHAME insight to analyse the same tissue sample with SRS and MSI.

5.2. Optimisation of the SRS system for tissue imaging

5.2.1. Conductive materials in SRS microscopy

Laser sources applied in SRS microscopy have an emission range within the near-infrared (NIR) spectrum (720 nm – 1031 nm). The conductive element in a MALDI slide, ITO, absorbs and reflects light in this spectral region[273] and thus, SRS measurements may be negatively affected by signal interference. GSK90 analyte was measured in the cell-silent region with the SRS system to determine whether ITO-doped slides are applicable in SRS microscopy studies. A Leica SP8 SRS system was used and employed a fixed 1031 nm pulsed laser and a tuneable 740 nm – 940 nm pulsed laser sources.

Pure GSK90 was dissolved in DMSO to a final concentration of 10 mM and spotted on 4 different surfaces: a standard microscopy glass slide, a quartz slide, an ITO-doped slide (Intellislide) and a low-concentrated ITO-doped slide. The sample was sealed with a cover glass. The SRS analysis was focused on the cell-silent region. The C≡C peak (~2230 cm^{-1}) of GSK90 was successfully detected on glass, quartz, and the ITO-doped slides with SNR = 12 for each slide (Fig. 5.1a). A strong background signal was recorded in the low-ITO slide and no alkyne peak was observed (SNR = 1). However, the image data revealed an imaging artifact along the vertical edges of the scanned area in samples on an Intellislide (Fig. 5.1b). The

positioning of these lines suggested that some material (potentially including ITO) was burning off during the scan and therefore no interference was observed. It is suspected that the noise arising from the slide with a low ITO concentration was detected because the amount of a metal oxide did not absorb enough energy to burn. This hypothesis was not explored further as it deviated from the project objectives.

The results of this experiment concluded that SRS imaging analysis should be conducted prior to an LDI MSI with a sample mounted on a non-conductive surface to avoid strong signal interference and material burn-off originating from the interaction between the laser source and the conductive components. The ideal slide substrate for sample handling was determined to be glass or quartz.

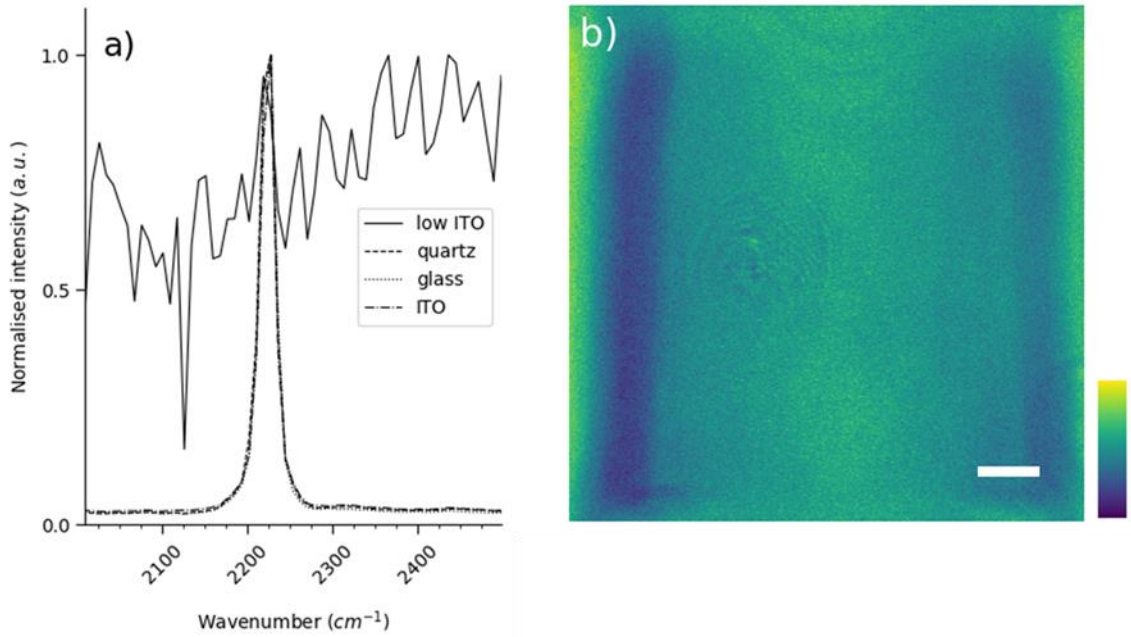

Figure 5.1 Effect of ITO-doped slides on SRS data quality of a pure GSK90 sample. GSK90 in DMSO was spotted on standard microscopy glass slide, ITO-doped slide (Intellislide), low-concentration ITO slide and quartz slide. a) The spectral data was normalised to a max value per individual scan. A use of standard ITO, quartz and glass slide resulted in the same SNR of the C≡C bond. Low-concentrated ITO (solid line) spectrum affected the spectrum by generating only noise signal. b) SRS microscopy of an Intellislide revealed a formation of linear artifacts at the edges of the scanned area during the SRS imaging. Image intensity is normalized to the maximum value pixel. Scale bar = 10 µm.

5.2.2. Comparison of animal tissues in aqueous and dry environments in SRS microscopy

Local safety requirements mandated that all biological samples used in the SRS microscope laboratory area were sealed from the lab environment. The sample was therefore prepared using 0.17 mm cover glass with a 0.5 mm silicon imaging spacer which was closed off by a second 0.17 mm cover glass with a sample on the glass surface, facing the gasket effectively sealing the sample from the environment (Fig. 5.2). This setup was designed to fit in the sample holder at a suitable distance from a short working distance condenser lens (1.1 mm) while not compressing and damaging the biological sample. A dry tissue sample was preferred over wet tissue for LDI MSI since it minimised structural and chemical changes of the sample. However, air inside the sample enclosure was expected to cause laser backscatter on interfaces between glass (refractive index = 1.51) and air (refractive index = 1). However, a dry sample was advantageous over a wet sample which was at risk of morphological and biochemical changes whilst in an aqueous environment. To evaluate the feasibility of dry tissues in the setup, wet and dry samples were compared.

A 12 µm rat brain cryosection was thaw-mounted on a square 0.17 mm cover glass. A double-sided adhesive spacer was used to join the sample cover glass and a clean cover glass together in either dry environment or in aqueous solution. The enclosed tissue was presented into the microscope sample holder (Fig. 5.2). The signal was collected in transmission configuration in a photodiode. The objective lens was corrected for water immersion with a 1.33 refractive index and 0.17 mm thick glass and the condenser lens was corrected for an oil immersion with a 1.51 refractive index.

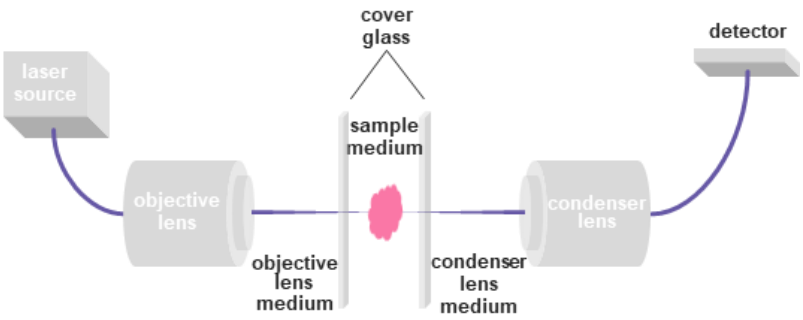

Figure 5.2 Sample configuration in the microscope light path. The SRS sample light path originated at the laser source generating pump and Stokes beams, which passed through an objective lens and a water immersion medium a sample in an optical medium and sandwiched between two cover glass squares. From the sample, the two beams moved through the condenser immersion medium to the detector photodiode.

Firstly, dry and wet rat brain tissue cryosections were used to compare the spatial and spectral contrast of both tissue states. The brain tissue sample was scanned by sweeping the pump and Stokes lasers between 2800 – 3050 cm^{-1}. The SRS hyperspectral data contained strong noise contribution, which was removed using a single value decomposition (SVD) filter (Chapter 3.10.3) whilst preserving the tissue-representative signal. Images of tissues at CH_2 (2866 cm^{-1})and CH_3 (2945 cm^{-1}) vibrational bands were captured for the purpose of highlighting the lipid and protein components of a sample, respectively. The imaging data of rat brain tissues exhibited poor contrast at the CH_3 vibrational band (2945 cm^{-1}) (Fig. 5.3a) and a slightly stronger contrast at the CH_2 vibrational band (2866 cm^{-1}) (Fig. 5.3b), where individual lipid-rich white matter bundles and fine lipid fibres were discernible unlike in the dry tissue images. CHR scans of rat brain tissues in PBS at CH_3 (Fig. 5.3c) and CH_2 (Fig. 5.3d) vibrational bands revealed high spatial contrast information about white matter bundles in tissues. The decreased signal outside the large bundles in CH_2 vibration image suggests the CH_3/CH_2 bond ratio is increased outside these regions. The voxels from the hyperspectral data cubes were averaged and normalised to the maximum intensity along the spectral domain to produce Raman spectra of the wet and dry samples (Fig. 5.3e). The spectral resolution and contrast appeared the same between the samples although the intensity at ~2950 cm^{-1} suggested increased proportion of the CH_3 bond, which is more prevalent in proteins. This result was likely caused by focusing on brain regions with different chemical distribution. Moreover, the wet sample baseline at 2800 cm^{-1} was lower than the wet sample baseline which suggested the scattering caused by the air

medium in the optical pathway generates spectral noise. The low intensity baseline in the high wavenumber spectral region in dry sample was caused by a lack of the O-H signal, which was otherwise observed in the wet sample, originating from the PBS at wavenumbers greater than 3000 cm^{-1}. These results confirm that wet tissue imaging leads to a high spatially-resolved image, albeit the difference between spectral information of wet and dry samples was small based on a comparative difference in contrast between CH_3 and CH_2 of the respective samples and their respective Raman spectra.

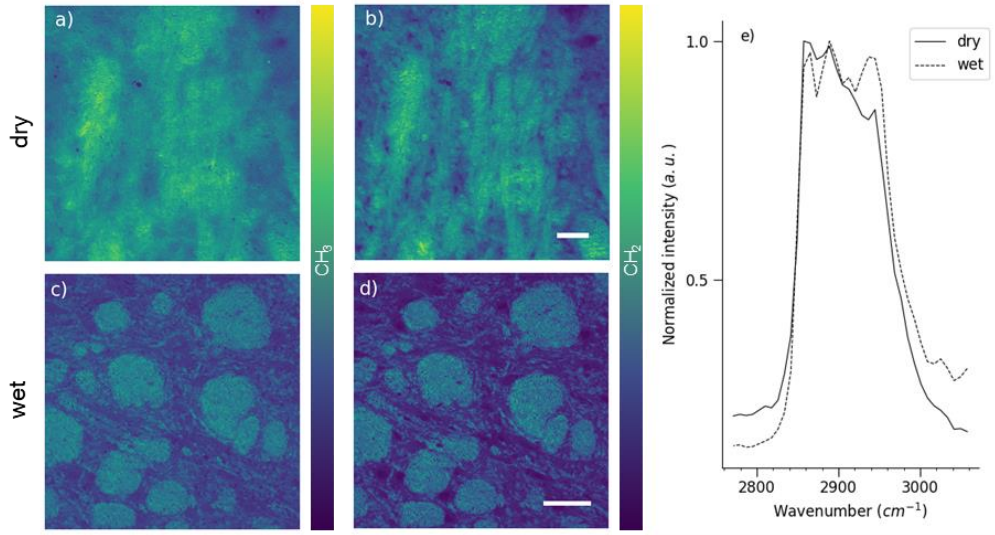

Figure 5.3 Evaluation of wet and dry brain tissues in SRS microscopy. The SRS image acquired at CH_3 (2945 cm^{-1}) vibrational band exhibited low contrast information *(a)* and an improved spatial contrast in the CH_2 (2866 cm^{-1}) image (*b*). CH_3 (*c*) and CH_2 (*d*) images of brain sections in aqueous solutions captured an improvement in contrast between white matter bundles (green circular structures) and the remaining tissue. *e*) The noise baseline of a dry sample was higher than the noise baseline of the wet sample based on the height of the initial flat line at 2800 cm^{-1}. A beginning of a broad O-H stretch is a component of the wet sample CHR of the Raman spectrum. Y axis was scaled to the highest intensity in each sample. Scale bars = 50 µm.

5.2.3. Stimulated Raman histology

The lipid/protein distribution information acquired through CH_3 and CH_2 SRS imaging could be further exploited in stimulated Raman histology (SRH). In SRH, the CH_2 SRS image is subtracted from the CH_3 SRS image which highlights the protein distribution in the sample and subtracts the lipid signal. The subtracted image is then overlaid with the CH_2 image. The look-up table (LUT) colour styles could be adjusted to resemble the haematoxylin and eosin (H&E) staining.[114] SRH imaging could prove highly valuable in MALDI tissue imaging experiments. In MALDI, an adjacent tissue

section is stained with H&E for morphology association with the MALDI imaging data. The adjacent section would be expected to be morphologically slightly different from the MALDI sample. This is an intrinsic issue of the MALDI MSI technique, since this is a destructive analytical method, which can be negatively affected by sample staining. Since MALDI MSI instruments are being developed with an increasingly improved spatial resolution,[176] this morphological approximation will become increasingly inaccurate. Therefore, the capability of the Leica SP8 SRS system in SRH was explored with the ultimate aim to generate SRH images of a tissue section which would eventually be analysed using MSI.

A 12 µm-thick mouse brain cryosection was enclosed in an imaging chamber filled with PBS and 2945 cm^{-1} (CH_3) and 2866 cm^{-1} (CH_2) 25 SRS tile images (291 µm × 291 µm) were acquired with a 5.76 µs pixel dwell time and a 0.569 µm pixel size. Tiles were automatically stitched together in LAS X (Chapter 3.10.4) with a 17 % tile overlap and smoothed in ImageJ, where each pixel was replaced by an average of 3×3 neighbouring pixels. Smoothing was necessary to improve the small mismatch between tiles, since both CH_2 and CH_3 tile mosaics were stitched separately, which resulted in a tile mismatch. The image generated from CH_3 signal (Fig. 5.4a) shows the protein and lipid structures in the edge of the brain tissue. The image generated from the CH_2 signal shows the same structures at higher contrast (Fig. 5.4b) highlighting white matter bundles in brain. The lipid signal removal through the $|CH_3 – CH_2|$ image subtraction highlighted cells and cell nuclei which were not observed in the raw data (Fig. 5.4c). The image subtraction highlighted non-lipid protein structures, such as cells, but it did not result in separation of cell nuclei. Additional CH_2 subtraction of the CH_3 signal ($|CH_3 – CH_2 – CH_2|$) removed most of the remaining signal apart from a suspected nuclear signal (Fig. 5.4d). The subtracted image (green) was overlaid with the CH_2 image (magenta) to highlight a cell nuclei distribution (cyan) and a lipid distribution (green) in the mouse brain. (Fig. 5.4e). The nuclei appear white because the cyan signal is always present in the cellular magenta signal. The inset image showed faint dark borders between the two channels. The borders were an artefact of mismatch between the automatically-stitched tiles of the two SRS scans and the subsequent Gaussian smoothing. Moreover, the samples were prone to an air bubble accumulation (dashed circle) caused by the gas exchange in the removable silicon gasket.

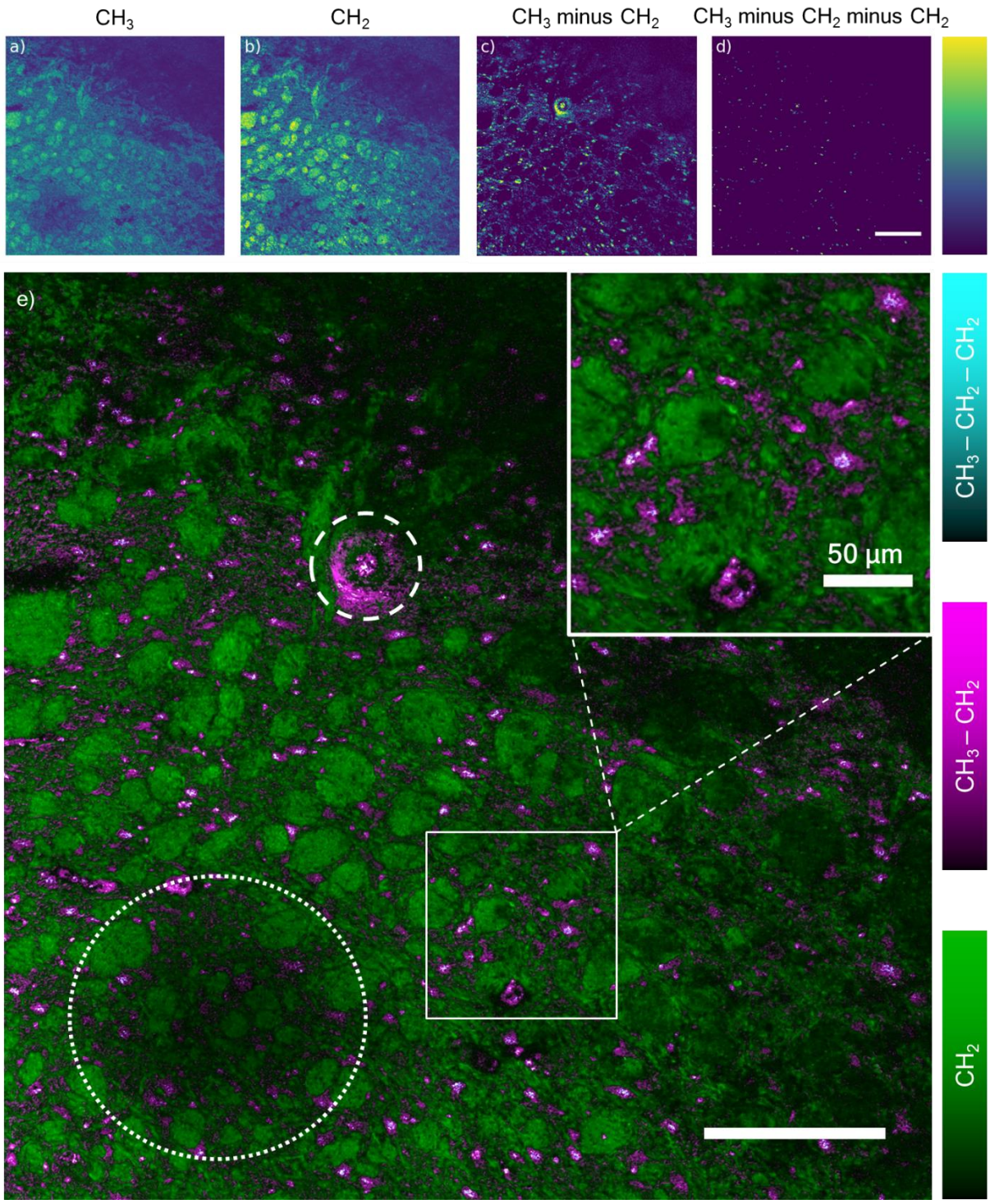

Figure 5.4 SRH in fresh murine brain tissues. A murine brain cryosection was imaged with the SRS microscope at a) CH_3 (2945 cm^{-1}) and at b) CH_2 (2866 cm^{-1}). Image subtraction (CH_3 – CH_2) highlighted cells and cell nuclei (c). Additional CH_2 image subtraction from the previous image calculation result removed all extracellular information and left only a potential faint nucleolar signal (d). The colour-coded image overlays the CH_2 signal (green) separated from the CH_3-CH_2 (magenta) and CH_3-CH_2-CH_2 (cyan) signal (e). The dotted circle highlights a darker region in the frame, likely caused by an air bubble in an oil immersion. The dashed circle marks light scattering on an air bubble in the PBS on the sample surface. The inset image shows the cyan signal (nuclei) and magenta signal (cells and nuclei) separated from the green lipid signal. Scale bars = 200 µm.

It was not possible to prevent air bubbles forming since the slides could not be sealed completely to enable for their later disassembly and use in LDI MSI. The dark region in the image was caused by an air bubble in the oil immersion.

The SRH methodology described in Sarri *et. al.* and Di *et. al.*[114,116] using the Leica SP8 SRS microscope resulted in successful separation of the lipid and protein components in the brain. The additional CH_2 subtraction highlighted only the nuclei of individual cells. However, the objects were highly irregular in shape with a poor signal intensity. The was likely the result of a low image resolution and the XY mismatch between the individual image CH_2 and CH_3 tiles. The low resolution was however a necessary trade-off for fast scanning acquisition. Low-speed acquisition was susceptible to loss of focus caused by sample drift in XYZ. The nuclei separation through the double CH_2 subtraction was however not confirmed through chemically-specific labelling. Chemically specific confirmation of the nuclei highlighted in the CH_3-CH_2-CH_2 image was necessary to confirm the SRS signal specificity enhancement of the additional image subtraction step.

To confirm the position of the nuclei, the same murine tissue cryosection was examined using SRS and fluorescence laser scanning microscopy. A 12 µm cryosection of mouse tissue was thaw-mounted on a standard glass slide. The section was stained with Hoechst – a nucleus fluorescence marker molecule, which binds to nucleic acids and is commonly used as a cell nucleus marker – dissolved in the ProLong Gold mounting medium (1:1000, v:v) with a cover glass. After ProLong Gold curing, which causes the mounting medium to harden and compress the sample, the CH_2 and CH_3 SRS images of a brain were acquired. The Prolong Gold is an organic solution and as such it is resonant in the CH region. Therefore, there was a strong background signal in the entire sample. The Hoechst stain was imaged using the SHG line and the SHG epi-detector simultaneously with the pump and Stokes CRS lasers and the forward SRS detector. Image calculations ($|CH_3 – CH_2 (– CH_2)|$) were conducted in Fiji ImageJ and plotted in Python. The SRS of CH_3 showed an overall image intensity change from left to right between the high-intensity lipid rich tissue area and the lower-concentrated lipid area of the brain tissue, which was possibly acquired at an interface of white and grey matter (Fig. 5.5a). The high intensity of lipids in CH_3 vibrational range was most likely correlated with their dense

spatial distribution. In contrast, the less hydrophobic proteins were distributed more sparsely and consequently, the CH_3 signal was of lower intensity. The CH_2 SRS scan revealed stronger contrast between the different lipid-concentrated regions. Furthermore, CH_2 signal intensity was very low in ~5-10 µm circular spots (Fig. 5.5b), which were assumed to be the locations of cell nuclei. To identify the location of the nuclei, a CH_3 – CH_2 image calculation was used to remove the lipid signal from the image (Fig. 5.5c). The remaining signal highlighted protein components including the originally low CH_3 intensity region. Moreover, the subtraction highlighted the potential nuclei positions which corresponded to the low CH_2 signal spots in Figure 5.5b. The contrast between the nuclei and the high-concentrated protein tissue section allowed for the distinct characterisation of the protein and nuclei components . Further subtraction of the CH_2 SRS signal led to the complete removal of the protein tissue signal. However, this also removed a substantial amount of the nuclear objects from the field of view and most of the nuclear signal in the originally lipid-rich region (Fig. 5.5d). The fluorescence of the Hoechst stain in nuclei was used as a positive control which highlighted the true nuclear structures in the tissue sections (Fig. 5.5e). The chemical labelling confirmed the trade-off between low specific high intensity single subtraction images and the high signal specificity of the double-subtracted CH_2 signal which can result in substantial signal loss. For the SRH application however, using a single subtraction and an overlay with the CH_2 image standardly resulted in sufficient highlight of cell nuclei.

The SRH capability of the Leica SP8 SRS microscope was deemed suitable for tissue imaging in an aqueous environment. To support same imaging in MALDI at a relevant scale, a full tissue sample was needed and therefore imaging the tissues in the aqueous enclosure using tile scan function of the SP8 system needed to be examined and adjusted.

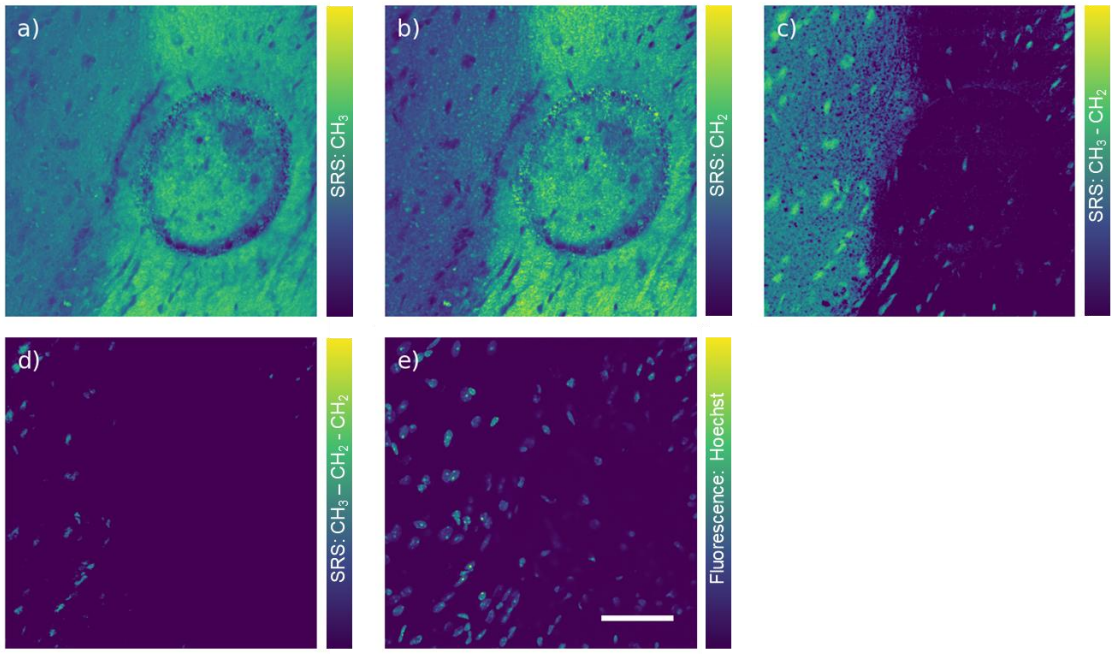

Figure 5.5 SRH specificity assessed by fluorescence microscopy. A mouse brain cryosection was imaged with the SRS microscope at a) CH_3 (2945 cm^{-1}) and at b) CH_2 (2866 cm^{-1}). Image subtraction of b) from a) image highlighted proteins in tissues and cell nuclei, whilst removing the lipid signal (c). *d)* Further CH_2 image subtraction from the previous image calculation result removed the highly protein concentrated tissue whilst highlighting only the strongest nuclear signal. *e)* The SHG channel was used to capture the fluorescence signal of the Hoechst-stained nuclei as an orthogonal control. Scale bar = 50 µm.

5.2.4. Stimulated Raman histology of full tissue sections

The in-house MALDI MSI instrument enabled data acquisition with ~10 µm lateral resolution of the full tissue section. Therefore, SRH mosaic images of full tissue sections were desirable as an image co-registration with MALDI MSI data. To examine the Leica SP8 capability of full tissue acquisition, a cover glass with a 12 µm thaw-mounted mouse brain tissue sectioned along the horizontal plane in PBS was used. The transversal section was imaged across an area of 15 mm × 13 mm by SRS image acquisition of 2295 tiles (256 × 256 pixel per tile, 20 % tile overlap) of CH3 and CH_2 in sequence with a 1.46 µm pixel size, and a 5.76 µs pixel dwell time. The tiles were stitched into a mosaic using the LAS X acquisition software (Chapter 3.10.4). The mosaic of the CH_3 (Fig. 5.6a) and CH_2 (Fig. 5.6b) brain SRS images showed the whole tissue section with multiple structural artifacts originating from the sample handling and preparation prior to SRS imaging. The right side of the brain cortex was structurally damaged on the edges during the cryosectioning. Furthermore, the snap-freezing of mouse brain in liquid nitrogen

often caused a crack in the middle of the tissue and a loss of the olfactory lobe at the top of the tissue section. The SRS mosaic data showed a large area of tiles with low or zero intensity across various parts of the tissues. This loss of signal in both vibrational modes in some tissue areas was attributed to the heterogeneous adherence of the tissue section to the cover glass. CH_2 SRS image highlighted the lipid-rich white matter throughout the brain, including the cerebellum. Conversely, these structures were faint or not detected at all in the CH_3 SRS data. The CH_2 and CH_3 SRS tile images were merged separately. The CH_3 and CH_2 mosaic images had to be precisely aligned in order to carry out image calculations, which can be applied in SRH visualisation. However, the mosaic images were mismatched in the spatial domain and could not be corrected in the LAS X software (Fig. 5.6c).

Data were exported in tiles to Fiji ImageJ for tile position correction. However, the images could not be merged due to the tile file formatting and metadata. A data processing tool with the tile correction capability and Leica metadata compatibility was not available at the time of the analysis. It was hypothesised that reduction of the scan area would potentially decrease the likelihood of losing focus which could in turn have improved the reproducibility of the mosaic stitching. This is because the accuracy of the mosaic stitching was highly dependent on the structures in the individual tiles.

A murine brain was sectioned on a cryostat along the frontal plane and prepared for SRS imaging in a PBS solution to test this hypothesis. Sectioning in this direction reduced the image size of an analysed organ by approximately one half. Pixel size was decreased from 1.5 µm to 0.9 µm and the tile logical size was increased from 256×256 pixels to 512 × 512 pixels in order to increase resolution. The change of parameters and sample sectioning plane resulted in decrease of a number of tiles to 858 (10 mm×6 mm) from 2295 (13 mm×15 mm). The resulting CH_3 (Fig. 5.6d) and CH_2 (Fig. 5.6e) SRS mosaics showed the caudal section in the diencephalon of a mouse brain highlighting the lipid rich corpus callosum, the cerebral cortex surrounding the outer layer of the corpus callosum, the low SRS intensity hippocampus and the thalamus. Moreover, the images showed the SRS microscope did not lose focus of the tissues across the entire sample albeit the high-resolution scan was temporally longer than the 2295-tile scan of the horizontal section. The overlay of the CH_3 and CH_2 mosaics spatially overlapped on the whole tissue scale (fig. 5.6f).

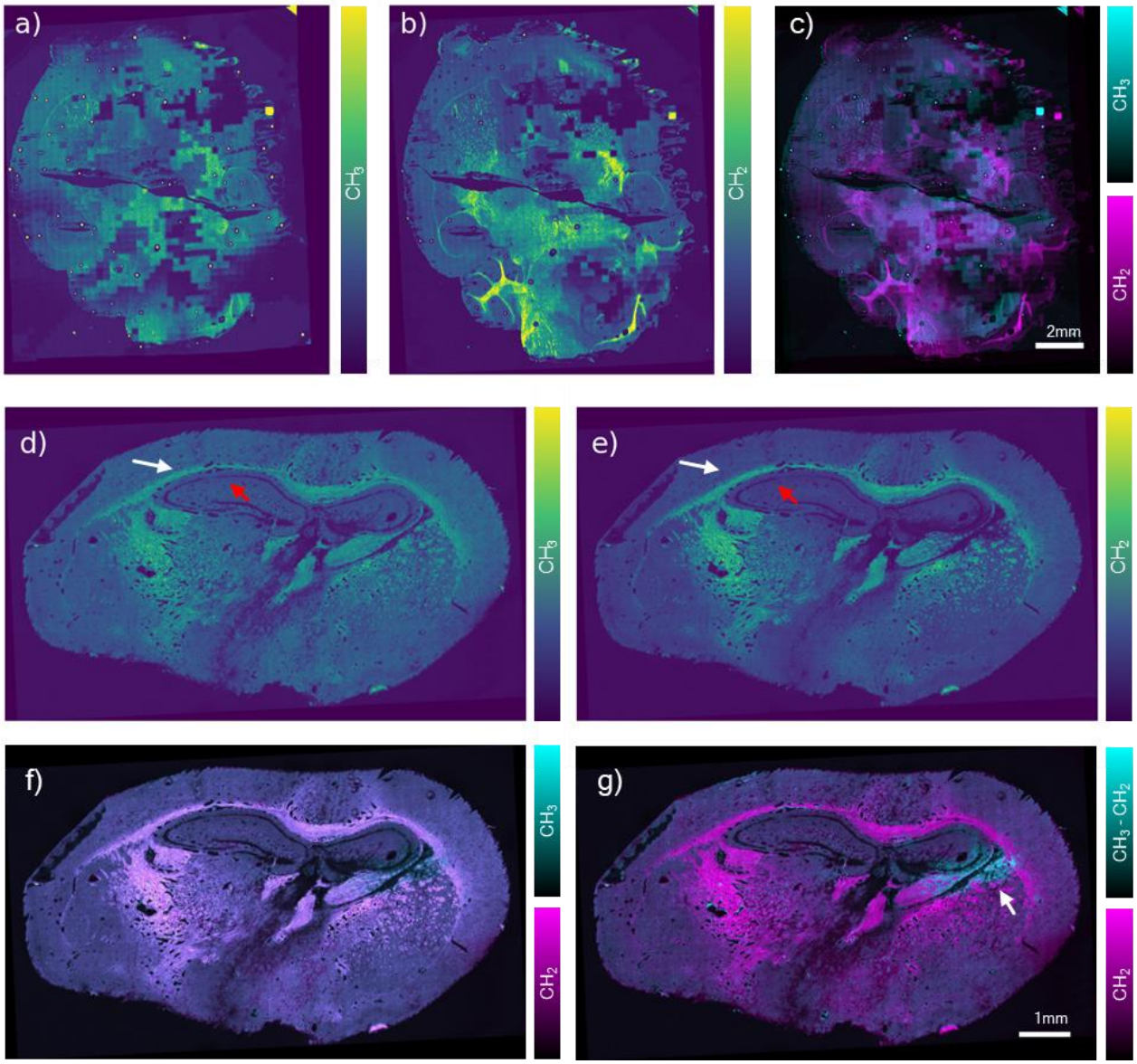

Figure 5.6 SRS imaging of a whole mouse brain cryosection. SRS microscopy of a mouse brain tissues sectioned along the horizontal (2295 tiles, 256 × 256 pixels) (a-c) and the frontal plane (858 tiles, 512 × 512 pixels) (d-g). a) The CH_3 vibrational bands highlighted the entire tissue including morphological aberrations from the tissue processing. Moreover, the CH_3 channel showed multiple areas consisting of multiple tiles with very low or zero signal. b) The CH_2 distribution in cells highlighted the lipid-rich regions in the cerebellum and the mesencephalon. Overlaying of the CH_3 (cyan) and CH_2 (magenta) channels revealed a large spatial mismatch (c). The CH_3 (d) and CH_2 (e) SRS images highlight a protein and a lipid distribution of a frontal plane section. The lipids were highly concentrated in the corpus callosum (white arrow) positioned above the hippocampus which contained a highly-concentrated area of cell nuclei with low SRS intensity (orange arrow). The CH_3 (cyan) and CH_2 (magenta) overlay resulted in a spatially matching stack on the whole organ scale (f). SRH image further highlighted the lipid distribution (magenta) in the tissue section with high contrast. Cell nuclei were not detected in the hippocampus. Moreover, slight signal loss was highlighted in the right-hand side hemisphere between the hippocampus and the thalamus.

The low intensity signal formed a dark line under the corpus callosum in the SRH brain image (Fig. 5.6g). The low intensity line in the hippocampus was expected to consist of spatially concentrated cell nuclei which were however not highlighted during the CH_3 – CH_2 image calculation. The failure to highlight these nuclei was caused by a spatial overlap misalignment by ~0-10 pixels. Partially, a false protein/DNA signal was detected in the right hemisphere between the thalamus and the hippocampus due to a slight change in the Z plane between the two vibrational scans of the sample and thus, it was not marked as an intrinsic tissue feature. It was concluded that highlighting nuclei in the whole-tissue through SRH was not feasible on the Leica SP8 SRS using the current hardware and software settings. A tile-stitching and tile-aligning script would need to be created in order to overcome this issue. However, this would have not been finished in time to meet the project deadline.

As well as these hardware and software issues, morphological warping and disintegration of the sample was also recognised as a potential problem. Tissue sections were prone to changes in structure during a time-demanding whole tissue imaging and thus resulted in an inaccurate and spatially mismatching CH_2 and CH_3 images. The perturbation of a lipid-rich brain tissue did not cause major structural changes due to its hydrophobic properties, however it was not clear whether the SRS microscopy in the solvent-filled imaging chamber would be applicable in other tissue types.

5.2.5. Effect of different solutions on tissue morphology

Mouse liver and kidney tissues were examined to determine whether this approach was feasible in less hydrophobic tissues. The effect of different water-based solvents in an imaging enclosure on sample integrity was also explored to assess which solution minimises structural damage of the sample whilst allowing SRS microscopy and the subsequent MSI.

Mouse liver and kidney tissues were cryosectioned at 16 µm thickness, thaw-mounted on a 0.17 mm cover glass and dried. The tissue sections were then sealed in an aqueous enclosure filled with either water or PBS. Alternatively, tissue cryosections were dried and attached to a microscopy glass slide (1 mm) using a Prolong Gold mounting medium. Liver tissues broke down during all mounting

attempts in an aqueous imaging chamber and hence were considered unsuitable for aqueous imaging while kidneys were successfully mounted. Therefore, mouse kidney samples were scanned at CH_3 and CH_2 vibrational frequencies (2945 cm^{-1}, 2866 cm^{-1}) at a single position. The high-resolution images (1024×1024 pixels) were acquired at a 227 nm pixel size and a 2.4 µs pixel dwell time. The SHG channel was used to capture the distribution of collagen.

Tissue sections submerged in water showed overall low SRS signal intensity accompanied by a low spatial contrast in CH_3 image (Fig. 5.7a) and more so in CH_2 image (Fig. 5.7d). Despite a low-speed scan, the images contained increased noise. Tissue imaged in PBS solution exhibited increased overall SRS signal and spatial contrast (Fig. 5.7b,e) in comparison with the images of water-submerged tissue sections. The Prolong Gold mounting medium introduced additional signal in the CH_3 SRS image (Fig. 5.7c). Nonetheless, the SRS signal contribution from the mounting media was minor in the CH_2 SRS image owing the low CH_2 signal observed outside the tissue section at the bottom right corner of the image(Fig. 5.7f). Tissue swelling, during which the tissue increased in volume was considered as the main reason behind the poor SRS signal in the water-submerged sample.

The tissue structure was cohesive and tightly arranged in the PBS and mounting medium samples and less so in water-submerged samples, which supported the hypothesis that tissue swelling had occurred. The tightly packed morphology of the sample likely enabled the observation of nuclear structures in a form of low-intensity circular regions (d = 6 µm – 10 µm). The nuclear information was however obscured in the water-immersed sample. Fine capsules surrounding groups of nephric cells were discernible in the CH_3 SRS image of the water-submerged mouse kidney. These structures were likely visible because of a partial tissue break down and swelling.

It was hypothesised that the hypotonic water environment caused sample swelling which increased the concentration of water molecules in the sample and conversely reduced the concentration of the biological material in a single optical plane and thus reduced the SRS signal of CH_3 and CH_2 bonds. Potentially, the swelling spatially displaced the fine tissue structures which facilitated their detection.

CH_3 – CH_2 (Fig. 5.6g-i) and CH_3 – CH_2 – CH_2 (Fig. 5.6j-l) image subtractions were applied and overlaid with CH_2 and SHG images to generate SHG images with the aim to highlight nuclear distribution and protein content (cyan), lipid content (magenta) and collagen (yellow) of predominantly epithelial cells arranged into renal tubules across the mouse kidney section. The SRH images of water-submerged kidney sections (Fig. 5.6g,j) captured the chemical information in a periductal region of a mouse kidney based on the strong SHG-intensity structure followed by an intraductal region, which was devoid of SHG and SRS signal. The image subtraction in water-submerged kidney sections showed no clear distinction between nuclei and cytoplasm. Instead, the subtracted SRS signal further highlighted fine structures encapsulating the individual tubules in the tissue, which was only accented by a second subtraction with the CH_2 signal (Fig. 5.6j). These structures anatomically resemble basal lamina to which the endothelial cells adhere to.[274] Basal lamina consists of laminins and collagens[275] which were detected using SRS at high intensities in the CH_3 vibrational band, but not in CH_2, which is more represented in lipids. Furthermore, collagen can be detected using SHG owing to their non-centrosymmetric structure.[127] The thickness of the basal lamina falls below the resolution limit standard laser scanning microscopes. Owing to SRH, it was possible to detect the putative submicron-sized basal lamina using SRS. The presence of collagen in these structures was not confirmed using SHG – likely due to a combination of a noise and a tissue autofluorescence which were also detected using the SHG photomultiplier tube (PMT).

SRH of PBS-submerged (Fig. 5.6h,k) kidney section resulted in improved nuclei (cyan) and cell cytoplasm (magenta) distinction. Furthermore, the second CH_2 subtraction resulted in better resolved separation between cytoplasmic and nuclear signals, albeit at a loss in the tissue pixel intensity of the subtracted channel (Fig. 5.6k). SRH (cyan) did not capture the presumable <100 nm-thin basal lamina. However, a large structure spanning vertically across the captured image was observed with SRH (cyan) and SHG (yellow). The structure was enveloping a long tubule and was considered to contain collagen due to the strong SHG signal.

The twice CH_2 subtracted SRH image of murine kidney tissue mounted in ProLong Gold also resulted in stronger nuclei-cytoplasm separation than the single-subtracted SRH image (Fig. 5.6i,l). The CH_3-CH_2(-CH_2) subtraction did not result in improved nuclear signal in contrast with the PBS sample in Fig. 5.6.k, despite the

above mentioned CH_3 SRS signal contribution from a glycerol-based mounting medium, which decreased the contrast between the tissue and the off-tissue SRS signal. Furthermore, the SRH image subtraction further exacerbated and highlighted a signal originating from the mounting medium outside the tissue (Fig. 5.6l) in addition to the unexpectedly poor improvement to nuclear signal separation.

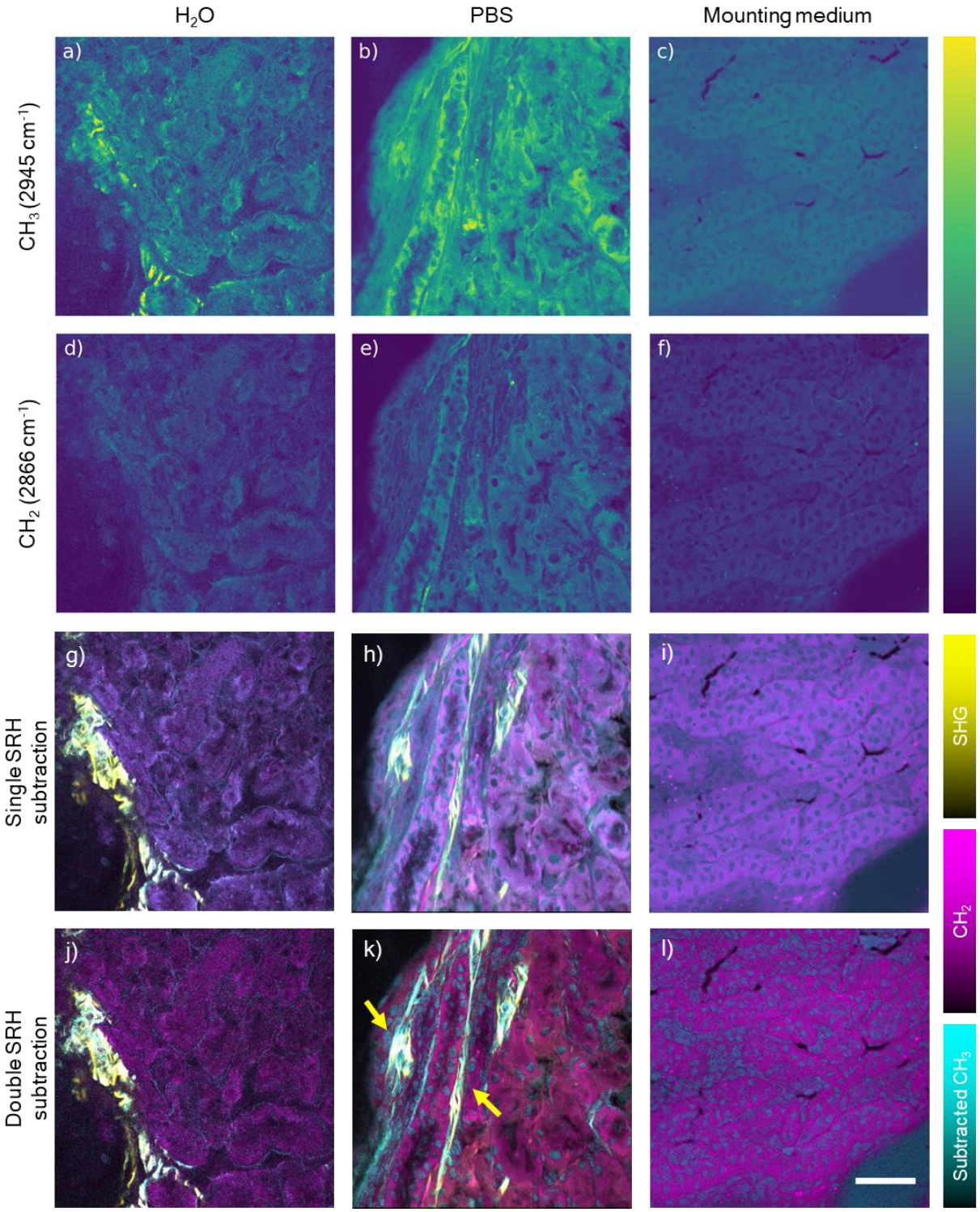

Figure 5.7 Effect of optical media on a kidney morphology. CH_3 (a-c) and CH_2 (d-f) SRS microscopy images of 16 µm kidney cryosections depict the difference in signal intensity, contrast, and sample morphology in H_2O (a, d), PBS (b, e) and a glycerol-based mounting agent (c, f). Water-submerged sample data showed low signal intensity in both SRS images (a, c). Kidney sections submerged in PBS showed increased signal intensity and strong contrast in both CH_2 and CH_3 images (b, d). ProLong Gold mounting medium introduced a homogeneous signal in addition to tissue CH_3 signal (c). The mounting medium signal was not observed in the CH_2 image (f). SRH images were created by combining CH_3-CH_2 (g-i) and CH_3-CH_2-CH_2 (j-l) SRS image subtractions (cyan) which were overlaid with both CH_2 SRS signal (magenta) and SHG signal which highlighted collagen structures (yellow). Image subtraction in water samples did not result in detection of nuclei in the sample. However, ultra-thin protein-based capsules were resolved in both single (g) and double (j) subtracted images. Single subtraction SRH images of PBS-submerged kidney (h) did not result in separation between the cytoplasm and nuclei. However, twice subtracted data generated a strong contrast between the two (k). SHG and subtracted protein SRH signal highlighted large vertical collagen capsules around the kidney tubules. CH_3-CH_2 subtraction in a ProLong Gold-mounted sample did not increase the pixel intensity of cell nuclei (i). The second CH_2 subtraction further highlighted the off-tissue mountant signal (l). Scale bar = 50 µm.

The same kidney cryosection samples were scanned with transmission SRS (2945 cm^{-1}) and epi-SHG along the Z-axis to explore the relationship between SRS signal quality, tissue morphology, tissue swelling, and solvent tonicity.

The H_2O kidney 3D render of the Z-stack was focused on a putative blood vessel and the surrounding, mostly cellular tissue (Fig. 5.7a). The frontal view (top) showed the distribution of the collagen (SHG) which was masked by a signal intensity of a CH_3 signal at the blood vessel wall. The signal intensity and morphological integrity of the surrounding cellular tissue was poor, which was consistent with the finding in the 2D image. The side view (bottom) showed the Z profile of the tissue reached 60 µm as opposed to the original 16 µm thickness. Moreover, the interface between the water solvent and the tissue edge was poorly defined, which was likely an effect of tissue swelling. The swelling-associated poor SRS signal was predominantly intrinsic to a cell-occupied tissue area, but not the less soluble duct wall. Similarly, to the 2D study, replacing H_2O with PBS resulted in an improved SRS intensities and improved the detection of morphologically distinct features in the 3D CH_3 SRS image data (Fig. 5.7b). Based on the Z-profile, the maximum thickness of a sample in a PBS solution that could be imaged successfully was ~30 µm. Albeit the tissue was sectioned at 16 µm thickness, the approximately doubled increase in tissue depth was a substantial improvement of tissue swelling in comparison with the water-submerged kidney sample. Furthermore, the side view of the 3D render showed the well-defined edges of the kidney cells and a collection

duct (yellow arrow), both of which appeared similarly thick. In agreement with the 2D images, cell nuclei (white arrows) were discernible from the rest of the biological matrix in the 3D render of the kidney section in PBS. The overall SRS intensity in a 3D image render of a dry mouse kidney cryosection in a mounting medium surpassed the signal intensity in PBS at lower contrast (Fig. 5.7c). Cell nuclei were again well discernible from the low signal circular regions spread across the tissue (white arrows). The Z profile averaged at a thickness of 10-13 µm, which led us to believe that the section had potentially shrunk during sample drying and during the Prolong Gold mounting medium curing process, which is known to dehydrate and compress the sample. Finally, the sample was uniformly flat and therefore considered least perturbed by the optical medium. Furthermore, the kidney tissue section was condensed and hence considered as an ideal sample for a large area SRS imaging analysis which relies strongly on signal intensity and contrast in autofocusing. However, this sample preparation method would render the samples inapplicable for MALDI MSI.

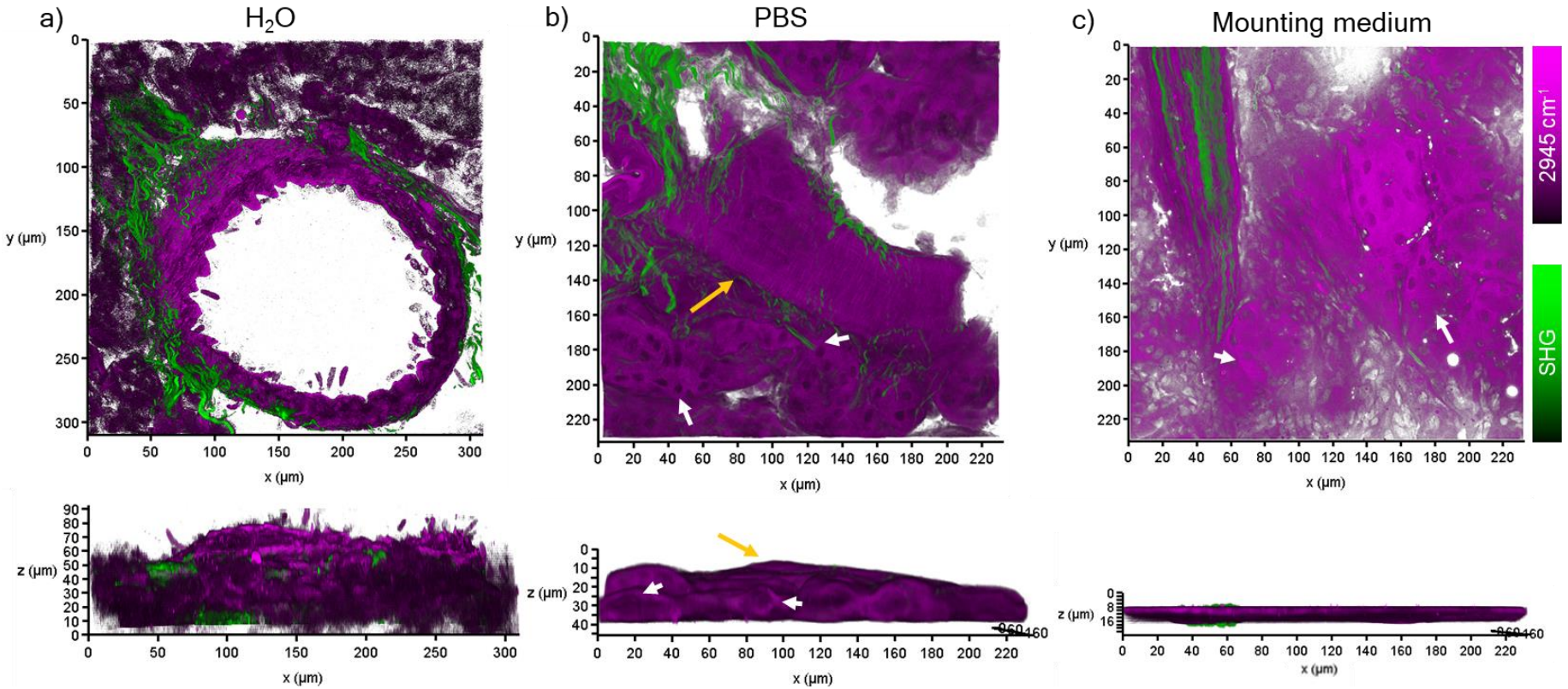

Figure 5.8 3D analysis of tissue in various optical media. Z stacks of CH_3 (2945 cm^{-1}) SRS (magenta) and SHG (green) images of mouse kidney cryosections (16 µm) were generated to probe the 3D morphology of tissue in water, PBS, and mounted in a glycerol-based medium. The 3D renders were captured from front and side views (top, bottom) in the LAS X software. a) Kidney blood vessel walls and presumably endothelial cells were captured in the water sample. The blood vessel walls encapsuled by collagen were concise with strong SRS signal, whilst the cell-dominated tissue area, which surrounded the blood vessel, exhibited overall low SRS intensities. The side view revealed a large delocalisation of the sample in the vertical direction and a ~60 µm optical thickness of the sample. b) PBS-immersed sample images showed an improvement in the SRS signal intensity and the contrast. Moreover, cell nuclei were observed in a form of low intensity spots (white arrows). The SRS signal intensity between the collagen-encapsuled duct (yellow arrow) and the cell mass was identical. The maximum sample thickness was 30 µm. c) Sample mounted ProLong Gold appeared to show overall higher SRS intensity. In conformity with (a) and (b) 3D data, the ROI consisted of cells tissue and a collagen-rich duct. Low-intensity circular spots were recognised as cell nuclei (white arrows) corresponding to the PBS sample. The overall average thickness of the sample measured in the Z-stack side view (bottom image) was approximately 10-13 µm. Unlike previous images, the tissue section was uniformly flat.

Although the spectral information remains largely unaffected, hydrating samples with either water or PBS may result in further risks in downstream MALDI applications. Water introduced less MALDI MSI-interfering chemical species, which was preferable for precise MSI measurements. However, the introduction of water resulted in tissue swelling which in turn rendered SRS analysis inefficient. This was most prevalent in SRH due to tissue displacement and deterioration which resulted in a poor SRS intensity and contrast. Although PBS caused tissue swelling into an abnormal thickness (~30 µm), the sample was 2× less delocalised in the Z dimension with minimal tissue displacement. Moreover, the extracted SRS information was sufficient for determination of nuclear distribution in the SRH experiment, where the PBS-submerged sample slightly outperformed the otherwise unperturbed ProLong Gold-mounted sample.

The use of Prolong Gold in the SRS-to-MSI analysis was not possible and therefore served as a reference sample. Since the refractive index of Prolong Gold was 1.46, the laser was likely focused deeper on the sample, which was unlikely the cause of tissue section compression. The compression was a result of Prolong Gold drying with the cover glass pressing down on the tissue section. The glycerol and other organic components of Prolong Gold were contributing to the total SRS signal intensity of CH_3 and CH_2 vibrational modes based on the CH_3 and CH_2 signal outside the tissue.

Despite the Prolong Gold SRS signal, SRH was successfully applied in highlighting protein and nuclear distribution in the sample by subtraction of a CH_3 image with a CH_2 image. This proved suitable in the brain tissues, which were lipid rich (i.e., strong CH_2 SRS band), but not in kidney tissues. Using CH_2 subtraction again resulted in stronger suppression of the cytosolic and extracellular protein signal and a further separation of a nuclear signal at a cost of reduced SRS signal in murine tissues and This approach was more suitable for kidney tissues.

In summary, it was determined that the use of wet tissue cryosections in PBS results in the best possible spatial resolution, and SRS signal intensities which were suitable for SRH and a subsequent MALDI MSI analysis.

5.3. Application of conductive materials on glass slide surfaces

Conductive materials and MALDI matrix, which are essential requirements for sample ionisation in MALDI MSI. In Chapter 5.2., it was shown that conductive components adversely interfered with the SRS signal and lead to conductive material melting. Therefore, conductive elements cannot be present in the SRS laser beam pathway. To overcome this issue, this work describes methods to generate the SRS data first and follow with MSI. The samples analysed by SRS, were mounted on a borosilicate cover glass without any conductive materials. To present conductivity, two methods for conductive material deposition on a sample were explored – a) conductive tape-supported MALDI analysis[183] and b) desorption ionisation using through-hole alumina membrane (DIUTHAME)[185,187,276]. Wu *et. al.* developed a procedure for MALDI analyses of formalin-fixed paraffin embedded brain tissue sections mounted on a glass slide with a conductive tape. In this paper, a copper tape was adhered to the reverse side of the glass slide after paraffin removal to support and direct the charge dissipation and the direction of the ion flow. The sample was then coated with MALDI matrix and successfully used for protein imaging analysis in the *m/z* 2500 – 35000 range with a Bruker Autoflex Speed MALDI TOF/TOF.[183]

5.3.1. Copper-tape glass slide modification in MALDI

The utilisation of insufficiently conductive surfaces could lead to a surface charging effect. A surface charging effect occurs in MALDI MS experiments in positive polarisation, where the negative charge in a form of photoelectrons does not dissipate efficiently, which leads to a negative charge build-up and results in a positive mass shift in mass spectra.[277] Adopting this methodology, a MALDI MSI experiment using non-conductive glass slide was performed in order to determine whether the conductive tape would successfully replace conductive glass slides. A mouse brain cryosection was thaw-mounted onto a 1 mm-thick SuperFrost® microscope glass slide and coated with a layer of αCHCA matrix using the HTX TM-Sprayer. After drying, the copper tape was adhered to the opposite side of the slide, and overhangs on each side of the tape were folded around the edges and attached

to the front of the glass slide without touching the biological sample. The overhangs were in place to ensure good contact between the conductive tape and the rest of the conductive sample holder (Fig. 5.9a).

Single-point MALDI mass spectra between *m/z* 100–1000 were acquired from the brain tissue at a 1 Hz and a 2 kHz ionising laser repetition rate, with the laser power attenuator set to 30%. The very low (1 Hz) laser repetition rate was used in addition to the 2 kHz repetition rate used by Wu *et. al.* since a surface charging effect was expected. The very low repetition rate spectrum showed a large number of ions in the *m/z* 100 – 400 range. A low number of ion peaks was detected in the *m/z* 600 – 900 range. At a standard laser repetition rate (2 kHz), the total number of auto-detected peaks and their overall ion intensity decreased (Fig. 5.9b). This finding suggested that low repetition rate improved the ionisation efficiency. However, a 20-fold decrease in raster scanning speed would not be practical in MSI experiments since it would extend data acquisition of large samples to multi-week experiments.

MALDI mass spectra captured from the copper tape-enhanced slide were compared with mass spectra acquired from a mouse brain tissue mounted on a conductive Intellislide in an absence of a copper tape. The mass spectra from the Intellislide mounted sample showed increases in the number of detected ions and their intensities in comparison with the SuperFrost-copper tape samples. In agreement with the spectra from a copper tape-modified sample, the increase in laser repetition rate (1 Hz → 2 kHz) resulted in a decrease in the overall ion intensity, albeit the number of peaks detected under both laser conditions did not change (Fig. 5.8c). The determination selection and assignment of the ion peaks in all of the scans was achieved using the automated peak finding function and saved as mass lists in Bruker flexAnalysis software. Mass lists were rounded to integers. A Venn diagram was used to contextualise and visualise the unique peaks of the individual mass lists and also their intersections, which showed common mass peaks between the different mass lists. The resulting diagram (Fig. 5.9d) showed the Intellislide data from 1 Hz and 2 kHz share most of the detected peaks, albeit 40 unique peaks were detected at the low firing speed. Interestingly, the standard repetition rate data from an Intellislide sample showed 17 unique peaks. The increased laser repetition rate also negatively affected the number of ions detected in samples mounted SuperFrost slides with a copper tape. Moreover, 11 unique peaks were observed in the standard repetition rate SuperFrost sample. The large number of ions detected in low laser

firing speed experiments was expected to be due to a prolonged time between the individual pulses for an ion-suppressing charge dissipation. The unique ions which were found in the 2 kHz repetition rate data suggested the peak picking process was not suitable for this analysis. Upon closer examination of spectral data, a spectrum shift was observed. The *m/z* 222 peak reached a maximum at *m/z* 221.984 at a 1 Hz acquisition mode on the Intellislide. This peak was observed at *m/z* 222.054 in the 2 kHz Intellislide data. This peak was detected at *m/z* 222.486 and *m/z* 222.711 in the copper-taped glass slide sample at a 1 Hz and 2 kHz laser fire speed (Fig. 5.9e).

Moreover, the full width at half maximum (FWHM) increased with the increase of laser fire which was the broadest in the copper tape-modified samples. The positive spectral shift and peak broadening were potentially caused by a charging effect.[277] Shift correction with a calibration curve using peaks in multiple points across the spectrum was considered. However, the peak-picking algorithm was prone to large error because of a broad and “fuzzy” peak shape in the 2 kHz Cu tape samples. Despite a > 2× increase in FWHM (Fig. 5.9e), the copper tape application was successful in single point MALDI MS analysis Although this method underperformed and led to positively shifted mass spectra (i.e., with increased *m/z* values) in comparison with the Intellislide, spectral information about the chemical composition of a sample was extracted. The charging effect was likely causing a shift due to delayed ion extraction which then affected the ion separation in the TOF analyser, since the charging is quadratically dependent on the ion drift distance. This issue could be addressed and resolved using a trapping Fourier transform-based mass analyser (Orbitrap or FTICR), where the sampled ions are not separated over a given distance after a single point energy excitement. Instead, the ions in an FTICR unit are continually driven in a circular magnetic field and separated based on their oscillation frequencies. Therefore, trapping mass analysers would not be expected to be affected by a spectral shift, however, such an instrument was not available for use.

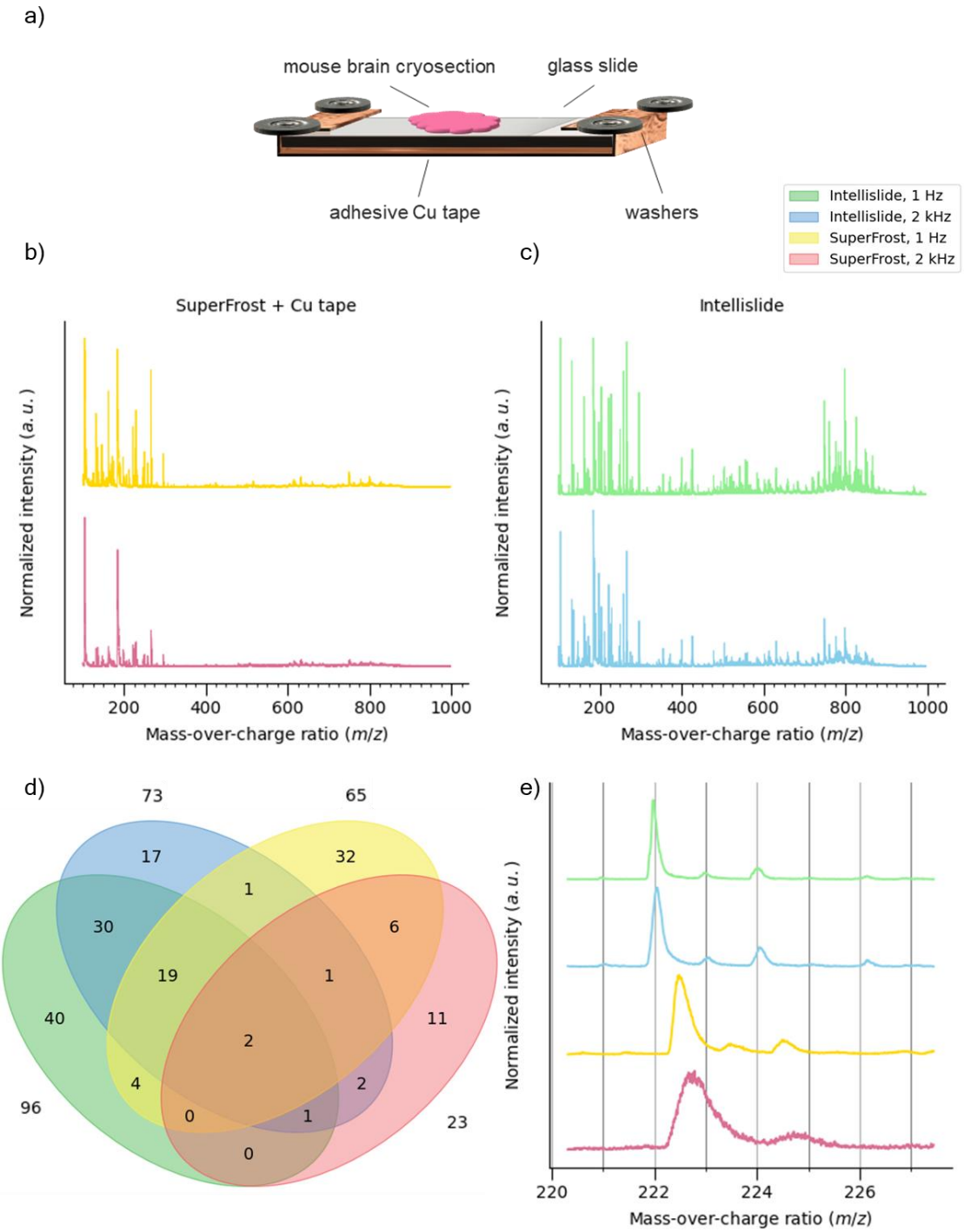

Figure 5.9 Single point MALDI MS of in brain tissues using a Cu-taped glass slide and an Intellislide. Mouse brain cryosection was thaw-mounted on a glass slide with a copper tape strip enveloping the backside of the slide and the edges to create a conductive contact between the sample holder and the glass slide (a). MALDI mass spectra were acquired between *m/z* 100-1000 in a copper taped glass slide (b) and in an Intellislide (c) at 1 Hz (top) and 2 kHz (bottom) ionising laser repetition rate. Unique and intersecting mass peaks shown in the b and c plots were visualised in a Venn diagram (d). The large amount of unique mass peaks in copper-taped samples led to a closer investigation of individual peaks. It was found that a positive spectral shift and increased FWHM were associated with the use of glass slide in combination with a copper tape (e).

The use of glass slides and copper tape were further evaluated for MALDI MSI using mouse cryosections to determine whether this method was suitable for raster scanned imaging experiments. To this end, a 12 µm sagittal mouse brain cryosection was thaw-mounted on a glass slide with copper tape. A brightfield image of the tissue was acquired using a TissueScout Reflecta scanner prior to αCHCA application and the MALDI MSI experiment (Fig. 5.10). The matrix coating was applied with the HTX TM-Sprayer at "Tissues" settings (see methods chapter for spraying details). The mass spectral window was limited to *m/z* 100 – 500 and the raster step size was set to 250 µm. Mass filters were set to *m/z* 185.45, *m/z* 266.112 and *m/z* 276.909 which highlighted three different regions of the mouse brain section on a false-coloured heat map. The data were correlated with Intellislide brain tissue data from a similar experiment where the spectral window was set to *m/z* 100 – 1500 and the spatial resolution was set to 200 µm. In agreement with the single point analysis (Fig. 5.9e), the selected peaks in the glass-copper tape sample were found to be positively shifted by ~*m/z* 1.1-1.6 in the data acquired on an Intellislide. Phosphatidyl choline head group (PCh), which was a phosphocholine fragment of phospholipids at *m/z* 184.29[278,279] (*m/z* 185.45) was detected in both samples, albeit in the Cu tape/glass slide-mounted mouse brain, the ion distribution was more uneven and at lower intensity.

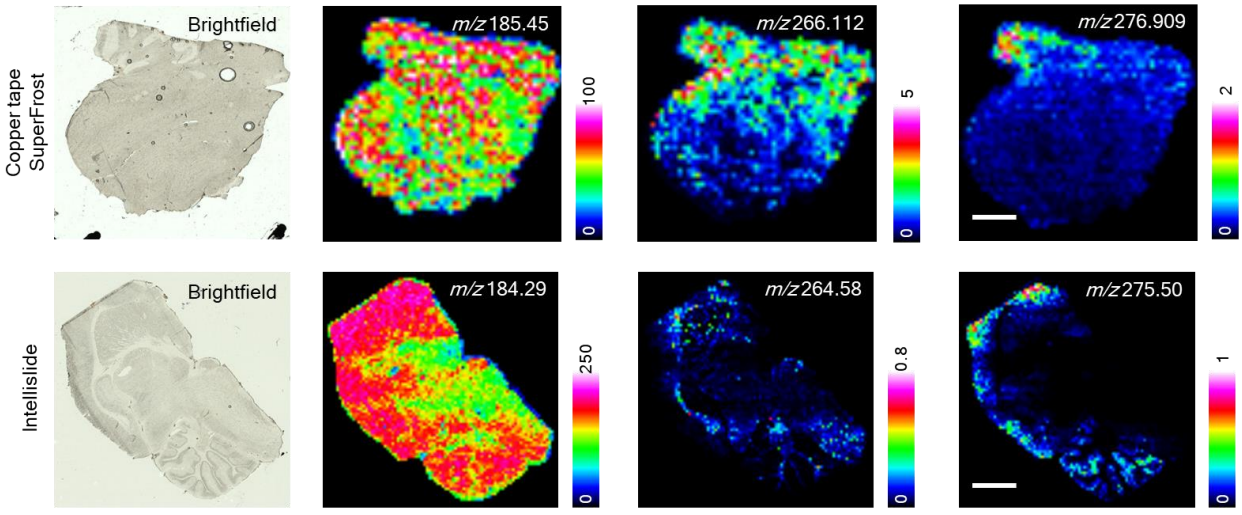

Figure 5.10 MALDI MSI comparison between a Cu-taped glass slide and an Intellislide in brain. Reference brightfield images of dried murine brain sections on a glass slide (top left) and on an Intellislide (bottom left) were acquired for MALDI sample registration. False-coloured heatmaps at a 250 µm (Cu tape/glass slide) and 200 µm (Intellislide) pixel size were generated for PCh (*m/z* 185.45, *m/z* 184.29) (2nd column), a white matter-associated ion (266.112*m/z*, 264.58 *m/z*) (3rd column) and a cortex associated grey matter ion (*m/z* 276.909, *m/z* 275.5) (4th column). Scale bars = 2 mm.

Similarly, the two ion heatmaps (at *m/z* 266.112, *m/z* 276.909) in the Cu tape/glass slide samples were poorer in spatial resolution in contrast with the Intellislide ion heatmap data (*m/z* 264.58, *m/z* 275.5). Note that the MALDI MSI data was not normalised, and each sample originated from a different study and therefore the sample processing and imaging conditions varied. Despite the incomplete dataset, it could still be concluded that copper tape was not a suitable alternative to conductive MALDI slides (e.g., Intellislide) mainly due to the observed positive spectral shift and the poor spatial resolution. Additionally, it is unsuitable due to the poor ion spatial distribution likely resulting from the surface charging effect on the slide, which was not observed in the conductive slide sample.

5.3.2. DIUTHAME as a candidate for SRS-to-MSI

Due to a putative poor ionisation efficiency of the copper tape application, it was concluded that current MALDI technology likely requires direct contact between a sample and a conductive surface, which is provided by the use of glass slides with conductive surfaces. Therefore, the use of surface-assisted laser desorption/ionisation (SALDI) was explored by applying a DIUTHAME.

DIUTHAME was examined as an alternative substrate to enable successful ionisation for MS detection, following SRS analysis. DIUTHAME was a surface-assisted laser desorption/ionisation (SALDI) commercially available adhesive substrate which utilizes an ultra-thin and porous membrane made from aluminium and coated with platinum oxides which interact directly with the biological sample on the face of the slide. The membrane pores were designed to extract the biomolecules from the sample onto the Pt-coated membrane surface which were coupled with a titanium frame ensuring complete charge dissipation during the sample ionisation via UV laser irradiation.[185] DIUTHAME offered advantages for robust data generation through the removal of the multi-step matrix deposition methods required for MALDI analysis, and also with the elimination of interfering background mass peaks arising from the matrix. There was no information regarding DIUTHAME membrane spectral characterisation in the low mass region (*m/z* 100 – 1500).[187] Therefore, a DIUTHAME plate was analysed on an UltrafleXtreme

TOF/TOF mass spectrometer to determine and characterise any background ions that may arise from the DIUTHAME membrane.

DIUTHAME was mounted on an empty cover glass which was on top of an Intellislide. This sample arrangement was necessary because the biological samples would be attached to a cover glass after the SRS analysis, which was planned to be executed prior to the SALDI MSI. (Fig. 5.11). An imaging TOF experiment in positive polarity was set up, where the DIUTHAME edge frame and membrane were analysed in the 100-1500 *m/z* mass range. A total of 1406 positions were acquired at a 200µm raster step size and 5000 shots per spot at maximum laser power.

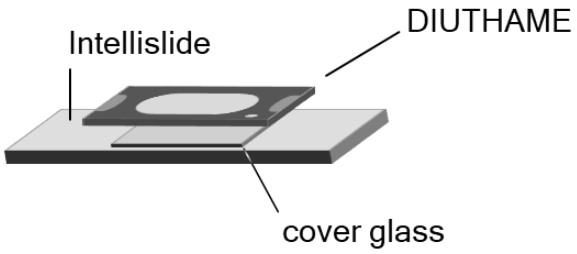

Figure 5.11 Sample schematic of a cover glass with an Intellislide and a DIUTHAME.

The area of ablation was clearly visible on the membrane surface (Fig. 5.12a). Average mass spectra of the membrane and the frame were extracted. The averaged spectra contained unknown low-weight ions were detected between 100 – 190 *m/z*. (full mass list shown in Appendix 5). These ions were described by the manufacturer as adhesive and bonding agent related ions. Furthermore, metal radical ion isotope patterns from the DIUTHAME membrane and the frame were detected. Single element platinum radical ions $[Pt]^{\bullet}$, $[Pt_2]^{\bullet}$, $[AlPt]^{\bullet}$, $[Pt_3]^{\bullet}$ were detected (Table 5.1, Appendix 6). The metal ions which were likely desorbed from the DIUTHAME surface dominated the mass spectrum (Fig. 5.12c). The ion intensity gathered from the frame edge area exceeded the membrane ion yield by greater than ten-fold based on the signal intensity measured in the platinum radical at *m/z* 194. Analysis of the data revealed a large difference (Δ) and an error in parts per million (ppm) between measured mass values and the expected masses. This error was most likely due to an error in the instrument calibration, during which standards spotted onto a steel plate were positioned at a different height than the DIUTHAME membrane surface. It also provided a different degree of conductivity.

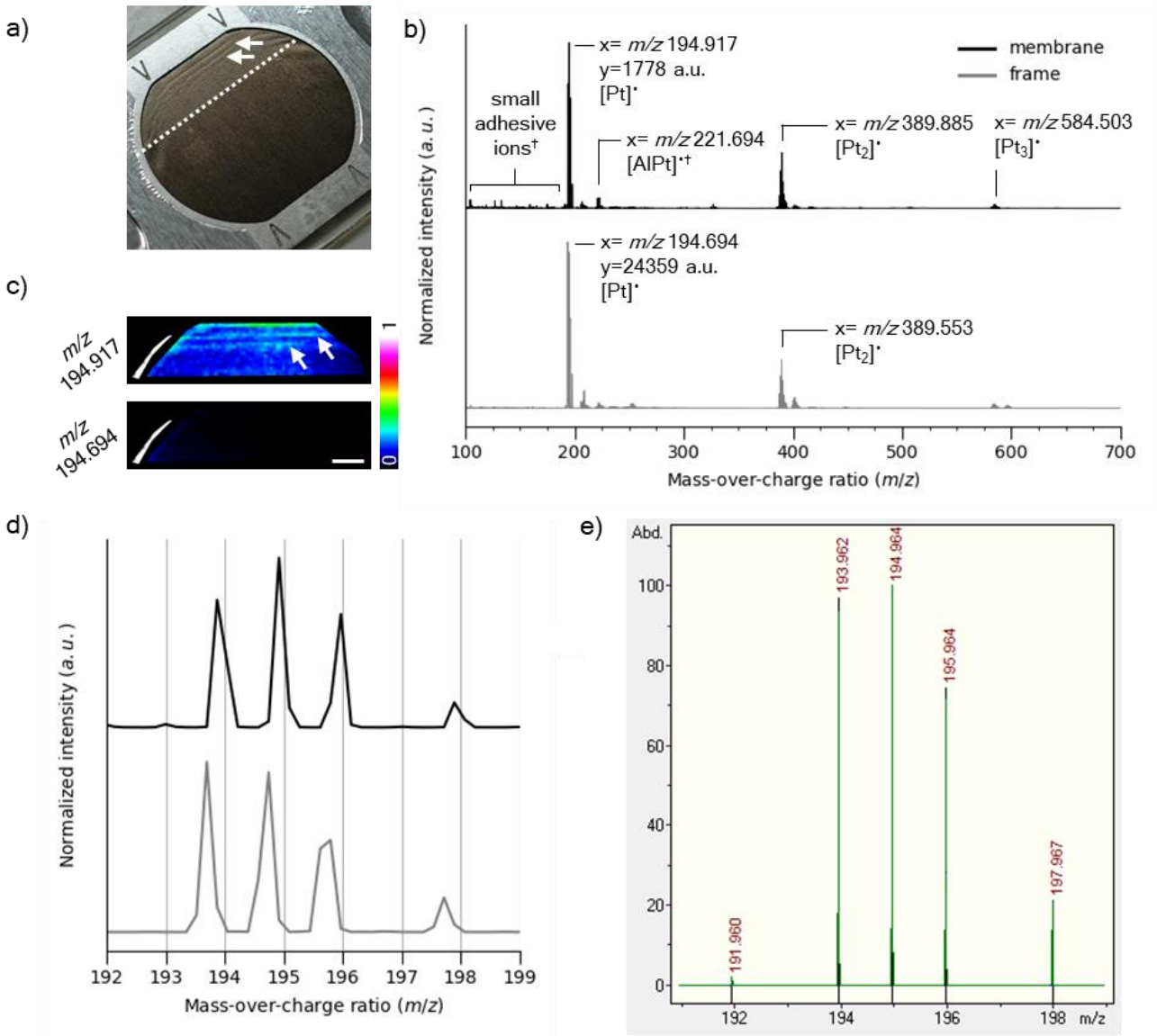

Figure 5.12 Analysis of background SALDI mass spectra of a DIUTHAME sample. a) DIUTHAME was placed on a cover glass and an Intellislide. A part of the DIUTHAME membrane and the frame were ablated by the ionising laser (above dashed line). b) The frame and the membrane were separated into ROIs and their respective voxels were averaged into single point spectra and cropped to *m/z* 100 – 700. The membrane spectrum captured small molecular weight ions (*m/z* 100 – 190). Both spectra captured strong presence of radical ion with *m/z* ≈ 0.3 spectral shift between a membrane and a frame. c) False-colour ion heat maps captured the *m/z* 194.917 and *m/z* 194.694 (± 0.1) ion distribution on a frame edge (saturated white streak) and a part of a membrane. Only *m/z* 194.917 captured the [Pt]• signal in the membrane ROI. Lines were observed in the membrane (white arrows) which corresponded to the ripples visible in the camera snapshot (a, white arrows). Scale bar = 2 mm. d) Negative spectral shift was confirmed in the zoomed in spectral window on a [Pt]• isotope pattern. e) Measured isotope pattern was confirmed in Bruker Compass IsotopePattern.

On examination of the signal homogeneity, false-coloured heatmap images with a mass filter set to *m/z* 194.917 ± 0.1 and *m/z* 194.694 ± 0.1 were generated using the Bruker flexImaging software. The frame and the membrane were separate by ROI cropping (Fig. 5.12c). *M/z* 194.917 imaging data showed strong signal in the frame region on the left of the image and ripples at the upper edge (white arrows) of the membrane at a lower signal intensity. These ripples were however likely caused by a movement of the cover glass between the DIUTHAME and the Intellislide (Fig.5.10a, white arrows). Furthermore, the ion peaks were spectrally shifted between the frame and a membrane by approximately 0.3 Da and therefore, the low intensity membrane $[Pt]^{\bullet}$ signal was poorly visible relatively to the frame at *m/z* 194.694. The 0.3Da negative spectral shift was further plotted in in mass spectrum window which focused on the isotope pattern of the platinum radical ion (Fig. 5.12d). The mass peak position acquired by the TOF instrument, and the peak isotope pattern matched with the reference isotope pattern provided by the Bruker Compass IsotopePattern software which provided sufficient confidence in the metal ion identification (Fig. 5.12e).

M/z	Molecular formula	Monoisotopic neutral mass	Δ(Da)	ppm
194.917	$[Pt]^{\bullet}$	194.965	0.048	246.198
221.908	$[AlPt]^{\bullet}$	221.946	0.038	171.213
389.885	$[Pt_2]^{\bullet}$	389.928	0.043	110.277
584.877	$[Pt_3]^{\bullet}$	584.893	0.016	27.355

Table 5.1 Radical metal ions in DIUTHAME membrane. Monoisotopic neutral masses were subtracted (Δ) from their correlating measured spectral data (*m/z*) and their respective parts per million error (ppm) was calculated.

The height difference between the membrane and the frame of DIUTHAME caused a small spectral shift (~0.3 Da). The additional measurement error shown in Table 5.1 was likely caused by the difference between sample carrier used for system calibration (steel plate) and Intellislide-DIUTHAME sample. Therefore, it was concluded that a difference in a surface distance and a conductivity-related charging results in a mass spectrum offset. The DIUTHAME spectrum was acquired at 95 %

of maximum laser power and thus it was highly probable that the contribution from the DIUTHAME membrane was reduced when analysing biological samples. The membrane provided a homogeneous signal apart from the rippled membrane which was caused by a movement of a cover glass attached by the membrane to the Intellislide. In biological experiments, these movements would not occur since the membrane would strongly adhere to the biological matrix, although ripples outside of the tissues may still occur.

In summary, the majority of the metal ion clusters were identified with high confidence. Although the majority of low intensity ions detected with the UltrafleXtreme instrument were not successfully assigned to known ions, they were recorded for future SALDI TOF background subtraction.

DIUTHAME has already been successfully employed in SALDI MS analyses of murine brain tissues at thicknesses >25 µm.[186,187] However, it was hypothesised that an analyte extraction from a thick tissue section could result in false positive close colocalisation of multiple ions, present in different layers of the tissue sample. Therefore, a best practice should be to prepare the thinnest possible tissue cryosections. This potential issue will become increasingly problematic as future MALDI/SALDI instrumentation reach improved spatial resolution. To determine whether the sample thickness could be reduced, a comparative experiment between thick (30 µm) and thin (12 µm) brain tissue sections were explored and then an extraction efficiency of the DIUTHAME was examined.

5.3.3. Evaluation of DIUTHAME in murine brain

GSK90/ponatinib was used as a probe for DIUTHAME extraction efficiency analysis. 30 µl of GSK90 (10 mM) was spotted on an Intellislide and dried. In a cryostat (-20 °C), a mouse brain was sectioned at 30 µm thickness and placed directly on the dried drug on an Intellislide without thawing. A DIUTHAME membrane was placed firmly onto the Intellislide with the tissue sample. Then, the full sample sandwich was thaw-mounted by pressing a finger against the reverse side of the Intellislide (Fig. 5.13a). A reference sample of a 12 µm cryosection of a murine brain along a horizontal axis was thaw-mounted on a second Intellislide in a cryostat (-20 °C). 30 µm and 12 µm thicknesses were used since these were both the

standard of practice in DIUTHAME SALDI MSI and MALDI MSI. Brightfield images were generated by the Reflecta scanner. The contrast of the brightfield image of the DIUTHAME sample was increased using Fiji ImageJ to improve the poor sample visibility caused by the membrane and the contrast of the reference sample was adjusted to match the DIUTHAME (Fig. 5.13b). White matter in SALDI samples appeared darker than the grey matter, whereas white matter in MALDI sample appeared light in contrast with the rest of the grey matter. An αCHCA matrix was deposited on the reference 12 µm sample using the HTX TM-Sprayer. The samples were analysed on an UltrafleXtreme MALDI-TOF instrument with 300 shots per spot at 2 kHz repetition rate with a UV laser attenuated to 35 % and 50 % of maximum power in MALDI and SALDI MSI, respectively. The system was set to a positive reflectron mode to capture ions in an *m/z* range 100 – 1500. The laser raster step size was 200 µm. The diameter of an individual spot was 50 µm which was ionised in a random pattern. A false-coloured heat map showed a distribution of $[PCh+H]^+$ by using an *m/z* 184.093 ± 0.2 mass filter window for both SALDI and MALDI sample.

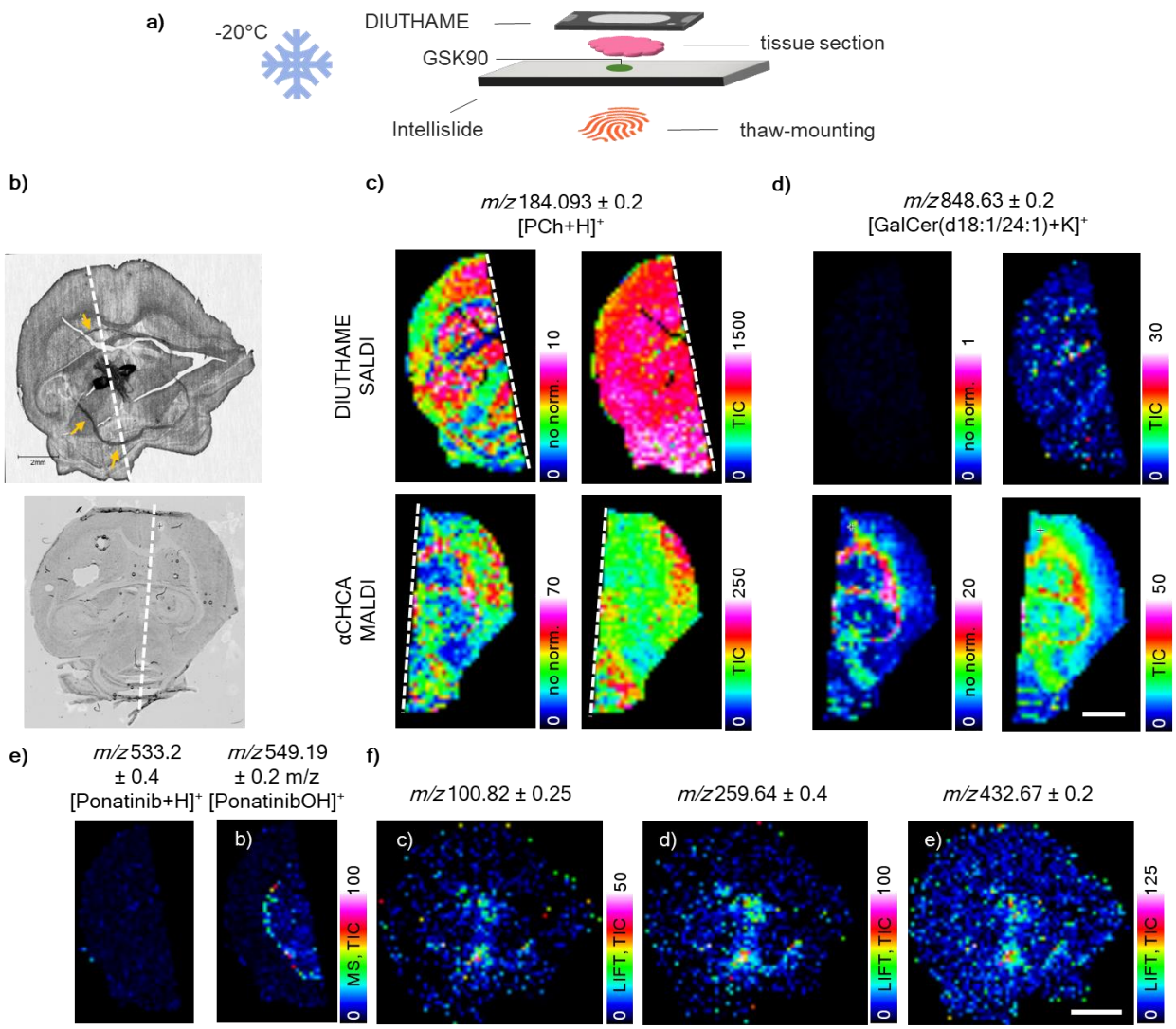

Figure 5.13 SALDI/MALDI comparison in brain tissues. a) SALDI (DIUTHAME) sample was prepared by spotting and drying of 30 µl of GSK90 (10 mM) on an Intellislide. A 30 µm tissue section was thaw-mounted between the Intellislide with dried drug and a DIUTHAME membrane. b) Brightfield images of brain sections (30 µm SALDI, 12 µm MALDI) were acquired. X marked the GSK90 position. White dashed line delimited borders of MS positive LDI MSI scans. Pseudo-coloured images of *m/z* 184.093 (c) and *m/z* 848.63 (d) values in SALDI and MALDI MSI capture the difference in ion distribution between data with and without TIC normalisation in two spatially distinctive chemical components. e) Pseudo-coloured images of 533.5 *m/z* data show no GSK90/ponatinib signal. A potential hydroxylated GSK90 ion was detected at 549.19 *m/z*. f) Three GSK90/ponatinib fragments (Chapter 4.3) were detected in a fragmentation imaging analysis (LIFT) Scale bars = 3 mm.

(Fig. 5.13c). The non-normalised SALDI brain image showed strong intensity of $[PCh+H]^+$ in grey matter of the cerebral cortex, the thalamus and a tentatively identified caudoputamen, whereas minimal signal intensity was observed in the lipid rich white matter, which consisted of corpus callosum and associated fibre tracts. On the other hand, MALDI analysis resulted in high intensity pixels in the white matter in the PCh-associated mass window and lower intensities in grey matter. Interestingly,

SALDI and MALDI imaging data of PCh showed inverse information about the ion distribution which was not anticipated. This phenomenon was possibly caused by three properties of lipids – solubility, viscosity, and ionisation efficiency. Lipid signal in DIUTHAME samples was affected by solubility and viscosity. The function of the DIUTHAME membrane depends on capillary forces extracting the liquid components of a biological sample and consequently the water-soluble components will reach the capillary surface more substantially than the highly viscous lipid components. Conversely, the extraction rate of lipids in MALDI is predominantly dependent upon their solubility in the selected matrix solvent (e.g., 70 % methanol), whereas a lipid extraction rate in water is much lower in comparison. However, lipids are prone to ionise more efficiently than other chemical components in the sample and thus result in higher signal intensities and seemingly higher concentrations. Consequently, lipids were considered as the major contributors to ion suppression effect (ISE) in MALDI MS.[178,180,252,255] Applying total ion current (TIC)[280] normalisation resulted in homogeneous ion distribution in both MALDI and SALDI $[PCh+H]^+$ images and partially corrected the ion intensity fluctuations caused by a heterogeneous lipid phase extraction and a lipid ISE. A V-shaped structural crack in a DIUTHAME tissue was used as a visual normalisation control since the area exhibited zero signal in both raw and TIC-normalised data. The ion tentatively assigned as Galactosyl ceramide $[GalCer(d18:1/24:1)+K]^+$ at *m/z* 848.630[281] was not observed in the non-normalised data of the SALDI sample. However, the ion was detected in non-normalised MALDI data. Upon TIC normalisation, the ion was observed in the SALDI data albeit with a very low intensity. The results in Figure 5.13d demonstrated that the slow capillary extraction rate of DIUTHAME had a more significant impact in SALDI then in MALDI whilst the increased ionisation efficiency of lipids had a major influence in the MALDI experiments.

The final part of this study was to investigate the extraction and ionisation of GSK90/ponatinib in brain tissues using DIUTHAME. Upon drying on the slide prior to the tissue thaw-mounting, GSK90 formed a “coffee ring”[272,282] (yellow arrows in Fig. 5.13a) – dried material deposit on the edge of the liquid phase. The expected GSK90/ponatinib ion at *m/z* 533.2 was not observed in the tissue sample in positive reflectron SALDI MSI. However, a strong signal at *m/z* 549.19, which was tentatively identified as a ponatinib hydroxylated metabolite,[283] was detected (Fig. 5.13e). This ion mapped to the edge of the coffee ring, but no signal was detected inside of the

ring. These results suggest that either most of a sample underwent hydroxylation and/or only the hydroxylated metabolite was extracted through the tissue into the DIUTHAME membrane as a result of the increased water solubility of the analyte after hydroxylation.[284]

A pseudo-MS/MS fragmentation experiment (LIFT) was set up to analyse fragments of ponatinib in the brain sample. The raster step size was set to 200 µm, where each point was scanned in a hexagonal geometry and 200 shots were fired per spot at 2 kHz frequency. The parent laser attenuator was set to 95 %, the fragment laser attenuator was set to 100 % and the parent ion *m/z* was set to *m/z* 549.19. Three peaks at *m/z* 100.82, *m/z* 259.64 and *m/z* 432.67 were generated which corresponded to the fragmentation pattern and the *m/z* values obtained for a standard of GSK90 as shown in Chapter 4.2 (Fig. 5.13f). Surprisingly, none of the observed peaks were hydroxylated. Moreover, the spatial distribution of these ions correlated with the distribution of the white matter in the brain and were not detected in the position of the edge of the coffee ring. Potentially, unmetabolised GSK90 with hydrophilic physicochemical properties was extracted through the white matter and partially through the DIUTHAME capillaries and was only detected via the high ionisation energy LIFT analysis. This hypothesis was supported by the known lipophilicity of GSK90 from the available physicochemical data (Chapter 4.1) and was confirmed in cell uptake study, where GSK90 strongly colocalised with cell membranes and other lipid bodies (Fig. 4.16).

5.3.4. Development of DIUTHAME application with improved analyte extraction

Solvent application was considered as an option to boost analyte extraction efficiency of the DIUTHAME membrane approach. Thus, solvent application was considered to improve the membrane-tissue adhesion in <12 µm tissues and therefore enable thin section SALDI MS imaging. To explore this, two solvent application methods were evaluated – solvent spraying and solvent droplet pipetting. A dry tissue section was also used in the experiment to determine whether DIUTHAME can be applied to tissues directly after an SRS analysis.

Two 12 µm murine brain cryosections cut along the horizontal axis were attached to Intellislides. One tissue section was attached to an Intellislide by thaw-mounting and subsequently dried on a bench. The DIUTHAME membrane was then carefully attached to the sample at a room temperature. The sample and the membrane were then sprayed over with a 70 % methanol solution using a HTX sprayer with a nozzle at 40mm distance from a sample at 75 °C, with a solvent flow rate of 0.12 ml/min and nozzle XY movement speed at 1200 mm/min, which passed over the sample 8 times with a 3 mm spacing (Fig. 5.14a). A second mouse brain slice was thaw-mounted on another Intellislide at room temperature followed by an adhesion of DIUTHAME membrane 100 µl of 70 % methanol was pipetted onto a DIUTHAME membrane (Fig. 5.14b), with the aim to examine whether DIUTHAME can be used for analyte extraction at room temperature following a potential SRS analysis.

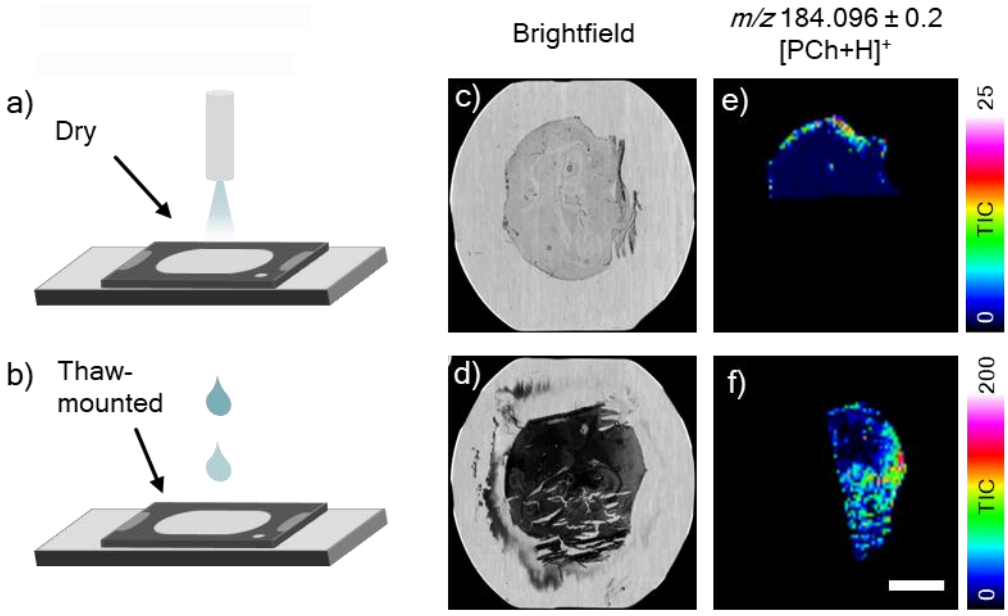

Figure 5.14 Solvent application in DIUTHAME. 12 µm mouse brain cryosections were thaw mounted on an Intellislide and whilst dry, attached to a DIUTHAME, 70 % methanol was raster-sprayed across the tissue (a). A second 12 µm mouse brain slice was thaw-mounted in a cryostat between an Intellislide and a DIUTHAME followed by deposition of two 50 µl droplets of 70 % methanol (b). Brightfield images were captured for sample registration in the mass spectrometer (c-d). Heatmaps of the $[PCh+H]^+$ (*m/z* 184.6) showed signal in sample edges in the matrix-sprayed sample (e) and across approximately half of the scanned area for the droplet application (f). Scale bar = 3 mm.

Brightfield images of the samples acquired by a Reflecta scanner showed an intact murine brain section which underwent solvent spraying (Fig. 5.14c), and a partially damaged mouse brain section which darkened during solvent drying.

Delocalised colour was also observed outside of the tissue perimeter (Fig. 5.14d), which suggested the solvent delocalised some components of the tissue. The discolouration was likely caused by a prolonged interaction between the DIUTHAME membrane, methanol, and the tissue. The mass spectrometer detection window was set to *m/z* 100 – 1500 acquisition window at a 200 µm raster step size and 300 laser shots per spot in positive reflectron mode in agreement with the settings of LDI MSI data acquisition depicted in Figure 5.15. LDI MSI data were TIC-normalised. The DIUTHAME extraction efficiency in this sample preparation procedure was evaluated by using a false coloured heatmap which highlighted the distribution of the $[PCh+H]^+$ by setting a mass filter window to *m/z* 184.096 ± 0.2. The solvent-sprayed sample resulted in a strong intensity response on the tissue edge but no $[PCh+H]^+$ signal was found deeper in the tissue (Fig. 5.14e). This result suggested that DIUTHAME only attached at the tissue edges meaning this solvent spraying approach did not generate enough pressure or contact with the DIUTHAME membrane surface to properly adhere to the 12 µm-thick tissue section. Although the second brain tissue underwent solvent administration by pipetting, which introduced a large volume of liquid, $[PCh+H]^+$ was detected heterogeneously in the scanned brain area (Fig. 5.14f). The pipetting approach was not further investigated due to visible delocalisation and physical displacement of tissue components. Additionally, cracking of the sample was observed in the brightfield image.

In summary, DIUTHAME appears not to adhere to a 12 µm-thin cryosection, and solvent application does not sufficiently improve the membrane-tissue adherence and analyte extraction. Therefore, a contact between the tissue cryosection and the DIUTHAME membrane is essential for successful analyte extraction in a SALDI experiment.

To determine what the minimum thickness Is needed for a successful SALDI MSI experiment, the murine brain cryosectioning thickness was increased to 16 µm. 30 µl of GSK90 (10 mM) was also pipetted on the Intellislide surface to observe the effect of solvent spraying on sample extraction. In a cryostat (-20 °C), mouse sections were carefully transferred on Intellislides and sealed with DIUTHAME from the opposite end (see Fig. 5.13a). Samples were thaw-mounted and analysed on the UltrafleXtreme with identical acquisition settings as in the previous paragraph. A brightfield image captured the morphology of the brain tissue section (Fig. 5.15a).

A large crack was observed spanning diagonally across the brain tissue section, which was a commonly observed tissue freezing artifact. $[PCh+H]^+$ and [GalCer/ (d18:1/24:1)+K]$^+$ ions were selected to contextualise the entire brain and the white matter, respectively (Fig. 5.15b). In non-normalised data, the $[PCh+H]^+$ signal was absent in the white matter brain regions in agreement with the prior 30 µm brain section analysis (see Fig. 5.13c). The $[PCh+H]^+$ signal homogeneity increased when the TIC normalisation was applied. The [GalCer/+K]$^+$ ion intensity appeared disparate across the section in the non-normalised data. However, TIC normalisation equilibrated the ion intensity across the tissue. The observed ion gradient across the tissue was most likely caused by an uneven DIUTHAME membrane adherence and/or extraction. Additionally, an ion suppression effect from the lipid ions may also be contributing to this observation.[178].

After the first analysis, the sample was sprayed on with a 0.2 % TFA in 70 % methanol at 65 °C, 0.12 ml/min flow rate, 1450 mm/min nozzle XY speed and with 4 passes. TFA was newly applied in this process because it was hypothesised the acidic solution can improve the generation of protonated adducts like it does in MALDI experiments. Samples were analysed with the mass spectrometer at the same settings and with a 100×100 µm spatial offset to avoid ablating/analysing already ablated spots from the previous analysis and thus creating false negative voxels. Solvent application resulted in a homogeneous distribution of the $[PCh+H]^+$ in the non-normalised data. Furthermore, the $[PCh+H]^+$ ion was detected in tissue edges and in a cerebellum after TIC normalisation. Interestingly, the solvent spraying resulted in an improved [GalCer/+K]$^+$ distribution in the white matter (Fig. 5.13c). Unexplainably, the $[PCh+H]^+$ distribution was delocalised in contrast with the TFA-free sample. Conversely, the ion yield and spatial contrast of the [GalCer/+K]$^+$ improved and thus suggested that TFA spraying improved lipid extraction in the white matter region. The drop in the $[PCh+H]^+$ intensity was likely an effect of an enhanced solvent-mediated lipid species extraction. Increased lipid concentration on a membrane surface would have likely resulted in an ISE through an increased competition over ionising energy between different types of lipids.[178]

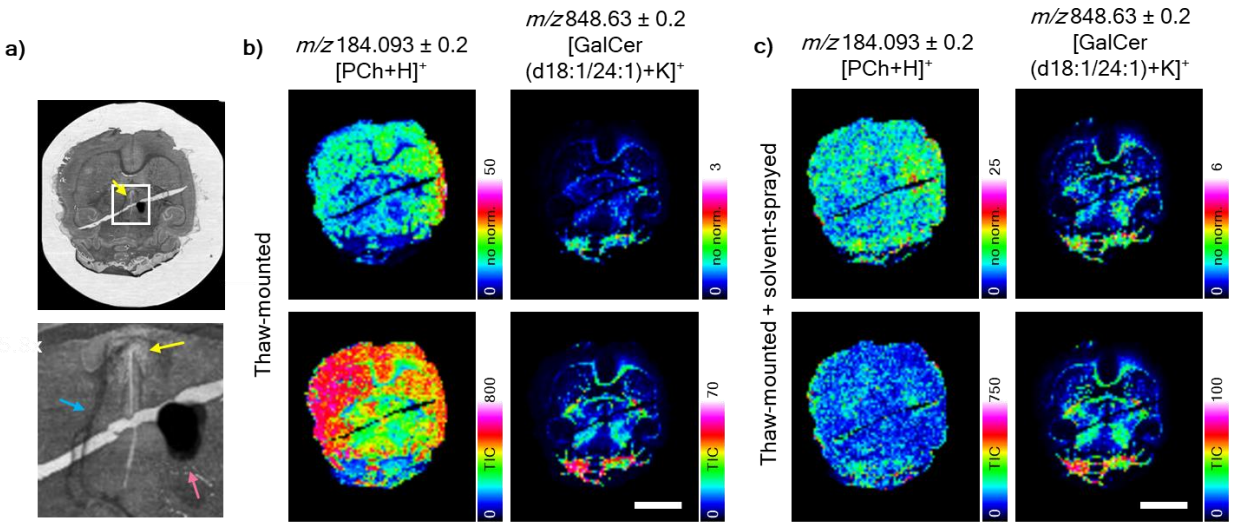

Figure 5.15 Evaluation of the solvent spraying effect on extraction of tissue components and the impact on SALDI MSI. a) A full tissue image and a zoomed-in image of the 16 µm-thin horizontal mouse brain tissue section capturing the centre spot of GSK90 deposition (red arrow), the GSK90 coffee ring border (blue arrow) and a tentatively identified third ventricle (yellow arrow) were acquired. b) False-coloured heatmaps of $[PCh+H]^+$ (*m/z* 184.093 ± 0.2) and ceramide (*m/z* 848.63 ± 0.2) of DIUTHAME-thaw-mounted brain tissues revealed a spatially exclusive relationship between these ions in thaw-mounted samples after a SALDI MSI analysis. c) TFA-methanol solvent was applied on the same sample and the data was reacquired. False-coloured heatmaps of $[PCh+H]^+$ (*m/z* 184.093 ± 0.2) and $[GalCer/+K]^+$ (*m/z* 848.63 ± 0.2) of DIUTHAME-thaw-mounted brain tissues revealed a spatially exclusive relationship between these ions in thaw-mounted samples. TIC normalisation corrected raw ceramide ion data which appeared gradually offset along a vertical axis. Scale bars = 3 mm.

The hyperspectral image data were flattened through voxel averaging from all scanned positions into a single spectrum per sample in TIC-normalised data in order to examine spectral variation induced by TFA deposition. The results show increase in the total ion yield in the DIUTHAME sample treated with a 0.2 % TFA in contrast with the DIUTHAME-only in both the small molecule region (*m/z* 100 - 350) (Fig. 5.16a) and in the lipid region (Fig. 5.16b) of mass spectra. The $[PCh+H]^+$ (*m/z* 184.093) was the most prominent peak in the DIUTHAME only spectrum. In agreement with the $[PCh+H]^+$ heatmap, relative intensity of PCh decreased in the second analysis after TFA spraying. A peak-picking algorithm was used to generate mass lists capturing *m/z* values of mass peaks. Extracted mass lists from mouse brain tissues analysed with DIUTHAME in TFA-free environment contained a total of 37 ions and the TFA-treated DIUTHAME sample contained 204 distinct ions. The samples intersected in of 36 common ions. A single unique ion was found in the TFA-free DIUTHAME mass list and 168 unique ions in a TFA-treated DIUTHAME mass list (Fig. 5.16c). Caution must be applied as these results may vary depending

on the mass filter setup and peak picking parameters. Prolonged hydration of the sample and the introduction of the proton donor, TFA. was considered the main cause of the observed increase in the number and the intensity of the ions.

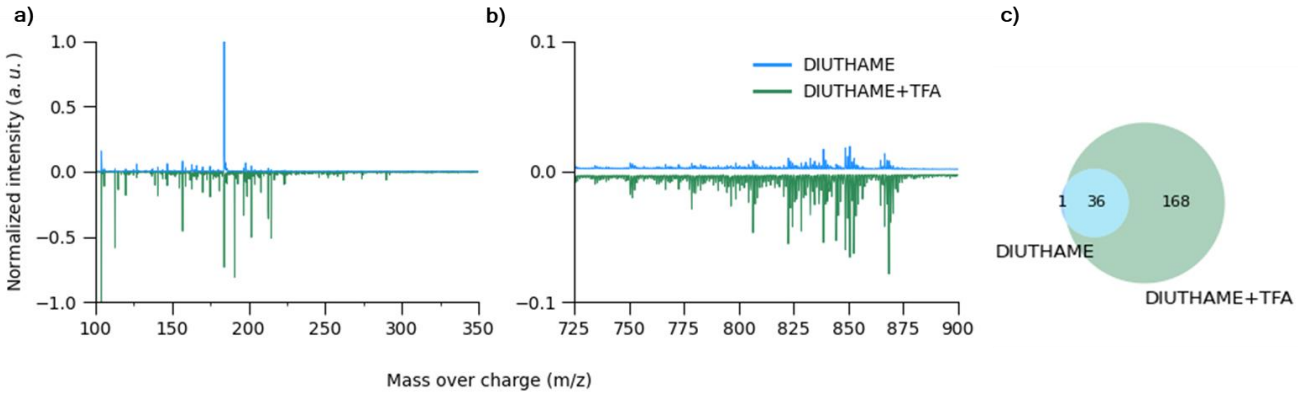

Figure 5.16 Evaluation of the solvent spraying effect on average mass spectra. Full tissue hyperspectral datacubes were flattened into averaged 2D mass spectra with a focus on a small molecular region (*m/z* 100 – 350) and a lipid region (*m/z* 725 – 900). The overall intensity of a mass spectrum increased after the TFA solution spray(d, e). A peak-picking algorithm was used to generate mass lists from both spectral measurements. A mass list volume and intersections were captured in a Venn diagram (f). The effect of TFA on GSK90 extraction enhancement was examined using GSK90/ponatinib ions.

The extraction efficiency of GSK90/ponatinib through the 16 µm brain tissue using thaw-mounted DIUTHAME was explored in both positive reflectron mode and in positive fragmentation LIFT mode (Fig. 5.17a). A protonated GSK90 $[Ponatinib+H]^+$ (*m/z* 533.20) was observed with low confidence only in the TIC-normalised image due to a poor SNR. The hydroxylated GSK90 ion $[PonatinibOH]^+$ (*m/z* 549.19) replicated the pattern of the dried droplet of GSK90 under the tissue section. However, the spatial distribution of the $[Ponatinib+K]^+$ (*m/z* 571.25) followed a short vertical line in the centre of the brain tissue. This line overlapped with a faint white line showed in the zoomed in brightfield image which was tentatively identified as a part of the third ventricle and cerebrospinal fluid (see Fig. 5.15a). It was considered that the cerebrospinal fluid and the ventricle section were easier for GSK90 to penetrate than the rest of the tissue. Moreover, cerebrospinal fluid contains a plethora of ions, including potassium, which in turn served as an adduct in the sample ionisation which led to the improved $[Ponatinib+K]^+$ signal. TFA application resulted in detection of $[Ponatinib+H]^+$ and $[Ponatinib+K]^+$ ions on an intersection between the GSK90 solvent spot and a diagonally spanning crack in the tissue. While the hydroxylated ion was detected in this imaging experiment an

increased signal intensity was not observed following TFA application (Fig, 5.13h). Thus, the hydroxylation was possibly the result of tissue metabolism which was not further affected by the application of TFA in the methanol solution. Finally, the detection of ponatinib was confirmed through a presence of the *m/z* 100.82, *m/z* 259.64 and *m/z* 432.67 ponatinib fragment ions (see Fig. 4.4) in the area of third ventricle using the LIFT fragmentation mode (Fig. 5.17c). Ion intensities of ponatinib fragments seemingly improved with the application of TFA, which suggested improved extraction through tissues. On the other hand, The SNR increased strongly only in *m/z* 259.64 and *m/z* 432.67 ion fragments. In addition, no analyte delocalisation within the tissue was observed which led to the conclusion that the addition of solvent on a DIUTHAME membrane improved the overall ion yield without a spatial delocalisation of analytes.

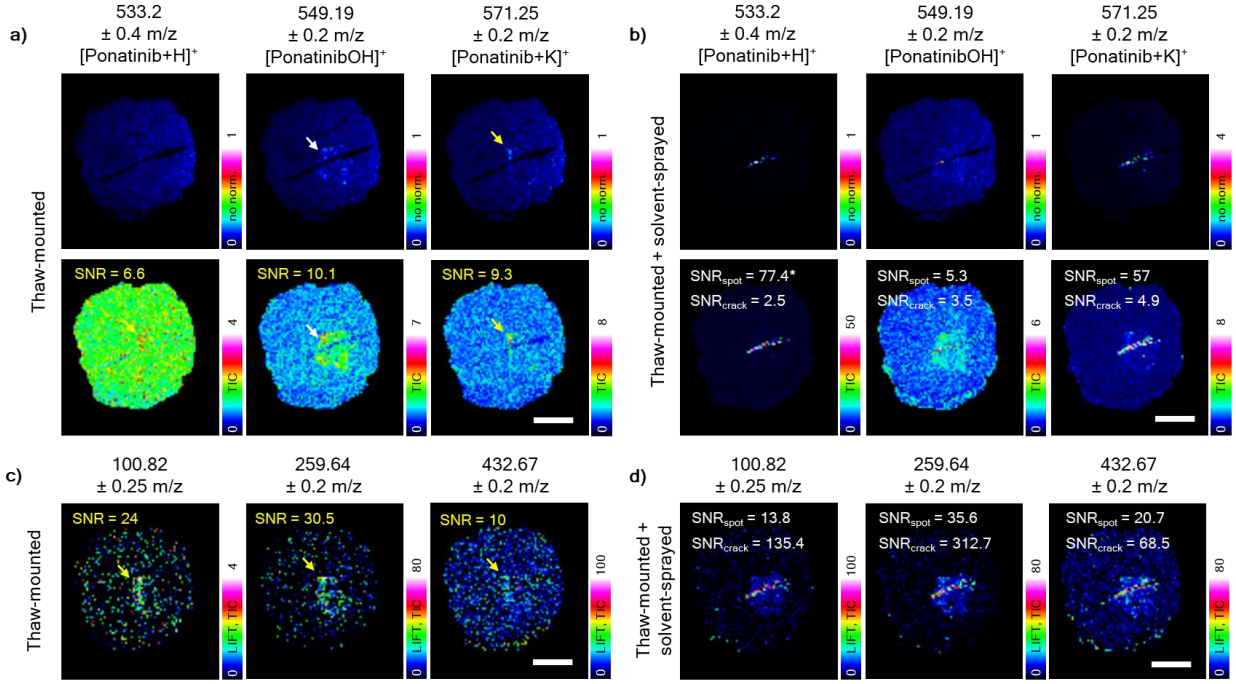

Figure 5.17 Evaluation of the solvent spraying effect on extraction of endogenous components and GSK90 in a brain section. a) Prior to TFA deposition, a $[Ponatinib+H]^+$ ion was not detected with confidence in the normalisation-free data, however a small line in the brain centre was highlighted in the TIC data. $[PonatinibOH]^+$ signal resembling the coffee ring shape (white arrow) seen in the brightfield image was detected. Similarly, to the protonated ion, $[Ponatinib+K]^+$ ion was also observed as a vertical line in the central brain region (yellow arrow). b) TFA spraying resulted in an increased detection of all GSK90 ions, including the hydrogenated ion and potassiated ions which were detected on the tissue crack interface. Fragmentation analysis (LIFT) in positive mode SALDI MSI showed a distribution of ions before and after TFA spraying. i) The known GSK90 fragments *m/z* 100.82, *m/z* 259.64, and *m/z* 432.67 were detected in vertical line in the brain centre after TFA spraying. *M/z* 259.64 fragment ion moreover resembled the hydroxylated ponatinib distribution. j) In consensus with the reflectron data, thaw-mounting resulted in ion extraction along the tissue crack edges in all examined fragments. Scale bars = 3 mm.

5.3.5. Comparison of MALDI and SALDI MSI in murine kidney

The use of DIUTHAME was further explored using murine kidney tissues to assess its feasibility in SALDI experiments in parallel with the SRS experiments with an outlook for an SRS-to-SALDI MSI. The kidney experiments were designed to evaluate the reproducibility and applicability of the sample preparation methods established for the murine brain SALDI MS experiments.

16 µm mouse kidney cryosections were prepared in a cryostat. Samples for the MALDI experiments were directly thaw-mounted onto Intellislides and dried at room temperature, whilst the kidney sections for the SALDI experiments were firmly sandwiched between a chilled Intellislide and a chilled DIUTHAME membrane in -20 °C. By applying heat from the palm of the hand on the reverse side of the Intellislide, the tissue was thaw-mounted to both the slide and the DIUTHAME membrane. Samples were fully dried on a benchtop at an ambient temperature. Using the TM Sprayer (Htx Technologies, USA), the MALDI samples were coated with αCHCA matrix with instrument settings that have been optimised for tissues and the 3-layer SALDI samples, which consisted of the Intellislide, the tissue and the DIUTHAME membrane, were sprayed with 0.2 % TFA in 70 % methanol with “D7” sprayer settings (chapter 3.5). All the samples were analysed across an *m/z* 100 – 1500 mass window with the UltrafleXtreme TOF/TOF mass spectrometer in the positive reflectron mode. The ablation diameter of a single raster pixel was set to 25 µm, and a raster step size was set to 75 µm to minimise a risk of oversampling which would then cause an intensity gradient at the sample edges. Additionally, small rectangular ROIs in tissues were created with a 25 µm step size. A total of 500 laser shots per position was fired.

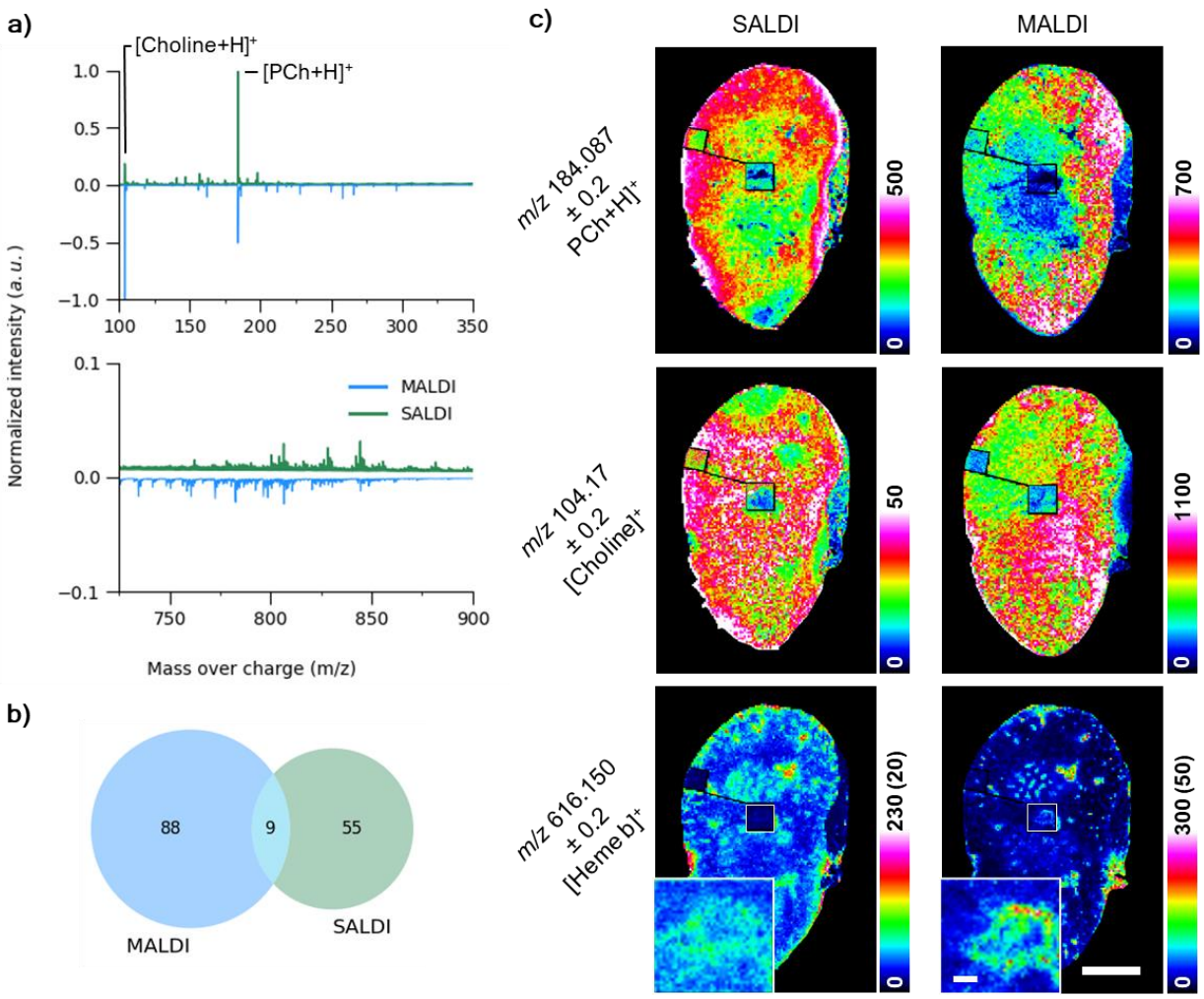

Figure 5.18 A comparison of MALDI and SALDI for mouse kidney cryosections. a) MS spectra comparison for MALDI and SALDI in the small molecule region (*m/z* 100 – 350) and the lipid region (*m/z* 725 – 900). b) 97 and 64 ions were detected by MALDI and SALDI, respectively with 9 common mass peaks. c) Single ion images of full mouse kidney sections depict the distribution and intensity of $[PCh+H]^+$ (*m/z* 184.087), $[choline]^+$ (*m/z* 104.17) and $[Heme\ b]^+$ (*m/z* 616.15) ions. Scale bar = 3 mm. Inset images captured the heme distribution in renal duct and collecting ducts in high definition. Inset scale bar = 200 µm, inset signal intensities in brackets.

The spectral information obtained from the MALDI and SALDI experiments showed differences in peak positions and intensities based on averaged spectra (Fig. 5.18a). The most prominent ions detected were $[Choline]^+$ and $[PCh+H]^+$ at *m/z* 104[285] and 184, respectively. Less prominent peaks did not spectrally overlap across the mass spectrum suggesting that MALDI and SALDI extracted different cellular components. Indeed, this finding was confirmed by comparing mass lists of the MALDI and SALDI data which showed that out 97 MALDI-related mass peaks (including αCHCA matrix peaks) and 64 SALDI-related mass peaks, and only 9 peaks were common to both (Fig. 5.18b). Peaks were filtered by distance (11 data

points ≈ *m/z* 2) and prominence (0.004 a.u.) of background corrected data. It is noteworthy to mention that the peak picking algorithm applied only a linear threshold and therefore some mass peaks were not detected and included in the mass lists. Next, single ion images of overlapping ions were assessed. Images were TIC-normalised (Fig. 5.18c). A $[PCh+H]^+$ was detected across the whole kidney section in both SALDI and MALDI imaging experiments with the highest signal intensity observed in the kidney capsule and the kidney cortex. Similarly, the $[Choline]^+$ (*m/z* 104.17) ion was detected in the cortex and the medulla of kidneys. Additionally, an ion at *m/z* 616.15, tentatively assigned as heme b^{286} gave a similar distribution pattern in both SALDI and MALDI, and thus demonstrating a consistency between the two techniques. In contrast to the MALDI single ion images of a $[Heme\ b]^+$, the ion yield in the SALDI single ion image was once again strongest at the tissue edges and gradually decreased in intensity towards a tissue centre. The ion images were TIC-normalised and therefore ion count fluctuations were not the source of the increased ion detection. Moreover, the MALDI and SALDI samples were ionised using the same instrument settings and therefore, oversampling – which would otherwise cause an intensity decline inside the tissue – would be observed in both MALDI and SALDI. Thus, the cause of this effect could not be explained. Furthermore, mismatches in spatial distribution of $[Choline]^+$ and $[PCh+H]^+$ were attributed to the use of non-consecutive tissue sections and the DIUTHAME extraction efficacy. Finally, high definition $[Heme\ b]^+$ ion heat maps revealed blood vessels and collection ducts in the mouse kidneys shown in Fig. 5.18c insets. The MALDI $[Heme\ b]^+$ ion image surpassed the same ion SALDI image in signal intensity and spatial contrast which was in agreement with the full tissue image at 200 µm raster step size. MALDI and SALDI overall intensities decreased, likely due to a lower amount of ionisable substrate. In conclusion, the TFA-spraying in combination with DIUTHAME was successfully applied to MSI analysis of murine kidney tissues as well as to a brain tissue indicting the potential application across further organs.

5.3.6. Evaluation of DIUTHAME in SALDI MSI of cells

In the final set of DIUTHAME feasibility studies, cell culture MSI was evaluated. MALDI MS analysis of cells is routinely performed with thousands of cells being analysed on high sample capacity plates[188,287,288], however imaging experiments are not so common. Mass spectrometry imaging of cell cultures grown on a flat surface requires LDI mass spectrometers to be capable of high resolution and high sensitivity to accommodate the cellular size and the low abundance of analytes for ionisation. For this reason, standard MALDI was employed in large cellular systems such as spheroids[289,290] and organoids[8] where it is feasible to ionise bulk cellular material. Albeit with the recent emergence of next generation MALDI-2 mass spectrometers, these instrument-imposed constraints have been overcome.[15]

Matrix crystal size (>1-10 µm)[164,166] now becomes the next constraint in MALDI MSI in terms of spatial resolution. However, since the DIUTHAME membrane pore diameter is 200 nm,[186] this offers an opportunity for cell analysis with sub-micron resolution.

Human colon carcinoma (Caco-2) cells were grown on poly-D-lysine-coated cover glass squares. Live cells were washed with PBS to remove the culture media, which can negatively impair the ionisation process.[287] Live cells designated for SALDI MSI were first scanned in brightfield whilst in PBS. Afterwards, the majority of the liquid was aspirated with a pipette with only a thin film of liquid remaining on the sample. With the cover glass on an Intellislide, a DIUTHAME membrane was immediately adhered to the sample, wherein the remaining sample liquid adhered to the membrane and dried without the need for any TFA sample wetting. Intellislides with the cells on a cover glass were scanned using the Reflecta brightfield scanner for registration with the mass spectrometer images (Fig 5.19a). A dark pattern shown in Fig. 5.19a confirmed the contact between the PBS solution and the DIUTHAME membrane. The cells with the DIUTHAME membrane were analysed by SALDI across an *m/z* 100 – 1500 mass range by raster scanning across a small area consisting of 748 pixels with a 50 µm pixel size encompassing two putative cell clusters (Fig. 5.19b). The ionising laser was set to fire 500 laser shots at 90 % laser power. $[PCh+H]^+$ (SNR = 172) single ion heat map was used to find location of the cells in the sample. Two cell clusters were observed matching in a size and position

to the brightfield image (Fig. 5.19c). Additionally, an *m/z* 881.66 ± 0.2 mass filter (SNR = 42) which captured a potential lipid components (either a sphingomyelin or a triacylglycerol)[11] was manually selected and correlated with the PCh and brightfield information (Fig. 5.19d). It was also observed that the mass filter (*m/z* 841.142 ± 0.2) focused on a noisy spectral position – albeit at low intensity (0.1 a.u, SNR = 3) – resulting in a false assignment of cells (Fig. 5.19e). However, TIC normalisation resulted in a random noise image for the same region (Fig. 5.19f) and thus emphasised the importance of using TIC normalisation. The non-normalised data was likely affected by an absence of ionisable material outside the cell boundaries, where the noise intensities were even smaller. Averaged spectra of cell and glass ROI revealed 9 overlapping peaks prevalently found in the *m/z* 100 – 200 mass spectrum region. The spectra were normalised to max intensity in cells (71.2 a.u.) and in glass (16.7 a.u.). More than 20 individual ion peaks were detected and confirmed through visual comparison of respective single ions in the lipid region (Fig. 5.19g). These results demonstrated that DIUTHAME is indeed applicable in SALDI MSI of cells without any cellular component delocalisation occurring.

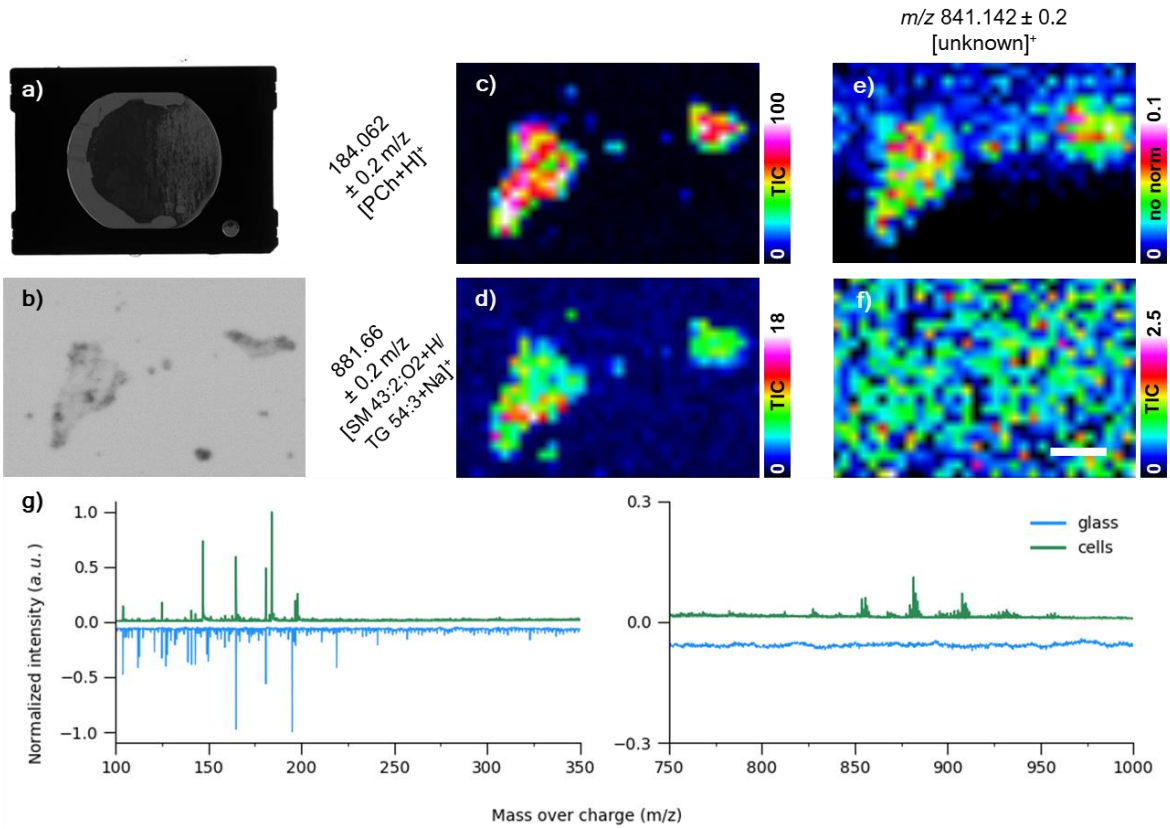

Figure 5.19 SALDI MSI in a 2D cell culture using DIUTHAME. a) A brightfield scan showed the DIUTHAME frame and the membrane with a dark spot stretching from centre to the right. b) Before DIUTHAME application, live cells in clusters were scanned with a brightfield slide scanner. TIC-normalised single ion images of c) a $[PCh+H]^+$ (*m/z* 184.062) and d) a lipid [SM 43:2;O2+H / TG 54:3+Na]$^+$ (*m/z* 881.66) were manually selected to compare the cell signal and the brightfield image. e) Analysis without normalisation revealed falsely assigned regions of cells at *m/z* 841,142. f) Noise was observed after TIC normalisation in the same spectral filter. g) Maximum intensity-normalised mass spectra from cell and glass ROIs revealed multiple ion peaks in small molecule and lipid region, whilst glass signal in the latter was consisting of noise only. Scale bar = 300 µm.

To conclude the comparisons of MALDI and SALDI, an Intellislide with Caco-2 cells was analysed using MALDI MSI in order to compare and relate the SALDI data to a robustly used method.

In the same culture experiment, Caco-2 cells were grown directly on an Intellislide coated with poly-D-lysine. Cells were washed with PBS, which was then completely aspirated. The cells were quickly dried under vacuum to reduce the size of the crystals, which were expected to form during drying. The Reflecta tissue scanner was used to capture an image of the dried cells which formed small dark spots throughout the slide centre (Fig. 5.20a). Using the HTX TM sprayer, the αCHCA was sprayed onto the MALDI cell samples with “dry” settings to decrease the potential for a cell component delocalisation (Chapter 3.5). The conditions for the

UltrafleXtreme mass spectrometer were as follows: UV laser intensity was attenuated from 90% to 40% and the raster step size was decreased to 25 µm. With the rest of the settings equivalent to the SALDI experiment, e.g., the data was acquired across the *m/z* 100 – 1500 mass spectral region. The acquired imaging data was TIC normalised.

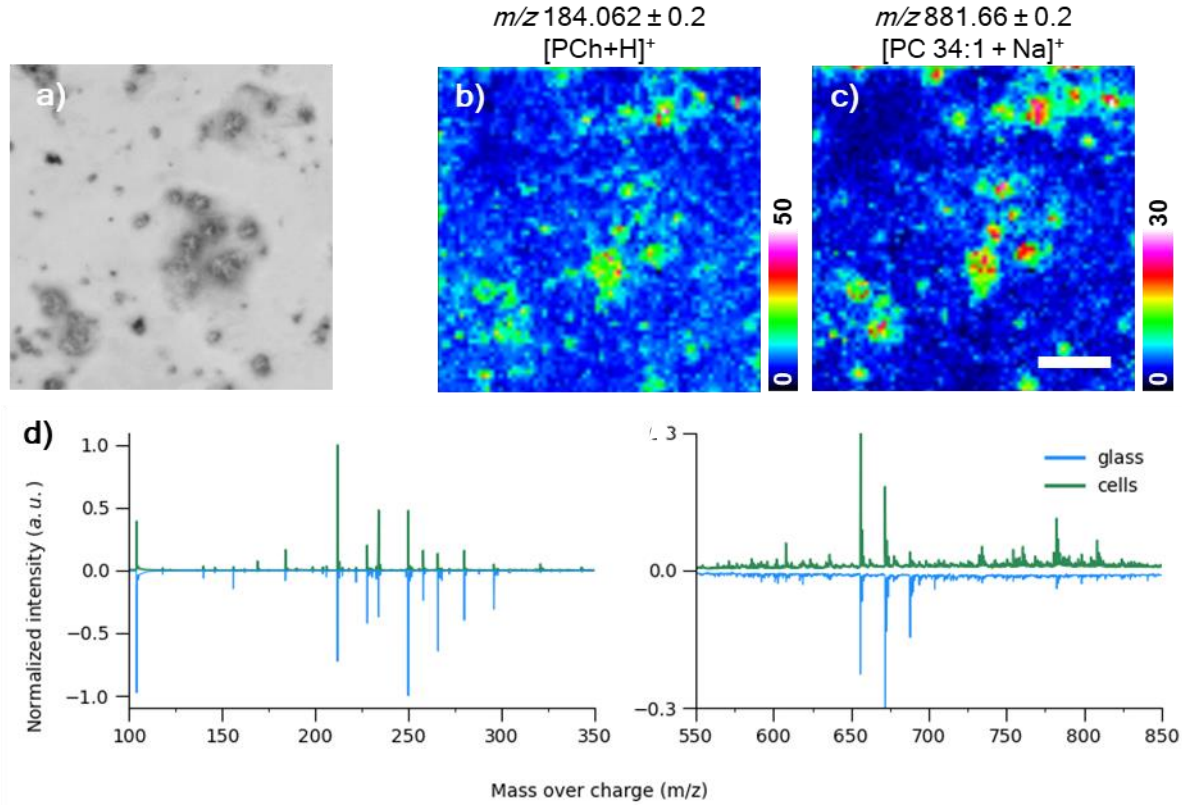

Figure 5.20 MALDI MSI in a 2D cell culture. a) A close-up of the dried cell clusters grown on an Intellislide was acquired prior to matrix deposition. b) The highest signal intensities in single ion heatmaps focused on $[PCh+H]^+$ at *m/z* 184.062 and c) the ion at *m/z* 881.66, which has been tentatively identified as the sodiated phosphatidyl choline $[PC\ 34:1 + Na]^+$, showed a correlation with the dried cell clusters in the brightfield image. d) Most of the detected ion peaks in the mass spectra was found inside and outside cells. In the low mass range, the majority of the detected ions were common to both inside and outside the cells. However, for the lipid region (*m/z* 550 – 850), there was a few of low abundant lipid peaks in the cells that were absent from the non-cell region. Scale bar = 400 µm.

The resulting single ion image of $[PCh+H]^+$ revealed a distribution of Caco-2 cells on the Intellislide (Fig. 5.20b). However, the *m/z* 184 ion was detected across an entire scanned area including areas absent of cells (see Fig. 5.20a). The sodium adduct of the phosphatidyl choline lipid $[PC\ 34:1 + Na]^+$ single ion image produced a comparable distribution to PC with only subtle differences in some ion positions and ion intensities in comparison with $[PCh+H]^+$ (Fig. 5.20d). The averaged mass spectra of cells and glass showed an overlap in almost all detected peaks including the PCh

the phosphatidyl choline lipid mass peaks. Since cell-related mass peaks were detected outside of cells, the single ion images were indeed showing lipids scattered across the scanned region. This suggested that a delocalisation of the cellular components and analytes was occurring. Due to the delocalisation of the putative cell components, background peaks could not be subtracted. Hence, a direct comparison of detected ions between MALDI and SALDI was not conducted.

To summarise, a conductive surface is essential for a sample ionisation and the subsequent direction of ions into the mass spectrometer in both MALDI and SALDI techniques. It was shown that the application of copper tape to the reverse side of a non-conductive slide resulted in a successful ionisation of a sample, but it was susceptible to surface charging effect, which caused a broadening and positive offset of mass peaks in the MALDI mass spectrum.

It was hypothesised that the conductive surface must be as close as possible to the sample to reduce the surface charging effect, which lead to the evaluation of a DIUTHAME-mediated SALDI technique. DIUTHAME is a conductive porous membrane designed for an analyte extraction and a subsequent ionisation in SALDI process. By placing the DIUTHAME membrane on a sample thaw-mounted to a non-conductive glass slide the conductive surface was in contact with the extracted analytes from the tissue below the DIUTHAME membrane, which in turn resulted in successful ionisation and generation of mass spectra in 30 µm-thick tissue section. The aim however was to use thinner tissues to reduce the light scattering during a prior SRS analysis and to improve the spatial resolution by extracting the thinnest possible layer. It was found that by spraying a solution of TFA in methanol, the ionisation efficiency of the DIUTHAME method improved and allowed for the SALDI MSI of 16 µm cryosections. Despite the method modification, MALDI outperformed DIUTHAME SALDI in terms of ion intensities and number of detected ion peaks. However, it was found that both techniques extract and ionise different ion species based on a fractional overlap of mass peaks between the two methods.

In addition, the extraction depth of DIUTHAME without the TFA deposition reached 30 µm, which was observed in a SALDI experiment where a spot of a dried GSK90 analyte was deposited below a 30 µm-thick mouse brain cryosection.

Finally, the limit of detection of SALDI was evaluated in MSI experiments of cell cultures using MALDI and SALDI, which resulted in successful detection of multiple

ion peaks which were tentatively assigned to cell-related lipid ions. However, the spraying of matrix on the cell sample resulted in a delocalisation since the lipid ions in MALDI were detected outside of the cells as well. Conversely, no analyte delocalisation was observed in the DIUTHAME-treated cell sample, where the lipid signal localised inside the cells only and thus suggested that the DIUTHAME membrane is highly efficient SALDI MSI of cell cultures.

5.4. Translation of the same sample between SRS and SALDI MSI

The previous two sections in this chapter identified that the incompatibilities between the MALDI MSI and SRS microscopy in the same biological, which lead to a development of a series of methods which overcome these issues and paved the way to conduct SRS-to-SALDI MSI experiments in biological samples. This technique combination was examined by generating a SRH of a full tissue section, which would then be used for a registration of SALDI MSI data.

Due to its hydrophobicity and morphological rigidity, mouse brain was used in the SRS-to-SALDI analysis. A 16 µm murine brain cryosection was thaw-mounted on a square cover glass (thickness = 0.17 mm ± 0.01). A second cover glass with a 1 mm-deep silicon gasket filled with PBS was attached to the brain sample cover glass. To create an SRH image with the SRS microscope, 874 tiles (256 × 256 px) with a 1.8 µm pixel size and 11.53 µs pixel dwell time were acquired with pump and Stokes beams tuned to CH_3 (2945 cm^{-1}) and CH_2 (2866 cm^{-1}) vibrational modes illuminating a sample with a 25× objective lens. Acquired tiles were stitched together using a Mosaic Merge tool in LAS X with a smooth overlap blending. Stitched SRS mosaic images were merged into a two-channel image and manually corrected in XY coordinates. The two-channel image (3013 × 5183 px) was exported to Fiji ImageJ, where a ratio-based image calculation ($x = |a - b|$) was selected over a subtraction ($x = a - b$) since it resulted in an output image with improved contrast.

The CH_3 image mosaic highlighted a distribution of protein and lipid components in the tissue (Fig. 5.21a), whereas CH_2 image highlights lipids with a stronger contrast (Fig. 5.21b) owing to the CH_2 bond prevalence in lipids.[291] The intensity of the corpus callosum and other lipid-rich white matter structures in the

brain surpassed the intensity from the grey matter which was richer in proteins. Nuclei contain low CH_2 bond concentration relative to the rest of the cell and the tissue, due to a low concentration of lipids.[292] Upon CH_3 – CH_2 signal subtraction, cell nuclei regions became faintly highlighted (Fig. 5.21c-d) in the dentate gyrus of the hippocampus, in the lateral ventricle, and the third ventricle as highlighted by the white arrows. The subtraction also resulted in a chemically non-specific increase in pixel intensity in tissue centre denoted by yellow arrows. This increase in intensity arose from a decreased overall intensity in the CH_2 image, where the microscope focused into a different Z position (yellow arrow). However, a spatial offset between CH_3 and CH_2 channels which was created during the tile stitching of the individual datasets prior to a channel merge led to very low intensity pixels in putative cell nuclei positions.

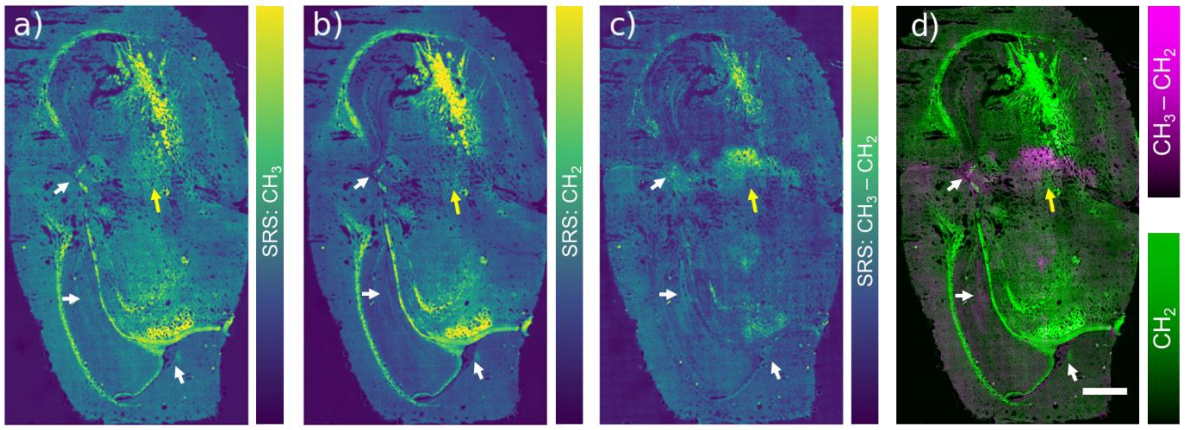

Figure 5.21 Stimulated Raman histology of a mouse brain tissue prior to mass spectrometry imaging. SRS mosaic images were acquired at two pump laser wavelengths corresponding to CH_3 (a) and CH_2 (b) vibrational frequencies relating to proteins and lipids. An image subtraction (a – b) revealed nucleus-rich regions in the tissue (c, d). Scale bar = 1 mm

The brain tissue on the cover glass was recovered from the sample enclosure and partially dried leaving a thin liquid film on the tissue surface and was then refrozen at -80 °C. The tissue on the cover glass was then transferred to a cryostat (-20 C°) and placed on a clean Intellislide before thaw-mounting to a DIUTHAME membrane. In addition, two adjacent mouse brain cryosections (16 µm) were thaw-mounted on two Intellislides, for the αCHCA matrix deposition for MALDI analysis and for a comparative DIUTHAME-mediated SALDI analysis without the cover glass. All samples were scanned using the brightfield Reflecta tissue scanner. Tissues with DIUTHAME membrane were sprayed with 0.2 % TFA in 70 % methanol with “D7”

sprayer settings (Chapter 3.5). using the HTX TM Sprayer to improve the sample extraction into the membrane. The second sample was used as a reference MALDI experiment where αCHCA matrix (7 mg/ml, 0.2 % TFA, 70 % methanol) was sprayed on the tissue using the “Tissues” setting TM Sprayer settings (Chapter 3.5). SALDI imaging was performed in the UltrafleXtreme TOF/TOF in positive ionisation reflectron mode focusing on a mass window of *m/z* 100 – 1500. The laser ablation position diameter was set to 25 µm, and the raster step size was 50 µm. The laser attenuated to 90 % fired 500 shots per each position. In MALDI imaging, the raster step size was set to 100 µm to reduce matrix build-up on the instrument source which would have caused a gradual decrease in ion yield. The laser power attenuator was set to 40 %.

The resulting TIC-normalised hyperspectral data were reduced by pixel averaging to single point spectra (Fig. 5.22a). Each sample resulted in clearly different spectral profiles. The difference between MALDI and SALDI mass spectra was expected since it was observed and discussed in chapter 5.3.5. The difference between the SALDI and the post-SRS SALDI sample was presumably caused by the prolonged exposure to the aqueous solution during SRS imaging. The SALDI-analysed sample generated a large number of ions between *m/z* 100 – 300 and thus surpassed the small molecule ion peak count of MALDI and post-SRS SALDI (see Fig. 5.22a). Furthermore, the intensity and number of ions detected in the lipid region (*m/z* 600 – 900) in the SALDI mass spectrum (max. SNR = 22, ~19 ions) was poor in comparison with MALDI (max. SNR = 142, ~25 ions) and post-SRS SALDI (max. SNR = 26, ~25 ions) mass spectra caused presumably by a relatively low analyte extraction efficiency. To accommodate for low extraction efficiency, ion intensity LOD was set to 2 in peak picking settings in the lipid region. It was unlikely that the difference between MALDI and SALDI spectra was the resolution since the size of the ablation spot in both analyses was the same. The post-SRS SALDI sample resulted in a seemingly reduced number of ions detected in the small mass region, however new ions that were observed in the *m/z* 600 – 700 mass spectral window were potentially a result of a prolonged exposure to abundant Na^+ and K^+ ions in PBS during the SRS analysis. However, the overall intensity of the lipid-associated mass peaks were lower in contrast with SALDI (without previous SRS) and MALDI data. The data was background-subtracted using a Savitzky-Golay filter[235] and using a variable threshold, spectral peaks were selected summed and

compared between the three samples (Fig. 5.22b). A total of 67, 73 and 35 prominent ion peaks (SNR ≥ 5) were detected in a mouse brain per MALDI, SALDI and post SRS SALDI samples, respectively. The overlap between SALDI and post-SRS SALDI ion peaks was expected to be greater since only 42 % of the post-SRS SALDI ion peaks overlapped with the SALDI ion peaks. Moreover, only 2 out of 153 total peaks were common between all samples which was unexpected based on a similar study by Müller et. al.[187] A close examination of the mass spectrum revealed a negative shift in the post-SRS SALDI mass spectrum. The $[PCh+H]^+$ ion (*m/z* 184.097) was shifted by – *m/z* 0.16 and an unknown ion mass peak at *m/z* 822 was shifted by – *m/z* 0.507. A linear offset function was calculated for the full range of *m/z* 100 – 1500 based on the two above mentioned ions. No other ions were found with high-enough confidence to improve the function precision. Admittedly, the relationship between the time of flight and mass-over-charge is quadratic.[190] Yet, it was found that the simpler to generate and apply linear correction fitting was sufficient to compensate the offset in the post-SRS SALDI mass spectrum (Fig. 5.22c). The resulting offset precisely overlapped with the *m/z* 184 ion, and while the offset spectrum was not completely aligned with the SALDI spectral peaks high mass spectral window, it was a sufficient approximation for peak binning, which reduced the variable data into a smaller and discrete number of bins. Despite the compensation offset in the post-SRS SALDI mass spectra, only a small improvement was observed – the overlap of all three spectra raised from 2 to 3 and the overlap between SALDI and post-SRS SALDI increased from 13 to 15 (Fig. 5.22d). The peak offset likely originated from an increased sample height due to a 0.17 mm-thick cover glass between the Intellislide and the tissue, because the TOF analysers separate the ions based on the time it takes them to travel over a given distance from a sample surface to the detector.[190] Thus, the reduction of the travel distance of the ion would most definitely affect the resulting mass spectrum. The peak picking algorithm was considered as the main cause for the mismatch between the two DIUTHAME samples/SALDI experiments as well as sample heterogeneity.

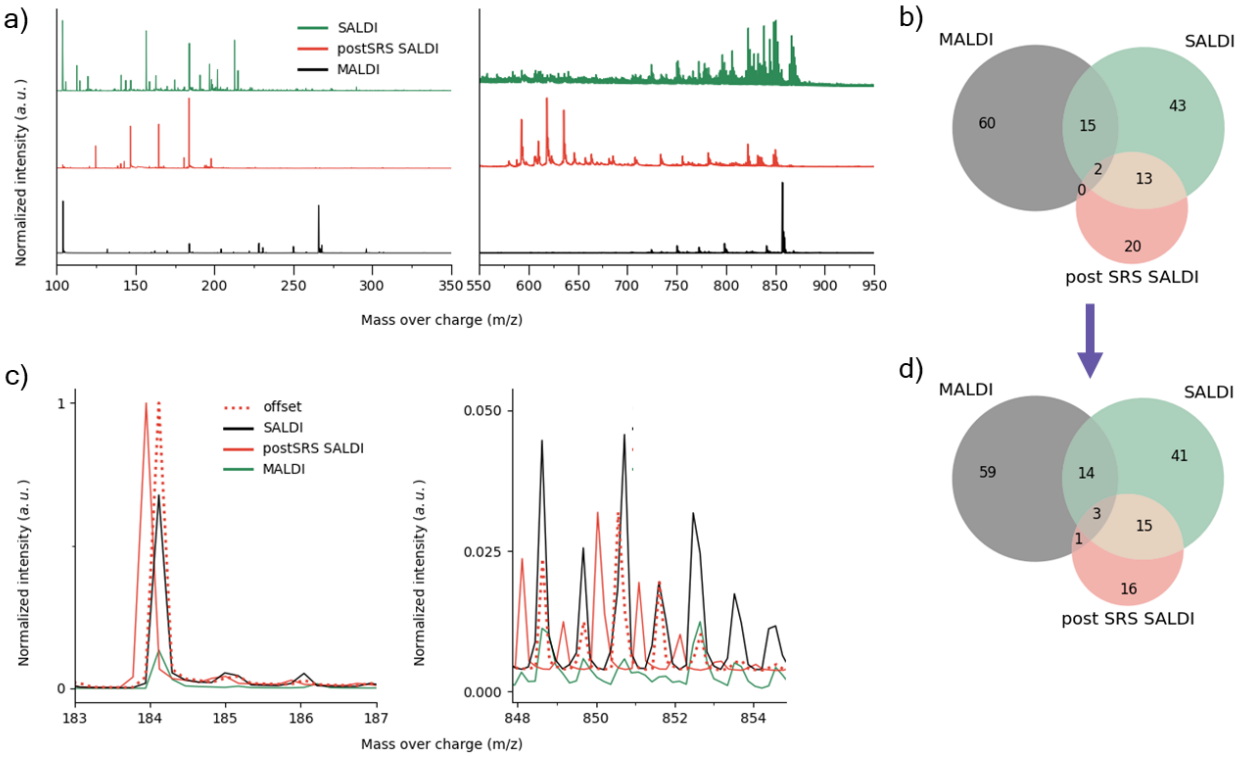

Figure 5.22 S/MALDI mass spectra of brain tissues. a) Hyperspectral MSI data of SALDI, post-SRS SALDI and a MALDI mouse brain samples showed heterogeneity in the number of peaks between individual samples and the signal to noise intensity in the low molecular weight region (left) and the lipid region (right). b) The relationship between the spectra was examined by comparison between the overlaps of mass lists which were generated based on spectral peak prominences per individual samples. c) A spectral negative offset of the post-SRS SALDI samples was corrected by fitting a linear calibration function on the spectrum. d) The mass lists were then compared again to determine how much did the spectral shift affect the relationships between individual samples.

In addition to mass peak binning, a spectral offset was applied to the generation of single ion images of the negatively offset data since the mass filters were typically set to narrow *m/z* 0.4 spectral windows. False-coloured heatmaps representing an intensity and a distribution of 5 annotated ions were generated per SALDI, MALDI and post-SRS SALDI of adjacent brain cryosections (Fig. 5.23). The post-SRS sample was morphologically warped during sample extraction from PBS. Selected mass filters reflected mass peaks which correlated with $[PCh+H]^+$ (*m/z* 184) $[heme\ b]^+$ (*m/z* 616), and an *m/z* 848 ion, which was tentatively associated with potassiated ceramides (GalCer (d18:1)/((24:1). An *m/z* 772 mass peak associated with either potassiated PC (32:0)[187,293,294] or potassiated PE (35:0) or PE(O-36:0)[187], potassiated PC (38:6)[187,295] was selected as well. $[PCh+H]^+$ was detected across the entire tissue, whereas in MALDI and post-SRS SALDI samples, the strongest

intensity was observed in the cerebral cortex (Fig. 23a). Therefore, a link between tissue heterogeneity and analyte extraction through co-crystallisation or capillary forces was suspected. Moreover, the highest $[PCh + H]^+$ intensity and spatial contrast were observed in the post-SRS sample which suggested that a prolonged exposure to PBS during the SRS analysis was possibly linked to the $[PCh + H]^+$ ion yield increase. $[Heme\ b]^+$ was successfully detected in both SALDI and MALDI experiments appearing to be in the ventricles where the blood vessels are located. However, the *m/z* 616 signal was not detected in the post-SRS SALDI sample and thus suggested that $[Heme\ b]^+$ had been delocalised whilst submerged in PBS in the imaging chamber during the SRS experiment. Furthermore, the potassiated PE (35:0) and PC (38:6) ions were not detected in the post-SRS sample in contrast with SALDI and MALDI samples. The *m/z* 848 ion was, however, succesfully detected in all samples, although the ion distribution in the MALDI sample was inverse to the expected distribution along the corpus callosum and the rest of the white matter. This result was unexpected since this ion had previously been detected in the white matter as shown in Fig. 5.15.

The unexpected absence of potassiated PC and PE in the post-SRS SALDI samples was examined since the lipids were unlikely to delocalise in an aqueous environment unlike the Heme b haemoglobin. Because the $[PCh+H]^+$ ions (*m/z* 184) were detected in the sample, an analyte fragmentation was suspected instead of delocalisation. Indeed, upon an examination of the mass spectrum (Fig. 5.23b) it was found that the putative lipids were fragmented into $[PCh+H]^+$ and the glycerol-acyl groups based on the loss of signal in the *m/z* 750 – 900 and the newly detected ions with *m/z* -183 shift. Although, the *m/z* -183 [PCh] offset moved the putative fragmented phospholipids into the expected lipid region (Fig. 5.23c), an ion pattern overlap between SALDI and post-SRS SALDI was found only in the *m/z* 864 – 872 (Fig. 5.23d), which was originally detected in the *m/z* ~680 – 690 mass range (see Fig. 5.23b inset). The most prominent shifted mass peaks were not overlapping with the MALDI and SALDI by an *m/z* + 3 either due to restructuralisation of the molecular structure of the phospholipids after fragmentation. Alternatively, new molecular species were ionised after the incubation in PBS.

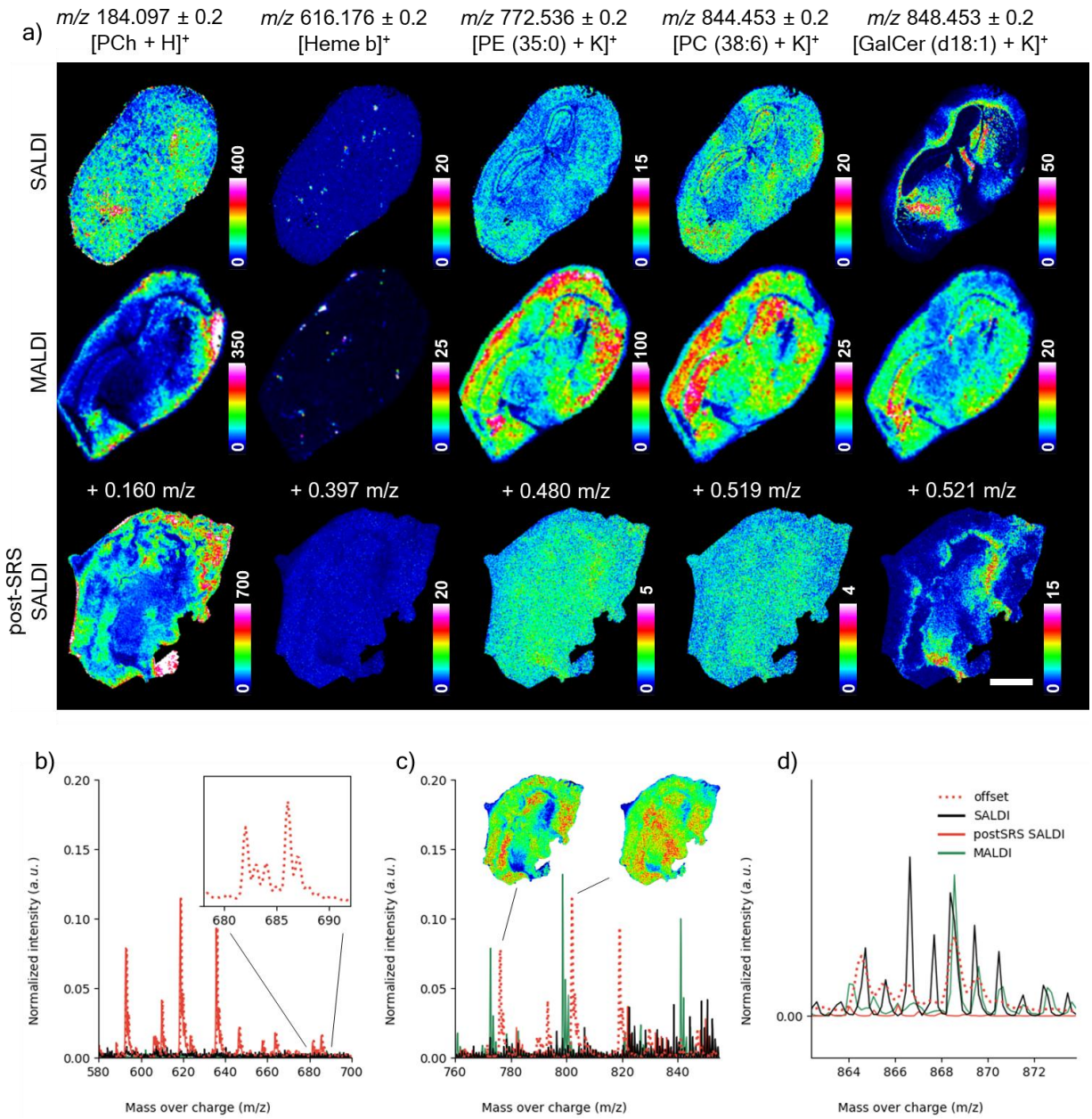

Figure 5.23 Effect of solvent exposure in MSI. a) $[PCh+H]^+$ (*m/z* 184.097), [heme b]$^+$ (*m/z* 616.176), [PE (35:0 + K]$^+$ (*m/z* 772.536), [PC (38:6) + K]$^+$ (*m/z* 844.453), [GalCer (d18:1)/ (24:1) + K]$^+$ (*m/z* 848.453) mass filters with a *m/z* 0.2 spectral window highlighted distribution of PCh, haemoglobin heme b and lipids with varying head groups in a SALDI (Intellislide + brain + DIUTHAME), MALDI (Intellislide + brain + matrix) and a post-SRS SALDI (Intellislide + cover glass + brain + DIUTHAME) samples. Post-SRS SALDI image data was offset by *m/z* 0.16, *m/z* 0.397, *m/z* 0.48, *m/z* 0.519, *m/z* 0.521. b) Potential fragmented acylglycerols were observed in a post-SRS SALDI sample after the mass spectrum correction. c) The suspected fragment peaks were found in lipid regions with a shift from potentially corresponding MALDI peak patterns by the further offsetting the fragments by *m/z* 183. A spectral pattern observed at approx. *m/z* 680 (inset spectrum in (b)) was found matching with a SALDI pattern ion peak pattern after a positive *m/z* 183 shift. Scale bar = 1 mm.

Moreover, the high signal intensity of $[PCh+H]^+$ and the acyl glycerol fragments relative to the remaining lipids in the mass spectrum suggested that these components were more prone to ionisation and fragmentation than other lipids in the tissue (see Fig. 5.22a). Interestingly, this was observed in the sample which underwent an SRS analysis in a PBS buffer which suggested that the buffer exposure was the main reason for the increased fragmentation in comparison with the SALDI mass spectra, where the fragmentation pattern was also observed but with an approximately 10× lower intensity.

The methods developed in chapters 5.2 and 5.3 were successfully utilised in whole cryosection analysis of a murine brain with SRS microscopy followed by SALDI MSI. However, SRS and MSI data was not overlapped due to an error during sample handling which caused the sample to warp. Although the experiment was planned to be repeated, the study was not finished due to a long and unexpected instrument down time and subsequent time constraints of the project.

SRH was only partially successful in highlighting the nuclear information in the brain. This was because of the spatial mismatch of the tiles and a Z drift of the sample during scanning. Going forward, the sample movement could be reduced by using an objective lens directly in contact with the samples. This was however not possible because the sample would need to be exposed, which was not allowed in the laboratory environment due to a lack of an appropriate containment at the time. Additionally, an analysis of a smaller are would also decrease the drift efect. The second identified source of CH_3 and CH_2 was the mosaic stitching with the LAS X software, which was not suitable for the image subtraction. Therefore, a development of an algorithm, which would correct the XY spatial mismatch between the CH_2 and CH_3 images and precisely stitched the tiles together would be highly benefitial to improve the applicability of the SRS-to-SALDI method.

The application of DIUTHAME membrane after SRS microscopy of the mouse brain cryosection lead to a succesful SALDI MSI experiment. Although, the sample attached to a cover glass was warped and could not be used for image co-registration, the chemical information was still extracted into mass spectra, which were compared with the MALDI technique and the SALDI technique where the tissue was directly sampled by the DIUTHAME membrane. It was found that the relative intensities of the $[PCh+H]^+$ at *m/z* 184 in the SALDI samples were more prone to

fragmentation as a result of the increased ionisation laser energy required for the analysis of DIUTHAME-treated samples. Additionally, it was observed that the incubation of the brain tissue in the PBS-filled imaging chamber during SRS analysis potentially increase the probability of fragmentation in comparison with a sample, which was directly sampled by the DIUTHAME membrane. Furthermore, the use of post-SRS sample on a cover glass also lead to a spectral shift caused by the decrease of the travel distance in the TOF instruments. Thus, going forward new calibration standards have to be measured at the same distance. This would ensure a suitable spectrum alignment occurring between the analysed samples without the need to offset and correct the spectra.

6. Imaging of liver-on-chip complex *in vitro* models

As outlined in the introductory chapter, complex *in vitro* models (CIVMs) provide an opportunity to avoid the duration, cost and use of animal models in pharmaceutical research by providing human-relevant and physiology relevant data early on in a drug development process.[199] In comparison with 2D cell cultures and other 3D cell cultures, CIVMs can be designed to organise the cells to mimic their arrangement in tissues thus generating reproducible data from highly ordered organ-like cell arrangements whilst maintaining a physiological flow of nutrients.[296] CIVM have been designed for various online and endpoint analyses, such as mass spectrometry[217,297], cell viability assays in drug screening,[298] and electrode array sensing.[299]

Imaging analyses including confocal fluorescence microscopy[217,220] second harmonic generation (SHG)[129], and spontaneous Raman microspectroscopy[221] have been previously reported. However, since a microscopy-enabling design is not the primary target in CIVM construction, only the upper layers of the samples are usually accessible to microscopy. Moreover, the CIVM cell scaffold are generally made of polystyrene and other plastics that are treated with bioorthogonal materials (e.g., collagen, polyethylene glycol, or polydimethylsiloxane), which improve cell surface adherence.[300] While plastics are perfectly suitable for most fluorescence microscopy applications, they are vibrationally active and can be observed in coherent Raman scattering (CRS) techniques.

Although the polystyrene scaffolding of some CIVM samples is a potential source of background signal in Raman techniques, the samples can be easily transferred, which was considered suitable for a translation study between CRS and mass spectrometry imaging (MSI). The liver-on-chip CIVM scaffolds (CN Bio, UK) were obtained in PBS after formalin fixation. Primary Human hepatocytes and Kupffer cells were seeded onto the CN Bio scaffolds as individual monoculture and 10:1 heterocultures. After 7 days of dynamic culture, the cells were treated with varying concentrations of A488-tagged antisense oligonucleotides (ASO) as part of an uptake and distribution study. Since the cells in the samples were not specifically labelled, label-free cell-type segmentation in the liver-on-chip scaffolds was required

to characterise the cell distribution. SRS and MSI were therefore examined as potential methods to identify hepatocytes and Kupffer cells and to determine ASO localisation inside different cell types by combining label-free SRS and MSI with fluorescence microscopy.

The aims of this chapter were to:

- Find methods which enable imaging of the CN Bio CIVM model using confocal fluorescence microscopy, SRS microscopy, LDI MSI, and light sheet fluorescence microscopy.
- Examine whether this model can be used as a platform for multi-modal imaging by incorporating the SRS-to-MSI method developed in chapter 5.

6.1. Characterisation of liver CIVM scaffolds with fluorescence and SRS microscopy

The CN Bio scaffolds were made of polystyrene coated with bioorthogonal collagen to improve cell adherence in a heteroculture. The scaffolds were approximately 180 µm thick circular chips, which were placed in plated perfused systems with a dynamic flow of nutrients (Fig. 6.1a). At the end of the cell incubation, the scaffolds were removed from the plate and fixed in formalin before being quartered for different analysis. The quarter-chip scaffold was made of a translucent material (Fig. 6.1b), with a large number of cells growing on the surface and inside the ~300µm pores (Fig. 6.1c). ASO uptake has been shown to follow different dynamics in murine hepatocyte and macrophage 2D cell cultures.[301] Therefore, the determination of cell type in a complex heteroculture model is necessary to establish a connection between ASO uptake and specific cell types and phenotypes.

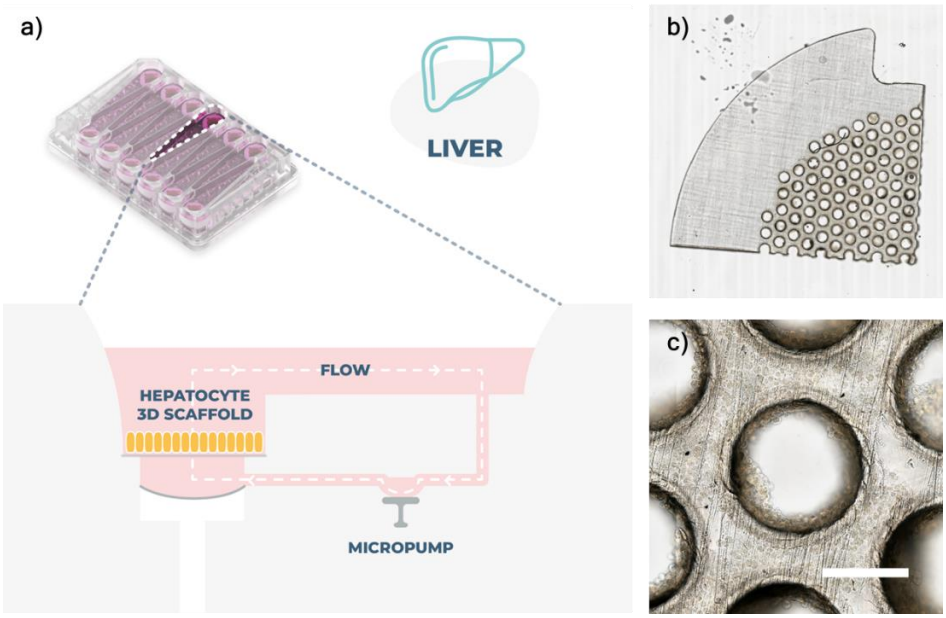

Figure 6.1 CN Bio perfused system. a) Diagram of liver PhysioMimix system with the cell scaffold. b) Overview of the quarter chip scaffold. c) Cells were grown and fixed on the scaffold surface and inside the pores. This image was a courtesy of Gareth Guenigault from CN Bio. Scale bar = 200 µm.

Using SRS instead of organelle-specific antibodies, three fluorescent channels (including a nucleic acid stain) can be used as alternative markers. Hyperspectral SRS was used to extract spectral features in untreated hepatocyte monoculture and a hepatocyte/Kupffer cell heteroculture to determine heterogeneities between individual cells.

The quarter chip was placed into a PBS-filled imaging chamber consisting of two 0.17mm cover glass squares on both ends and sealed by two adhesive SecureSeal^{TM} gaskets (2×0.12 mm deep, Fisher Scientific, UK), as described in Fig. 5.2. The scaffolds were then scanned using a Reflecta scanner with a TissueScout automated sample scanner routinely used for MALDI sample brightfield image acquisition. The sample was then imaged using a Leica SP8 fluorescence confocal microscope. An Argon 488 nm laser was used to excite the A488 dye in an epi-detection configuration through a 40× water-immersion lens. 25 tiles (1024 × 1024 px) at a 0.15 µm pixel size and a 2.88 µs pixel dwell time at two Z positions (0µm, 28.5µm) were acquired and stitched into a mosaic image (Fig. 6.2a). ASO was detected in cells that covered the entire face of the scaffold. However, the signal intensity decreased when the focus plane moved further into the sample, where only cells on the surface of the bulk cell mass contained within the pores were detected.

The depth-related loss of fluorescence signal was associated with the scattering of light caused by the tissues and polystyrene in the optical pathway of exciting laser and the emitted fluorescence.

Because of the strong scattering inside the sample, the majority of the imaging was focused on the interface between a pore and the scaffold face to extract maximum information with single-photon fluorescence confocal microscopy. With this configuration it was possible to observe ASO distribution in the heteroculture at a sub-cellular level. A Z stack consisting of 45 slices (z = 0.5 µm) at a 0.11 µm pixel size was acquired to generate a maximum intensity projection image that highlighted all the signals through a depth of 22 µm (Fig. 6.2b). A distinct, high-intensity, homogeneous A488 signal was observed in round objects. Moreover, punctate signals were observed in a presumed cytoplasm of the circular-shaped cells. By focusing on a single plane in the Z-stack (Fig. 6.2c), faint lines of A488 fluorescence signals were observed in the cell mass (white arrows). The large objects (5 – 12 µm) colocalising with the homogeneous A488 labels were considered to be nuclei of cuboidal hepatocytes, and the faint line-shaped A488 signal was considered to originate from an ASO that colocalized with a cuboidal hepatocyte membrane. The punctate signal was assumed to originate from circular cells, which were a combined population of Kupffer cells and circular hepatocytes. Cuboidal shape of a hepatocyte is accepted as the physiologically-relevant morphology which can be found lining liver sinusoids,[302] whereas the circular shape was assumed to be associated with improper cell-to-substrate and cell-to-cell adherence.

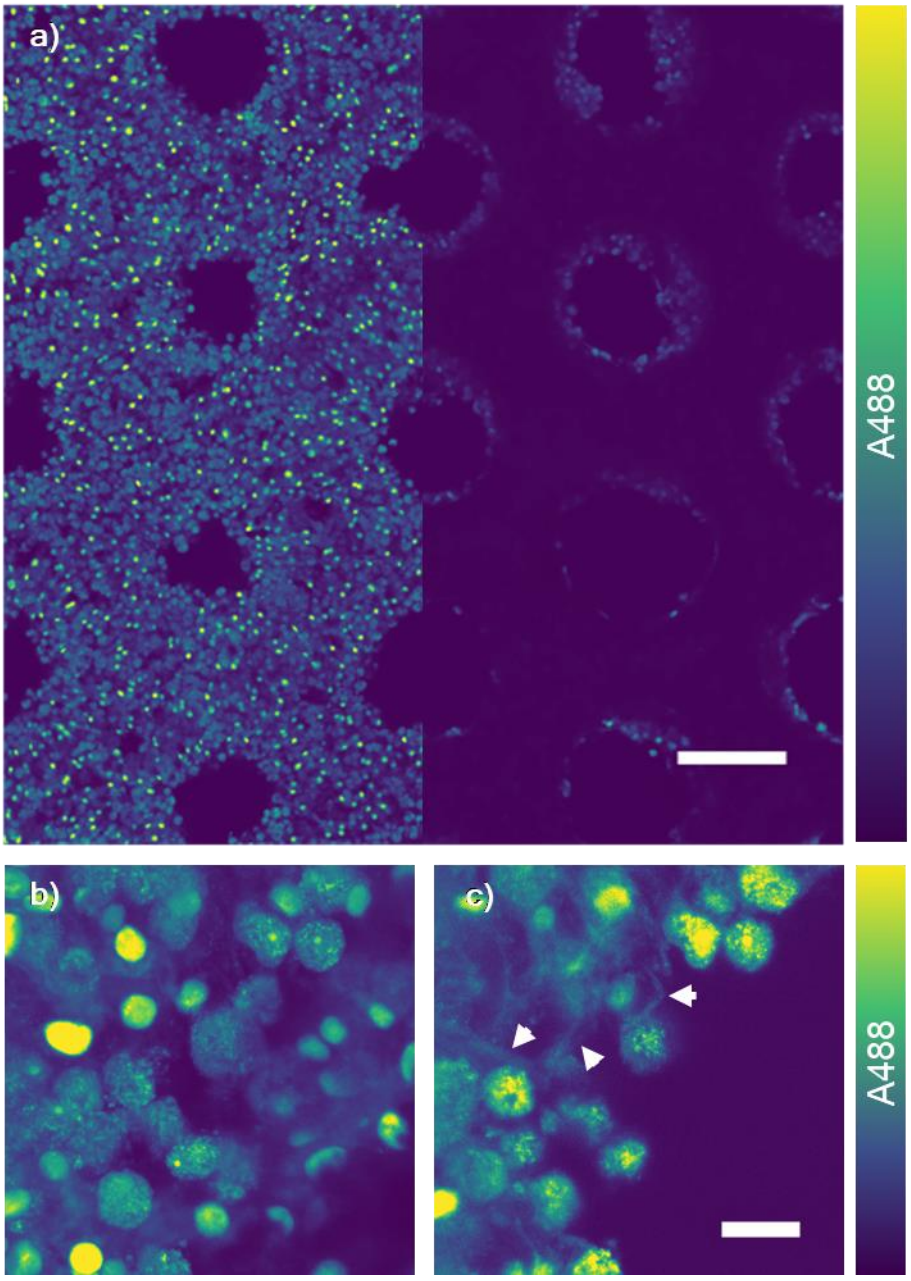

Figure 6.2 Characterisation of a liver-on-chip CIVM with fluorescence microscopy. a)Confocal fluorescence microscopy revealed ASO-A488 signal intensity inside cells on the scaffold surface and at 28.5 µm deep inside the scaffold. b) The maximum intensity projection and c) single focal plane image show the distribution of ASO at the subcellular level. White arrows indicate faint A488 signal-copying cell membranes. Scale bars = 200 µm (a), and 20 µm (b-c).

Potential SRS signal interference from the A488 fluorophore was examined after the initial fluorescence microscopy, which shed light on the cell and ASO distribution as well as the area of best imaging with a single-photon fluorescence confocal microscope, which captured a mass of cells instead of a single layer that was mostly found on the edge of the scaffold pores. A scaffold treated with the

highest concentration of ASOA488 (50 µM) was analysed using hyperspectral SRS and SHG in a forward and epi-configuration, respectively. The Leica SP8 was configured to acquire images of CH region (1024 × 1024 px) with a 0.17 µm pixel size and 1.92 µs dwell time between 2757 cm^{-1} and 3074 cm^{-1} at a step size of 16 cm^{-1}. SRS data were de-noised using singular value decomposition (SVD) factorization using the SciPy Python toolbox. Due to performance issues with the instrument at the time of data acquisition, the SRS channel images contained a line patterning artefact. Fast Fourier transform (FFT) was used to linearise this repetitive image motive which was then removed using Fiji ImageJ (chapter 3.5.2.1).

Hyperspectral data was acquired for the purpose of an SVD noise reduction tool in the SHG and SRS channels. Although SHG was originally developed to detect autofluorescence associated with the microtubules of collagen fibres, it also detected A488 fluorescence excited by a pulsed Stokes laser (1031 nm) and the pump laser at approximately wavelengths above ~800 nm through two-photon excitation. The detection of A488 signal with the SHG detector confirmed the presence of ASO-A488 in spherical structures (5 – 10 µm), which were tentatively identified as cell nuclei, with a homogeneous distribution as well as in punctate spots in circular and fusiform shapes (Fig. 6.3a), which suggested that the ASO localised exclusively either into nuclei or into putative cytoplasmic vesicles. The SHG signal was cross-validated in the fluorescence channel set for precise A488 emission detection (Appendix 7). By focusing on a CH_2 vibrational band (2866 cm^{-1}), the lipid distribution in the cells was highlighted (Fig. 6.3b).

Based on the fluorescence, SHG and SRS CH_2 data, ASO and lipid droplet positions were clearly visible in the seemingly empty cytoplasm of cuboidal hepatocytes, which constituted the majority of observed cell phenotypes in the field of view. In the centre of these phenotypes were likely nuclei structures, which in the fluorescence data appeared as high-intensity round shapes, whereas in contrast, in the SRS CH_2, the circular signal was darker in comparison with the surrounding environment, which suggested that the circular shapes were indeed nuclei, since CH_2 signal is most intense in lipids. SRS images were contrast-modified to suppress a highly concentrated unknown organic chemical contaminant in the solvent, in which the samples were transported. It was suspected that the contaminant was an

antibiotic agent. This solvent was later replaced with fresh PBS. Observing nuclei through SRH was not possible because of an extremely low residual signal after the image subtraction. Furthermore, by focusing on the 3074 cm^{-1} vibrational mode, polystyrene in the scaffold wall was highlighted (Fig 6.3c).

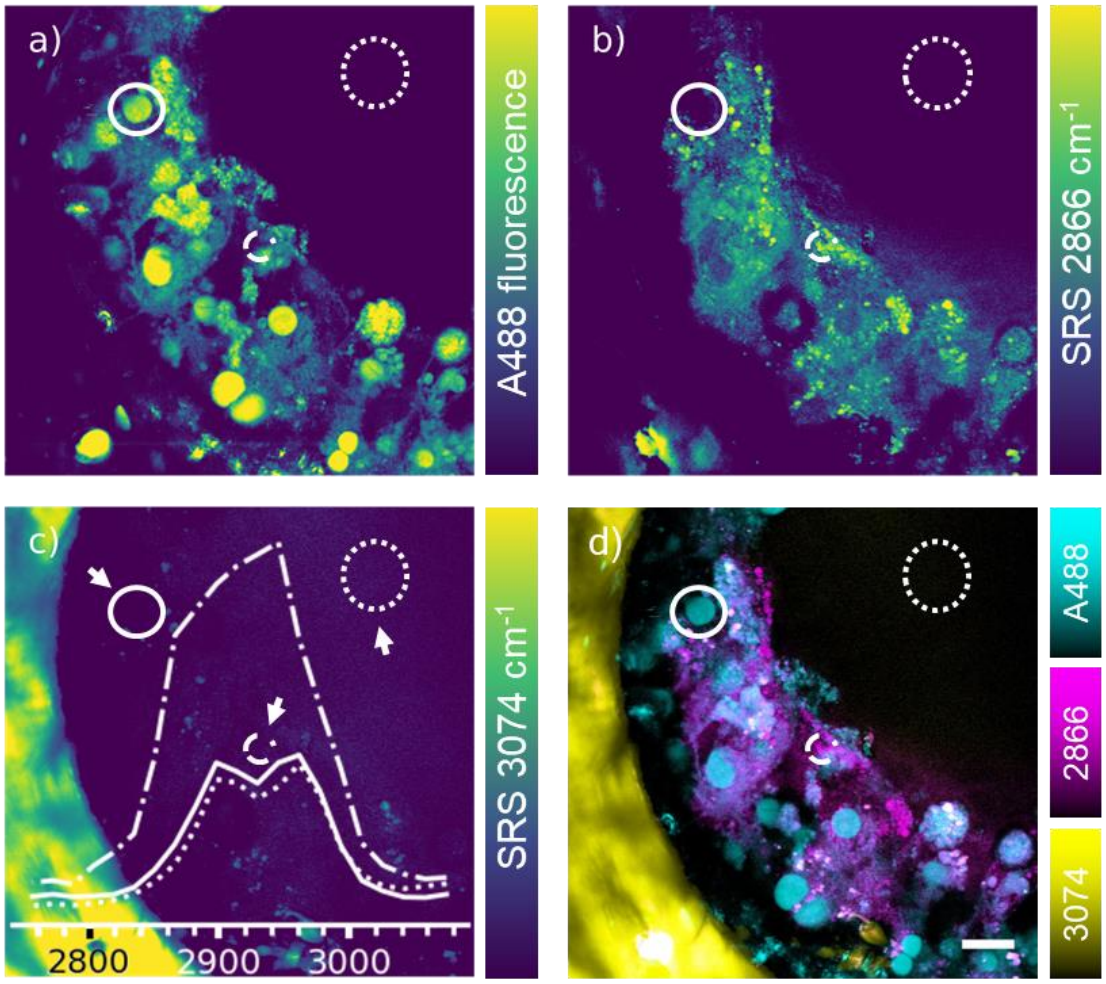

Figure 6.3 Simultaneous SRS and fluorescence microscopy of a CIVM scaffold. a) A488-labelled GalNAc ASO was detected in an epi-SHG detector in a hepatocyte/Kupffer cell heteroculture. b) By acquiring hyperspectral SRS data, a single CH_2 molecular vibrational mode at 2866 cm^{-1}, highlighting mostly lipid droplets (b), and a polystyrene vibrational mode at 3074 cm^{-1}, which highlighted the rim of the scaffold pore (c), were extracted. Averaged SRS spectra of A488-positive voxels (solid circle), solvent voxels (dotted circle) and lipid droplets-positive voxels (dot-dash circle) were extracted from the hyperspectral data to investigate fluorescence-SRS interference. Moreover, spatial overlap was observed between the fluorophore and SRS images (d). Scale bar = 20 µm.

A fluorophore-related interference in the SRS signal was evaluated in the SRS and SHG channels. The SRS and fluorescence signals did not spatially overlap (Fig. 6.3d), and thus indicated the possibility to image fluorescently-labelled samples. Furthermore, A488 fluorophore interference was examined in the spectral domain.

Three ROIs focusing on lipid droplet-rich structures (dash-dot circle), solvent (solid circle), and the A488-positive putative nucleus were selected as shown in Fig 6.2c. The Raman spectra corresponding to each ROI showed clearly distinct spectral profiles of each chemical component in the samples, albeit the nuclear and solvent Raman spectra were dominated by the contaminant spectral profile. However, non-Raman signal (e.g., static, or high baseline) was not found. The capability to image a single fluorescent label and hyperspectral chemical information with SHG and SRS, without interference, using a Leica SP8 SRS microscope demonstrated the potential for future hyperspectral analyses combined with selected fluorescent dyes.

6.2. Cell classification in CIVM scaffolds with hyperspectral SRS

The assessment of the capability of the SRS microscope system to separate cell types in a heteroculture was motivated by the prospect of using the fluorescent labels for highly specific antigens in cells in subsequent studies. Therefore, high resolution hyperspectral images of the CIVM samples were acquired along the CH region of the Raman spectrum to determine, whether any heterogeneities between the two cell types can be discerned and applied in the heteroculture cell segmentation.

Hyperspectral SRS images of fixed hepatocytes and hepatocytes/Kupffer cells heteroculture samples were acquired in a forward configuration with a 40× water immersion objective lens over a CH region (2757 cm^{-1} – 3074 cm^{-1}) at 8 cm^{-1} spectral step size, 0.19 µm pixel size and a 9-10 µs pixel dwell time. An example workflow is shown in a heteroculture CH_3 (2945 cm^{-1}) image with a logical size of 306×306 pixels (Fig. 6.4a). Images were not averaged; therefore, the raw data suffered from background noise. However, high-intensity and low-intensity circular signals were assigned to the cells and nuclei, respectively. Noise was significantly suppressed after SVD filtering (Chapter 3.10.3), which enabled an observation of fine lipid structures, which appeared as micron-sized high-intensity spots (Fig. 6.4b). SRS spectra were extracted by firstly manually selecting ROIs in the sample, which roughly enveloped the individual cells (Fig. 6.4c). Then, the spectra in all pixels inside each ROI were averaged to a single spectrum per ROI and normalised to the

maximum intensity of the averaged spectrum (Fig. 6.4.d). Faint variability in the spectrum was observed in the CH_2-associated left shoulder of the single broad peak at approximately 2860 cm^{-1}. Reduced CH_2 intensity (i.e., absence of said shoulder) in ROIs 1-3 was associated with putative cuboidal cells, which contained a lower number of punctate lipid droplets and prevalently consisted of low-contrasting homogeneous signal (see Fig. 6.3b-c). This heterogeneity in cytoplasmic signal between circular and cuboidal cells was considered the main chemical difference between circular and cuboidal cells in a Raman analysis.

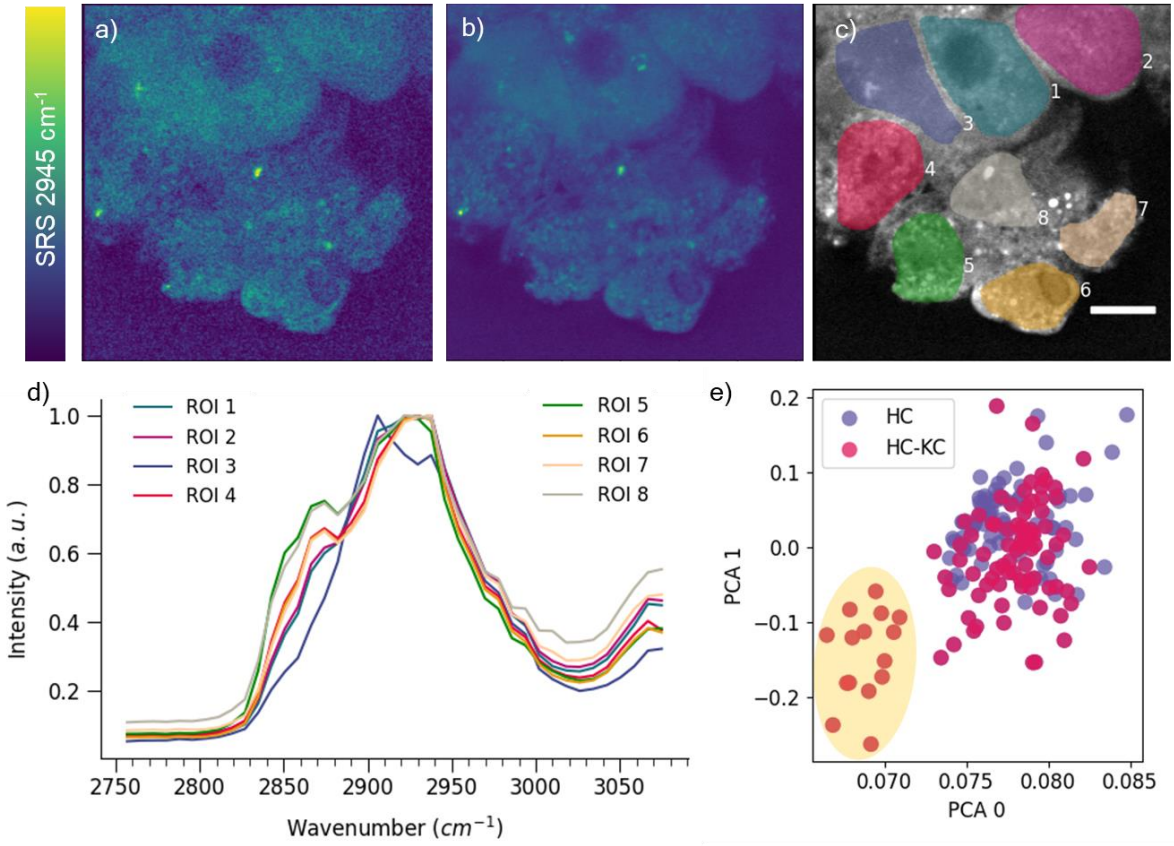

Figure 6.4 PCA of hyperspectral SRS of CIVM cells. a) The untreated coculture was scanned using SRS across the CHR with a significant noise contribution. b) Noise was removed using the SVD filtering algorithm, which highlighted the fine features of the cells in the images. c) ROIs were used to extract average spectral information from a sample. ROIs were manually drawn over the voxels of a sharp-contrast image. d) The extracted SRS spectra of the CHR region were plotted for each ROI. e) Separation of data caused by inconsistencies in instrumentation imaging was detected using PCA. Scale bar = 10 µm.

The observed spectral differences in ROIs in the samples were a promising stepping stone for spectral-based cell segmentation using principal component analysis (PCA). PCA is an established, fast, unsupervised factorisation and dimensionality reduction tool. A 99 % variance in a sample was explained by two

principal components in a dataset consisting of 168 cell ROI spectra which were extracted from hepatocyte and heteroculture samples. Plotting of these components (PCA 0, PCA 1) revealed a large cluster of the hepatocyte and the heteroculture samples overlapping, suggesting a strong correlation between the hepatocytes and the heteroculture spectra. A small cluster of heterocultured cells was clearly separated from the remaining data points, which suggested a difference in the data (Fig. 6.4e). However, the spectra associated with the separated clusters originated from the same hyperspectral scan. Therefore, it was concluded that the separation was a result of the imaging conditions rather than a different cell type. This result led to a conclusion that cell-type classification with hyperspectral SRS using the Leica SP8 SRS system, where the whole averaged spectrum was used for classification instead of imaging data, was accompanied by putative spectral fluctuations, which were specific to each scan and complicated image acquisition caused by the XYZ drift of a sample. Therefore, the ability of the SRS microscope to separate cell types based on Raman spectra was explored in 2D cell cultures, which reduced the issue of sample drift (see Chapter 7).

After spectrum-only analysis, where cells were separated based on the average Raman spectra, images were examined along spatial and spectral dimensions simultaneously to qualitatively determine heterogeneities between cells by separating the individual chemical/spectral components. The fastest and simplest visualisation of the 3D image was to flatten the spectral information into a colour code (Fig. 6.5a,i). This dimensionality reduction generated images where cytoplasm of cuboidal and circular cells were separated by different hues of a colour spectrum. Moreover, this approach highlighted two differently false-coloured vesicular structures in the cells. The difference between cuboidal and circular hepatocytes was contrasted further by application of the previously described SRH (Chapter 5.2.3), where the CH_2 image was subtracted from the CH_3 image (Fig 6.5a,ii). An additional characteristic was the lipid (CH_2) signal distribution, which appeared low in the cuboidal cells, whereas high intensity punctate forms were mostly associated with circular cells.

Non-negative matrix factorisation (NMF) based data reduction was used to decompose the hyperspectral images into individual chemical components based on spectral and spatial information. The Python sklearn.NMF module[234] (sklearn NMF),

which was used in the in-house built data processing pipeline, was compared with an NMF-based FSC^3 method developed by Masia et al.[106,107] The sklearn NMF revealed 4 different components which were distributed at varying intensities across analysed images (Fig. 6.5b) and their corresponding SRS spectra (Fig. 6.5c). Component *i* captured combined CH_3 symmetric and asymmetric molecular bond stretches[303,304] and was associated a protein-like signal which was observed across all the cuboidal hepatic and circular cells. However, the SRS spectrum of component *i* included a CH_2 asymmetric stretching mode (~2920 cm^{-1}) [303,304] which suggested that the NMF-based component separation was not fully efficient. Water, which was distributed at the highest concentration outside and in between cells was captured in component *ii* based on the start of an O-H stretch peak (2900 cm^{-1}) in the SRS spectrum. Similarly, to the SRH visualisation, lipids were concentrated the most in circular cells as shown in component *iii* which consisted of CH_2 symmetric and asymmetric molecular bond stretches in the Raman spectrum. [303,304] Interestingly, cuboidal hepatocytes were captured in component *iv* at various intensities, which were attributed to heterogeneity between the cuboidal cells and the position of the focal plane in the cells. The component *iv* was also found in other cells and consisted of the combination of CH_3 symmetric and asymmetric stretching modes.

Separation of the hyperspectral data using FSC^3 resulted in differentiation of six chemical components in the CH region, which was two more than with the sklearn NMF method. FSC^3 components were plotted into concentration maps (Fig 6.5d) and an SRS spectrum (Fig. 6.5e) as well. The FSC^3 separated individual components with improved spectral contrast based on the improved definition between the CH vibrational modes shown as dips in the spectral profile. The FSC^3 component *i* revealed the spatial distribution of a cuboidal hepatic cytoplasm and their improved separation from the remaining cells in contrast with fast NMF component *i*. Moreover, the spectral profile of FSC^3 component consisted of the CH_2 and CH_3 asymmetric vibrational stretches and only partially CH_3 symmetric stretch. The remaining extracted components contained a spatial and spectral combination of water and unidentified cell structures (*ii*), lipids (*iii*), water (*iv*), and two separated cytoplasmic signals, which contained CH_2 asymmetric stretch and partially both CH_3 stretching modes (*v*) and only the CH_3 stretching vibrational modes (*vi*).

The separation of the Fast NMF component *iii* and the FSC^3 component *i* both resulted in separation and visualisation of cuboidal hepatocyte cytoplasm.

Although both algorithms prioritised different components, both spectral/chemical components were likely to be present in the sample/data. The improved image contrast and spatial separation of components in combination with the ability to separate a higher number of spectral components led to a conclusion that the FSC[3] is the stronger tool in the analysis of the hyperspectral data. However, neither of the above-mentioned label-free methods extracted nuclear information from the hyperspectral SRS data. It was also observed, that apart from the cell segmentation, the cell separation with the SRS and SHG was complicated by the intertwined and overlapping growth of cell culture in the 3D scaffold. Going forward, this needs to be addressed in order to obtain precise data by either using fluorescent labels or by employing other label-free techniques, such as third harmonic generation,[34] which is capable generating signal in the water-lipid interfaces, and thus has a potential in imaging of cellular membranes.

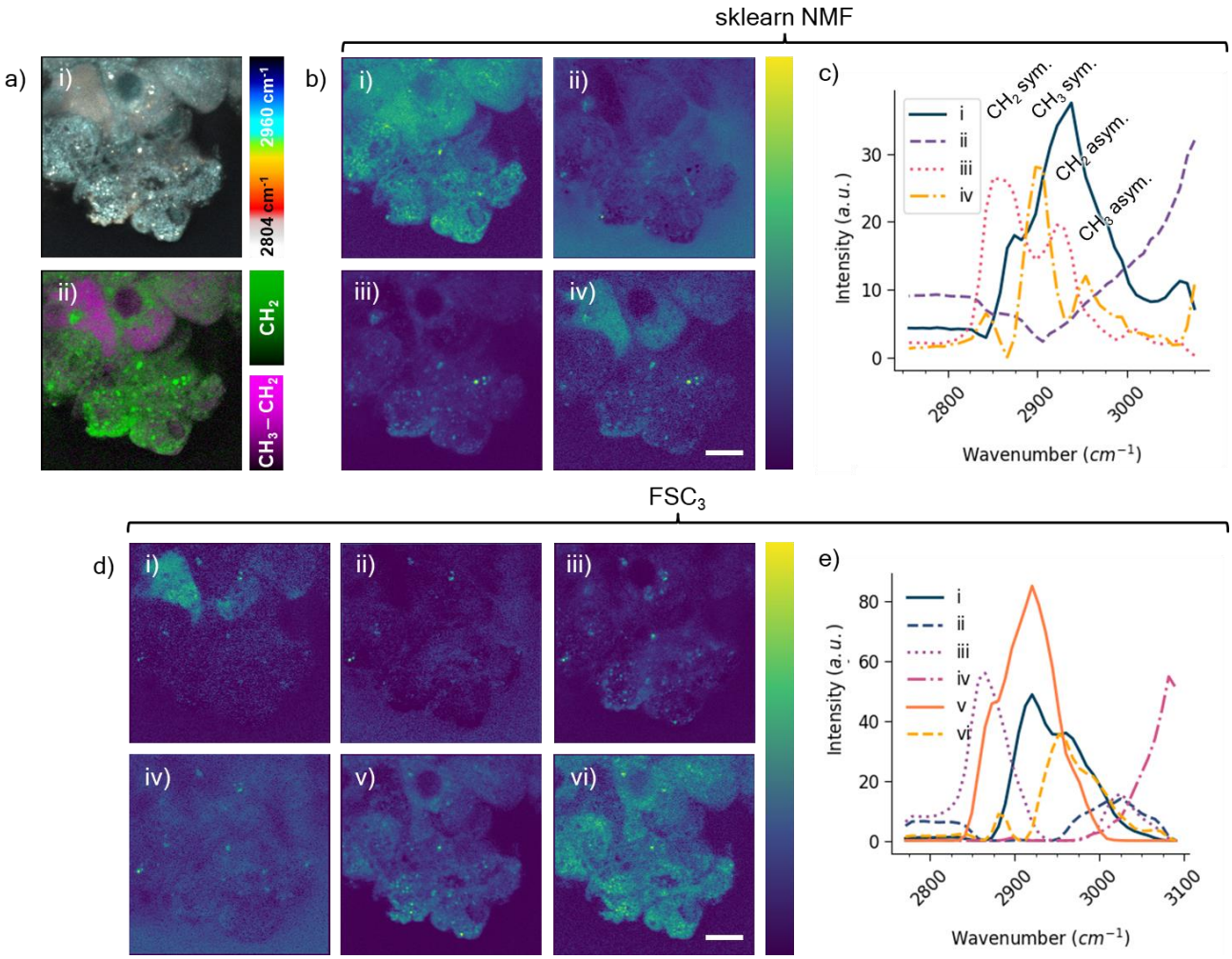

Figure 6.5 Heterogeneity of hepatocyte physiology using hyperspectral SRS. a) Coculture data were cropped to 2804 cm^{-1} – 2962 cm^{-1} and colour-coded to highlight intercellular heterogeneities in sharp contrast (i). Cellular lipids (green) and cuboidal hepatocyte cytoplasm (magenta) were highlighted by SRH image subtraction (ii). Sklearn NMF was used to separate the hyperspectral data into four components based on the spatial and spectral information. Individual components captured spatial distribution and concentration (b) and spectra (c) of i) proteins, ii) water, ii) lipids, and iv) an assumed cuboidal hepatocyte cytoplasm. Application of the FSC^3 method resulted in improved separation of six chemical components in the sample. d) The FSC^3 images highlight i) cuboidal hepatocyte cytoplasm, ii) unknown water-related vesicles, iii) lipids, iv) water, and v-vi) putative cytoplasmic lipids and proteins. e) The component Raman spectra had an improved baseline offset and spectral separation compared with Fast NMF. Scale bar = 10 µm.

6.3. CIVM imaging with light sheet microscopy

While the Leica SP8 system provided an understanding of cell distribution using the SRS modality and ASO subcellular localisation using fluorescence, the orientation of the optical path perpendicular to the face of the chip enabled only a fraction of the CIVM scaffold to be analysed. Light scattering from the bulk cell mass and CIVM scaffold pores caused insufficient sample illumination and signal collection from inside of the scaffolds in single photon confocal setups.

To address this restriction, the use of a Zeiss Lightsheet Z.1 was explored to provide additional imaging of the CIVM scaffolds. The Zeiss Lightsheet Z.1 features two-sided sample illumination laser sheets positioned at perpendicular angles to the collection cameras. Moreover, the enhanced ability to orientate the sample (XYZ and rotation along one axis) were expected to improve sample illumination by manipulating the sample in the microscope light path.

A scaffold with a hepatocytes/Kupffer cells coculture treated with GalNAc-ASO-A488 (2 µM, 1h) was stained with Hoechst in order to observe the localisation of nuclei and the ASO. The cell segmentation was described as a major issue in label-free techniques. Therefore, the scaffolds were stained with a fluorescent label with CellMask 647[305] and with Concanavalin A (ConA) tetramethylrhodamine to highlight the cell surface. CellMask label was substituted with ConA due to known poor incorporation of the label into fixed samples. ConA is a lectin, which is binds to sugars.[306] By avoiding cell permeabilization, only extracellular membrane-associated sugar moieties were expected to bind the ConA dye and thus, label exclusively the cell surface. The scaffolds were washed in PBS after 1 h incubation. Scaffolds were cut into strips, which were thin enough to fit into the light sheet capillaries. The strips were partially mounted in agarose inside a light sheet capillary (Fig. 6.6). The samples were imaged in an imaging chamber filled with PBS using a Zeiss Lightsheet Z.1. Z stacks of triple-labelled scaffolds were acquired with a 20× lens. File sizes of datasets generated were large due to the number of z-sections captured and so were processed in Arivis – a software tool optimised for complex 3D datasets.

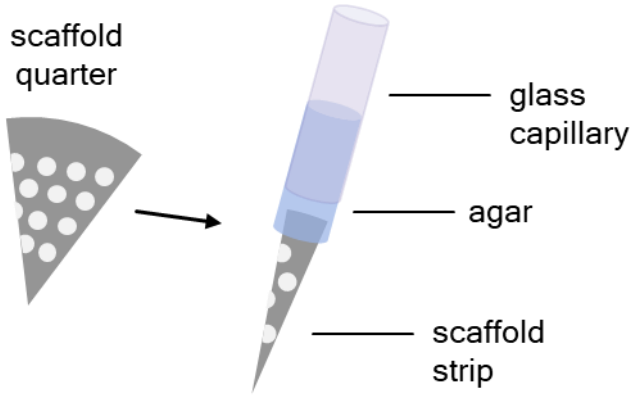

Figure 6.6 Schematic of embedding the CN Bio scaffold strip into a glass capillary.

A scaffold surface and a single well were imaged in the same scan by appropriate rotation of the scaffold which allowed the two excitation laser sheets to illuminate the inside of a pore and the scaffold surface simultaneously. The resulting 3D image was flattened into a maximum intensity projection which revealed the distribution of the ASO (Fig. 6.7a), Hoechst-stained nucleic acids (Fig. 6.7b), and cell surfaces stained with Cell Mask (Fig. 6.7c) throughout a sample. Cell Mask distribution was punctate and not dispersed across the cells. Therefore, the staining procedure was adjusted, with Concanavalin A replacing Cell Mask as the cell surface stain. Using this new staining technique, a single pore wall was imaged using the Lightsheet system. The maximum intensity projection of a single pore (Fig. 6.7 e-h) highlighted ASO-A488 localised in large bright spots (d ≈ 5 – 10 µm) and very small bright spots inside of faintly fluorescent spots (d ≈ 5 – 10 µm) (Fig. 6.7e). It was likely that these structures were cell nuclei since a majority of the faintly-labelled objects in the ASO channel were also detected in the Hoechst channel.

High intensity nuclear signal in the Hoechst channel (cyan) did not fully spatially overlap with the ASO signal (yellow) as shown in Figures 6.7h, l (green arrows). The faint Hoechst signal was tentatively associated with the nucleic acids in the nuclei. High intensity objects in the Hoechst channel were found at the cell mass surface (green asterisk), where more than ten bright objects were observed (Fig. 6.7f) and less so below the cell mass surface. The loss of the UV-excited Hoechst fluorescence intensity was likely caused by light scattering inside the pore. Although scattering was registered in all channels, the low wavelength light was expected to be scattered the most. Interestingly, the faint objects appeared stronger in intensity on a surface in comparison with the object centres. Despite their unexpected

fluorescence, the objects were annotated as nuclei. Although spatial overlap between A488 and Hoechst dyes was observed in a majority low intensity nuclei, only a small portion of high intensity nuclei colocalised with the ASO. The heterogeneities were compared with the SRS-fluorescence study, where ASO was observed either concentrated inside the nuclei whilst the cytoplasm remained free of the A488 signal or it was distributed in punctae in cell cytoplasm, whilst no signal was assigned to a nucleus.

Cuboidal hepatocytes were difficult to locate in a max intensity projection, which highlighted the most prominent signal in the stack and thus mostly cell mass surface structures were observed. The cuboidal hepatocytes were best visible in single plane images which provided a cell distribution information in a cross section through the cell mass (Fig. 6.7i-l). The cuboidal hepatocyte membranes were detected based on an A488 signal which originated from the ASO adhered to the cell membrane which was already established with SHG in the SRS/SHG scaffold analysis. Additionally, high intensity ASO signal overlapped with the high intensity Hoechst signal, whilst the remainder of the cellular cytoplasm did not contain any labelled oligonucleotides and thus confirmed the ASO localisation in nuclei in cuboidal hepatocytes. Moreover, the cytoplasmic localisation ASO was also confirmed by lightsheet microscopy in circular cells which were found in the top layer of the cells in the scaffolds.

The use of light sheet microscopy allowed to examine both on the scaffold surface and inside the pores, where the majority of cells could be found. With the application of fluorescent dyes, which highlighted cell surfaces and cell nuclei deep inside pores, which was not yet reported. It was concluded that in terms of penetration depth, the light sheet microscopy surpassed the single photon excitation confocal microscopy, which was limited in terms of light penetration through a sample. However, its successful combination with SRS showed an opportunity for analyte tracking inside cells which can be highlighted through an exploitation of endogenous vibrational properties. By using SRS, fluorescent channels can be utilised to identify highly specific cellular epitopes instead of being used as general fluorescent markers for cell membranes and nuclei. Moreover, cell classification was achieved with NMF techniques in hyperspectral SRS images, cuboidal cell cytoplasm was separated from the remainder of a cell mass in a CIVM scaffold, albeit Kupffer cell-specific components were not successfully extracted in this study.

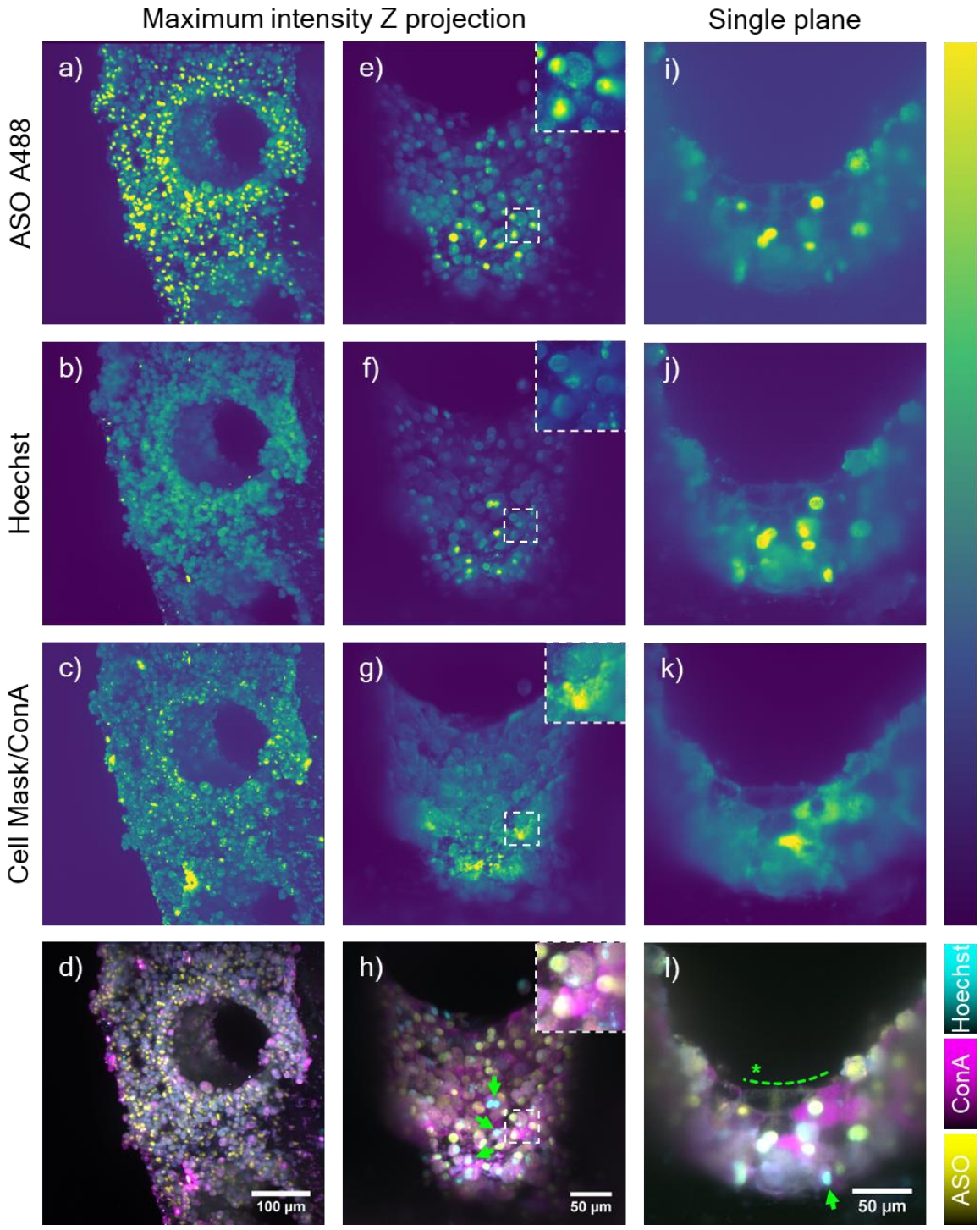

Figure 6.7 Lightsheet microscopy of CIVM scaffolds. ASOs tagged with Alexa Fluor 488 were captured in the yellow channel (a, e, i), nucleic acids in cell nuclei were labelled with Hoechst 33342 in the cyan channel (b, f, j) and cellular surfaces were dyed with Cell Mask 647 in (c) and with Concanavalin A in (g, k) in the magenta channel. A maximum Z projection showed the distribution of ASOs in cells on a scaffold surface and in a scaffold pore which was captured with 673 × 673 × 577 µm image size with a 0.35 µm XY pixel size and a 0.42 µm Z step size. (a-d). A detailed image of a scaffold pore shows the ASO, and nuclei distribution and their spatial overlay captured in a 403 × 403 × 187 µm image with a 0.2 µm and 0.4 µm pixel size, respectively. (e-h). Green asterisk and dashed line denote the cell mass surface in a single plane image (i-l). The lack of overlap between the ASO-A488 signal and Hoechst signal was pinpointed by green arrows (h, l).

6.4. Mass spectrometry imaging of liver CIVM scaffolds

Cells grown on CIVM scaffolds are an advantageous sample for SRS-to-MSI analyses because they can be easily transferred from a microscopy suitable substrate (e.g., cover glass) to a conductive surface. The liver organ-on-chip polystyrene scaffold with a ~0.2 mm thickness was however considered disadvantageous for MALDI and SALDI MSI experiments, where adherence to slide and the efficient conductivity on the scaffold surface were expected to be significantly reduced due to the hard, non-adherent and highly insulating properties of polystyrene. Hence introduction of conductive material on a scaffold surface was necessary to direct a charge flow. An application of DIUTHAME, which was introduced in Chapter 5, was expected to improve sample adherence and conductivity.

The feasibility of the liver CIVM sample in MALDI and SALDI MSI was examined in a full, intact scaffold and in a cryo-sectioned scaffold. In an initial experiment, a sample preparation of a full scaffold was examined by the blotting DIUTHAME membrane, which was reinforced in membrane thickness in comparison with the standard DIUTHAME membranes. The blotting DIUTHAME membrane was carefully attached to a wet (PBS) scaffold and an Intellislide. The relatively sharp and solid polystyrene did not cause any tears in the membrane (Fig. 6.8a), which otherwise occurred in the standard DIUTHAME membranes. The CIVM scaffold with the blotting DIUTHAME membrane were then sprayed with 0.2 % TFA using the HTX TM Sprayer to improve the analyte extraction.

A widefield scan was used for registration in the UltrafleXtreme II TOF/TOF mass spectrometer. The image showed liquid still present in the middle rows of pores in the scaffold (Fig. 6.6b). In the mass spectrometer, the samples were imaged in a positive reflectron mode over an *m/z* 100 – 1500 mass range. The Smartbeam-II laser fired 500 shots per spot at 90 % of the maximum laser power. The initial imaging run was set to a 75 µm raster step size and a 50 µm spot diameter. Data were TIC-normalised. The initial scan with large raster size lead to a detection of ~6 unique ions in the lipid region of the mass spectrum (*m/z* 600 – 900), which in turn encouraged a second scan at a 25 µm laser raster step size and a 25 µm spot

diameter, which positively impacted the ion image definition, but also scanned already ablated sample spots, which resulted in a dark pixel grid.

Single ion images with an *m/z* 0.2 tolerance were generated with *m/z* 130.88, *m/z* 194.75, *m/z* 165.89 and *m/z* 854 mass filters (Fig. 6.8Tc). These images showed distribution of 4 spatially distinct ions which were not successfully annotated. The *m/z* 130.88 ion was detected in the middle two rows of a chip which correlated with the accidental extended liquid exposure, which was apparent in water droplets inside the central pores in the Fig. 6.8b. This however suggested that increased solvent exposure yielded improved analyte extraction. Moreover, the standard $[PCh+H]^+$ ion (*m/z* 184) was not observed. Instead, a presumed lipid ion at *m/z* 854 was found in the vicinity of pores and the adjacent scaffold surface. The spatial distribution of a $[Pt]^+$ ion at *m/z* 194.75 and the distribution of the unassigned lipid (*m/z* 854) were mutually exclusive despite the homogeneous distribution of platinum across a sample. Therefore, it was suspected that platinum was less likely to ionise in a presence of competing ions which is analogous to the ion suppression of lipids as described in Chapter 5. In support of this statement, the $[Pt]^+$ intensity was increased in scaffold pore centres, where no cellular material was expected. Finally, multiple peaks were observed with a dissimilar spatial distribution from platinum and cells, such as in the *m/z* 165.89 single ion image, which was likely scaffold-related. The scaffold was made of plastic and the surface was treated with collagen. Therefore, it was suspected that the ions originated from the scaffold surface rather than the DIUTHAME membrane.

Mass spectrum evaluation was done with the averaged spectra extracted from a ROI which encompassed the porous area of the scaffold, whereas the membrane only ROI was used to create background spectra from DIUTHAME (Fig. 6.6d). Common mass peaks between the DIUTHAME membrane in the high and low raster definition included $[Pt]^+$ and $[PtAl]^+$ ions were confirmed at *m/z* 194.75 and *m/z* 389.55 positions, respectively. The lipid peaks in high *m/z* region were detected at a higher intensity in low raster definition in comparison with the mass spectrum from the high raster definition scan. This was likely due to a reduction of the sampling area and the amount of material available for ionisation on the DIUTHAME surface, which was also ablated in the low raster definition SALDI MSI experiment. This led to an increased detection of the $[Pt]^+$ (*m/z* 194.75) ionised from the DIUTHAME membrane surface (Fig. 6.8d). Additionally, the second SALDI imaging revealed the

pattern of the original sample ablation spots as shown in Fig. 6.8c. A total number of mass peaks per analysis was calculated to quantify the difference between the imaging experiments. Mass peaks were detected using a local maximum detection tool with a linear threshold to cut off noise in the mass spectrum. The low-definition image data showed 6 % and 43 % more peaks in contrast with high definition data and membrane data, respectively. The increase in high definition-membrane intersect in comparison with the low definition-membrane intersect was likely caused by low biological material abundance and thus, an increase in ionisation of the membrane under the extracted sample components occurred. This was further supported by the $[Pt]^+$ and $[Pt_2]^+$ ion intensity of the high-raster definition imaging, which showed significantly stronger relative intensity related to the low raster definition data.

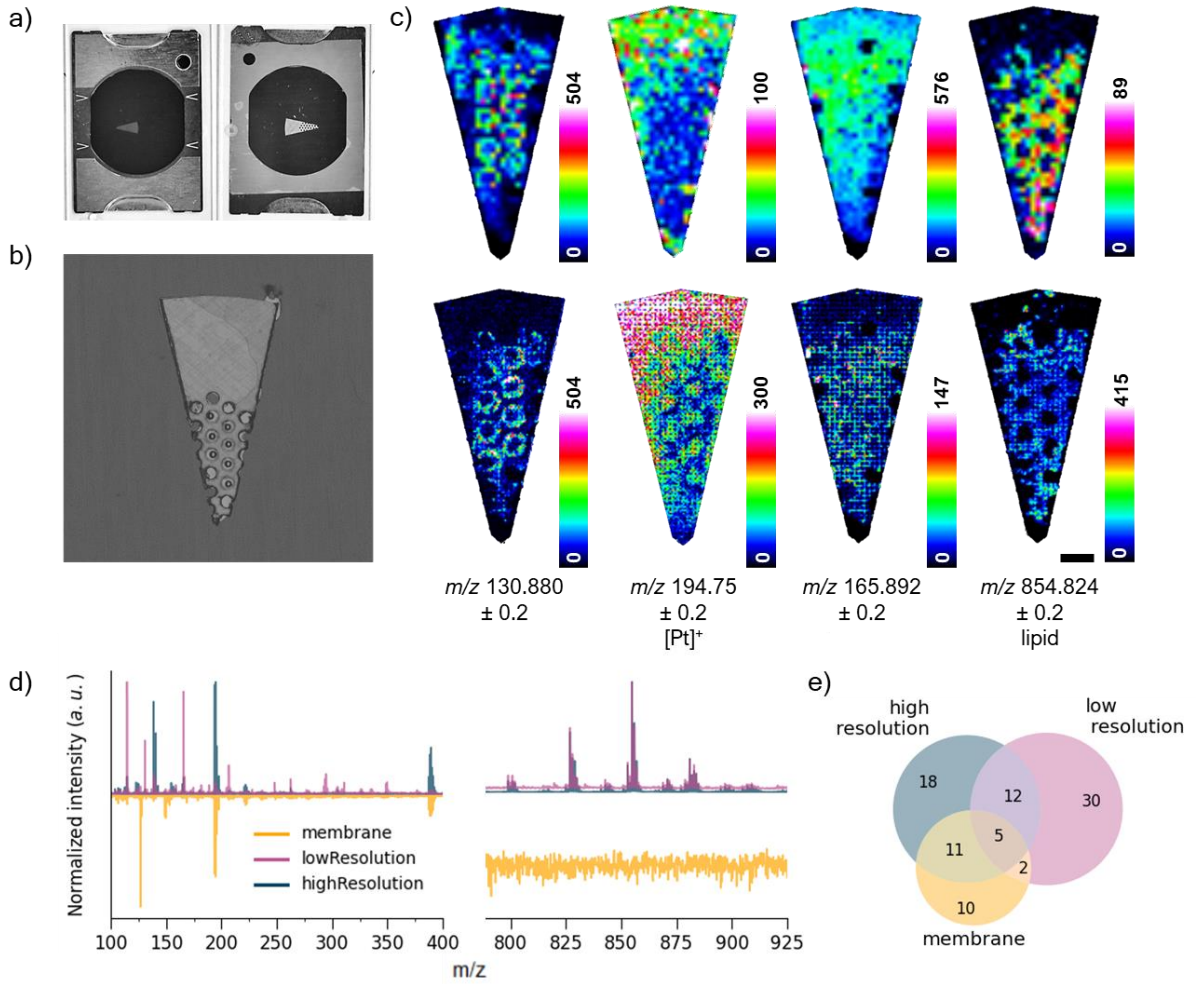

Figure 6.8 DIUTHAME-mediated SALDI MSI of intact CIVM scaffolds. a) Overview images of an Intellislide-scaffold-DIUTHAME sandwich were captured from above (left) and below (right) after MSI analysis. b) A contrast-enhanced brightfield scan of a liver-on-chip scaffold covered with a DIUTHAME was acquired for a mass spectrometer image-sample registration. c) Samples were scanned at 75 µm (top row) and 25 µm (bottom row) raster size which resulted in a detection of multiple ions including *m/z* 130.880, *m/z* 194.75, *m/z* 165.892, and *m/z* 854.824 ions. d) Averaged spectra of samples with high and low raster step size, and an off-sample membrane control highlighted unique mass peaks predominantly in low weight mass spectrum region (*m/z* 100 – 400) and a lipid spectrum region (*m/z* 780 – 925). e) Mass lists generated from the spectra in subfigure d were compared in a Venn diagram which showed an increasing number of detected peaks in the membrane, the 75 µm-raster step size scaffold sample and the 25 µm-raster step size scaffold sample and their intersections. Scale bar (c) = 0.5 mm

Next, an analysis of cells in pores without a scaffold surface was attempted. A sample thickness reduction is desirable in MSI experiments in order to generate spatially precise data without a chemical contribution from undesired planes which was relevant for analysis of pores without the sample surfaces. Cryosectioning was used to generate thin scaffold slices for a DIUTHAME-mediated SALDI imaging. Scaffolds were mounted in a 2-hydroxypropyl methacrylate (HPMA) polymer and frozen to prevent sample breaking. Afterwards, samples were sectioned at a 16 µm thickness onto an adhesive tape which prevented a sample curling Fig. 6.9a). The sample was placed on an Intellislide, facing towards a non-blotting DIUTHAME (thickness ≈ 5 µm) and thaw-mounted. Unfortunately, while the sample remained intact, the DIUTHAME membrane broke around the scaffold edges (Fig. 6.9b). Although the majority of the membrane remained intact, it was not suitable for MSI imaging using the same settings as described in the experiment related to the Fig. 6.8. A single ion image of at *m/z* 184.24 showed patterning and empty pixels near one of the membrane cracks (Fig. 6.9d). However, the use of adhesive tape clearly improved the adhesion of the membrane to the sample. It was assumed that the improved adherence in combination with a solid, sharp sample created acute angle stress on the membrane which resulted in the cracks.

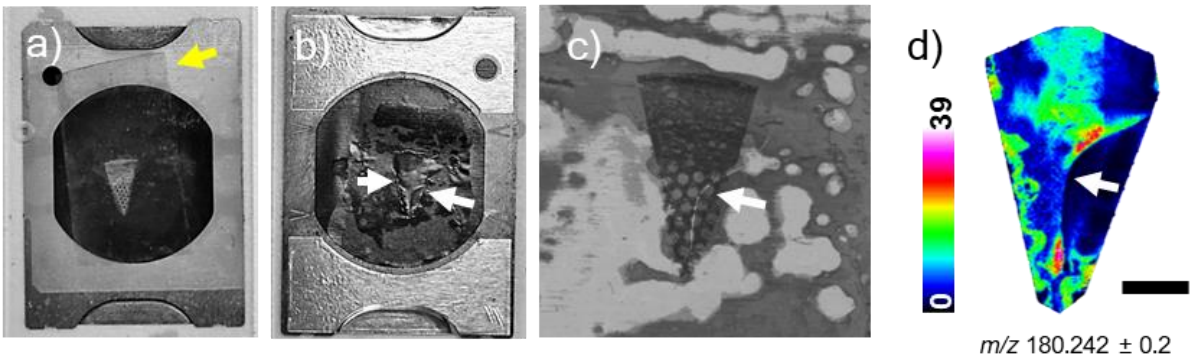

Figure 6.9 DIUTHAME-mediated SALDI MSI of CIVM scaffold sections. a) A liver CIVM scaffold was cryosectioned in HPMA and transferred on an Intellislide with an adhesive cryotape (yellow arrow). b) The membrane cracked near the sample edges (white arrows) during sample drying due to an excessive angular stress. c) A close up brightfield scan highlighted thawed HPMA (white spots) around the scaffold. d) A single ion image with an *m/z* 184.24 ± 0.2 mass filter exhibited patterning and dark pixels near the broken membrane which corresponded to a crack visible in (c). Scale bar = 1 mm.

A decrease of sample thickness was tested to determine whether a risk of a standard DIUTHAME membrane breaking would decrease as well. The scaffold was then treated with a 0.2 % TFA. 10 µm cryosections were found to not break the DIUTHAME membrane (Fig. 6.10a). The scaffold remained attached to the Intellislide following the sample sectioning using the adhesive transfer tape (Fig. 6.10b). However, a lack of adherence of a DIUTHAME membrane was observed. In parallel, the sample preparation was also examined for MALDI analyses. Scaffold sample preparation for MALDI MSI was unsuccessful as well, because of scaffold curling caused by lack of an adherence to a slide. A 6 µm scaffold cryosection was successfully transferred and attached on an Intellislide with an adhesive tape, which was subsequently removed by first thaw-mounting the Intellislide with the scaffold section sealed with the tape. Then, the sample was refrozen to the Intellislide while the tape was swiftly removed using a freeze spray, leaving a flat scaffold on the Intellislide. Brightfield scans of the sample composing of the Intellislide, the 10 µm scaffold section, the adhesive tape and a DIUTHAME (Fig 6.10d) and the Intellislide with a 6 µm scaffold only (Fig. 6.10c) which both showed a detailed structure of the scaffolds. Samples were analysed over *m/z* 100 – 1500 mass spectral region in the UltrafleXtreme II instrument at a 50 µm raster step size using the settings from data in Figure 6.6. The DIUTHAME-treated single ion image of an unknown component at *m/z* 207.05 showed unexpected patterns which did not resemble the scaffold architecture (Fig. 6.10e). It was concluded that the DIUTHAME membrane did not attach sufficiently to allow an analyte extraction based on the spatial ion distribution and the observed non-adherence of the membrane. Upon closer examination, the *m/z* 207.05 ion partially copied a structure of the scaffold. A putative $[PCh+H]^+$ ion at *m/z* 184.06 was observed at the upper edge of the analysed region in a honeycomb formation. Moreover, the corresponding brightfield images show an absence of the polystyrene scaffold in this region. Therefore, it was suspected that membrane interacted mostly with the edges of the scaffold and with polystyrene-free areas of the sample. The large patterns were a possibly result of solvent which was not sprayed on a flat surface. *M/z* 184.06 $[PCh+H]^+$ was also observed in MALDI data. A single ion image showed a distribution of this ion within the individual pores of a sample (Fig. 6.10f). However, the ion was found to be present in the scaffold as well. The increased ion intensity in the pores was likely connected with the absence of the polystyrene based on low intensity $[PCh+H]^+$ ion signal in the scaffold. Moreover, no

phospholipids were detected in the high *m/z* region and therefore a presence of the cells was not confirmed.

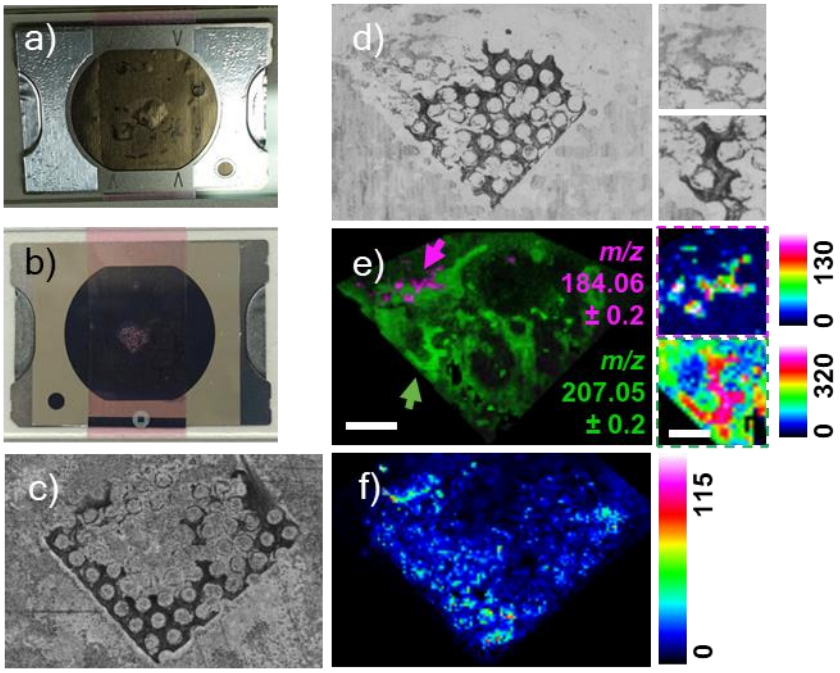

Figure 6.10 Thin CIVM scaffold cryosections in MALDI and SALDI. a, b) A 10 µm scaffold cryosection on an adhesive tape was thaw-mounted between an Intellislide and a DIUTHAME without a proper sample-membrane adherence. Brightfield images of c) the 10 µm DIUTHAME sample and d) a 6 µm cryosection on an Intellislide for a MALDI analysis showed a scaffold architecture. e) *m/z* 184.06 ion was detected in a polystyrene-free sample part (magenta arrow), whereas the *m/z* 207.05 ion was detected across an entire sample at unexpected distribution. Part of a scaffold was however detected at the sample edge (green arrow). Scale bar = 500 µm. f) A single ion image showed a distribution of *m/z* 184.06 ion in the scaffold pores. Scale bar = 1 mm.

From all MS sample preparation methods, a full scaffold SALDI method using a blotting DIUTHAME yielded the best results in hyperspectral mass spectrometry data which successfully revealed cell-related ions in the lipid region across the porous chip. An oversampling and an analyte depletion through prior laser ablation gave rise to membrane-related platinum ions, which were otherwise not suppressed, likely due to an ion suppression effect.

Scaffold sectioning was enabled by a scaffold mounting in a HPMA polymer, which was not expected to ionise in positive mode. Thick scaffold cryosections increased a risk of DIUTHAME membrane breaking, but a thin scaffold section was found as a way forward. However, scaffold sections were less likely to adhere to a

DIUTHAME membrane surface; possibly, because of a lack of soft biological material on the surface, which in the full scaffold sample was covered in cells.

Finally, it was found that generating ultrathin sections improved scaffold adherence to an Intellislide and thus opened a path towards scaffold analysis with MALDI. Typically, the cell-related $[PCh+H]^+$ (*m/z* 184) ion was accompanied by lipid-high molecular weight related ions (*m/z* ~600 – 900). The presence of cells was suspected in a small region of the CIVM scaffold sample based on the detection of the $[PCh+H]^+$ ion with a low confidence since no lipid related ions were found in the MSI data.

7. SRS-based cell segmentation with the Leica SP8

7.1. Introduction

The CHR-focused cell classification of hepatocytes and Kupffer cells using the SRS microscope was previously conducted in CIVM scaffold samples (Chapter 6.2). Although the spectral difference was observed between cuboidal hepatocytes and circular hepatocytes, Kupffer cells were not separated from the bulk cell spectra based on their spectral profile mainly due to a lack of pure Kupffer cell reference samples, which could be used for reference and for a potential machine learning model.

Label-free segmentation and classification of cells (i.e. separation the boundaries between cells and determination of a cell type) in a heteroculture has been extensively explored using spontaneous Raman microspectroscopy.[72-74,307,308] Spontaneous Raman techniques can result in robust, reproducible data by using long sample exposure to continuous wave lasers and the application of refraction grating which enables high spectral resolution acquisition. However, the disadvantages of spontaneous Raman scattering are low sensitivity, long acquisition time, and fluorescence-related background. In contrast, stimulated Raman scattering (SRS) is a fast-acquisition technique where single pixel exposure can be <1 µs. Since the coherent process probes only a small vibrational band, the probing laser wavelengths need to be repeatedly tuned to analyse the sample across a large Raman spectral region. This tuning can be prone to fluctuations in efficiency.

In order to address the cell segmentation in polyculture using the SRS, an imaging study was conducted in collaboration with an internal team researching the electrophysiology in a live, beating heart cell triculture grown in plates (primary cardiomyocytes, fibroblasts, and endothelial cells).[309] In this chapter, the cells were grown in a 2D culture on a glass slide to reduce the issues of loss of focus and poor imaging depth, which was found in the CIVM pores. Cardiomyocyte beating was incompatible with time consuming hyperspectral analysis and therefore all samples were PFA-fixed prior to SRS imaging. The aim of this study was to determine the composition ratio of cells in a sample batch without fluorescence labels, which were planned for different epitopes and targets in the cell.

The Leica TCS SP8 CARS/SRS microscope, equipped with a picoEmerald laser, generated two beams – a pump (720 nm – 940 nm) and a Stokes (1032 nm). The pump laser beam was tuned using an optical parametric oscillator (OPO). A hyperspectral image acquisition of SRS data was collected for wavelengths over a C-H region of the Raman spectrum (CHR) at 784 nm – 801 nm with a 0.5 nm step size. This corresponded to 3059 cm^{-1} – 2780 cm^{-1} and 7.8 cm^{-1} wavenumbers following the wavelength-wavenumber relationship shown in equation 3.1.

It was observed that the picoEmerald in combination with the LAS X software tuned imprecisely to given wavelengths in terms of laser power and spectrum position during high speed or time-consuming hyperspectral scans. Although they were not typically observed, the spectral errors were 0.1 nm – 0.3 nm off the set value and the pump power error was ≤ 5 %. The actual pump wavelength and power values were however not recorded in the LAS X software. Spectral and power fluctuations were also observed in recent analyses. Therefore, potential effects of these instrument artifacts were examined by comparing identical datasets.

The aims of this chapter were to:

- Examine whether the SRS Leica SP8 microscope equipped with a spectral-tuning OPO system can be used for label-free cell type classification of heart cell heteroculture by:
    - Acquiring high-resolution hyperspectral images of a CHR
    - Identify laser source-related noise in SRS spectra and separate it from a chemical information.
    - Evaluate the spectra denoising with ML models.

7.2. SRS and SHG of cell monocultures and tricultures

Cardiomyocytes, endothelial cells, and fibroblasts in individual monocultures were characterised using SRS/SHG hyperspectral microscopy with a 0.19 µm pixel size and a 3.28 µs pixel dwell time. Lock-in time constant was set to 2 µs to avoid over-extended sampling which would result in scan line artifacts, where the lock-in amplifier could record the signal from more than one pixel and generated lines instead of square pixels. SRS and SHG signal was collected in forward and epi-direction, respectively. The CHR of Raman spectrum was acquired with a 0.5 nm

tuning step size. Hyperspectral SRS and SHG data were denoised using an SVD algorithm. CH_3 and CH_2 SRS images were extracted from the data cube and subtracted ($|CH_3 – CH_2|$) using Fiji ImageJ Image Calculator function. A final three colour image overlay consisted of the $CH_3 – CH_2$ image representing the cell proteins, CH_2, which represented the lipids and the SHG data which captured the distribution of non-centrosymmetric structures in cells.

CH_3 images of Cardiomyocytes showed cells orientated in 3D clusters which were difficult to segment manually (Fig. 7.1a). A sharp contrast between cytoplasm and nuclei was observed in CH_2 images of Cardiomyocytes, which improved the visibility enhancement of nuclei through the image subtraction which had been, in contrast, poor in the CIVM scaffold samples. Interestingly, the CH_2 signal was observed prevalently in an immediate perinuclear area. A high concentration of fibrils which were most prominent in the CH_3 images were observed. These fibrils prevalently overlapped with a SHG signal which highlighted striated fibril structures, which were associated with myosin in sarcomeres.[131] Myocytes contained spherical depots observable in all three channels, which were likely centres of a myosin synthesis or storage.

Fibroblasts exhibited elongated morphology and a high variability in cell size as shown in the CH_3 image (Fig. 7.1b). The CH_2 images highlighted small droplets throughout the cellular cytoplasm in most cells and a diffuse signal which was homogeneously distributed across the cytoplasm of all observed cells. The overall CH_2 signal was higher, in comparison with Cardiomyocytes, which improved the contrast between cytoplasm and nuclei of cells. Furthermore, a punctate SHG signal, possibly collagen, originating from the fibroblast cytoplasm was observed in a majority of cells.

Endothelial cells grew in fusiform and squamous morphologies (Fig. 7.1c). The CH_3 signal showed the most prominent nuclear signal as opposed to the previous cell types. However, due to the relatively low cytoplasmic intensity of CH_2 signal, which was predominantly observed in the perinuclear region, the $CH_3 – CH_2$ subtraction resulted in approximately the same contrast between a nucleus and the cytoplasm. An SHG signal was observed both in the perinuclear region and in large punctae. Fibril-like SHG signal was not observed in the endothelial cells despite an observation of faint fibrils in CH_3 images and thus were unlikely myosin-related.

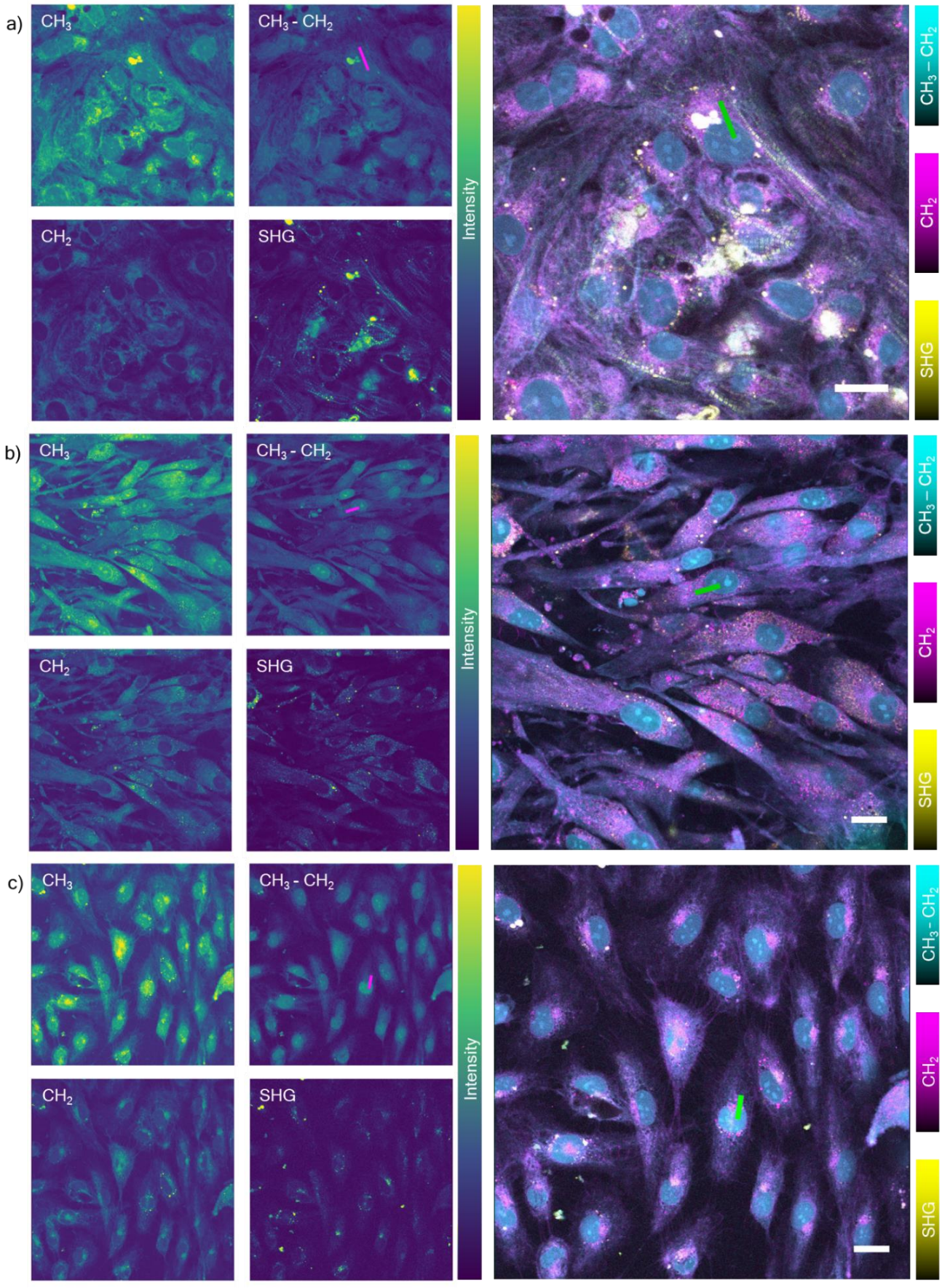
a)
CH3
CH3 - CH2
CH2
SHG
Intensity
CH3 – CH2
CH2
SHG
b)
CH3
CH3 - CH2
CH2
SHG
Intensity
CH3 – CH2
CH2
SHG
c)
CH3
CH3 - CH2
CH2
SHG
Intensity
CH3 - CH2
CH2
SHG

Figure 7.1 CH_3 and CH_2 SRS and SHG microscopy in a cell culture. Cardiomyocytes (a), cardiac fibroblasts (b) and endothelial (c) monocultures were imaged using hyperspectral SRS and SHG. CH_3 (2945 cm^{-1}) and CH_2 (2866 cm^{-1}) SRS images (2945 cm^{-1}) captured the lipid and protein distribution in the cells. A $|CH_3 – CH_2|$ image ratio was used to remove the lipid signal and highlight low-concentrated lipid nuclei. SHG highlighted putative myosin in muscle fibrils of Cardiomyocytes and intracellular collagen depots in fibroblasts and endothelial cells. Magenta lines in subtraction visualisation images and green lines in the overlay images were used to profile the $|CH_3 – CH_2|$ signal intensity between cytoplasm and nuclei in all cell types. Scale bars = 20 µm.

Intensity profiles of the interfaces between cell cytoplasm and cell nuclei in $CH_3 – CH_2$ images in Figure 7.1 were generated using the Fiji ImageJ “Plot Profile” tool, where a line selection was used to select pixels in the cytoplasm and a nucleus. The intensity profiles confirmed a low contrast between the cytoplasm, nucleus, and nucleolus in Cardiomyocytes (Fig. 7.2a), suggesting a low level of lipid components in this cell line. Conversely a clear intensity disparity between these cellular compartments was observed in cardiac fibroblasts (Fig. 7.2b), which suggested an increased concentration of lipids in the perinuclear cytoplasm. In endothelial cells, the ratio between the nuclear and cytoplasmic intensities was high in comparison with the cardiomyocyte profile plot, but not as high as the fibroblast nucleus/cytoplasm intensity ratio. Moreover, the nucleolus was not accompanied by a significant increase in signal intensity (Fig. 7.2c) as observed in the fibroblasts.

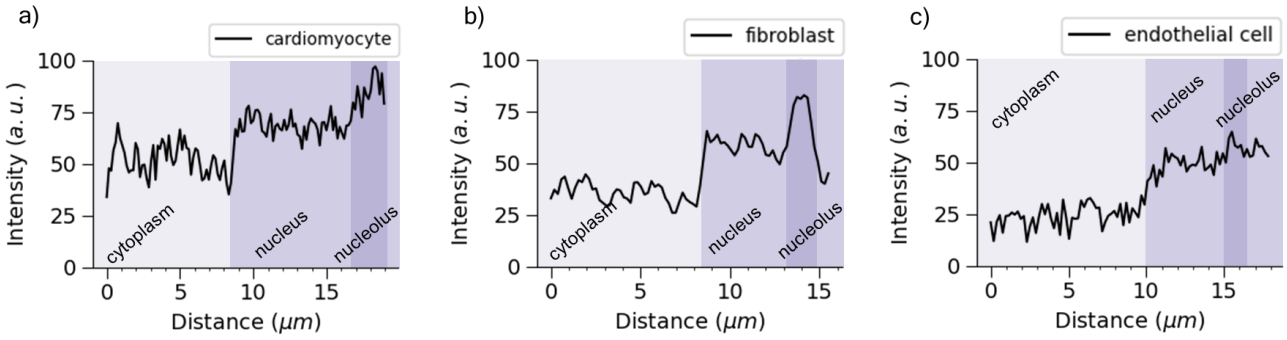

Figure 7.2 Intensity line profiles of cell nuclei and cytoplasm. Line profiles were generated in Fiji ImageJ, using the “Analyse>Plot Profile” function. Straight lines were drawn across the perinuclear cytoplasm the nuclei in Cardiomyocytes (a), fibroblasts (b),and endothelial cells (c).

Cellular features of each cell type captured with two-image SRS and SHG were summarised in Table 7.1. The SHG signal showed the most significant variability between individual cell types. Therefore, the SHG channel was considered as the most important data component in cell classification decision. Secondary

denominator was the CH_2 channel which varied in a signal intensity and a distribution in cytoplasm.

Cell type	CH_2	Cytoplasm/ nucleus contrast	SHG
Cardiomyocytes	• perinuclear	• low	• striated fibrils • large blobs
Fibroblasts	• cytoplasmic • punctae • homogeneous	• high	• cytoplasmic • small punctae
Endothelial cells	• perinuclear	• low	• perinuclear • medium punctae

Table 7.1 Heart triculture features observed with SRS and SHG.

Cells in a cardiac triculture were classified, based on the observed SHG and SRS phenotype of the individual cell types acquired from cell monocultures. The triculture was imaged using the same microscope configuration as for the SHG/SRS hyperspectral image acquisition of cell monocultures.

After obtaining the information about the phenotypes of cells in the individual monocultures gathered with the SRH and SHG images a triculture consisting of fibroblasts, Cardiomyocytes and endothelial cells was analysed with the SRS microscope. The SRS images showed a combination of all 3 phenotypes in the channels (Fig. 7.3). The manually drawn boundaries of all cells were approximated using the CH_2 channel. Cardiomyocytes were manually classified based on the striated fibrils and large circular structures (2 µm – 5 µm) detected in the SHG channel. Putative cardiac fibroblasts were highlighted based on the combination of the cytoplasmic punctae in the SHG channel and the homogeneous intensity and distribution of the CH_2 signal. Cells with increased CH_2 and SHG signals in the perinuclear region were identified as endothelial cells. Endothelial cells and Cardiomyocytes were prone to form clusters and grow in intertwined structures. Moreover, fibroblasts formed elongated, thin cell bodies connecting to other cells throughout the sample, which made manual label-free segmentation complex and inaccurate.

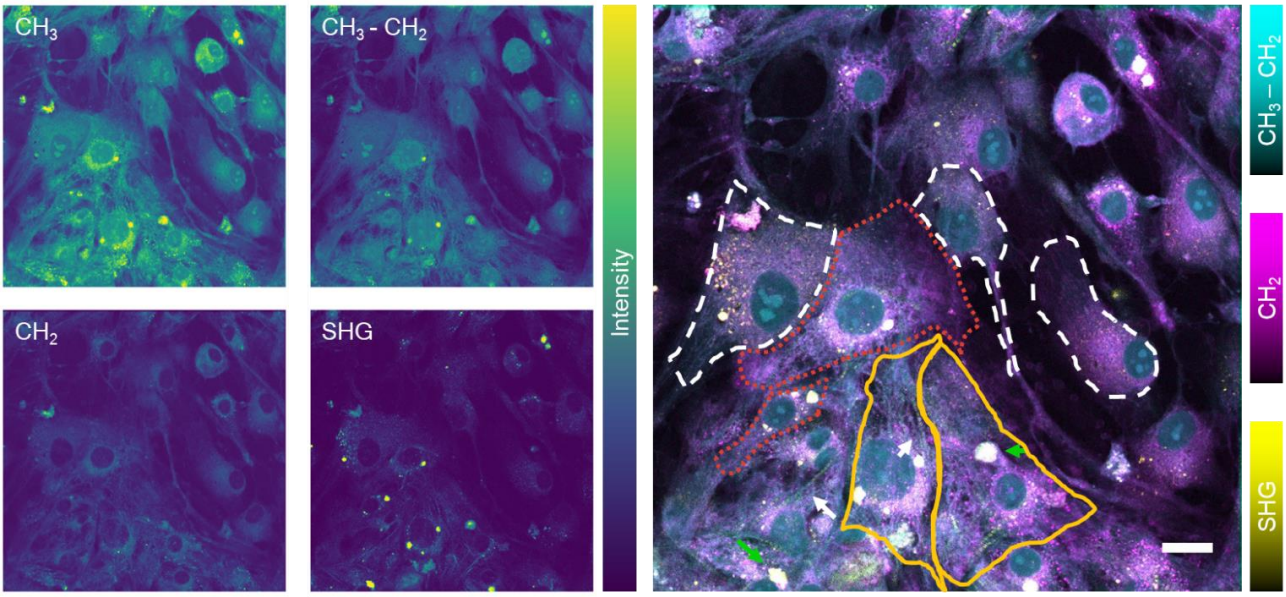

Figure 7.3 CH_3 and CH_2 SRS and SHG microscopy of a heart triculture. Hyperspectral data of the triculture consisting of Cardiomyocytes (yellow, solid line), fibroblasts (white, dashed line) and endothelial cells (red, dotted line) were acquired and plotted into images showing CH_3, CH_2, CH_3 – CH_2, and an SHG signal distribution. Myosin SHG signal was highlighted with white arrows, large depots in cardiomyocytes were marked with green arrows. Scale bar = 20 µm.

Despite the imprecise manual cell segmentation, cell phenotypes observed in the heart triculture in the SRS CH_3 and CH_2 images and the SHG image were successfully associated with respective monocultures, based on the SHG and CH_2 signals distribution. The main challenge of this analysis was that the overlapping growth of cells resulted in unanalysed clusters of unknown cells. Ideally, a cell segmentation would be improved by introducing cell membrane fluorescent labels, but these were not available at the time of the imaging experiments.

7.3. Cell classification with SRS spectra

The applicability of hyperspectral SRS (hSRS) of the CHR in cell classification of heterocultures was examined. In this chapter, data processing and analysis methods, which flattened the cytoplasmic SRS signal into a single spectral line and separated the individual spectra Principal Component Analysis (PCA) and random forest machine learning were created and evaluated using monocultures with the outlook of application in heterocultures. The goal of data acquisition was to collect maximum heterogeneity from the 3 different cell types. Therefore, cell nuclei were

omitted from the analysis since the chemical composition of nuclei is conserved (i.e., is not expected to differ between samples).

The cytoplasm of individual cells were manually extracted from the SVD-denoised hyperspectral SRS scans of the CHR of endothelial cell (endothelial cells) and cardiac fibroblast (fibroblasts) monocultures. The total number of samples used in this analysis was 91 (endothelial cell = 34, fibroblast = 57).

The sum pixel spectral values were averaged into a single spectrum per cytoplasm. The average SRS spectra revealed a high sample variability in intensity ratio between the 2945 cm^{-1} peak and OH peak at ~3070 cm^{-1} in the endothelial cell samples, whereas the fibroblast samples exhibited equal and stable ratio between the same wavenumber values (Fig. 7.4a). Spectra were scaled using a MinMax scaler to generalise the data and reduce the effect of unknown discrepancies during scanning conditions. The spectrum scaling reduced the variability in the 2800 cm^{-1} – 3000 cm^{-1} region in the fibroblast samples. Moreover, the variabilities in the 2850 cm^{-1} – 2930 cm^{-1} and the OH regions became more prominent relative to the ~2945 cm^{-1} peak (Fig. 7.4b).

PCA was conducted using the scikit.decomposition Python package[234] which reduced the dimensionality of the scaled data along the Raman spectrum. Interestingly, principal components (PC) 0 and 1 were in an anti-correlative relationship based on the angular shape of the sample scatter distribution (Fig. 7.4c). Moreover, a partial separation of endothelial cells and fibroblasts was found. However, none of the examined PCs showed clear spatial separation (Fig. 7.4c-d).
To examine the anti-correlative relationship between PC 0 and 1 and their connection to the SRS spectrum, loading matrix was accessed. In the loadings matrix, the relationship between individual wavenumbers and PCs was shown in a hierarchical order, where the PCs were aligned along the Y axis based on their explained variability from the highest to lowest value. Loadings (or weights) – shown as pixel intensity – described how much each wavenumber variable contributed to a specific PC (Fig. 7.4e). PC0 loadings indicated a negative relationship with the O-H vibration-related peaks (≥ 3000 cm^{-1}), whereas PC1 loadings indicated a positive relationship in the same spectral region, which confirmed the observed separation under an angle in the PCA plot. Dynamic loading gradients were found to negatively or positively correlate with the highest intensities associated with O-H stretch

maximum value at 3059 cm^{-1} (PC0-1) and a CH_3 peak at ~2945 cm^{-1} (PC0-2) and suggesting the PCs extracted chemically relevant information. A weighing anti-correlation was found between the OH and cell-related CH vibrational bands in PC0 and thus confirmed the most significant separation indicator was the ratio between the H_2O and CH SRS signals. Furthermore, the loadings at CH_3 and CH_2 (2866 cm^{-1}) peaks of PC2 showed a positive and negative relationships, respectively and thus revealed a lipid/protein separation between samples.

The scores matrix provided a concise information about a relationship between samples and PCs varying in values between -1 and 1. These values (scores) were used as coordinates in 2D PCA plots (Score plots). The score matrix was also hierarchically constituted of PCs with decreasing explained variability, which herein correlated with a decrease in positive and negative score values (Fig. 7.4f). The matrix revealed that PC0 was the most successful component in terms of spectral-based separation of endothelial cells and fibroblasts. Interestingly, PCs 3 – 13 with low explained variability showed similarities in score values between closely neighbouring samples, which were acquired in the same imaging experiment. Therefore, it was concluded that the SRS imaging with the Leica SP8 microscope generated data with a small variability between each scan.

The presence of artifacts originating from the Leica SP8 microscope was thought to potentially skew data by masking important components in the PCA analysis. Laser intensities and small variables in tuned laser frequencies were considered as the source of the artifacts. However, it was not possible to record these values in the LAS X GUI. Therefore, a calibration in the form of an internal standard, such as a lipid mixture or polystyrene beads, was necessary. This was fortuitously resolved as a result of the spectral window used for the acquisition of CHR partially captured the O-H vibrational band of H_2O in the sample and was therefore used as a calibration standard.

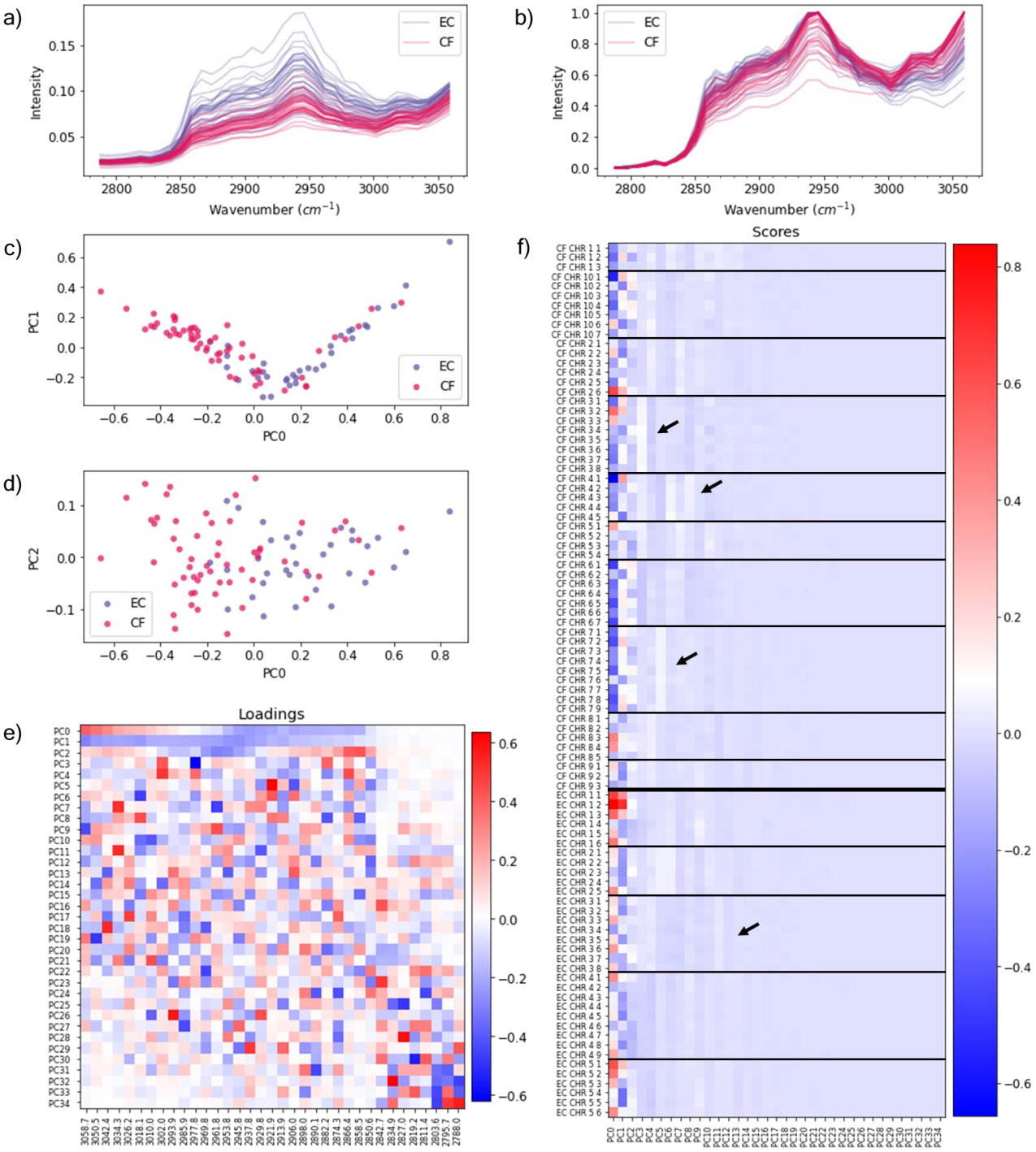

Figure 7.4 PCA with SRS spectra of fibroblasts and endothelial cells. a) CHR SRS spectra of endothelial cell and fibroblast cytoplasms (samples) were manually extracted from hyperspectral SRS images. b) Spectra were normalised to min and max values. c) PC 0 and 1 separated the samples in an anti-correlative relationship based on the angular data shape. d) Nonetheless, no clear separation of components was observed in the most significant PCs. e) Loadings of PC 0 – 2 showed dynamic loadings intensity correlating with water and cell related spectral peaks. Each loading (pixel) described the strength of a positive or negative relationship between a PC and a wavenumber variable. f) Score matrix revealed the scoring of each sample (Y axis) relative to all PCs (X axis). endothelial cells were mostly projected on a PC 0 with negative scores, where fibroblasts were dominantly projected with positive scores. PCs 3 – 13 exhibited similar scorings (black arrows) for samples acquired in the same hyperspectral SRS scan (black line separators).

Scan average H_2O SRS spectra were extracted from the full data set using the ROI selection hSRS script and averaged into a single spectrum (Fig. 7.5a). The low wavenumber region was the most conserved region in the spectra. The largest variability was observed in the CH bond related region which was likely caused by chemical components inside the ROIs. A polynomial curve was fitted through the averaged H_2O to further reduce the variability in the measured data. Afterwards, the individual averaged scans were divided by the total H_2O average spectrum of all scans which resulted in spectral corrections per each imaging scan (Fig. 7.5b).

Then, the spectral samples of cell cytoplasms were corrected by multiplication with corresponding spectral corrections. As a result, the average non-normalised and MinMax-normalised spectra for each sample exhibited smooth spectral points with less variations in (Fig. 7.5c-d). Notably, the fibroblast sample spectra exhibited a conserved shape in the normalised H_2O spectral region, which was expected to potentially improve the cell type separation in the PC0.

Indeed, the PC0 separation of fibroblast and endothelial cell spectra was slightly improved whilst still exhibiting an anti-corelative relationship with PC1. Similarly, partially improved separation of samples was observed in PC4. However, no significant improvement in sample separation was observed in other PCs (Fig. 7.5f).

Scores matrix confirmed an improvement in PC0 separation of fibroblast and endothelial cell samples by evaluating the samples with opposite scores. Although the samples separation was slightly improved by water normalisation, the scanning artifacts which connected samples from the same scan were not sufficiently suppressed as they were still found in PC3 and further (Fig. 7.5g). The PCs 0, 1 and 2 showed similar loadings along the SRS spectrum as the non-normalised PCs. Additionally, PC 3 and 4 loading values were distributed in gradients and thus suggesting spectra-relevant separation, rather than random noise (Fig. 7.5h) and therefore confirmed that the water normalisation improved the PCA-based dimensionality reduction precision.

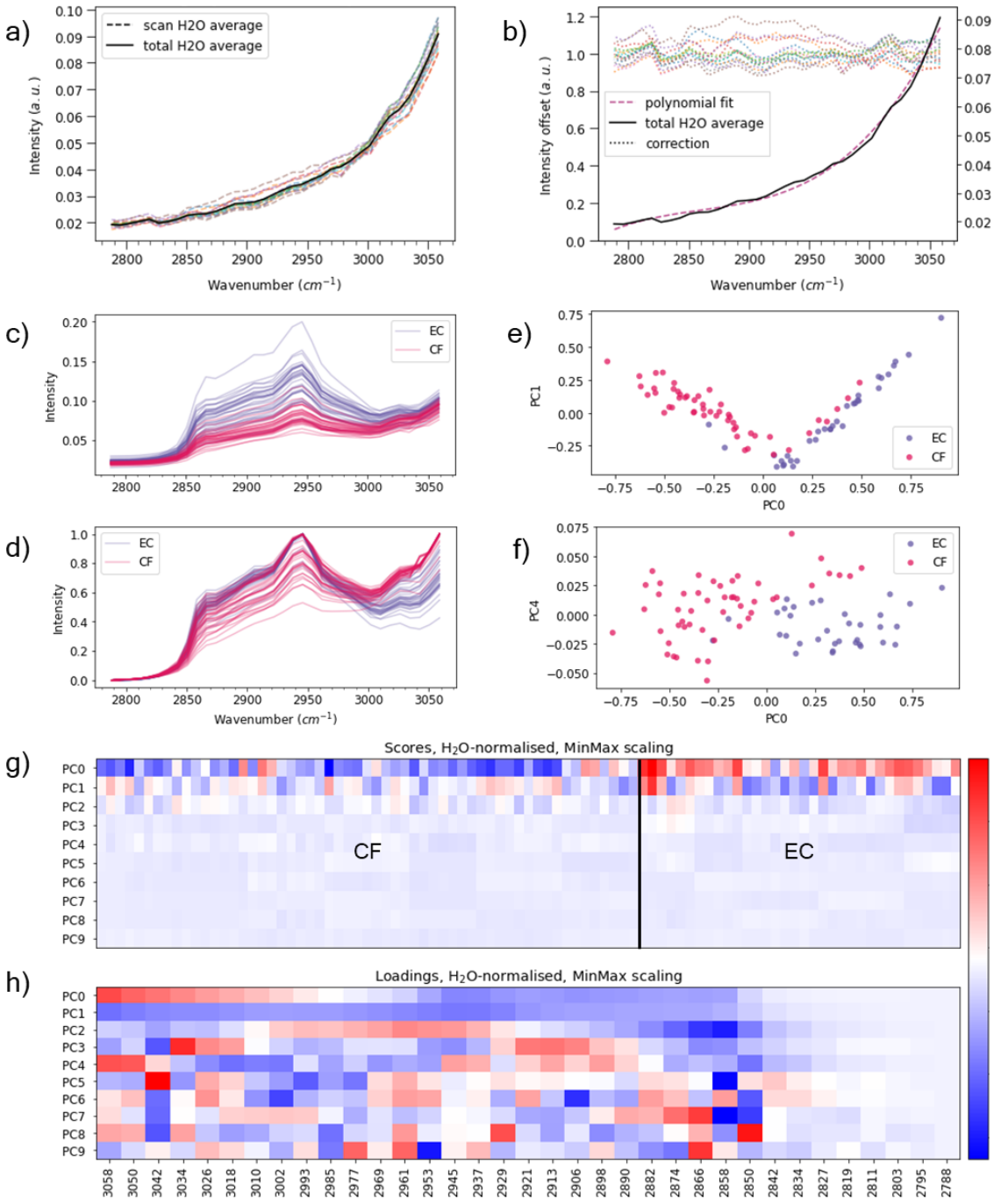

Figure 7.5 PCA with H_2O-normalised SRS spectra of fibroblasts and endothelial cells. Multiple averaged H_2O ROIs per each SRS acquisition (endothelial cell = 6, fibroblast = 10) were further averaged into a single "total H_2O average" spectrum (a), which was fitted with a polynomial curve (order = 5). The H_2O acquisition average spectra were divided by the polynomial curve to create a correction spectrum (b). By spectra multiplication, respective cell cytoplasm ROIs (samples) were corrected (c) and normalised to minimum and maximum values (d). PCA confirmed an anticorrelation between PC0 and 1 (e) and showed an improved separation of endothelial cell and fibroblast samples (f). The score matrix showed an increase of weights (scores) in PC0 component in comparison with non-normalised score matrix. Scan-related adjacent score clusters were observed in PC4 and onward (g). The loading matrix of H_2O-normalised PCA data showed dynamic loadings (weights) distribution which additionally correlated (positively or negatively) with SRS spectral peaks in PCs 3 and 4 in comparison with Figure 7.4f (h).

The H_2O normalisation effect on sample separation was further evaluated with the K-means clustering[234] in a PC0 and PC1 space, which generated two best fitting centroids best matching the sample clusters. Clustering of non-normalised PCA separation resulted in approximately 23 % of fibroblast samples associated with the main endothelial cell cluster and ~14 % of endothelial cell samples was found within the fibroblast boundary of K-means (Fig. 7.6a). The H_2O data normalisation decreased the mis-separated percentage of fibroblast and endothelial cell was 6 % and 14 %, respectively in H_2O -normalised K-means clustering of the same PC space. (Fig. 7.6b), which was above ~10 % classification error.

Therefore, the H_2O -normalised and normalisation-free principal components of endothelial cell and fibroblast monocultures were analysed using the random forest machine learning method for cell type classification.[310] PCs 0 – 4 were used as features in the analysis and the rest of the PCs was excluded owing to their low significance. A confusion matrix visualisation of random forest analysis of PCs before water normalisation showed a good overall classification precision of approximately 80 % (Fig. 7.6c). The water-normalisation further improved the overall classification accuracy >90 % (Fig. 7.6d). A significant variability (>10 %) was observed in non-normalised data cell classification and less 10% variability noticed in normalised data. Train-test machine learning models were run multiple times since single analyses were skewed by random training sample pool. Nevertheless, an accuracy of >90 % was considered sufficient for label-free cell classification despite the low number of available samples. No further samples were analysed due project delays and cancellation. however, this work shows a cell classification pipeline capable of a cell heteroculture has been laid out.

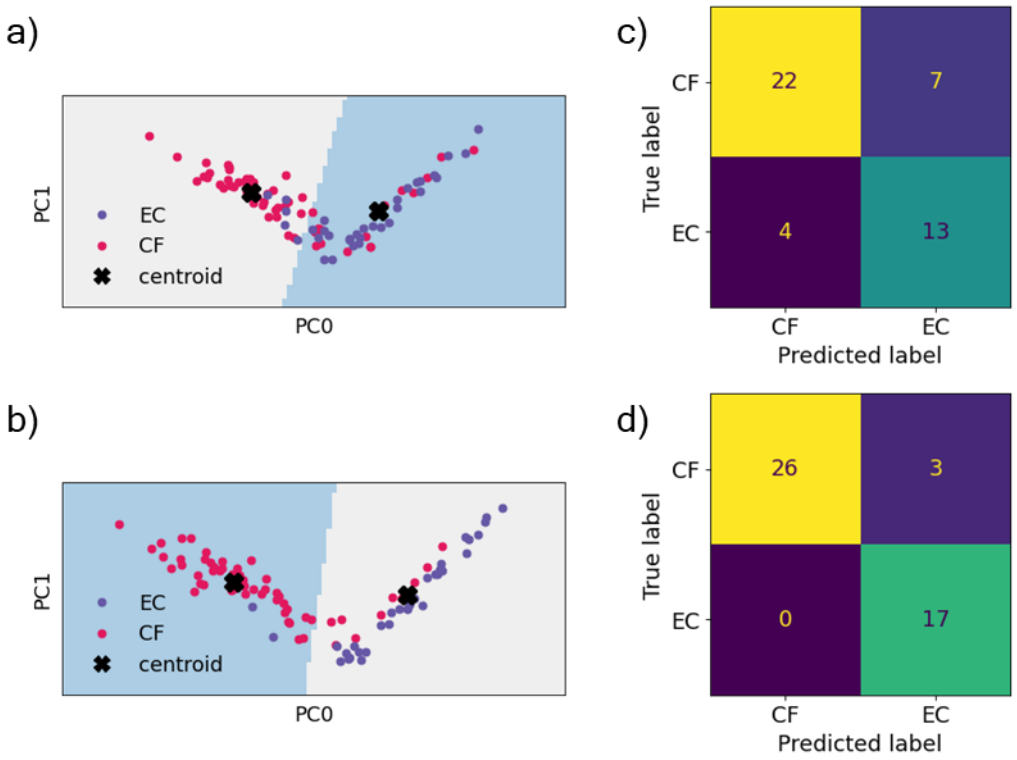

Figure 7.6 K-means and random forest analyses of principal component in monocultures data. K-means clustering separated the PC 0 and 1 in a 2D plot into 2 areas (grey and blue) based on centroid positioning and cluster shape in non-normalised data (a) and in H_2O-normalised data (b). A confusion matrix was used to visualise the prediction precision of a random forest classification in non-normalised data (c) and H_2O-normalised data (d) by separating 46 samples into true fibroblasts (top left), true endothelial cells (bottom right) and falsely classified fibroblasts (bottom left) and endothelial cells (top right).

7.4. Chapter summary

Cell classification in a heteroculture was successfully achieved by the combination of SHG and SRS. It was found that the SHG signal originating from the putative myosin was distributed significantly differently in cardiomyocytes as opposed to the punctate distribution of collagen (SHG). Whereas SHG signal originating from collagen and lipids (SRS CH_2) droplets were the most prominent cytoplasmic structures of endothelial cells and fibroblasts. However, the manual cell segmentation was not precise owing to a proneness of cells to cluster and grow over one another.

Furthermore, it was concluded that the ratio between H_2O -related wavenumbers and cell related wavenumbers of the Raman spectrum was the most significant factor in PCA, which lead to partial separation of fibroblast and endothelial

cell cytoplasm SRS spectra which were acquired in separate cell monoculture experiments.

Moreover, instrument-related imaging artifacts were indeed discovered in PCA of the SRS spectra. Low scoring PCs found a relationship between cytoplasms sampled from the same hyperspectral imaging scans. A normalisation to a H_2O SRS signal as an internal standard improved the separation of endothelial cell and fibroblast samples based on SRS measurements using PCA as a dimensionality reduction tool and K-means clustering. However, the H_2O normalisation did not result in a complete removal of the artifacts as seen in the PCA scores matrices. It was hypothesised that contribution of H_2O to the Raman spectrum exponentially decreases with a decrease in the wavenumber values and hence the normalisation becomes less efficient in low wavenumber regions. Therefore, the development of an internal standard with an improved SNR in the CHR is needed to improve the normalisation for cross-sample analyses.

Although two cell types in monocultures were successfully separated, cardiomyocyte monocultures and complex heteroculture analyses were not completed due to a lack of samples after the cancellation of the project which supplied the cell cultures for imaging.

8. Discussion and future perspectives

8.1. Identification of samples suitable for SRS-LDI translation method development

The aim of the first research section of this thesis was to find small molecules which could be detected in various biological matrices, using SRS and MALDI. To this end, a test compound set was assembled. The test compounds selected for evaluation were small molecules expected to generate Raman peak in the cell silent region of the Raman spectrum whilst also being compatible with MALDI MS Imaging. Both techniques were assessed in parallel in a series of increasingly complex environments with the aim to ultimately collect imaging data on SRS-and then MSI on the same sample. This analysis was also correlated with solubility, permeability, lipophilicity, and protein affinity properties of each test compound in order to determine which physicochemical properties are affecting the ionisation efficiency and detection for each test compound.

The majority of the test compounds, which were predominantly deuterium-labelled compounds had been selected due to their ability to produce a C-D signal in the silent region of the SRS spectrum. Unfortunately, many of these selected deuterium-labelled compounds did not produce a strong enough signal in the cell silent region in SRS experiments and/or generated a poor ion yield in the MALDI experiments and were therefore removed from the sample set. This outcome was expected since alkynes were more polarizable than C-D bonds. The remaining test compounds contained alkyne bonds, which were typically associated with higher SNR in the cell silent region when using SRS. It was found that compounds which contained alkynes in a π-conjugated system with aromatic structures exhibited enhanced SRS signal intensity of the alkyne peak.[96] In the MALDI MS study, two compounds – GSK4(x) and GSK90 – showed strong alkyne SRS intensities and gave high SNR ion yields in MALDI MS. GSK90 was expected to be a stronger ionising analyte in comparison with GSK4(x) based on its higher nitrogen-to-oxygen ratio in its molecular structure, which in turn increased the probability of the molecule to ionise in a positive polarity MS instrument. The measured solubility of GSK4(x)

was greater than for GSK90 and was therefore likely a secondary factor of the analyte ion yield in a pure sample powder form.

SRS analysis of deuterated samples produced low SNR C-D Raman peaks, which were accompanied by additional peaks, which were observed consistently at ~2300 cm^{-1} regardless of compound or sample concentration. The peak was thought to be an artifact of the experiment and related to N_2, based on available literature.[262] N_2 is a gas which forms ~78 % of Earth's atmosphere, however it is not soluble in aqueous solutions, however it was unlikely that the N_2 is soluble in aqueous solutions. Therefore, the source of the N_2 Raman peak was unexplained. Since this peak became prominent in low-concentrated analyte samples, it hindered the detection of the analyte by obscuring the C-D bond SRS signal in the cell silent region. This was also observed in low-concentrated alkyne containing compounds.

8.1.1. Physicochemical properties in MALDI

Analysis of test compounds spotted on tissue sections showed heterogeneity in ionisation efficiency between the analytes, but it also showed a dependency on the spot positioning in mouse brain tissues. For example, there was a clear difference in the ion intensity of the analyte compound when spotted on grey matter compared with white matter of the brain tissue sections. As described earlier (Section 4.3), this difference was due to an ion suppression effect, where molecules with a higher ionisation probability (typically lipids) become charged ions at the expense of less ionisation-prone molecules in the sample. In addition, although the MS signal heterogeneity in brain tissues reveals important interactions between myelinated axon-rich white matter and cell body-rich grey matter in brain ROIs, it is difficult to quantify owing to the variability between biological samples and the manual positioning of the analyte spot for each sample. To overcome this, tissue homogenates (mimetic models), which are devoid of high structures in tissues, were used instead.

The MALDI MSI of mimetic models, which consisted of serial dilutions of drug-spiked homogenates, revealed enhancement of the GSK4(x) signal in liver tissues which was in contrast to the MALDI results in pure compounds. No differences in signal intensity were observed with MALDI between GSK4(x) and GSK90 in brain

mimetic models. This was surprising since a brain is a lipid-rich organ and as such, was expected to reveal ionisation differences between low weakly lipid binding GSK4(x) and strongly lipid binding GSK90. It was likely that any interaction between the analytes and lipids was masked by the ion suppression effect in the brain tissues. The impact of lipid binding, on the detection of the analyte, is therefore very unlikely to be determined since the ion suppression effect is intrinsic to the lipids present in the brain tissue. As illustrated in Chapter 4.3, the signal intensity observed for GSK4(x) was greater than that generated for GSK90 in the 12 µm liver mimetic models. Based on these results a preliminary correlation relationship was proposed, where solubility and permeability of the test compounds were expected to positively influence the analyte ionisation efficiency, by improving the rate of matrix-mediated analyte dissolution and transportation through the tissue. Additionally, the correlation of protein binding and signal intensity is worthy of consideration, as this phenomenon was expected to negatively affect the signal intensity observed by preventing or slowing down the transport of the analyte through the tissue during matrix-mediated extraction.

It was also suspected that the 12 µm mimetic model sections were likely saturated with matrix which prolonged the matrix exposure of samples and an analyte extraction. This led to a 3 – 5× increase in signal intensity for the 12 µm section in comparison with 16µm sections in all samples apart from a GSK90 mimetic model.

To summarise, the mimetic models were too complex a model to investigate the correlation study between a test compound ionisation efficiency and physicochemical properties. Further sample preparation methods and analyte environments, which could give a better understanding of the link between physicochemical properties and ionisation efficiency needed to be considered. The replacement of a MALDI matrix with DIUTHAME membrane (as observed in chapters 5 and 6) was an excellent alternative approach, which could change the importance of the solubility by using the tissue moisture only without the additional wetting during matrix spraying. Furthermore, internal standards can potentially be useful in an analysis of protein affinity by removing the permeability and lipid binding properties owing to their deposition on a tissue surface by spraying.[311] More test

compounds need to be analysed in order to provide a robust dataset and prove the discussed statements.

8.1.2. Physicochemical properties in SRS

The SRS analyses of the pure solid test compound, GSK90, generated a stronger alkyne signal in the cell silent region in comparison with GSK4(x). The enhanced alkyne signal in GSK90 was most likely caused by the alkyne positioning between the two π-conjugated heterocycles, which were shown to play a major role in alkyne signal modifications.[91,96]

Unlike the MALDI MS analysis of the analyte spiked mimetic models, GSK4(x) was not detected in either the brain or liver mimetic models by SRS, whereas GSK90 was detected. The SRS signal of both analytes was accompanied by background noise from the associated intrinsic fluorescent components within the liver homogenate. The brain homogenate displayed less interference and produced much smoother spectrum baselines. A study of liver mimetic models with spontaneous Raman microscopy suggested an improvement in LOD through sample photobleaching which reduces the intensity of the autofluorescent background.[99] As expected, the sensitivity of SRS was found to be inferior to MALDI MS, which detected analytes in the lowest mimetic model concentration (100 µg/g). A significant finding of this work was that SRS did not appear to be affected by the physicochemical properties previously discussed, i.e., solubility and permeability, since the analytes were imaged *in situ* without MALDI matrix solution extraction, as demonstrated by the GSK90 and GSK4(x) mimetic model results. However, the spotting on tissue analysis showed a poorer GSK90 ion intensity in comparison to GSK4(x). This finding was likely caused by GSK90 penetrating deeper into the tissue than GSK4(x). GSK4(x) with a poorer permeability than GSK90 would be less able to pass across biological membranes and thus remained closer to the tissue surface.

This finding highlights a major difference between MALDI MS and SRS Imaging. For MALDI MSI experiments it is pre-requisite to perform a matrix solvent application/extraction process to elute the drug from within the tissue section onto the tissue surface and co-crystallize with the matrix upon drying. Such an extraction procedure is not required for SRS imaging, the drug molecules are analysed in-situ

within the tissue. One consequence of this disparity is that the precise location of the drug (at subcellular level) is lost, whereas with SRS Imaging, the exact location of the drug is maintained *in-situ*.

Secondly, the extraction process for MSI also increases the concentration of the drug on the surface of the tissue by extracting drug from within each particular voxel of the tissue section analysed onto the surface of the tissue section. This phenomenon explains why better signal intensities are observed for the drug in MALDI MSI compared to SRS imaging, where the analyte is being detected across a very thin optical plane. The degree of drug extraction is influenced by the physicochemical properties of the drug, in particular solubility and permeability. The more soluble and greater permeability of the drug the more extraction and co-crystallization with the matrix will occur compared to a drug which is poorly soluble in the matrix application solvent and has poor permeability (i.e., the less ability to pass across biological membranes). As SRS imaging does not require an extraction step, these particular physicochemical parameters do not need to be considered in SRS imaging of analytes *in situ*. Although protein binding and lipid binding physicochemical properties were considered to play a role in the success/failure to detect a drug in a tissue section. It was considered that the intrinsic background of strongly autofluorescent liver tissue was the cause of the absence of SRS GSK90 in a liver mimetic model at concentrations below 300 µg/g and the absence of GSK4(x) signal was directly proportionate to the lower SNR of the GSK4(x) alkyne bond in SRS of a pure sample in contrast with the GSK90 alkyne SNR and thus can be used to directly reflect the analyte concentrations in the sample. This was supported in an external collaborative study, where the same samples were analysed by a spontaneous Raman confocal microscope, which suffered from a strong Raman background in the liver mimetic model. However, photobleaching of the fluorescent liver components improved the LOD and served as further evidence that fluorescent background can mask the SRS signal.[99]

Finally, the dry tissue sample introduction to the SRS microscope resulted in a reduction of signal passing through the highly refractive optical media (glass – air) and thus resulted in overall low SRS signal. The sample was in a dry environment to prevent the homogenate delocalisation, which would occur in aqueous solutions and to comply with the local safety rules, which stated that all biological samples must be

sealed. Going forward, the overall detection sensitivity in mimetic models could be potentially improved using a dipping objective lens in an open sample, which would likely reduce the scattering. Alternatively, an introduction of a hardening mounting medium, such as MOWIOL could improve the SRS signal intensity of alkyne bonds in the cell-silent region, where it is expected that the mounting medium is not Raman active unlike in the fingerprint and the CH regions.

Such important discoveries afforded by these experiments breathe caution into the interpretation of the imaging experiments afforded by the combination of SRS and MALDI MS imaging on the same tissue sample. As with all aspects of drug discovery, the physicochemical properties of the drug are very important contributors to the success of drug imaging.

In consensus with the MALDI analyses, the analysis of additional new test compounds are required to confirm whether protein and lipid affinity are the driving force behind drug permeation through tissues.

8.1.3. GSK4(x) and GSK90 in cell cultures

For the final comparison, both techniques were examined for their feasibility to detect test compounds in a cell culture.

GSK4(x) and GSK90 were successfully detected in Calu-3 cells, although the latter induced a cytotoxic effect, which strongly affected the number of living cells in the experiment at the time of formalin fixation. Nonetheless, GSK4(x) was detected in small punctae in cell cytosol, some of which overlapped with lipid-rich vesicles. Furthermore, a punctate distribution suggested that GSK4(x) was actively endocytosed by cells, rather than penetrating the cell membrane which would have created a more diffuse SRS signal. GSK90 was however detected in entire cells, including membrane structures and large punctae. Additionally, GSK90-treated Calu-3 cells exhibited cytotoxic phenotype, such as membrane blebbing and very large vesicular bodies, which also exhibited GSK90 signal. The different uptake mechanism of GSK4(x) and GSK90 was likely connected to their lipophilicity and permeability, where GSK4(x) was labelled as poorly permeable according to the DCS chart (Figure 4.2) and weakly binding to lipids but GSK90 was a highly lipophilic

and permeable molecule, indicating that the latter was more likely to pass through cell membranes.

GSK4(x) was successfully detected in the MALDI MS study of frozen (-80 °C) cell pellets, which required multi-step washing, where the presence of cells in a pellet was confirmed by the detection of the phospholipid head group fragment (PCh) at *m/z* 184. The detection of GSK4(x) and the corresponding PCh ion was however unsuccessful in the MALDI MS imaging experiment. GSK4(x) and the PCh ions were not detected owing to the sample fixation in methanol prior to MALDI MS analysis. This result suggested that the lipids and the endocytosed GSK4(x) were delocalised below the MALDI instrument sensitivity level, which was poorer in comparison with the cell pellet MALDI MS due to the reduced amount of ionisable material in an imaging experiment in comparison with cell-rich pellet in the spot on a MALDI plate. Therefore, it was concluded that cell samples should preferably be fixed with formalin, although this generates new chemical species through protein cross-linking.[258]

A consideration of a drug-target interaction is pertinent in “chemical” SRS microscopy and MSI. A covalent inhibition – such as the mechanism of target interaction of GSK2 and a UL97 kinase – results in a chemical link between the protein and drug. This connection increases the molecular mass and thus complicates the search for the analyte using MS. On the other hand, the ability to detect a cell silent region tag (deuterium or triple-bond) in a drug using SRS is dependant only on the site of binding and a loss of SRS signal will occur only when the triple bond reaction or loss of deuterium. Albeit triple bonds are highly reactive, GSK90 and possibly GSK4 (mechanism of action of GSK4 is not publicly known) are steric inhibitors, i.e., their interaction with the target do not change the molecular structure of the drugs.

8.2. Translation of biological samples from SRS microscopy to MALDI/SALDI MS

8.2.1. Conductive materials in SRS microscopy

MALDI mass spectrometer instruments typically require conductive surfaces onto which the biological samples are placed in order to efficiently dissipate oppositely polarised surface charge and to direct ions into the mass analyser. This is typically done by using glass slides coated with a conductive surface, usually, indium tin oxide (ITO). Unfortunately, ITO absorbs near infra-red (NIR) light[273] in the region in which the majority of SRS microscopes operate. The NIR absorption was confirmed using the Leica SP8 SRS microscope with a pure analyte standard sample spotted onto ITO slides coated with low -concentrated-ITO and standard concentrated ITO. The SRS spectrum from the low-concentrated ITO slide contained noise, whereas slides with the standard-concentration ITO coating in SRS analysis appeared to perform better, showing spectra with the same SNR as unmodified glass slides. However, on closer examination, it was discovered that the scanned area of the standard ITO glass slide appeared to have been burnt-off. Therefore, it was hypothesised that the NIR lasers quickly burnt off the ITO from the glass slide surface, which then allowed the collection of the SRS signal. Unfortunately, this sample would then not be applicable in MALDI experiments, due to the non-homogeneous sample conductivity. Therefore, it was established that any translation experiment should begin with the analysis of the sample on a non-conductive surface. This prompted a search for methods, which would allow SRS analysis of a sample on a glass slide, followed by the application of MALDI.

The first approach considered was to adhere copper tape to the reverse side of a glass slide prior to MALDI analysis of tissue sections as proposed by Wu *et. al*[183]*.* This approach was replicated and successfully generated mass spectra; however, it was accompanied by surface charging during which the ion extraction was delayed and possibly reduced. This caused a positive mass shift of ions and a broadening of ion peaks in the mass spectrum. A reduction of a MALDI laser repetition rate by 2000 times slightly reduced the issue, but it rendered the approach inapplicable in large tissue imaging experiments by extending them from a range of hours to weeks.

The second approach applied DIUTHAME, a thin conductive membrane consisting of platinum and aluminium, which when placed on the sample surface extracted the analytes from the sample using capillary force. DIUTHAME is a SALDI technique since it does not use matrix for analyte extraction and thus has the advantage of not producing any matrix-related background ions. Background ions, however, were still observed in the SALDI MS analysis of the DIUTHAME membrane. These ions were associated with platinum, aluminium and their alloys and the low molecular weight adhesives from the DIUTHAME membrane. These background ions were supressed in intensity in in the analysis of biological samples.

DIUTHAME membranes are designed for the use with thick tissue sections, circa 30 µm. However, a 30 µm thick section is considered too thick for traditional MALDI MS Imaging experiments as it represents the analysis of drug from multiple vertically stacked cells within the tissue cryosection. Thick tissue sections reduce the spatial precision of the method because the extracted analytes may originate from an entire tissue section, which may not be representative of the optical image generated before the analysis. Additionally, the extraction process, which uses capillary forces was expected to favour the extraction of water-soluble analytes more than hydrophobic analytes. Therefore, to improve extraction, a methanol solvent spraying deposition was used. Indeed, the application of DIUTHAME using the solvent deposition process on a 16 µm-thick mouse brain cryosection followed by analysis in the low mass molecular weight range generated mass spectra with a better signal intensity. Additionally, 4.5× more mass peaks were detected than for the sample with no solvent application, hence indicating an improvement in analyte extraction from a sample. However, it was necessary to optimise the analyte spray to afford a balance between the maximum analyte extraction but without saturating the sample with solvent liquid. Due to the very fine pore diameters (~200 nm) of the DIUTHAME membranes, drug delocalisation was minimal and therefore, any analyte delocalisation caused by the solvent spraying method was likely to be below the spatial resolution of the UltrafleXtreme mass spectrometer. The absence of delocalisation was proven in the examination of the spatial distribution of GSK90, which was spotted below the tissue prior to thaw-mounting. The spraying of solvent increased the signal intensity of the analyte, whilst not delocalising the analyte from the boundaries of the analyte spot. Therefore, it was likely that no delocalisation occurred at 200 µm spatial resolution after a solvent spraying. The evaluation of the

migration of the GSK90 through the tissue experiment shed light on the extraction efficiency of DIUTHAME, which was detected using DIUTHAME prior to solvent spraying. This result showed that the DIUTHAME membrane indeed extracted analytes through 16 µm and even 30 µm of brain tissue, which could have an impact on the spatial precision of the method when looking at drug disposition in thick tissue sections. Interestingly, different ion adducts of GSK90 ionised in different spatial patterns, which was likely caused by a localised and heterogeneous presence of various salts and salt concentrations in the sample. This heterogeneity was however lost after the solvent spraying, with all the adduct ions exhibiting the same spatial distribution.

Although the solvent deposition significantly increased the analyte extraction and ionisation efficiency, the number of ions detected by SALDI MSI with DIUTHAME was lower than for MALDI MSI. The superior MALDI ionisation efficiency was attributed to a more efficient analyte extraction by the matrix solution, which would additionally co-crystallise more analyte species owing to its direct contact with the sample. However, it is important to consider the matrix-related ions, which can be also present in the MS spectrum and therefore it was proposed that the difference in the number of detected mass peaks between improved DIUTHAME SALDI and MALDI after matrix mass peak subtraction may reach similar mass peak counts. Interestingly, there were few common ions and poor overlap between the mass spectra generated by the two methods which suggested that both techniques extract different analyte species and at varying efficiencies. Some ions, however, such as the PCh ion were consistent between SALDI and MALDI.

DIUTHAME membranes were also successfully applied to the SALDI MS imaging of lipids in 2D cell cultures showing a potential in drug uptake analyses in future studies. DIUTHAME was applied directly onto cells grown on conductive glass slides, which immediately extracted the analytes from the cells. This direct application to live samples was preferred over the analysis of methanol-fixed cells as the fixing process was shown to wash off the lipids to levels that were below the detection sensitivity levels of the instrument and formalin-fixing the cells caused crosslinking between the cellular biomolecules, which could also decrease ionisation efficiency and result in physiologically irrelevant mass spectra.

8.2.2. SRS microscopy of tissues in an aqueous sample chamber

Equipment and laboratory risk assessments did not permit the use of open (i.e., unsealed) biological samples on the SRS microscope. This is because there was no biological safety containment on the microscope. All biological samples had to be sealed before any SRS analysis. To address this, a sample chamber consisting of two glass cover slips and a sealing gasket was proposed and evaluated with a sample mounted onto either of the glass cover slips facing inward. From a MALDI MSI perspective, the submersion of a sample into an aqueous solution would be undesirable and could result in analyte delocalisation or initiate chemical reactions in the sample particularly as the tissues are not fixed. Therefore, to be in keeping with the MALDI MSI approach, the SRS microscopy should ideally be dry samples too. However, the available SRS microscope required close working distance lenses (<1.1 mm) which were designed for aqueous and oil immersion. The use of a dry sample would therefore cause backscattering due to the air-tissue interphase created by the large refractive index mismatch between the glass cover slip and the air in the imaging chamber. The backscattering effect was expected to be less prominent in submerged tissue sections due to the absence of the air tissue interphase.

The Hyperspectral SRS data showed that while the overall spectral profile of the CH Raman region of dry and wet brain tissue cryosections did not differ, the structural details in the brain tissue, such as white matter bundles were observed in the wet brain sections, but not in the dry brain section. This was likely due to a combination of sample hydration, which restored the physiological morphology and a decrease of refractive index difference in the tissue-water interphase. Hence the sample chamber filled with an aqueous solvent was deemed the most suitable approach in terms of achieving an acquisition of the highest possible resolution for biologically relevant information from tissues in SRH and hyperspectral SRS.

Stimulated Raman histology (SRH) is a non-invasive histological tool, which can be used for an optical separation of cytoplasm and cell nuclei based on a ratio of CH_2 and CH_3 SRS signal,[291] which after an overlay with the CH_2 image creates

images which are similar to H&E images.[312] Using SRH instead of the gold standard H&E in conjunction with MALDI analysis was considered desirable since it would maximise spatial and chemical information from the sample. The SRH technique has been conducted with dual Stokes laser systems,[114,115] where the two vibrational frequencies were collected at the same time, whereas here, the Leica SP8 microscope employed a single Stokes laser line and thus required image acquisition in sequence in order to obtain CH_2 and CH_3 images.

Using the single Stokes system, in murine brain cryosections, it was observed that the CH_3 and CH_2 images did not precisely overlap in XY coordinates, which resulted in artifacts in the image subtraction. This issue of CH_3 and CH_2 mismatching was proportional to the image size and acquisition speed. The overlap mismatch was caused by the following factors: a) microscope stage mis-positioning between finalising the first SRS image and initialising a second SRS image of the same region, b) a loss of focus which was likely caused by an increase of sample temperature caused by the SRS lasers, c) inconsistent image tile-stitching. The loss of focus was not possible to correct in the manufacturer's acquisition software owing to incomplete integration of the SRS module in the sample acquisition corrections GUI, which was otherwise available for fluorescence image acquisition modes. Moreover, the separate tile runs could not be overlayed and stitched into a mosaic in the software. Although such corrections were easily executable outside the Leica software, the large tissue images were not successfully merged with the available tools and could not be reimported and processed in the Leica software. Hence, to overcome this, the scan size was reduced by half thus minimising the impact of the XYZ drift during the image acquisition. The spatial mismatch was removed by intensity averaging.

The subtraction of CH_2 from CH_3 led to detection and resolution of putative cytosolic structures from the white matter bundles in brain tissues. However, this subtraction did not highlight specifically cell nuclei. By performing a second CH_2 subtraction from the subtracted image, the SRS signal for the regions outside of the cell nuclei were supressed and consequently improved the specificity of this method. CH_2 and CH_3 peaks are broadly referred to as the lipid and protein peaks, respectively,[291] however, this does not mean these vibrational modes are exclusive

to either. Both molecular bonds are present in almost all organic molecules present in the cell. The lipids contain both molecular bonds, but the CH_2 bond is more concentrated in lipids than in proteins due to the prevalence of the long saturated fatty acid chains contained within lipids. Moreover, the hydrophobic properties of lipids result in their compact spatial distribution. Therefore, the CH_2 subtraction subtracts signal for proteins and lipids alike, but the subtraction in lipids is associated with larger weight. Cell nuclei contain almost no lipids in comparison with cytoplasm and therefore the subtraction there does not alter the CH_3 SRS image. The second subtraction further subtracted CH_2 signal from the CH_3 signal. The position of the double-subtracted nuclear signal was confirmed by chemical staining with a fluorescent Hoechst dye. This experiment also showed the applicability of the SRS in a simultaneous multimodal imaging with fluorescent microscopy as no signal interference was found from the dye. It was hypothesised that the second subtraction was most likely necessary due to an unexplained low protein signal intensity in the sample possibly caused by an interaction between the tissue section and the aqueous solution (Section 5.2.5). The tissue cryosections were found to swell in a water environment, during which the sections increased in volume by taking up water, which in turn displaced the tissue from the focal plane and reduced the overall signal intensity. This likely affected lipids to a lower extent owing to their hydrophobic properties. Similarly, less soluble collagen structures which were detected with SHG were less prone to signal intensity issues in water solutions. The swelling was partially reduced by replacing H_2O, which was hypotonic, with PBS. Incubating in PBS partially improved the nuclei intensity in the single-subtracted SRS images. To remove the swelling completely, tissues were also imaged in a Prolong Gold mounting medium, which reversed the swelling of the tissue samples observed with the water solution. It also increased the background signal because the mounting medium was based on glycerol and other organic compounds, which were active in the cell silent region. The increase in the background SRS signal resulted in the same separation of nuclei and cytoplasm in the subtracted images as the tissues in the PBS samples, which was devoid of background signal.

8.2.3. SRS-to-MSI with DIUTHAME

The same sample analysis approach was explored in brain tissues using SRS and SALDI, where the same sample was a brain tissue cryosections, which was thaw-mounted on a cover glass and enclosed in a PBS-filled imaging chamber for SRH image acquisition. After the SRH acquisition, the cover glass with the sample was removed from the enclosure and it was refrozen again to allow thaw-mounting of the tissue to the DIUTHAME membrane. The DIUTHAME mounted sample was analysed in the MALDI TOF mass spectrometer, whilst placed on a conductive slide. The obtain mass spectra were compared with additional cryosections of the same tissue which were used for a MALDI analysis and a direct SALDI analysis with DIUTHAME without the SRS imaging step. The resulting mass spectra of the post-SRS SALDI sample were negatively shifted in their mass-over-charge values in comparison with the mass spectra of the samples, which were directly analysed with SALDI and MALDI. The negative shift in the post-SRS mass spectrum was thought to be caused by a shorter travel distance from the sample surface to the ion detector in the MS instrument, which was reduced by the introduction of a 0.17 mm-thick cover glass. Post-SRS SALDI spectra therefore required a positive shift correction, which was approximated based on the measurements of known mass peaks and mass peak patterns. Striking differences were observed between the two SALDI mass spectra obtained from 1) a tissue mounted between a conductive slide and DIUTHAME and 2) post-SRS SALDI mass spectra, where the tissue was additionally mounted on a glass cover necessary for SRS microscopy and had been submerged in PBS. The first major difference was that the total number of detected ions in the post-SRS sample was approximately half of those observed in the SALDI MS spectrum that was likely an outcome of tissue submersion in the PBS, where the analytes potentially delocalised. Secondly, only half of the post-SRS SALDI ions matched the SALDI ions. This was predominantly caused by an increased lipid fragmentation in the sample, due to the extended exposure to PBS during SRS imaging, which may have been accompanied unknown enzymatic reactions in the unfixed tissue or by an unknown mechanism between the tissue, water and the DIUTHAME membrane.

Finally, the spatial overlap between SRS and SALDI MSI in the same tissue sample was not achieved due to the time limitation of this project. Generation of full tissue section SRH images was cumbersome and despite the experimental modifications suffered a high failure rate caused by the loss of sample focus in the microscope. Therefore, only a single SRS-to-SALDI MSI experiment was finished, in which the tissue warped during sample handling after SRH image acquisition, which made the spatial co-registration of the SRS and MSI data impossible. Nevertheless, this method was proven as a successful path towards the same sample analysis and if time permitted, this experiment would have been fully finished by overlaying the images from two imaging modalities.

8.3. Imaging of liver organ-on-chip complex *in vitro* models

The organ-on-chip complex *in vitro* models (CIVMs) are structurally complicated samples which are not typically designed for high resolution optical imaging and/or MSI. Therefore, the imaging analyses are often superficial. Label-free imaging approaches of these samples is an unexplored opportunity., In this work, liver CIVM scaffolds were used to evaluate the ability of the in-house label-free imaging techniques – SRS/SHG and SALDI and compare their output with fluorescent microscopy using a light sheet microscope at Cardiff University. The scaffolds were covered with formalin-fixed hepatocytes and Kupffer cells, which were treated with fluorescently labelled anti-sense oligonucleotides (ASOs), which were a part of a study, which was unrelated to this thesis.

In Chapter 5, it shown that the Leica SP8 SRS microscope can be used to collect UV-excited fluorescence signals and hyperspectral SRS signals simultaneously. In Chapter 6, tuning across the CH region of the Raman spectrum, cell lipids, polystyrene scaffold, and a green laser-excited fluorescence signal of ASOs was detected without any signal interference between SRS and fluorescence channels, in the dual SRS-fluorescence analysis, which showed the presence fluorescent tags excited in a wavelength range of UV to 488 nm were unlikely to hinder the hyperspectral SRS analysis. The hepatocytes were separated into cuboidal and circular hepatocytes based on the fluorescence signal accumulated in the cell nuclei and cytoplasm, respectively. The hyperspectral SRS imaging in

combination with NMF and FSC^3 algorithms revealed Raman features which confirmed the presence of both hepatic phenotypes. However, Kupffer cells were not found using the hyperspectral SRS of CH region, possibly because of a low heterogeneity of the cell signal in this spectrum region. It should be considered to undergo future cell segmentation studies in the fingerprint region of the Raman spectrum since it is more likely to capture heterogeneity between cell phenotypes and cell types.[73] However, to achieve this, the unwanted sample drift must be mitigated since the acquisition of fingerprint spectrum with the tuning SRS system is more time demanding.

Fluorescence light sheet microscopy enabled the capture of the entire CIVM scaffolds including the scaffold surface and pores within a single image, which was not possible to execute with the standard inverted confocal microscopes, where the signal would not penetrate an entire sample due to light scattering. The possibility to rotate a sample to a specific angle allowed simultaneous excitation and detection in a right-angled light path between the objectives and the sample. The light sheet imaging with a combination of fluorescent labels confirmed that the majority of fluorescent ASO were observed in cell nuclei in cuboidal hepatocytes and in cytoplasm of circular hepatocytes.

A previous study in murine models in 2D culture showed that the ASO localised mostly in the circular hepatocyte cytoplasm.[301] Results in the organ-on-chip liver model however suggest that in physiological conditions, which were mimicked by the CIVM model, hepatocytes are prone to form cuboidal cells, which changed the ASO localisation and the overall cell physiology based on the observed ASO distribution in the fluorescence channel and the cell morphology in the SRS channel.

The organ-on-chip scaffolds were constructed from a >200 µm-thick, porous layer of polystyrene. Polystyrene is an isolator and therefore, it was unlikely the cell on a scaffold surface and in pores would ionise in positive mode MALDI mass spectrometer. However, by applying DIUTHAME on the surface of the scaffold and by connecting the DIUTHAME to a conductive slide, a new conductive pathway for the negative charge to dissipate was created. This approach resulted in the successful analyte extraction and ionisation from the organ-on-chip sample. The ionisation efficiency of the cells and scaffold were low based on the increased ion

intensity of platinum ions, which was considered as a marker of low amount of analyte on a DIUTHAME membrane surface, where a layer of platinum was deposited to promote sample ionisation.[185] The detection of DIUTHAME-related platinum ions was unexpected since platinum ions had been observed at very low intensities in 2D cell SALDI MSI in Chapter 5 where the platinum ion detection was associated with low amount of analyte available for ionisation. The detection of platinum was considered to be related to a possible partial isolation from the polystyrene cell scaffold, wherein a local resistance imposed by the scaffold could lead to a prolonged thermal energy build up during the ionisation process[171]. This would be more likely to separate a platinum ion from the DIUTHAME membrane surface with a very low analyte concentration which could act as an energy acceptor. The ions were not characterised due to the expected positive mass-to-charge ratio shift in the mass spectrum owing to the large sample thickness and because the tissue sample was supported by glass cover slip glass. In future experiments, calibration samples need to be present on the membrane surface at the same height as the analyte to provide reliable mass spectra.

8.4. SRS-based cell segmentation with the Leica SP8

The ability of an SRS microscope to separate different cell types in a heteroculture was tested using a heart triculture consisting of cardiomyocytes, cardiac fibroblasts, and endothelial cells. Firstly, the separation was examined using a $|CH_3 - CH_2|$ image subtraction, to approximate a protein ratio between a cell nucleus and cytoplasm. The lowest protein ratio was found in cardiomyocytes and the highest ratio was found in fibroblasts. In addition to this information SHG distribution of collagen and myosin in cells was used as a second cell type marker. This improved the accuracy of cell type prediction and was conducted manually in a heteroculture. The manual segmentation and separation were however cumbersome since only a small population of the cells within an image were identified with enough confidence due to the change of morphology of the majority of cells in a heteroculture in comparison with their morphologies in monocultures.

Hyperspectral SRS analysis of the cells in monocultures was conducted to determine whether spectra from the CH region can be used in cell classification studies. A PCA analysis[73] of fibroblasts and endothelial cells resulted in a poor

separation. Principal components which explained the largest variance percentage in the analysis separated samples based on their H_2O-protein-lipid ratio, but upon a closer examination, the low-weight principal components were found to be affected by individual scans instead of the chemical composition of the sample. After a microscope system investigation, it was concluded that the laser source fluctuations during the hyperspectral SRS imaging were prominent enough to be detected by PCA. Therefore, the spectra were normalised using H_2O as the internal standard, which resulted in a partial improvement in the PCA-based separation of the two cell types. It was hypothesised that the dimensionality reduction for cell classification removes important datapoints from the dataset. On the other hand, random forest is non-discriminatory to any feature (wavenumber) which may be important in low-variable data. Indeed, the Random Forest classification of the two cell lines resulted in highly precise spectra separation (>85 % accuracy).

This mini-project, where SRS-based cell separation was explored, was supporting a research project of Kavita Raniga (GSK), who studied the cardiovascular toxicity through electrophysiology and brightfield microscopy of the heart heteroculture. The aim of the SRS-based cell segmentation was to determine how different cell types reacted to treatments. The project was unfortunately cancelled before all the proposed analyses were completed and thus the evaluation of the outcomes could not be achieved using this method.

8.5. Future perspectives

The main goal of this thesis, which was to develop a method for the analysis of the same biological sample by the combination of MALDI MSI and SRS microscopy, was achieved. However, the proof-of-concept experiment, where the SRS and MSI data could be merged, was not finished due to unforeseen delays in training and gaining access to the necessary analytical instruments. These factors also negatively impacted the remaining small research projects.

Nonetheless, it was demonstrated that conductive surfaces can interfere with SRS microscopy and therefore procedures where conductive properties were successfully applied to a sample slide after an SRS analysis were developed. One of these was the use of copper tape, but sadly, this achieved limited success. However, the use of a SALDI technique incorporating DIUTHAME membranes proved successful, In future, other SALDI methods, such as spraying a layer of conductive nanoparticles, such as platinum[272], or as more recently published, the use of a nanoparticle substrate consisting of modified gold nanostructures applied in a combinatory tissue analysis using SALDI MSI and surface-enhanced Raman spectroscopy.[313] However, this method is likely to be inapplicable in coherent Raman processes due to the NIR laser absorption by the conductive materials.

In accordance with GSK Policy, the SRS microscopy was conducted in samples which were sealed in an aqueous solution. This caused swelling in the non-fixed tissues negatively affecting the performance of SRH. However, performing the experiments in a standard biological laboratory, the use of imaging chamber could have been replaced by lowering the condenser or the objective lens directly on a sample.[114] This would have reduced the swelling effect and improved the SRH contrast between the cytoplasm and cell nuclei.

To generate SRH images of full tissue sections, SRS images focusing 2 vibrational modes were acquired in sequence, which was inadvertently accompanied by a Z focus mismatch between the two modes. This mismatch made the image calculations necessary for SRH difficult. The need to scan the tissue in sequence was caused by the application of only one pump and one Stokes laser. The next generation of new laser sources employing two Stokes beams will significantly reduce this issue by imaging two vibrational modes, e.g. CH2 and CH3 vibrational modes, at the same time.[113]

Expectedly, the limit of detection of MALDI surpassed the limit of detection in the cell-silent region of the SRS significantly in drug spiked mimetic models. The limit of detection of the alkyne-labelled GSK90 (ponatinib) with SRS was approximately 200µg/g of analyte per tissues, whereas the limit of detection using MALDI was in the lowest analyte concentration (100 µg/g) in this sample and even below this concentration as shown in Appendix 8. It was also observed that although SRS is virtually label-free, the autofluorescence from the liver mimetic models appeared to be creating an electronic background which reduced the LOD in liver.

Despite the superior detection sensitivity, MALDI ionisation efficiency is susceptible to variation depending on the local chemical composition. It has been shown that lipids can cause ion suppression, which decreases the ion intensity of other analytes in the vicinity.[178,314] Additionally, a recent study showed a dependence of vibrating edge spray ionisation MS technique on physicochemical properties, such as proton affinity and a partition coefficient.[315] Herein, it was proposed that analyte solubility and permeability influence analyte ionisation efficiency and detection in tissues. Additionally, lipid and protein binding reduce the tissue penetration speed and thus negatively affect the extraction efficiency and ultimately the detection of the analyte by MALDI. Furthermore, the physicochemical properties will also affect the distribution of the analyte in tissues and within cells. Preliminary SRS data showed that a low protein- and lipid-binding analyte may be prone to be sequestered in vesicles, whereas a high lipid- and protein-binding analyte was likely to penetrate membranes and localise throughout a cell. An imaging analysis of methanol-fixed cells using MALDI was not possible, most likely due to a washing off of lipids during fixation or matrix application (Section 4.4). The use of DIUTHAME however resulted in successful cell detection in SALDI MSI, albeit with low number of detected ions well above the LOD (SNR < 10) which included ~3 putative lipid ions and the $[PCh + H]^+$ cell and tissue marker ion. Nonetheless, this number of positively cell-related ions is very low and is likely insufficient for advanced analyses. This is likely due to the low amount of ionisable cellular material in each raster spot which be a limiting factor in high resolution MALDI MSI.

Recent advances in MALDI MSI culminated in the addition of a post-ionisation laser, a technique known as MALDI-2. MALDI-2 offers a formidable opportunity for increasing the sensitivity of a number of classes of small molecules, in many occasions by up to 2-3 orders of magnitude.[316] This will help alleviate the issues of

low sensitivity from sampling small raster spots and spatial resolution. MALDI-2 employs a second laser which ionises the chemical plume of created by the impact of the first laser. This technology has demonstrated an improvement in spatial resolution to sub-cellular levels with high SNR and has also been used successfully in MSI-based cell classification experiments.[15] This innovation in MALDI technology brings improvements to the method which would be highly beneficial to the research of small structures in tissues and the SRS-to-MALDI MSI analyses in tissues, cells and CIVMs at high resolution due to its capability to visualise subcellular structures.

The combination of SRS and lightsheet fluorescence showed a correlation between the difference in chemical composition and ASO uptake of cuboidal and circular hepatocytes grown in organ-on-chip CIVMs. A recently published study of ASO uptake in hepatocytes in a 2D cell culture, where hepatocytes sequestered the ASO similarly as the circular cells in CIVM scaffolds. However, this study has shown exclusively circular phenotype of hepatocytes. Herein, the hepatocytes grown in the CIVM scaffolds exhibited cuboidal morphology in addition to the circular morphology. The ASO distribution in circular hepatocytes was cytoplasmic and punctate, which was in consensus with the previous study in 2D cell cultures. However, it was shown that the ASO localised in cell nuclei in cuboidal hepatocytes instead. The cuboidal hepatocytes were thought to be the physiological morphology, which can be found in liver tissues and thus proved the pitfalls of 2D cell analyses and supported the need for CIVM studies. The ASO distribution in Kupffer cells was suspected to resemble the cytoplasmic punctate distribution, which were found in the circular cells since only two ASO distribution patterns were observed, and the nuclear signal was exclusive to hepatocytes. However, future studies need to include specific fluorescent labels to confirm the hepatocyte and Kupffer cell in order to assign the ASO distribution with confidence.

Finally, the Leica SP8 SRS microscope was assessed for its use in cell classification experiments. The results obtained demonstrated that the instrument laser source fluctuation affected the spectral information and the resulting segmentation. Although the effect of the laser fluctuation was partially supressed in the cell segmentation analysis, this was merely due to the presence of O-H vibrational mode associated with an omnipresent H_2O signal in the CH region. This

was incorporated into subsequent studies as an internal standard. Future hyperspectral SRS analyses in the fingerprint region would benefit from the application of internal standards which would be used for spectrum normalisation.

To summarise, the methodology for the analysis of a biological sample with MALDI MS imaging and SRS microscopy was established. It was found that conductive elements necessary for successful ionisation in MALDI were a major hindrance in SRS microscopy. To circumvent this issue, non-conductive glass slides were used for SRS imaging, which were then modified with conductive DIUTHAME membranes, which replaced the role of conductive slides and matrix. Apart from animal tissues, this approach was successfully applied in SALDI MSI of cells and complex *in vitro* models.

The complementarity of SRS and MALDI was explored by an analysis of small drug molecules in various biological environments based in correlation with their physicochemical properties. The physicochemical properties were likely dictating the analyte extraction in tissues efficiency in the first step of MALDI and SALDI MS. SRS was used as a reference technique of drug distribution in tissues since it shed light on *in situ* distribution of drugs, unlike MALDI and SALDI techniques which sampled the analytes from the entire depth of a tissue.

Leica SP8 SRS microscope showed a potential in cell classification in CIVMs and 2D cell heterocultures. Small variabilities in the hyperspectral SRS data were found during laser tuning, which had an impact on the machine learning segmentation. The tuning effect was partially reduced by using water as an internal standard. However, improved internal standards should be explored in future analyses to improve the correction efficiency. Alternatively, alternative hyperspectral SRS system (e.g., spectral tuning) should be considered for cell classification analyses between samples.

Finally, the light sheet microscope laser configuration allowed an illumination and collection of the pores and surface of the CIVM scaffolds, which lead to the confirmation of the presence of cuboidal cells inside the pores and the confirmation of the colocalisation between nuclei and ASO deep inside the scaffold pores. Therefore, light sheet microscopy considered the best available approach for a fluorescent microscopy of the liver organ-on-chip CIVM.

9. References

1 Wang, G. & Fang, N. in *Methods in Enzymology* Vol. 504 (ed P. Michael conn) 83-108 (Academic Press, 2012).

2 Malamy, J. E. & Shribak, M. An orientation-independent DIC microscope allows high resolution imaging of epithelial cell migration and wound healing in a cnidarian model. *Journal of Microscopy* **270**, 290-301 (2018). https://doi.org/10.1111/jmi.12682

3 Wang, X. *et al.* Single-shot isotropic differential interference contrast microscopy. *Nature Communications* **14** (2023). https://doi.org/10.1038/s41467-023-37606-6

4 Imai, R. *et al.* Density imaging of heterochromatin in live cells using orientation-independent-DIC microscopy. *Molecular Biology of the Cell* **28**, 3349-3359 (2017). https://doi.org/10.1091/mbc.e17-06-0359

5 Valm, A. M., Oldenbourg, R. & Borisy, G. G. Multiplexed Spectral Imaging of 120 Different Fluorescent Labels. *PLoS One* **11**, e0158495 (2016). https://doi.org/10.1371/journal.pone.0158495

6 Valm, A. M. *et al.* Applying systems-level spectral imaging and analysis to reveal the organelle interactome. *Nature* **546**, 162-167 (2017). https://doi.org/10.1038/nature22369

7 Pirman, D. A., Reich, R. F., Kiss, A., Heeren, R. M. A. & Yost, R. A. Quantitative MALDI Tandem Mass Spectrometric Imaging of Cocaine from Brain Tissue with a Deuterated Internal Standard. *Analytical Chemistry* **85**, 1081-1089 (2013). https://doi.org/10.1021/ac302960j

8 Liu, X., Flinders, C., Mumenthaler, S. M. & Hummon, A. B. MALDI Mass Spectrometry Imaging for Evaluation of Therapeutics in Colorectal Tumor Organoids. *Journal of The American Society for Mass Spectrometry* **29**, 516-526 (2018). https://doi.org/10.1007/s13361-017-1851-4

9 Shariatgorji, M. *et al.* Comprehensive mapping of neurotransmitter networks by MALDI–MS imaging. *Nature Methods* **16**, 1021-1028 (2019). https://doi.org/10.1038/s41592-019-0551-3

10 Claes, B. S. R. *et al.* MALDI-IHC-Guided In-Depth Spatial Proteomics: Targeted and Untargeted MSI Combined. *Analytical Chemistry* **95**, 2329-2338 (2023). https://doi.org/10.1021/acs.analchem.2c04220

11 Sommella, E. *et al.* MALDI Mass Spectrometry Imaging Highlights Specific Metabolome and Lipidome Profiles in Salivary Gland Tumor Tissues. *Metabolites* **12**, 530 (2022). https://doi.org/10.3390/metabo12060530

12 Kaya, I., Jennische, E., Lange, S. & Malmberg, P. Multimodal chemical imaging of a single brain tissue section using ToF-SIMS, MALDI-ToF and immuno/histochemical staining. *The Analyst* **146**, 1169-1177 (2021). https://doi.org/10.1039/d0an02172e

13 Deutskens, F., Yang, J. & Caprioli, R. M. High spatial resolution imaging mass spectrometry and classical histology on a single tissue section. *Journal of Mass Spectrometry* **46**, 568-571 (2011). https://doi.org/10.1002/jms.1926

14 Patterson, N. H. *et al.* Next Generation Histology-Directed Imaging Mass Spectrometry Driven by Autofluorescence Microscopy. *Analytical Chemistry* **90**, 12404-12413 (2018). https://doi.org/10.1021/acs.analchem.8b02885

15 Bien, T., Koerfer, K., Schwenzfeier, J., Dreisewerd, K. & Soltwisch, J. Mass spectrometry imaging to explore molecular heterogeneity in cell culture. *Proceedings of the National Academy of Sciences* **119** (2022). https://doi.org/10.1073/pnas.2114365119

16 Li, D. *et al.* Deep Learning for Virtual Histological Staining of Bright-Field Microscopic Images of Unlabeled Carotid Artery Tissue. *Molecular Imaging and Biology* **22**, 1301-1309 (2020). https://doi.org/10.1007/s11307-020-01508-6

17 Rivenson, Y. *et al.* Virtual histological staining of unlabelled tissue-autofluorescence images via deep learning. *Nature Biomedical Engineering* **3**, 466-477 (2019). https://doi.org/10.1038/s41551-019-0362-y

18 Meng, X., Li, X. & Wang, X. A Computationally Virtual Histological Staining Method to Ovarian Cancer Tissue by Deep Generative Adversarial Networks. *Computational and Mathematical Methods in Medicine* **2021**, 1-12 (2021). https://doi.org/10.1155/2021/4244157

19 Race, A. M. *et al.* Correlative Hyperspectral Imaging Using a Dimensionality-Reduction-Based Image Fusion Method. *Analytical Chemistry* **92**, 10979-10988 (2020). https://doi.org/10.1021/acs.analchem.9b05055

20 Race, A. M. *et al.* SpectralAnalysis: Software for the Masses. *Analytical Chemistry* **88**, 9451-9458 (2016). https://doi.org/10.1021/acs.analchem.6b01643

21 Ryabchykov, O., Popp, J. & Bocklitz, T. Fusion of MALDI Spectrometric Imaging and Raman Spectroscopic Data for the Analysis of Biological Samples. *Frontiers in Chemistry* **6** (2018). https://doi.org/10.3389/fchem.2018.00257

22 Aggarwal, R. L. *et al.* Measurement of the absolute Raman cross section of the optical phonon in silicon. *Solid State Communications* **151**, 553-556 (2011). https://doi.org/10.1016/j.ssc.2011.01.011

23 Kastrup, L. & Hell, S. W. Absolute Optical Cross Section of Individual Fluorescent Molecules. *Angewandte Chemie International Edition* **43**, 6646-6649 (2004). https://doi.org/10.1002/anie.200461337

24 Li, Y. *et al.* Review of Stimulated Raman Scattering Microscopy Techniques and Applications in the Biosciences. *Advanced Biology* **5**, 2000184 (2021). https://doi.org/10.1002/adbi.202000184

25 Fung, A. A. & Shi, L. Mammalian cell and tissue imaging using Raman and coherent Raman microscopy. *WIREs Systems Biology and Medicine* **12**, e1501 (2020). https://doi.org/10.1002/wsbm.1501

26 Wei, M. *et al.* Volumetric chemical imaging by clearing-enhanced stimulated Raman scattering microscopy. *Proceedings of the National Academy of Sciences* **116**, 6608-6617 (2019). https://doi.org/10.1073/pnas.1813044116

27 Lu, F.-K. *et al.* Label-free DNA imaging *in vivo* with stimulated Raman scattering microscopy. *Proceedings of the National Academy of Sciences* **112**, 11624-11629 (2015). https://doi.org/10.1073/pnas.1515121112

28 Sarri, B. *et al.* Discriminating polymorph distributions in pharmaceutical tablets using stimulated Raman scattering microscopy. *Journal of Raman Spectroscopy* **50**, 1896-1904 (2019). https://doi.org/10.1002/jrs.5743

29 Brattekås, B., Gauteplass, J., Brekke, N., Fernø, M. A. & Ersland, G. Unlocking multimodal PET-MR synergies for geoscience. *Advances in Water Resources* **142**, 103641 (2020). https://doi.org/10.1016/j.advwatres.2020.103641

30 Wang, S., Baxter, L. & Fonseca, F. Biomass fly ash in concrete: SEM, EDX and ESEM analysis. *Fuel* **87**, 372-379 (2008). https://doi.org/10.1016/j.fuel.2007.05.024

31 Neumann, E. K., Djambazova, K. V., Caprioli, R. M. & Spraggins, J. M. Multimodal Imaging Mass Spectrometry: Next Generation Molecular Mapping in Biology and Medicine. *Journal of the American Society for Mass Spectrometry* **31**, 2401-2415 (2020). https://doi.org/10.1021/jasms.0c00232

32 Krijnen, K. *et al.* A Multimodal SIMS/MALDI Mass Spectrometry Imaging Source with Secondary Electron Imaging Capabilities for Use with timsTOF Instruments. *Journal of the American Society for Mass Spectrometry* **34**, 720-727 (2023). https://doi.org/10.1021/jasms.2c00381

33 Vasquez, D. *et al.* Multimodal Scanning Microscope Combining Optical Coherence Tomography, Raman Spectroscopy and Fluorescence Lifetime Microscopy for Mesoscale Label-Free Imaging of Tissue. *Analytical Chemistry* **93**, 11479-11487 (2021). https://doi.org/10.1021/acs.analchem.1c01637

34 Lee, J. H. *et al.* Simultaneous label-free autofluorescence and multi-harmonic imaging reveals *in vivo* structural and metabolic changes in murine skin. *Biomedical Optics Express* **10**, 5431-5444 (2019). https://doi.org/10.1364/BOE.10.005431

35 Heilemann, M. *et al.* Subdiffraction-Resolution Fluorescence Imaging with Conventional Fluorescent Probes. *Angewandte Chemie International Edition* **47**, 6172-6176 (2008). https://doi.org/10.1002/anie.200802376

36 Betzig, E. *et al.* Imaging Intracellular Fluorescent Proteins at Nanometer Resolution. *Science* **313**, 1642-1645 (2006). https://doi.org/10.1126/science.1127344

37 Sharonov, A. & Hochstrasser, R. M. Wide-field subdiffraction imaging by accumulated binding of diffusing probes. *Proceedings of the National Academy of Sciences* **103**, 18911-18916 (2006). https://doi.org/doi:10.1073/pnas.0609643104

38 Zhao, Y. *et al.* Photosensitive Fluorescent Dye Contributes to Phototoxicity and Inflammatory Responses of Dye-doped Silica Nanoparticles in Cells and Mice. *Theranostics* **4**, 445-459 (2014). https://doi.org/10.7150/thno.7653

39 Dixit, R. & Cyr, R. Cell damage and reactive oxygen species production induced by fluorescence microscopy: effect on mitosis and guidelines for non-invasive fluorescence microscopy. *The Plant Journal* **36**, 280-290 (2003). https://doi.org/10.1046/j.1365-313X.2003.01868.x

40 Eggeling, C., Widengren, J., Rigler, R. & Seidel, C. A. M. Photobleaching of Fluorescent Dyes under Conditions Used for Single-Molecule Detection: Evidence of Two-Step Photolysis. *Analytical Chemistry* **70**, 2651-2659 (1998). https://doi.org/10.1021/ac980027p

41 Geertsma, E. R., Groeneveld, M., Slotboom, D.-J. & Poolman, B. Quality control of overexpressed membrane proteins. *Proceedings of the National Academy of Sciences* **105**, 5722-5727 (2008). https://doi.org/10.1073/pnas.0802190105

42 Köhler, C. *et al.* Cdc45 is limiting for replication initiation in humans. *Cell Cycle* **15**, 974-985 (2016). https://doi.org/10.1080/15384101.2016.1152424

43 Heo, M. *et al.* Impact of fluorescent protein fusions on the bacterial flagellar motor. *Scientific Reports* **7** (2017). https://doi.org/10.1038/s41598-017-11241-w

44 Liu, A. *et al.* pHmScarlet is a pH-sensitive red fluorescent protein to monitor exocytosis docking and fusion steps. *Nature Communications* **12** (2021). https://doi.org/10.1038/s41467-021-21666-7

45 Kim, J. H. *et al.* Dynamic measurement of the pH of the Golgi complex in living cells using retrograde transport of the verotoxin receptor. *Journal of Cell Biology* **134**, 1387-1399 (1996). https://doi.org/10.1083/jcb.134.6.1387

46 Reth, M. Matching cellular dimensions with molecular sizes. *Nature Immunology* **14**, 765-767 (2013). https://doi.org/10.1038/ni.2621

47 Fang, T. *et al.* Nanobody immunostaining for correlated light and electron microscopy with preservation of ultrastructure. *Nature Methods* **15**, 1029-1032 (2018). https://doi.org/10.1038/s41592-018-0177-x

48 Ries, J., Kaplan, C., Platonova, E., Eghlidi, H. & Ewers, H. A simple, versatile method for GFP-based super-resolution microscopy via nanobodies. *Nature Methods* **9**, 582-584 (2012). https://doi.org/10.1038/nmeth.1991

49 Mitchell, L. S. & Colwell, L. J. Comparative analysis of nanobody sequence and structure data. *Proteins: Structure, Function, and Bioinformatics* **86**, 697-706 (2018). https://doi.org/10.1002/prot.25497

50 Schilling, K., Brown, E. & Zhang, X. NAD(P)H autofluorescence lifetime imaging enables single cell analyses of cellular metabolism of osteoblasts *in vitro* and *in vivo* via two-photon microscopy. *Bone* **154**, 116257 (2022). https://doi.org/10.1016/j.bone.2021.116257

51 Stringari, C. *et al.* Multicolor two-photon imaging of endogenous fluorophores in living tissues by wavelength mixing. *Scientific Reports* **7** (2017). https://doi.org/10.1038/s41598-017-03359-8

52 Schaefer, P. M., Kalinina, S., Rueck, A., Von Arnim, C. A. F. & Von Einem, B. NADH Autofluorescence-A Marker on its Way to Boost Bioenergetic Research. *Cytometry Part A* **95**, 34-46 (2019). https://doi.org/10.1002/cyto.a.23597

53 Ung, T. P. L. *et al.* Simultaneous NAD(P)H and FAD fluorescence lifetime microscopy of long UVA–induced metabolic stress in reconstructed human skin. *Scientific Reports* **11** (2021). https://doi.org/10.1038/s41598-021-00126-8

54 Lakowicz, J. R. in *Principles of Fluorescence Spectroscopy.* 1-26 (Springer, 2006).

55 Raman, C. V. & Krishnan, K. S. A New Type of Secondary Radiation. *Nature* **121**, 501-502 (1928). https://doi.org/10.1038/121501c0

56 Landsberg, G. & Mandelstam, L. Über die Lichtzerstreuung in Kristallen. *Zeitschrift für Physik* **50**, 769-780 (1928). https://doi.org/10.1007/bf01339412

57 Rigneault, H. & Berto, P. Tutorial: Coherent Raman light matter interaction processes. *APL Photonics* **3**, 091101 (2018). https://doi.org/10.1063/1.5030335

58 Crawford-Manning, F. *et al.* Multiphoton imaging and Raman spectroscopy of the bovine vertebral endplate. *The Analyst* **146**, 4242-4253 (2021). https://doi.org/10.1039/d1an00702e

59 Schorr, H. C. & Schultz, Z. D. Chemical conjugation to differentiate monosaccharides by Raman and surface enhanced Raman spectroscopy. *The Analyst* (2023). https://doi.org/10.1039/d2an01762h

60 Buric, M. P., Chen, K. P., Falk, J. & Woodruff, S. D. Enhanced spontaneous Raman scattering and gas composition analysis using a photonic crystal fiber. *Applied Optics* **47**, 4255 (2008). https://doi.org/10.1364/ao.47.004255

61 McCullagh, E. A., Poleg, S., Stich, D., Moldovan, R. & Klug, A. Coherent Anti-Stokes Raman Spectroscopy (CARS) Application for Imaging Myelination in Brain Slices. *J Vis Exp* (2022). https://doi.org/10.3791/64013

62 Zumbusch, A., Holtom, G. R. & Xie, X. S. Three-Dimensional Vibrational Imaging by Coherent Anti-Stokes Raman Scattering. *Physical Review Letters* **82**, 4142-4145 (1999). https://doi.org/10.1103/physrevlett.82.4142

63 Shrivastava, A. *et al.* Diagnostic and prognostic application of Raman spectroscopy in carcinoma cervix: A biomolecular approach. *Spectrochimica Acta Part A: Molecular and Biomolecular Spectroscopy* **250**, 119356 (2021). https://doi.org/10.1016/j.saa.2020.119356

64 Xu, J. *et al.* Unveiling Cancer Metabolism through Spontaneous and Coherent Raman Spectroscopy and Stable Isotope Probing. *Cancers* **13**, 1718 (2021). https://doi.org/10.3390/cancers13071718

65 Chau, A. H. *et al.* Fingerprint and high-wavenumber Raman spectroscopy in a human-swine coronary xenograft *in vivo*. *J Biomed Opt* **13**, 040501 (2008). https://doi.org/10.1117/1.2960015

66 Zhang, X. *et al.* Label-Free Live-Cell Imaging of Nucleic Acids Using Stimulated Raman Scattering Microscopy. *ChemPhysChem* **13**, 1054-1059 (2012). https://doi.org/10.1002/cphc.201100890

67 Song, C. *et al.* High-Sensitive Assay of Nucleic Acid Using Tetrahedral DNA Probes and DNA Concatamers with a Surface-Enhanced Raman Scattering/Surface Plasmon Resonance Dual-Mode Biosensor Based on a Silver Nanorod-Covered Silver Nanohole Array. *ACS Applied Materials & Interfaces* **12**, 31242-31254 (2020). https://doi.org/10.1021/acsami.0c08453

68 Lin, H. *et al.* Microsecond fingerprint stimulated Raman spectroscopic imaging by ultrafast tuning and spatial-spectral learning. *Nature Communications* **12** (2021). https://doi.org/10.1038/s41467-021-23202-z

69 Kruglik, S. G. *et al.* Raman tweezers microspectroscopy of circa 100 nm extracellular vesicles. *Nanoscale* **11**, 1661-1679 (2019). https://doi.org/10.1039/c8nr04677h

70 Krafft, C., Neudert, L., Simat, T. & Salzer, R. Near infrared Raman spectra of human brain lipids. *Spectrochimica Acta Part A: Molecular and Biomolecular Spectroscopy* **61**, 1529-1535 (2005). https://doi.org/10.1016/j.saa.2004.11.017

71 Guleken, Z. *et al.* Correlation between endometriomas volume and Raman spectra. Attempting to use Raman spectroscopy in the diagnosis of endometrioma. *Spectrochimica Acta Part A: Molecular and Biomolecular Spectroscopy* **274**, 121119 (2022). https://doi.org/10.1016/j.saa.2022.121119

72 Wen, J. *et al.* Detection and Classification of Multi-Type Cells by Using Confocal Raman Spectroscopy. *Frontiers in Chemistry* **9** (2021). https://doi.org/10.3389/fchem.2021.641670

73 Akagi, Y., Mori, N., Kawamura, T., Takayama, Y. & Kida, Y. S. Non-invasive cell classification using the Paint Raman Express Spectroscopy System (PRESS). *Scientific Reports* **11** (2021). https://doi.org/10.1038/s41598-021-88056-3

74 Hsu, C.-C. *et al.* A single-cell Raman-based platform to identify developmental stages of human pluripotent stem cell-derived neurons. *Proceedings of the National Academy of Sciences* **117**, 18412-18423 (2020). https://doi.org/10.1073/pnas.2001906117

75 Zheng, Q. *et al.* Raman spectroscopy as a potential diagnostic tool to analyse biochemical alterations in lung cancer. *The Analyst* **145**, 385-392 (2020). https://doi.org/10.1039/c9an02175b

76 Ma, D. *et al.* Classifying breast cancer tissue by Raman spectroscopy with one-dimensional convolutional neural network. *Spectrochimica Acta Part A: Molecular and Biomolecular Spectroscopy* **256**, 119732 (2021). https://doi.org/10.1016/j.saa.2021.119732

77 Guerenne-Del Ben, T. *et al.* Multiplex coherent anti-Stokes Raman scattering highlights state of chromatin condensation in CH region. *Scientific Reports* **9** (2019). https://doi.org/10.1038/s41598-019-50453-0

78 Boorman, D. *Multimodal coherent anti-stokes raman scattering (CARS) microscopy for the detection of isotope-labelled molecules*, Cardiff University, (2019).

79 Yan, S. *et al.* Hyperspectral Stimulated Raman Scattering Microscopy Unravels Aberrant Accumulation of Saturated Fat in Human Liver Cancer. *Analytical Chemistry* **90**, 6362-6366 (2018). https://doi.org/10.1021/acs.analchem.8b01312

80 Bergner, G. *et al.* Quantitative detection of C-deuterated drugs by CARS microscopy and Raman microspectroscopy. *Analyst* **136**, 3686-3693 (2011). https://doi.org/10.1039/c0an00956c

81 Li, S. *et al.* Conjugated Polymer with Intrinsic Alkyne Units for Synergistically Enhanced Raman Imaging in Living Cells. *Angewandte Chemie International Edition* **56**, 13455-13458 (2017). https://doi.org/10.1002/anie.201707042

82 Wei, L. *et al.* Live-cell imaging of alkyne-tagged small biomolecules by stimulated Raman scattering. *Nature Methods* **11**, 410-412 (2014). https://doi.org/10.1038/nmeth.2878

83 Yamakoshi, H. *et al.* Imaging of EdU, an Alkyne-Tagged Cell Proliferation Probe, by Raman Microscopy. *Journal of the American Chemical Society* **133**, 6102-6105 (2011). https://doi.org/10.1021/ja108404p

84 Yamakoshi, H. *et al.* Alkyne-Tag Raman Imaging for Visualization of Mobile Small Molecules in Live Cells. *Journal of the American Chemical Society* **134**, 20681-20689 (2012). https://doi.org/10.1021/ja308529n

85 Li, M. *et al.* Alkyne- and Nitrile-Anchored Gold Nanoparticles for Multiplex SERS Imaging of Biomarkers in Cancer Cells and Tissues. *Nanotheranostics* **3**, 113-119 (2019). https://doi.org/10.7150/ntno.30924

86 Tang, Y. *et al.* Azo-Enhanced Raman Scattering for Enhancing the Sensitivity and Tuning the Frequency of Molecular Vibrations. *ACS Central Science* **7**, 768-780 (2021). https://doi.org/10.1021/acscentsci.1c00117

87 Miao, Y., Qian, N., Shi, L., Hu, F. & Min, W. 9-Cyanopyronin probe palette for super-multiplexed vibrational imaging. *Nature Communications* **12**, 4518 (2021). https://doi.org/10.1038/s41467-021-24855-6

88 Chen, Z. *et al.* Multicolor Live-Cell Chemical Imaging by Isotopically Edited Alkyne Vibrational Palette. *Journal of the American Chemical Society* **136**, 8027-8033 (2014). https://doi.org/10.1021/ja502706q

89 Israelsen, N. D., Wooley, D., Hanson, C. & Vargis, E. Rational design of Raman-labeled nanoparticles for a dual-modality, light scattering immunoassay on a polystyrene substrate. *Journal of Biological Engineering* **10** (2016). https://doi.org/10.1186/s13036-015-0023-y

90 Hu, F. *et al.* Supermultiplexed optical imaging and barcoding with engineered polyynes. *Nature Methods* **15**, 194-200 (2018). https://doi.org/10.1038/nmeth.4578

91 Wei, L. *et al.* Super-multiplex vibrational imaging. *Nature* **544**, 465-470 (2017). https://doi.org/10.1038/nature22051

92 Allen, F. H. *et al.* Tables of bond lengths determined by X-ray and neutron diffraction. Part 1. Bond lengths in organic compounds. *Journal of the Chemical Society, Perkin Transactions 2*, S1 (1987). https://doi.org/10.1039/p298700000s1

93 Egoshi, S., Dodo, K. & Sodeoka, M. Deuterium Raman imaging for lipid analysis. *Current Opinion in Chemical Biology* **70**, 102181 (2022). https://doi.org/10.1016/j.cbpa.2022.102181

94 Okotrub, K. A., Shamaeva, D. V. & Surovtsev, N. V. Raman spectra of deuterated hydrocarbons for labeling applications. *Journal of Raman Spectroscopy* **53**, 297-309 (2022). https://doi.org/10.1002/jrs.6279

95 Uematsu, M. & Shimizu, T. Raman microscopy-based quantification of the physical properties of intracellular lipids. *Communications Biology* **4** (2021). https://doi.org/10.1038/s42003-021-02679-w

96 Sepp, K. *et al.* Utilizing Stimulated Raman Scattering Microscopy To Study Intracellular Distribution of Label-Free Ponatinib in Live Cells. *Journal of Medicinal Chemistry* **63**, 2028-2034 (2020). https://doi.org/10.1021/acs.jmedchem.9b01546

97 Aljakouch, K. *et al.* Raman Microspectroscopic Evidence for the Metabolism of a Tyrosine Kinase Inhibitor, Neratinib, in Cancer Cells. *Angewandte Chemie International Edition* **57**, 7250-7254 (2018). https://doi.org/10.1002/anie.201803394

98 El-Mashtoly, S. F. *et al.* Label-free imaging of drug distribution and metabolism in colon cancer cells by Raman microscopy. *The Analyst* **139**, 1155 (2014). https://doi.org/10.1039/c3an01993d

99 Woodhouse, N., Majer, J., Marshall, P., Hood, S. & Notingher, I. Quantification of Drugs in Brain and Liver Mimetic Tissue Models Using Raman Spectroscopy. *Applied Spectroscopy* **0**, 00037028221139494 (2022). https://doi.org/10.1177/00037028221139494

100 Gentner, C. e., Burri, S., Charbon, E., Bruschini, C. & Hilton. Compressive Raman microspectroscopy parallelized by single-photon avalanche diode arrays. *arXiv pre-print server* (2023). arxiv:2301.07709

101 Rocha-Mendoza, I. *et al.* Rapid spontaneous Raman light sheet microscopy using cw-lasers and tunable filters. *Biomed Opt Express* **6**, 3449-3461 (2015). https://doi.org/10.1364/boe.6.003449

102 E. J. Woodbury & Ng, W. K. Ruby laser operation near IR. *Proc. Inst. Radio Eng. (IRE)* **50**, 2369 (1962).

103 Hu, F., Shi, L. & Min, W. Biological imaging of chemical bonds by stimulated Raman scattering microscopy. *Nature Methods* **16**, 830-842 (2019). https://doi.org/10.1038/s41592-019-0538-0

104 Gachet, D., Billard, F., Sandeau, N. & Rigneault, H. Coherent anti-Stokes Raman scattering (CARS) microscopy imaging at interfaces: evidence of interference effects. *Opt. Express* **15**, 10408 (2007). https://doi.org/10.1364/oe.15.010408

105 Valensise, C. M. *et al.* (IEEE).

106 Masia, F., Glen, A., Stephens, P., Borri, P. & Langbein, W. Quantitative Chemical Imaging and Unsupervised Analysis Using Hyperspectral Coherent Anti-Stokes Raman Scattering Microscopy. *Analytical Chemistry* **85**, 10820-10828 (2013). https://doi.org/10.1021/ac402303q

107 Masia, F., Karuna, A., Borri, P. & Langbein, W. Hyperspectral image analysis for CARS, SRS, and Raman data. *Journal of Raman Spectroscopy* **46**, 727-734 (2015). https://doi.org/10.1002/jrs.4729

108 Burns, K. H., Srivastava, P. & Elles, C. G. Absolute Cross Sections of Liquids from Broadband Stimulated Raman Scattering with Femtosecond and Picosecond Pulses. *Analytical Chemistry* **92**, 10686-10692 (2020). https://doi.org/10.1021/acs.analchem.0c01785

109 Ni, H. *et al.* Multiwindow SRS Imaging Using a Rapid Widely Tunable Fiber Laser. *Analytical Chemistry* **93**, 15703-15711 (2021). https://doi.org/10.1021/acs.analchem.1c03604

110 Fu, D., Holtom, G., Freudiger, C., Zhang, X. & Xie, X. S. Hyperspectral Imaging with Stimulated Raman Scattering by Chirped Femtosecond Lasers. *The Journal of Physical Chemistry B* **117**, 4634-4640 (2013). https://doi.org/10.1021/jp308938t

111 Audier, X., Heuke, S., Volz, P., Rimke, I. & Rigneault, H. Noise in stimulated Raman scattering measurement: From basics to practice. *APL Photonics* **5**, 011101 (2020). https://doi.org/10.1063/1.5129212

112 Heuke, S. *et al.* Shot-noise limited tunable dual-vibrational frequency stimulated Raman scattering microscopy. *Biomedical Optics Express* **12**, 7780-7789 (2021). https://doi.org/10.1364/BOE.446348

113 He, R. *et al.* Dual-phase stimulated Raman scattering microscopy for real-time two-color imaging. *Optica* **4**, 44 (2017). https://doi.org/10.1364/optica.4.000044

114 Sarri, B. *et al.* Stimulated Raman histology: one to one comparison with standard hematoxylin and eosin staining. *Biomed Opt Express* **10**, 5378-5384 (2019). https://doi.org/10.1364/boe.10.005378

115 Sarri, B. *et al.* Observation of the compatibility of stimulated Raman histology with pathology workflow and genome sequencing. *Translational Biophotonics* **3** (2021). https://doi.org/10.1002/tbio.202000020

116 Di, L. *et al.* Stimulated Raman Histology for Rapid Intraoperative Diagnosis of Gliomas. *World Neurosurgery* **150**, e135-e143 (2021). https://doi.org/10.1016/j.wneu.2021.02.122

117 Hollon, T. C. *et al.* Near real-time intraoperative brain tumor diagnosis using stimulated Raman histology and deep neural networks. *Nature Medicine* **26**, 52-58 (2020). https://doi.org/10.1038/s41591-019-0715-9

118 Oheim, M., Michael, D. J., Geisbauer, M., Madsen, D. & Chow, R. H. Principles of two-photon excitation fluorescence microscopy and other nonlinear imaging approaches. *Advanced Drug Delivery Reviews* **58**, 788-808 (2006). https://doi.org/10.1016/j.addr.2006.07.005

119 Squirrell, J. M., Wokosin, D. L., White, J. G. & Bavister, B. D. Long-term two-photon fluorescence imaging of mammalian embryos without compromising viability. *Nature Biotechnology* **17**, 763-767 (1999). https://doi.org/10.1038/11698

120 Kobat, D., Horton, N. & Xu, C. *In vivo* two-photon microscopy to 1.6-mm depth in mouse cortex. *Journal of Biomedical Optics* **16**, 106014 (2011).

121 Aggarwal, A. *et al.* Glutamate indicators with improved activation kinetics and localization for imaging synaptic transmission. *Nature Methods* (2023). https://doi.org/10.1038/s41592-023-01863-6

122 Ozbay, B. N. *et al.* Three dimensional two-photon brain imaging in freely moving mice using a miniature fiber coupled microscope with active axial-scanning. *Scientific Reports* **8**, 8108 (2018). https://doi.org/10.1038/s41598-018-26326-3

123 Zhang, T. *et al.* Kilohertz two-photon brain imaging in awake mice. *Nature Methods* **16**, 1119-1122 (2019). https://doi.org/10.1038/s41592-019-0597-2

124 Qin, Y. & Xia, Y. Simultaneous Two-Photon Fluorescence Microscopy of NADH and FAD Using Pixel-to-Pixel Wavelength-Switching. *Frontiers in Physics* **9** (2021). https://doi.org/10.3389/fphy.2021.642302

125 Cao, R., Wallrabe, H. & Periasamy, A. Multiphoton FLIM imaging of NAD(P)H and FAD with one excitation wavelength. *J Biomed Opt* **25**, 1-16 (2020). https://doi.org/10.1117/1.Jbo.25.1.014510

126 Kolenc, O. I. & Quinn, K. P. Evaluating Cell Metabolism Through Autofluorescence Imaging of NAD(P)H and FAD. *Antioxid Redox Signal* **30**, 875-889 (2019). https://doi.org/10.1089/ars.2017.7451

127 Campagnola, P. J. & Loew, L. M. Second-harmonic imaging microscopy for visualizing biomolecular arrays in cells, tissues and organisms. *Nature Biotechnology* **21**, 1356-1360 (2003). https://doi.org/10.1038/nbt894

128 Barad, Y., Eisenberg, H., Horowitz, M. & Silberberg, Y. Nonlinear scanning laser microscopy by third harmonic generation. *Applied Physics Letters* **70**, 922-924 (1997). https://doi.org/10.1063/1.118442

129 Bischel, L. L., Beebe, D. J. & Sung, K. E. Microfluidic model of ductal carcinoma in situ with 3D, organotypic structure. *BMC Cancer* **15**, 12 (2015). https://doi.org/10.1186/s12885-015-1007-5

130 Van Steenbergen, V. *et al.* Molecular understanding of label-free second harmonic imaging of microtubules. *Nature Communications* **10**, 3530 (2019). https://doi.org/10.1038/s41467-019-11463-8

131 Plotnikov, S. V., Millard, A. C., Campagnola, P. J. & Mohler, W. A. Characterization of the Myosin-Based Source for Second-Harmonic Generation from Muscle Sarcomeres. *Biophysical Journal* **90**, 693-703 (2006). https://doi.org/10.1529/biophysj.105.071555

132 Schürmann, S., von Wegner, F., Fink, R. H., Friedrich, O. & Vogel, M. Second harmonic generation microscopy probes different states of motor protein interaction in myofibrils. *Biophys J* **99**, 1842-1851 (2010). https://doi.org/10.1016/j.bpj.2010.07.005

133 Tokarz, D., Cisek, R., Prent, N., Fekl, U. & Barzda, V. Measuring the molecular second hyperpolarizability in absorptive solutions by the third harmonic generation ratio technique. *Analytica Chimica Acta* **755**, 86-92 (2012). https://doi.org/10.1016/j.aca.2012.09.049

134 Watanabe, T. *et al.* Characterisation of the dynamic behaviour of lipid droplets in the early mouse embryo using adaptive harmonic generation microscopy. *BMC Cell Biology* **11**, 38 (2010). https://doi.org/10.1186/1471-2121-11-38

135 Rehberg, M., Krombach, F., Pohl, U. & Dietzel, S. Label-Free 3D Visualization of Cellular and Tissue Structures in Intact Muscle with Second and Third Harmonic Generation Microscopy. *PLoS One* **6**, e28237 (2011). https://doi.org/10.1371/journal.pone.0028237

136 Capitaine, E. *et al.* Fast epi-detected broadband multiplex CARS and SHG imaging of mouse skull cells. *Biomed Opt Express* **9**, 245-253 (2018). https://doi.org/10.1364/boe.9.000245

137 Pope, I., Langbein, W., Watson, P. & Borri, P. Simultaneous hyperspectral differential-CARS, TPF and SHG microscopy with a single 5 fs Ti:Sa laser. *Opt. Express* **21**, 7096-7106 (2013). https://doi.org/10.1364/OE.21.007096

138 Griffiths, J. A Brief History of Mass Spectrometry. *Analytical Chemistry* **80**, 5678-5683 (2008). https://doi.org/10.1021/ac8013065

139 Shan, L. *et al.* Plasma and serum exosome markers analyzed by matrix-assisted laser desorption/ionization time-of-flight mass spectrometry coupled with electron multiplier. *Talanta* **247**, 123560 (2022). https://doi.org/10.1016/j.talanta.2022.123560

140 Mathew, A., Eijkel, G. B., Anthony, I. G. M., Ellis, S. R. & Heeren, R. M. A. Characterization of microchannel plate detector response for the detection of native multiply charged high mass single ions in orthogonal-time-of-flight mass spectrometry using a Timepix detector. *Journal of Mass Spectrometry* **57**, e4820 (2022). https://doi.org/10.1002/jms.4820

141 Chong, Y.-K., Ho, C.-C., Leung, S.-Y., Lau, S. K. P. & Woo, P. C. Y. Clinical Mass Spectrometry in the Bioinformatics Era: A Hitchhiker's Guide. *Computational and Structural Biotechnology Journal* **16**, 316-334 (2018). https://doi.org/10.1016/j.csbj.2018.08.003

142 Yamashita, M. & Fenn, J. B. Electrospray ion source. Another variation on the free-jet theme. *The Journal of Physical Chemistry* **88**, 4451-4459 (1984). https://doi.org/10.1021/j150664a002

143 Konermann, L., Ahadi, E., Rodriguez, A. D. & Vahidi, S. Unraveling the Mechanism of Electrospray Ionization. *Analytical Chemistry* **85**, 2-9 (2013). https://doi.org/10.1021/ac302789c

144 Van Berkel, G. J. & Kertesz, V. Using the Electrochemistry of the Electrospray Ion Source. *Analytical Chemistry* **79**, 5510-5520 (2007). https://doi.org/10.1021/ac071944a

145 Li, Z. *et al.* Single-Cell Mass Spectrometry Analysis of Metabolites Facilitated by Cell Electro-Migration and Electroporation. *Analytical Chemistry* **92**, 10138-10144 (2020). https://doi.org/10.1021/acs.analchem.0c02147

146 Sakamoto, W., Azegami, N., Konuma, T. & Akashi, S. Single-Cell Native Mass Spectrometry of Human Erythrocytes. *Analytical Chemistry* **93**, 6583-6588 (2021). https://doi.org/10.1021/acs.analchem.1c00588

147 Chen, S., Zeng, J., Zhang, Z., Xu, B. & Zhang, B. Recent advancements in nanoelectrospray ionization interface and coupled devices. *Journal of Chromatography Open* **2**, 100064 (2022). https://doi.org/10.1016/j.jcoa.2022.100064

148 Susa, A. C. *et al.* Submicrometer Emitter ESI Tips for Native Mass Spectrometry of Membrane Proteins in Ionic and Nonionic Detergents. *J Am Soc Mass Spectrom* **29**, 203-206 (2018). https://doi.org/10.1007/s13361-017-1793-x

149 Towers, M. W., Karancsi, T., Jones, E. A., Pringle, S. D. & Claude, E. Optimised Desorption Electrospray Ionisation Mass Spectrometry Imaging (DESI-MSI) for the Analysis of Proteins/Peptides Directly from Tissue Sections on a Travelling Wave Ion Mobility Q-ToF. *J Am Soc Mass Spectrom* **29**, 2456-2466 (2018). https://doi.org/10.1007/s13361-018-2049-0

150 Parrot, D., Papazian, S., Foil, D. & Tasdemir, D. Imaging the Unimaginable: Desorption Electrospray Ionization – Imaging Mass Spectrometry (DESI-IMS) in Natural Product Research. *Planta Medica* (2018). https://doi.org/10.1055/s-0044-100188

151 Piras, C. *et al.* LAP-MALDI MS coupled with machine learning: an ambient mass spectrometry approach for high-throughput diagnostics. *Chemical Science* **13**, 1746-1758 (2022). https://doi.org/10.1039/D1SC05171G

152 Elia, E. A., Niehaus, M., Steven, R. T., Wolf, J.-C. & Bunch, J. Atmospheric Pressure MALDI Mass Spectrometry Imaging Using In-Line Plasma Induced Postionization. *Analytical Chemistry* **92**, 15285-15290 (2020). https://doi.org/10.1021/acs.analchem.0c03524

153 Kompauer, M., Heiles, S. & Spengler, B. Atmospheric pressure MALDI mass spectrometry imaging of tissues and cells at 1.4-μm lateral resolution. *Nature Methods* **14**, 90-96 (2017). https://doi.org/10.1038/nmeth.4071

154 Liu, W., Nie, H., Liang, D., Bai, Y. & Liu, H. Phospholipid imaging of zebrafish exposed to fipronil using atmospheric pressure matrix-assisted laser desorption ionization mass spectrometry. *Talanta* **209**, 120357 (2020). https://doi.org/10.1016/j.talanta.2019.120357

155 Campbell, D. I., Ferreira, C. R., Eberlin, L. S. & Cooks, R. G. Improved spatial resolution in the imaging of biological tissue using desorption electrospray ionization. *Analytical and Bioanalytical Chemistry* **404**, 389-398 (2012). https://doi.org/10.1007/s00216-012-6173-6

156 Yin, R., Burnum-Johnson, K. E., Sun, X., Dey, S. K. & Laskin, J. High spatial resolution imaging of biological tissues using nanospray desorption electrospray ionization mass spectrometry. *Nature Protocols* **14**, 3445-3470 (2019). https://doi.org/10.1038/s41596-019-0237-4

157 Roach, P. J., Laskin, J. & Laskin, A. Molecular Characterization of Organic Aerosols Using Nanospray-Desorption/Electrospray Ionization-Mass Spectrometry. *Analytical Chemistry* **82**, 7979-7986 (2010). https://doi.org/10.1021/ac101449p

158 Li, X. *et al.* High-Throughput Nano-DESI Mass Spectrometry Imaging of Biological Tissues Using an Integrated Microfluidic Probe. *Analytical Chemistry* **94**, 9690-9696 (2022). https://doi.org/10.1021/acs.analchem.2c01093

159 Yang, M. *et al.* Nano-DESI Mass Spectrometry Imaging of Proteoforms in Biological Tissues with High Spatial Resolution. *Analytical Chemistry* **95**, 5214-5222 (2023). https://doi.org/10.1021/acs.analchem.2c04795

160 Karas, M. & Hillenkamp, F. Laser desorption ionization of proteins with molecular masses exceeding 10,000 daltons. *Analytical Chemistry* **60**, 2299-2301 (1988). https://doi.org/10.1021/ac00171a028

161 Buchberger, A. R., Delaney, K., Johnson, J. & Li, L. Mass Spectrometry Imaging: A Review of Emerging Advancements and Future Insights. *Analytical Chemistry* **90**, 240-265 (2018). https://doi.org/10.1021/acs.analchem.7b04733

162 Beavis, R. C., Chaudhary, T. & Chait, B. T. α-Cyano-4-hydroxycinnamic acid as a matrix for matrixassisted laser desorption mass spectromtry. *Organic Mass Spectrometry* **27**, 156-158 (1992). https://doi.org/10.1002/oms.1210270217

163 Strupat, K., Karas, M. & Hillenkamp, F. 2,5-Dihydroxybenzoic acid: a new matrix for laser desorption—ionization mass spectrometry. *International Journal of Mass Spectrometry and Ion Processes* **111**, 89-102 (1991). https://doi.org/10.1016/0168-1176(91)85050-V

164 Tressler, C. *et al.* Factorial Design to Optimize Matrix Spraying Parameters for MALDI Mass Spectrometry Imaging. *Journal of the American Society for Mass Spectrometry* **32**, 2728-2737 (2021). https://doi.org/10.1021/jasms.1c00081

165 Gemperline, E., Rawson, S. & Li, L. Optimization and Comparison of Multiple MALDI Matrix Application Methods for Small Molecule Mass Spectrometric Imaging. *Analytical Chemistry* **86**, 10030-10035 (2014). https://doi.org/10.1021/ac5028534

166 Li, S. *et al.* Electrospray deposition device used to precisely control the matrix crystal to improve the performance of MALDI MSI. *Scientific Reports* **6**, 37903 (2016). https://doi.org/10.1038/srep37903

167 Ly, A. *et al.* Site-to-Site Reproducibility and Spatial Resolution in MALDI–MSI of Peptides from Formalin-Fixed Paraffin-Embedded Samples. *PROTEOMICS – Clinical Applications* **13**, 1800029 (2019). https://doi.org/10.1002/prca.201800029

168 Huizing, L. R. S. *et al.* Development and evaluation of matrix application techniques for high throughput mass spectrometry imaging of tissues in the clinic. *Clinical Mass Spectrometry* **12**, 7-15 (2019). https://doi.org/10.1016/j.clinms.2019.01.004

169 Xie, H., Wu, R., Hung, Y. L. W., Chen, X. & Chan, T. W. D. Development of a Matrix Sublimation Device with Controllable Crystallization Temperature for MALDI Mass Spectrometry Imaging. *Analytical Chemistry* **93**, 6342-6347 (2021). https://doi.org/10.1021/acs.analchem.1c00260

170 Shanmugaraj, N., Rutten, T., Svatoš, A., Schnurbusch, T. & Mock, H.-P. Fast and Reproducible Matrix Deposition for MALDI Mass Spectrometry Imaging with Improved Glass Sublimation Setup. *Journal of the American Society for Mass Spectrometry* **34**, 513-517 (2023). https://doi.org/10.1021/jasms.2c00301

171 Chu, K. Y. *et al.* Thermal Proton Transfer Reactions in Ultraviolet Matrix-Assisted Laser Desorption/Ionization. *Journal of The American Society for Mass Spectrometry* **25**, 310-318 (2014). https://doi.org/10.1007/s13361-013-0792-9

172 Lu, I. C., Lee, C., Lee, Y.-T. & Ni, C.-K. Ionization Mechanism of Matrix-Assisted Laser Desorption/Ionization. *Annual Review of Analytical Chemistry* **8**, 21-39 (2015). https://doi.org/10.1146/annurev-anchem-071114-040315

173 Barré, F. *et al.* Faster raster matrix-assisted laser desorption/ionization mass spectrometry imaging of lipids at high lateral resolution. *International Journal of Mass Spectrometry* **437**, 38-48 (2019). https://doi.org/10.1016/j.ijms.2018.09.015

174 Wäldchen, F., Mohr, F., Wagner, A. H. & Heiles, S. Multifunctional Reactive MALDI Matrix Enabling High-Lateral Resolution Dual Polarity MS Imaging and Lipid C=C Position-Resolved MS2 Imaging. *Analytical Chemistry* **92**, 14130-14138 (2020). https://doi.org/10.1021/acs.analchem.0c03150

175 Zavalin, A., Yang, J. & Caprioli, R. Laser beam filtration for high spatial resolution MALDI imaging mass spectrometry. *J Am Soc Mass Spectrom* **24**, 1153-1156 (2013). https://doi.org/10.1007/s13361-013-0638-5

176 Dreisewerd, K., Bien, T. & Soltwisch, J. in *Mass Spectrometry Imaging of Small Molecules: Methods and Protocols* (ed Young-Jin Lee) 21-40 (Springer US, 2022).

177 Niehaus, M., Soltwisch, J., Belov, M. E. & Dreisewerd, K. Transmission-mode MALDI-2 mass spectrometry imaging of cells and tissues at subcellular resolution. *Nature Methods* **16**, 925-931 (2019). https://doi.org/10.1038/s41592-019-0536-2

178 Boskamp, M. S. & Soltwisch, J. Charge Distribution between Different Classes of Glycerophospolipids in MALDI-MS Imaging. *Analytical Chemistry* **92**, 5222-5230 (2020). https://doi.org/10.1021/acs.analchem.9b05761

179 Szaéjli, E., Feheér, T. & Medzihradszky, K. F. Investigating the Quantitative Nature of MALDI-TOF MS. *Molecular & Cellular Proteomics* **7**, 2410-2418 (2008). https://doi.org/10.1074/mcp.M800108-MCP200

180 Taylor, A. J., Dexter, A. & Bunch, J. Exploring Ion Suppression in Mass Spectrometry Imaging of a Heterogeneous Tissue. *Analytical Chemistry* **90**, 5637-5645 (2018). https://doi.org/10.1021/acs.analchem.7b05005

181 Groseclose, M. R. & Castellino, S. A Mimetic Tissue Model for the Quantification of Drug Distributions by MALDI Imaging Mass Spectrometry. *Analytical Chemistry* **85**, 10099-10106 (2013). https://doi.org/10.1021/ac400892z

182 Aboulmagd, S. *et al.* Dual Internal Standards with Metals and Molecules for MALDI Imaging of Kidney Lipids. *Analytical Chemistry* **89**, 12727-12734 (2017). https://doi.org/10.1021/acs.analchem.7b02819

183 Wu, R. *et al.* Copper adhesive tape attached to the reverse side of a non-conductive glass slide to achieve protein MALDI-imaging in FFPE-tissue sections. *Chemical Communications* **57**, 10707-10710 (2021). https://doi.org/10.1039/D1CC03629G

184 Goodwin, R. J. A. *et al.* Conductive carbon tape used for support and mounting of both whole animal and fragile heat-treated tissue sections for MALDI MS imaging and quantitation. *Journal of Proteomics* **75**, 4912-4920 (2012). https://doi.org/10.1016/j.jprot.2012.07.006

185 Naito, Y., Kotani, M. & Ohmura, T. A novel laser desorption/ionization method using through hole porous alumina membranes. *Rapid Communications in Mass Spectrometry* **32**, 1851-1858 (2018). https://doi.org/10.1002/rcm.8252

186 Kuwata, K., Itou, K., Kotani, M., Ohmura, T. & Naito, Y. DIUTHAME enables matrix-free mass spectrometry imaging of frozen tissue sections. *Rapid Communications in Mass Spectrometry* **34** (2020). https://doi.org/10.1002/rcm.8729

187 Müller, M. A., Bhandari, D. R. & Spengler, B. Matrix-Free High-Resolution Atmospheric-Pressure SALDI Mass Spectrometry Imaging of Biological Samples Using Nanostructured DIUTHAME Membranes. *Metabolites* **11**, 624 (2021).

188 De Cesare, V. *et al.* High-throughput matrix-assisted laser desorption/ionization time-of-flight (MALDI-TOF) mass spectrometry–based deubiquitylating enzyme assay for drug discovery. *Nature Protocols* **15**, 4034-4057 (2020). https://doi.org/10.1038/s41596-020-00405-0

189 Croxatto, A., Prod'hom, G. & Greub, G. Applications of MALDI-TOF mass spectrometry in clinical diagnostic microbiology. *FEMS Microbiology Reviews* **36**, 380-407 (2012). https://doi.org/10.1111/j.1574-6976.2011.00298.x

190 Boesl, U. Time-of-flight mass spectrometry: Introduction to the basics. *Mass Spectrometry Reviews* **36**, 86-109 (2017). https://doi.org/10.1002/mas.21520

191 Trimpin, S., Inutan, E. D., Herath, T. N. & McEwen, C. N. Matrix-Assisted Laser Desorption/Ionization Mass Spectrometry Method for Selectively Producing Either Singly or Multiply Charged Molecular Ions. *Analytical Chemistry* **82**, 11-15 (2010). https://doi.org/10.1021/ac902066s

192 Mamyrin, B. A., Karataev, V. I., Shmikk, D. V. & Zagulin, V. A. The mass-reflectron A new nonmagnetic time-of-flight high resolution mass-spectrometer. *Zhurnal Ehksperimental'noj i Teoreticheskoj Fiziki* **64**, 82-89 (1973).

193 Shenar, N., Sommerer, N., Martinez, J. & Enjalbal, C. Comparison of LID versus CID activation modes in tandem mass spectrometry of peptides. *Journal of Mass Spectrometry* **44**, 621-632 (2009). https://doi.org/10.1002/jms.1535

194 Suckau, D. *et al.* A novel MALDI LIFT-TOF/TOF mass spectrometer for proteomics. *Analytical and Bioanalytical Chemistry* **376**, 952-965 (2003). https://doi.org/10.1007/s00216-003-2057-0

195 Nikolaev, E. N., Kostyukevich, Y. I. & Vladimirov, G. N. Fourier transform ion cyclotron resonance (FT ICR) mass spectrometry: Theory and simulations. *Mass Spectrometry Reviews* **35**, 219-258 (2016). https://doi.org/10.1002/mas.21422

196 Eliuk, S. & Makarov, A. Evolution of Orbitrap Mass Spectrometry Instrumentation. **8**, 61-80 (2015). https://doi.org/10.1146/annurev-anchem-071114-040325

197 Ghaste, M., Mistrik, R. & Shulaev, V. Applications of Fourier Transform Ion Cyclotron Resonance (FT-ICR) and Orbitrap Based High Resolution Mass Spectrometry in Metabolomics and Lipidomics. *International Journal of Molecular Sciences* **17**, 816 (2016).

198 Philippidis, A. The Unbearable Cost of Drug Development: Deloitte Report Shows 15% Jump in R&D to $2.3 Billion. *GEN Edge* **5**, 192-198 (2023). https://doi.org/10.1089/genedge.5.1.39

199 Ekert, J. E. *et al.* Recommended Guidelines for Developing, Qualifying, and Implementing Complex *In vitro* Models (CIVMs) for Drug Discovery. *SLAS Discovery* **25**, 1174-1190 (2020). https://doi.org/10.1177/2472555220923332

200 Franzen, N. *et al.* Impact of organ-on-a-chip technology on pharmaceutical R&D costs. *Drug Discovery Today* **24**, 1720-1724 (2019). https://doi.org/10.1016/j.drudis.2019.06.003

201 Singh, V. K. & Seed, T. M. How necessary are animal models for modern drug discovery? *Expert Opinion on Drug Discovery* **16**, 1391-1397 (2021). https://doi.org/10.1080/17460441.2021.1972255

202 Van Norman, G. A. Limitations of Animal Studies for Predicting Toxicity in Clinical Trials: Is it Time to Rethink Our Current Approach? *JACC: Basic to Translational Science* **4**, 845-854 (2019). https://doi.org/10.1016/j.jacbts.2019.10.008

203 Han, J. J. FDA Modernization Act 2.0 allows for alternatives to animal testing. *Artificial Organs* **47**, 449-450 (2023). https://doi.org/10.1111/aor.14503

204 Białkowska, K., Komorowski, P., Bryszewska, M. & Miłowska, K. Spheroids as a Type of Three-Dimensional Cell Cultures—Examples of Methods of Preparation and the Most Important Application. *International Journal of Molecular Sciences* **21**, 6225 (2020). https://doi.org/10.3390/ijms21176225

205 Lin, R.-Z., Chou, L.-F., Chien, C.-C. M. & Chang, H.-Y. Dynamic analysis of hepatoma spheroid formation: roles of E-cadherin and β1-integrin. *Cell and Tissue Research* **324**, 411-422 (2006). https://doi.org/10.1007/s00441-005-0148-2

206 Schmitz, C., Potekhina, E., Irianto, T., Belousov, V. V. & Lavrentieva, A. Hypoxia Onset in Mesenchymal Stem Cell Spheroids: Monitoring With Hypoxia Reporter Cells. *Frontiers in Bioengineering and Biotechnology* **9** (2021). https://doi.org/10.3389/fbioe.2021.611837

207 Perche, F. & Torchilin, V. P. Cancer cell spheroids as a model to evaluate chemotherapy protocols. *Cancer Biol Ther* **13**, 1205-1213 (2012). https://doi.org/10.4161/cbt.21353

208 Liu, Z. G. & Jiao, D. Necroptosis, tumor necrosis and tumorigenesis. *Cell Stress* **4**, 1-8 (2019). https://doi.org/10.15698/cst2020.01.208

209 Zanoni, M. *et al.* 3D tumor spheroid models for *in vitro* therapeutic screening: a systematic approach to enhance the biological relevance of data obtained. *Scientific Reports* **6**, 19103 (2016). https://doi.org/10.1038/srep19103

210 Zhao, Z. *et al.* Organoids. *Nature Reviews Methods Primers* **2**, 94 (2022). https://doi.org/10.1038/s43586-022-00174-y

211 Hofer, M. & Lutolf, M. P. Engineering organoids. *Nature Reviews Materials* **6**, 402-420 (2021). https://doi.org/10.1038/s41578-021-00279-y

212 De Pieri, A., Korman, B. D., Jüngel, A. & Wuertz-Kozak, K. Engineering Advanced *In vitro* Models of Systemic Sclerosis for Drug Discovery and Development. *Advanced Biology* **5**, 2000168 (2021). https://doi.org/10.1002/adbi.202000168

213 Skardal, A. *et al.* Multi-tissue interactions in an integrated three-tissue organ-on-a-chip platform. *Scientific Reports* **7**, 8837 (2017). https://doi.org/10.1038/s41598-017-08879-x

214 Edington, C. D. *et al.* Interconnected Microphysiological Systems for Quantitative Biology and Pharmacology Studies. *Scientific Reports* **8** (2018). https://doi.org/10.1038/s41598-018-22749-0

215 Jodat, Y. A. *et al.* Human-Derived Organ-on-a-Chip for Personalized Drug Development. *Current Pharmaceutical Design* **24**, 5471-5486 (2019). https://doi.org/10.2174/1381612825666190308150055

216 Ortega-Prieto, A. M. *et al.* 3D microfluidic liver cultures as a physiological preclinical tool for hepatitis B virus infection. *Nature Communications* **9** (2018). https://doi.org/10.1038/s41467-018-02969-8

217 Kostrzewski, T. *et al.* Modelling human liver fibrosis in the context of non-alcoholic steatohepatitis using a microphysiological system. *Communications Biology* **4** (2021). https://doi.org/10.1038/s42003-021-02616-x

218 Deng *et al.* Engineered Liver-on-a-Chip Platform to Mimic Liver Functions and Its Biomedical Applications: A Review. *Micromachines* **10**, 676 (2019). https://doi.org/10.3390/mi10100676

219 Dixon, L. J., Barnes, M., Tang, H., Pritchard, M. T. & Nagy, L. E. Kupffer Cells in the Liver. *Comprehensive Physiology* (2013). https://doi.org/10.1002/cphy.c120026

220 Schimek, K. *et al.* Integrating biological vasculature into a multi-organ-chip microsystem. *Lab on a Chip* **13**, 3588 (2013). https://doi.org/10.1039/c3lc50217a

221 Zbinden, A. *et al.* Non-invasive marker-independent high content analysis of a microphysiological human pancreas-on-a-chip model. *Matrix Biology* **85-86**, 205-220 (2020). https://doi.org/10.1016/j.matbio.2019.06.008

222 Spencer, C. E. *et al.* Role of MALDI-MSI in combination with 3D tissue models for early stage efficacy and safety testing of drugs and toxicants. *Expert Review of Proteomics* **17**, 827-841 (2020). https://doi.org/10.1080/14789450.2021.1876568

223 Kogler, S. *et al.* Organoids, organ-on-a-chip, separation science and mass spectrometry: An update. *TrAC Trends in Analytical Chemistry* **161**, 116996 (2023). https://doi.org/10.1016/j.trac.2023.116996

224 Jo, K. *et al.* Mass spectrometric imaging of peptide release from neuronal cells within microfluidic devices. *Lab on a Chip* **7**, 1454-1460 (2007). https://doi.org/10.1039/B706940E

225 Meanwell, N. A. Improving Drug Candidates by Design: A Focus on Physicochemical Properties As a Means of Improving Compound Disposition and Safety. *Chemical Research in Toxicology* **24**, 1420-1456 (2011). https://doi.org/10.1021/tx200211v

226 Lipinski, C. A., Lombardo, F., Dominy, B. W. & Feeney, P. J. Experimental and computational approaches to estimate solubility and permeability in drug discovery and development settings. *Advanced Drug Delivery Reviews* **23**, 3-25 (1997). https://doi.org/10.1016/s0169-409x(96)00423-1

227 Butler, J. M. & Dressman, J. B. The Developability Classification System: Application of Biopharmaceutics Concepts to Formulation Development. *Journal of Pharmaceutical Sciences* **99**, 4940-4954 (2010). https://doi.org/10.1002/jps.22217

228 Bunally, S. B., Luscombe, C. N. & Young, R. J. Using Physicochemical Measurements to Influence Better Compound Design. *SLAS Discovery* **24**, 791-801 (2019). https://doi.org/10.1177/2472555219859845

229 Hoteling, A. J., Erb, W. J., Tyson, R. J. & Owens, K. G. Exploring the Importance of the Relative Solubility of Matrix and Analyte in MALDI Sample Preparation Using HPLC. *Analytical Chemistry* **76**, 5157-5164 (2004). https://doi.org/10.1021/ac049566m

230 Hou, Y., Wang, S., Bai, B., Chan, H. C. S. & Yuan, S. Accurate Physical Property Predictions via Deep Learning. *Molecules* **27**, 1668 (2022). https://doi.org/10.3390/molecules27051668

231 Mathur, S. *et al.* Evaluation of Cell Permeation of a Potent 5α-Reductase Inhibitor Using MALDI-TOF MS. *Journal of Enzyme Inhibition and Medicinal Chemistry* **19**, 425-429 (2004). https://doi.org/10.1080/14756360410001733739

232 Hann, E., Malagu, K., Stott, A. & Vater, H. in *Progress in Medicinal Chemistry* Vol. 61 (eds David R. Witty & Brian Cox) 163-214 (Elsevier, 2022).

233 Barry, J. A., Groseclose, M. R., Fraser, D. D. & Castellino, S. Revised Preparation of a Mimetic Tissue Model for Quantitative Imaging Mass Spectrometry. *Protocol Exchange* (2018). https://doi.org/10.1038/protex.2018.104

234 Lars *et al.* API design for machine learning software: experiences from the scikit-learn project. *arXiv pre-print server* (2013). arxiv:1309.0238

235 Savitzky, A. & Golay, M. J. E. Smoothing and Differentiation of Data by Simplified Least Squares Procedures. *Analytical Chemistry* **36**, 1627-1639 (1964). https://doi.org/10.1021/ac60214a047

236 Zhang, X., Hamblin, M. H. & Yin, K.-J. The long noncoding RNA Malat1: Its physiological and pathophysiological functions. *RNA Biology* **14**, 1705-1714 (2017). https://doi.org/10.1080/15476286.2017.1358347

237 Parslow, A., Cardona, A. & Bryson-Richardson, R. J. Sample Drift Correction Following 4D Confocal Time-lapse Imaging. *Journal of Visualized Experiments* (2014). https://doi.org/10.3791/51086

238 Gavish, M. & David. The Optimal Hard Threshold for Singular Values is 4/sqrt(3). *arXiv pre-print server* (2014). arxiv:1305.5870

239 Peharz, R. & Pernkopf, F. Sparse nonnegative matrix factorization with ℓ0-constraints. *Neurocomputing* **80**, 38-46 (2012). https://doi.org/10.1016/j.neucom.2011.09.024

240 Lee, D. D. & Seung, H. S. Learning the parts of objects by non-negative matrix factorization. *Nature* **401**, 788-791 (1999). https://doi.org/10.1038/44565

241 Abdi, H. & Williams, L. J. Principal component analysis. *WIREs Computational Statistics* **2**, 433-459 (2010). https://doi.org/10.1002/wics.101

242 Jain, A. K. Data clustering: 50 years beyond K-means. *Pattern Recognition Letters* **31**, 651-666 (2010). https://doi.org/10.1016/j.patrec.2009.09.011

243 Breiman, L. Random Forests. *Machine Learning* **45**, 5-32 (2001). https://doi.org/10.1023/a:1010933404324

244 Biau, G. & Scornet, E. A random forest guided tour. *TEST* **25**, 197-227 (2016). https://doi.org/10.1007/s11749-016-0481-7

245 Hinz, B., Cheremina, O. & Brune, K. Acetaminophen (paracetamol) is a selective cyclooxygenase-2 inhibitor in man. *The FASEB Journal* **22**, 383-390 (2008). https://doi.org/10.1096/fj.07-8506com

246 Fung, M., DeVoe, C., Spottiswoode, N. & Doernberg, S. B. Maribavir for Cytomegalovirus Treatment in the Real World—Not a Silver Bullet. *Open Forum Infectious Diseases* **10**, ofac686 (2023). https://doi.org/10.1093/ofid/ofac686

247 Griffiths, P. & Reeves, M. Pathogenesis of human cytomegalovirus in the immunocompromised host. *Nature Reviews Microbiology* **19**, 759-773 (2021). https://doi.org/10.1038/s41579-021-00582-z

248 Sun, K., Fournier, M., Sundberg, A. K. & Song, I. H. Maribavir: Mechanism of action, clinical, and translational science. *Clinical and Translational Science* **17** (2024). https://doi.org/10.1111/cts.13696

249 Leth, R., Elander, B., Haglund, U., Olbe, L. & Fellenius, E. Histamine H2-receptor of human and rabbit parietal cells. *American Journal of Physiology-Gastrointestinal and Liver Physiology* **253**, G497-G501 (1987). https://doi.org/10.1152/ajpgi.1987.253.4.G497

250 te Beek, E. *et al.* Pharmacokinetics and central nervous system effects of the novel dopamine D3 receptor antagonist GSK598809 and intravenous alcohol infusion at pseudo-steady state. *Journal of Psychopharmacology* **26**, 303-314 (2012). https://doi.org/10.1177/0269881111431750

251 Molica, M., Scalzulli, E., Colafigli, G., Foà, R. & Breccia, M. Insights into the optimal use of ponatinib in patients with chronic phase chronic myeloid leukaemia. *Therapeutic Advances in Hematology* **10**, 2040620719826444 (2019). https://doi.org/10.1177/2040620719826444

252 Tomlinson, L. *et al.* Using a single, high mass resolution mass spectrometry platform to investigate ion suppression effects observed during tissue imaging. *Rapid Communications in Mass Spectrometry* **28**, 995-1003 (2014). https://doi.org/10.1002/rcm.6869

253 Brandt, H., Ehmann, T. & Otto, M. Solvent selection for matrix-assisted laser desorption/ionization time-of-flight mass spectrometric analysis of synthetic polymers employing solubility parameters. *Rapid Communications in Mass Spectrometry* **24**, 2439-2444 (2010). https://doi.org/10.1002/rcm.4668

254 Wang, Z., Zhang, Q., Shen, H., Yang, P. & Zhou, X. Optimized MALDI-TOF MS Strategy for Characterizing Polymers. *Frontiers in Chemistry* **9** (2021). https://doi.org/10.3389/fchem.2021.698297

255 Li, G. *et al.* Characterizing and alleviating ion suppression effects in atmospheric pressure matrix-assisted laser desorption/ionization. *Rapid Commun Mass Spectrom* **33**, 327-335 (2019). https://doi.org/10.1002/rcm.8358

256 Park, H. J., Kim, H. J., Park, H.-K. & Chung, J.-H. Protective effect of histamine H2 receptor antagonist ranitidine against rotenone-induced apoptosis. *NeuroToxicology* **30**, 1114-1119 (2009). https://doi.org/10.1016/j.neuro.2009.08.005

257 Schrammel, J. C. *et al.* Histamine H1- and H4-receptor expression in human colon-derived cell lines. *Naunyn-Schmiedeberg's Archives of Pharmacology* **396**, 3683-3693 (2023). https://doi.org/10.1007/s00210-023-02565-8

258 Metz, B. *et al.* Identification of Formaldehyde-induced Modifications in Proteins: REACTIONS WITH MODEL PEPTIDES. *Journal of Biological Chemistry* **279**, 6235-6243 (2004). https://doi.org/10.1074/jbc.M310752200

259 Bowman, A. P. *et al.* Ultra-High Mass Resolving Power, Mass Accuracy, and Dynamic Range MALDI Mass Spectrometry Imaging by 21-T FT-ICR MS. *Analytical Chemistry* **92**, 3133-3142 (2020). https://doi.org/10.1021/acs.analchem.9b04768

260 Cheng, Q., Miao, Y., Wild, J., Min, W. & Yang, Y. Emerging applications of stimulated Raman scattering microscopy in materials science. *Matter* **4**, 1460-1483 (2021). https://doi.org/10.1016/j.matt.2021.02.013

261 Tipping, W. J., Lee, M., Serrels, A., Brunton, V. G. & Hulme, A. N. Imaging drug uptake by bioorthogonal stimulated Raman scattering microscopy. *Chemical Science* **8**, 5606-5615 (2017). https://doi.org/10.1039/c7sc01837a

262 Soudi, A., Khan, E. H., Dickinson, J. T. & Gu, Y. Observation of Unintentionally Incorporated Nitrogen-Related Complexes in ZnO and GaN Nanowires. *Nano Letters* **9**, 1844-1849 (2009). https://doi.org/10.1021/nl803830n

263 Parslow, A., Cardona, A. & Bryson-Richardson, R. J. Sample drift correction following 4D confocal time-lapse imaging. *J Vis Exp* (2014), e51086. https://doi.org/10.3791/51086

264 van Manen, H.-J., Kraan, Y. M., Roos, D. & Otto, C. Intracellular Chemical Imaging of Heme-Containing Enzymes Involved in Innate Immunity Using Resonance Raman Microscopy. *The Journal of Physical Chemistry B* **108**, 18762-18771 (2004). https://doi.org/10.1021/jp046955b

265 Lee, Y. J., Moon, D., Migler, K. B. & Cicerone, M. T. Quantitative Image Analysis of Broadband CARS Hyperspectral Images of Polymer Blends. *Analytical Chemistry* **83**, 2733-2739 (2011). https://doi.org/10.1021/ac103351q

266 Cortes, J. E. *et al.* Ponatinib in Refractory Philadelphia Chromosome–Positive Leukemias. *New England Journal of Medicine* **367**, 2075-2088 (2012). https://doi.org/10.1056/NEJMoa1205127

267 Romero, M. D. M. *et al.* Treatment of Rats with a Self-Selected Hyperlipidic Diet, Increases the Lipid Content of the Main Adipose Tissue Sites in a Proportion Similar to That of the Lipids in the Rest of Organs and Tissues. *PLoS One* **9**, e90995 (2014). https://doi.org/10.1371/journal.pone.0090995

268 O'Brien, J. S. & Sampson, E. L. Lipid composition of the normal human brain: gray matter, white matter, and myelin*. *Journal of Lipid Research* **6**, 537-544 (1965). https://doi.org/10.1016/S0022-2275(20)39619-X

269 Robinson, K. N., Steven, R. T. & Bunch, J. Matrix Optical Absorption in UV-MALDI MS. *Journal of The American Society for Mass Spectrometry* **29**, 501-511 (2018). https://doi.org/10.1007/s13361-017-1843-4

270 Soltwisch, J., Jaskolla, T. W., Hillenkamp, F., Karas, M. & Dreisewerd, K. Ion Yields in UV-MALDI Mass Spectrometry As a Function of Excitation Laser Wavelength and Optical and Physico-Chemical Properties of Classical and Halogen-Substituted MALDI Matrixes. *Analytical Chemistry* **84**, 6567-6576 (2012). https://doi.org/10.1021/ac3008434

271 Hislop, E. W., Tipping, W. J., Faulds, K. & Graham, D. Label-Free Imaging of Lipid Droplets in Prostate Cells Using Stimulated Raman Scattering Microscopy and Multivariate Analysis. *Analytical Chemistry* **94**, 8899-8908 (2022). https://doi.org/10.1021/acs.analchem.2c00236

272 Hu, J.-B., Chen, Y.-C. & Urban, P. L. Coffee-ring effects in laser desorption/ionization mass spectrometry. *Analytica Chimica Acta* **766**, 77-82 (2013). https://doi.org/10.1016/j.aca.2012.12.044

273 Maniyara, R. A. *et al.* Highly transparent and conductive ITO substrates for near infrared applications. *APL Materials* **9**, 021121 (2021). https://doi.org/10.1063/5.0040864

274 Laurie, G. W., Leblond, C. P., Inoue, S., Martin, G. R. & Chung, A. Fine structure of the glomerular basement membrane and immunolocalization of five basement membrane components to the lamina densa (basal lamina) and its extensions in both glomeruli and tubules of the rat kidney. *American Journal of Anatomy* **169**, 463-481 (1984). https://doi.org/10.1002/aja.1001690408

275 Hozan, C. T. *et al.* Rapid Screening of Retrieved Knee Prosthesis Components by Confocal Raman Micro-Spectroscopy. *Applied Sciences* **10**, 5343 (2020). https://doi.org/10.3390/app10155343

276 Müller, W. H. *et al.* Imaging Metabolites in Agar-Based Bacterial Co-Cultures with Minimal Sample Preparation using a DIUTHAME Membrane in Surface-Assisted Laser Desorption/Ionization Mass Spectrometry**. *ChemistrySelect* **7** (2022). https://doi.org/10.1002/slct.202200734

277 Ibáñez, A. J., Muck, A. & Svatoš, A. Dissipation of charge on MALDI-TOF polymeric chips using an electron-acceptor: analysis of proteins. *Journal of Mass Spectrometry* **42**, 634-640 (2007). https://doi.org/10.1002/jms.1192

278 Löhmann, C., Schachmann, E., Dandekar, T., Villmann, C. & Becker, C.-M. Developmental profiling by mass spectrometry of phosphocholine containing phospholipids in the rat nervous system reveals temporo-spatial gradients. *Journal of Neurochemistry*, no-no (2010). https://doi.org/10.1111/j.1471-4159.2010.06836.x

279 Russo, C. *et al.* Quantitative Investigation of Terbinafine Hydrochloride Absorption into a Living Skin Equivalent Model by MALDI-MSI. *Analytical Chemistry* **90**, 10031-10038 (2018). https://doi.org/10.1021/acs.analchem.8b02648

280 Deininger, S.-O. *et al.* Normalization in MALDI-TOF imaging datasets of proteins: practical considerations. *Analytical and Bioanalytical Chemistry* **401**, 167-181 (2011). https://doi.org/10.1007/s00216-011-4929-z

281 Wang, Z. *et al.* Improved MALDI imaging MS analysis of phospholipids using graphene oxide as new matrix. *Scientific Reports* **7**, 44466 (2017). https://doi.org/10.1038/srep44466

282 Bhardwaj, R., Fang, X., Somasundaran, P. & Attinger, D. Self-Assembly of Colloidal Particles from Evaporating Droplets: Role of DLVO Interactions and Proposition of a Phase Diagram. *Langmuir* **26**, 7833-7842 (2010). https://doi.org/10.1021/la9047227

283 Lin, D., Kostov, R., Huang, J. T. J., Henderson, C. J. & Wolf, C. R. Novel Pathways of Ponatinib Disposition Catalyzed By CYP1A1 Involving Generation of Potentially Toxic Metabolites. *Journal of Pharmacology and Experimental Therapeutics* **363**, 12-19 (2017). https://doi.org/10.1124/jpet.117.243246

284 Corso, M. *et al.* in *Advances in Botanical Research* Vol. 98 (eds Pierre Pétriacq & Alain Bouchereau) 35-70 (Academic Press, 2021).

285 Neumann, E. K. *et al.* Spatial Metabolomics of the Human Kidney using MALDI Trapped Ion Mobility Imaging Mass Spectrometry. *Analytical Chemistry* **92**, 13084-13091 (2020). https://doi.org/10.1021/acs.analchem.0c02051

286 Yang, H.-J. *et al.* Characterization of heme ions using MALDI-TOF MS and MALDI FT-ICR MS. *International Journal of Mass Spectrometry* **343-344**, 37-44 (2013). https://doi.org/10.1016/j.ijms.2013.03.014

287 Heap, R. E., Segarra-Fas, A., Blain, A. P., Findlay, G. M. & Trost, M. Profiling embryonic stem cell differentiation by MALDI TOF mass spectrometry: development of a reproducible and robust sample preparation workflow. *The Analyst* **144**, 6371-6381 (2019). https://doi.org/10.1039/c9an00771g

288 Korte, A. R., Morris, N. J. & Vertes, A. High Throughput Complementary Analysis and Quantitation of Metabolites by MALDI- and Silicon Nanopost Array-Laser Desorption/Ionization-Mass Spectrometry. *Analytical Chemistry* **91**, 3951-3958 (2019). https://doi.org/hydroxyvalerylcarnitine

289 Machálková, M. *et al.* Drug Penetration Analysis in 3D Cell Cultures Using Fiducial-Based Semiautomatic Coregistration of MALDI MSI and Immunofluorescence Images. *Analytical Chemistry* **91**, 13475-13484 (2019). https://doi.org/10.1021/acs.analchem.9b02462

290 Li, H. & Hummon, A. B. Imaging Mass Spectrometry of Three-Dimensional Cell Culture Systems. *Analytical Chemistry* **83**, 8794-8801 (2011). https://doi.org/10.1021/ac202356g

291 Freudiger, C. W. *et al.* Multicolored stain-free histopathology with coherent Raman imaging. *Laboratory Investigation* **92**, 1492-1502 (2012). https://doi.org/10.1038/labinvest.2012.109

292 Cascianelli, G. *et al.* Lipid microdomains in cell nucleus. *Mol Biol Cell* **19**, 5289-5295 (2008). https://doi.org/10.1091/mbc.e08-05-0517

293 Sugiura, Y. *et al.* Visualization of the cell-selective distribution of PUFA-containing phosphatidylcholines in mouse brain by imaging mass spectrometry[S]. *Journal of Lipid Research* **50**, 1776-1788 (2009). https://doi.org/10.1194/jlr.M900047-JLR200

294 Sugiura, Y., Zaima, N., Setou, M., Ito, S. & Yao, I. Visualization of acetylcholine distribution in central nervous system tissue sections by tandem imaging mass spectrometry. *Analytical and Bioanalytical Chemistry* **403**, 1851-1861 (2012). https://doi.org/10.1007/s00216-012-5988-5

295 Puolitaival, S. M., Burnum, K. E., Cornett, D. S. & Caprioli, R. M. Solvent-free matrix dry-coating for MALDI imaging of phospholipids. *Journal of the American Society for Mass Spectrometry* **19**, 882-886 (2008). https://doi.org/10.1016/j.jasms.2008.02.013

296 Long, T. J. *et al.* Modeling Therapeutic Antibody–Small Molecule Drug-Drug Interactions Using a Three-Dimensional Perfusable Human Liver Coculture Platform. *Drug Metabolism and Disposition* **44**, 1940-1948 (2016). https://doi.org/10.1124/dmd.116.071456

297 Gallagher, E. M. *et al.* Normalization of organ-on-a-Chip samples for mass spectrometry based proteomics and metabolomics via Dansylation-based assay. *Toxicology in vitro* **88**, 105540 (2023). https://doi.org/10.1016/j.tiv.2022.105540

298 Vit, F. F. *et al.* A modular, reversible sealing, and reusable microfluidic device for drug screening. *Analytica Chimica Acta* **1185**, 339068 (2021). https://doi.org/10.1016/j.aca.2021.339068

299 Zhu, Y. *et al.* State of the art in integrated biosensors for organ-on-a-chip applications. *Current Opinion in Biomedical Engineering* **19**, 100309 (2021). https://doi.org/10.1016/j.cobme.2021.100309

300 Ding, C., Chen, X., Kang, Q. & Yan, X. Biomedical Application of Functional Materials in Organ-on-a-Chip. *Front Bioeng Biotechnol* **8**, 823 (2020). https://doi.org/10.3389/fbioe.2020.00823

301 Mukherjee, P. *et al.* Differential Uptake of Antisense Oligonucleotides in Mouse Hepatocytes and Macrophages Revealed by Simultaneous Two-Photon Excited Fluorescence and Coherent Raman Imaging. *Nucleic Acid Ther* **32**, 163-176 (2022). https://doi.org/10.1089/nat.2021.0059

302 Tutty, M. A., Movia, D. & Prina-Mello, A. Three-dimensional (3D) liver cell models - a tool for bridging the gap between animal studies and clinical trials when screening liver accumulation and toxicity of nanobiomaterials. *Drug Delivery and Translational Research* **12**, 2048-2074 (2022). https://doi.org/10.1007/s13346-022-01147-0

303 Workman Jr, J. J. J. *Concise Handbook Of Analytical Spectroscopy, The: Theory, Applications, And Reference Materials (In 5 Volumes)*. (World Scientific, 2016).

304 Beekes, M., Lasch, P. & Naumann, D. Analytical applications of Fourier transform-infrared (FT-IR) spectroscopy in microbiology and prion research. *Veterinary microbiology* **123 4**, 305-319 (2007).

305 Luo, Q. *et al.* Enterotoxigenic Escherichia coli secretes a highly conserved mucin-degrading metalloprotease to effectively engage intestinal epithelial cells. *Infect Immun* **82**, 509-521 (2014). https://doi.org/10.1128/iai.01106-13

306 Gunther, G. R., Wang, J. L., Yahara, I., Cunningham, B. A. & Edelman, G. M. Concanavalin A derivatives with altered biological activities. *Proc Natl Acad Sci U S A* **70**, 1012-1016 (1973). https://doi.org/10.1073/pnas.70.4.1012

307 Huang, W. *et al.* Raman spectroscopy and machine learning for the classification of esophageal squamous carcinoma. *Spectrochimica Acta Part A: Molecular and Biomolecular Spectroscopy* **281**, 121654 (2022). https://doi.org/10.1016/j.saa.2022.121654

308 Managò, S., Mirabelli, P., Napolitano, M., Zito, G. & De Luca, A. C. Raman detection and identification of normal and leukemic hematopoietic cells. *Journal of Biophotonics* **11**, e201700265 (2017). https://doi.org/10.1002/jbio.201700265

309 Raniga, K., Stebbeds, W., Shivalingam, A., Pemberton, M. & Denning, C. Design of experiments for the automated development of a multicellular cardiac model for high-throughput screening. *SLAS Discovery* **28**, 410-417 (2023). https://doi.org/10.1016/j.slasd.2023.10.006

310 Seifert, S. Application of random forest based approaches to surface-enhanced Raman scattering data. *Scientific Reports* **10** (2020). https://doi.org/10.1038/s41598-020-62338-8

311 Bergman, H.-M., Lundin, E., Andersson, M. & Lanekoff, I. Quantitative mass spectrometry imaging of small-molecule neurotransmitters in rat brain tissue sections using nanospray desorption electrospray ionization. *Analyst* **141**, 3686-3695 (2016). https://doi.org/10.1039/C5AN02620B

312 Orringer, D. A. *et al.* Rapid intraoperative histology of unprocessed surgical specimens via fibre-laser-based stimulated Raman scattering microscopy. *Nature Biomedical Engineering* **1**, 0027 (2017). https://doi.org/10.1038/s41551-016-0027

313 Iakab, S.-A. *et al.* SALDI-MS and SERS Multimodal Imaging: One Nanostructured Substrate to Rule Them Both. *Analytical Chemistry* **94**, 2785-2793 (2022). https://doi.org/10.1021/acs.analchem.1c04118

314 McMillen, J. C., Fincher, J. A., Klein, D. R., Spraggins, J. M. & Caprioli, R. M. Effect of MALDI matrices on lipid analyses of biological tissues using MALDI-2 postionization mass spectrometry. *J Mass Spectrom* **55**, e4663 (2020). https://doi.org/10.1002/jms.4663

315 Jayasundara, K. U. *et al.* Physicochemical Property Correlations with Ionization Efficiency in Capillary Vibrating Sharp-Edge Spray Ionization (cVSSI). *J Am Soc Mass Spectrom* **32**, 84-94 (2021). https://doi.org/10.1021/jasms.0c00100

316 Barré, F. P. Y. *et al.* Enhanced Sensitivity Using MALDI Imaging Coupled with Laser Postionization (MALDI-2) for Pharmaceutical Research. *Analytical Chemistry* **91**, 10840-10848 (2019). https://doi.org/10.1021/acs.analchem.9b02495

Appendix

Analyte	Solubility (µM aq.)	Permeability (nm/s)	HSA binding (%)	IAM binding (%)
GSK1	341	6.5	24	2.9
GSK2	426	1	93	36
GSK4(x)	329	39	58	28
GSK10	401	313	94	40
GSK90	157	318	97	56

Appendix 1. Physicochemical properties of test compounds. Solubility or kinetic aqueous solubility was shown with "µM aq." Values, which described the concentration of analyte which was dissolved from DMSO into PBS. Permeability was denoted in nm/s, which described the speed of permeation of an analyte through an artificial membrane. The human serum albumin (HSA) binding values described the percentage of the analyte which was bound to albumin. The lipid binding was shown as the percentage of analyte which was bound an immobilisation artificial membrane.

	100 µg/ml	10 µg/ml	1 µg/ml	0 µg/ml
GSK1	133	14	12	2
GSK2	118	42	26	3
GSK4	188	201	73	2
GSK10	221	319	21	2
GSK90	383	438	3	2

Appendix 2. MALDI SNR of tool compound ions. Supplementary table to Figure 4.3.

Drug conc. (mM)	GSK90	GSK4	GSK2	GSK2 N2	DMSO	PBS	Glass	Air
100	142.4	45.2	3.0	1.3	nan	nan	nan	nan
50	123.9	29.1	2.2	2.7	nan	nan	nan	nan
10	41.2	1.9	0.1	2.9	nan	nan	nan	nan
5	18.4	1.3	0.1	2.7	nan	nan	nan	nan
0	nan	nan	nan	nan	3.6	8.8	5.1	2.1

Appendix 3. SRS SNR of pure tool compounds. Supplementary table to Figure 4.13.

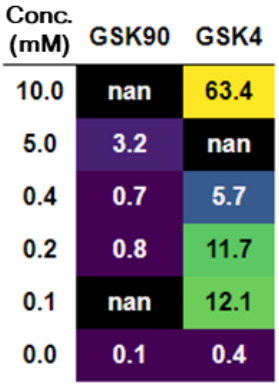

Appendix 4. SRS SNR of tool compounds in tissue homogenate spot analysis. Supplementary table to Figure 4.14.

Frame				Membrane	
m/z	SNR	*m/z*	SNR	*m/z*	SNR
104.904	12	391.761	48	103.931	9
159.927	7	392.787	16	105.039	18
161.942	21	393.774	14	133.066	31
191.78	10	399.757	19	190.928	9
193.77	521	400.763	38	193.944	197
194.776	465	401.777	51	194.946	183
195.784	342	402.776	29	195.947	119
197.803	95	403.791	20	197.952	33
205.802	24	404.827	11	207.958	7
206.805	26	405.778	8	220.933	13
207.809	27	446.719	6	221.947	16
208.805	85	581.718	7	222.934	11
211.814	11	582.772	21	327.006	10
212.813	8	583.785	32	387.93	37
220.807	10	584.776	28	388.928	58
221.794	20	585.773	25	389.926	85

222.793	16	586.781	13	390.935	34
223.794	10	587.787	9	391.926	27
224.797	8	594.778	14	393.946	8
225.800	9	595.731	21	401.948	8
251.735	16	596.810	23	403.910	6
252.723	11	597.802	17	432.886	6
253.726	17	598.842	9	489.672	7
255.728	7	599.797	8	583.945	9
387.736	78	778.763	6	586.963	6
388.736	150	790.784	8		
389.745	173	791.762	6		
390.751	82	792.647	8		

Appendix 5. List of all low molecular weight ions in the DIUTHAME membrane and frame.

M/z	Mol. Formula	Monoisotopic neutral mass	Δ
194.917	[Pt]•	194.965	0.048
221.908	[AlPt]•	221.946	0.038
326.940	[C4H2Al3Pt+H]$^{+}$┤	326.933	0.007
326.940	[C2Al4Pt]$^{+}$†	326.891	0.049
389.885	[Pt2]•	389.928	0.043
584.877	[Pt3]•	584.893	0.016

Appendix 6. A list of putative metal ions in a DIUTHAME membrane.

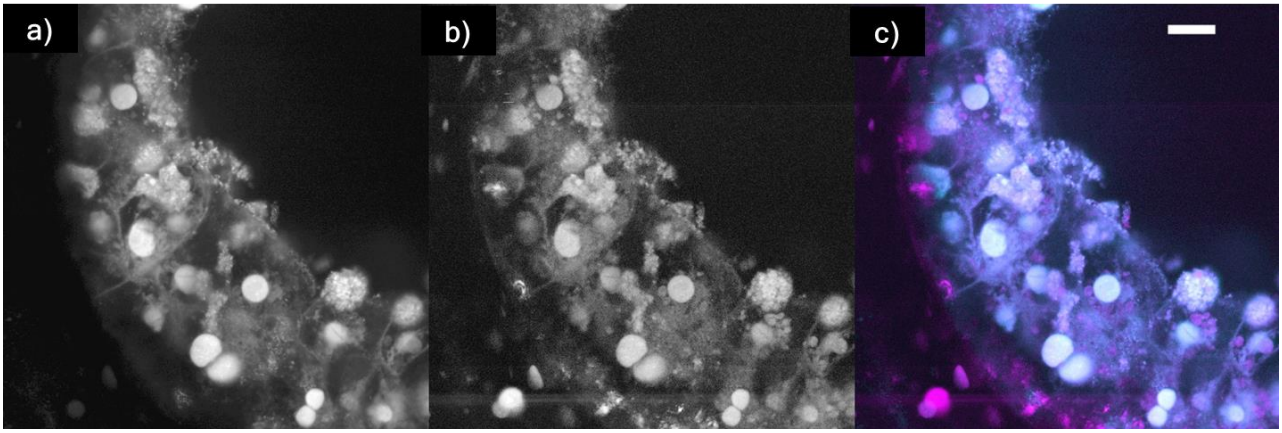

Appendix 7. Detection of ASO A488 signal in a) fluorescence channel and b) in SHG channel. c) The overlay of a) and b) was shown in cyan and magenta, respectively. Scale bar = 20 µm.

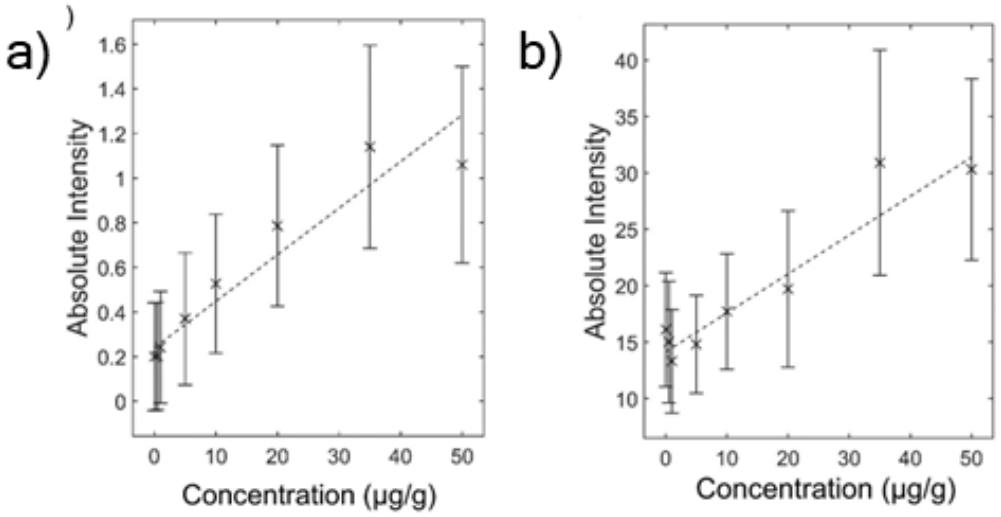

Appendix 8. Calibration curves of GSK4 (a) and GSK90(b) murine brain mimetic models at low concentrations. Figure by Woodhouse *et. al.*, copyright CC BY 4.0.[99]